Final Technical Report (FTR)

Agency/Office/Program	DOE/EERE/Solar Energy Technology Office	
Award Number	DE-EE0002064	
Project Title	Library of Advanced Models of large-scale PV (LAMP)	
Principal Investigator	Suman Debnath Senior R&D Staff debnaths@ornl.gov (865) 341-1467	
Business Contact	Madhu Chinthavali chinthavalim@ornl.gov (865) 341-1411	
Submission Date	11/15/2023	
DUNS Number	099114287	
Recipient Organization	Oak Ridge National Laboratory	
Project Period	**Start:** 04/01/2020	**End:** 09/30/2023

Suman Debnath — *Signature of Certifying Official*

03/20/2023 — *Date*

By signing this report, I certify to the best of my knowledge and belief that the report is true, complete, and accurate. I am aware that any false, fictitious, or fraudulent information, misrepresentations, half-truths, or the omission of any material fact, may subject me to criminal, civil or administrative penalties for fraud, false statements, false claims or otherwise. (U.S. Code Title 18, Section 1001, Section 287 and Title 31, Sections 3729-3730). I further understand and agree that the information contained in this report are material to Federal agency's funding decisions and I have any ongoing responsibility to promptly update the report within the time frames stated in the terms and conditions of the above referenced Award, to ensure that my responses remain accurate and complete.

Acknowledgement: “This material is based upon work supported by the U.S. Department of Energy’s Office of Energy Efficiency and Renewable Energy (EERE) under the Advanced Power Electronics Design for Solar Applications FOA Award Number 36352.”

Executive Summary: A suite of dynamic models of photovoltaic (PV) systems is developed in this project to accurately capture PV system dynamics during different contingencies. The following models are included: (i) quasi-dynamic, (ii) high-fidelity electromagnetic transient (EMT), (iii) advanced, and (iv) baseline. The models have the flexibility to consider different control functionalities at different controller levels. The study's requirements determine the type of model needed. For example, high-fidelity EMT models are recommended for contingency studies. Advanced models are recommended for online or real-time implementations with resource constraints, whereas quasi-dynamic models are useful for studying the impact of weather variations.

The high-fidelity EMT model of a PV plant has shown greater than 98% accuracy and speed up to 326 times faster than that of baseline models. This model incorporates a switched system dynamic model of each individual PV inverter with or without dc-dc converters in a PV plant along with the model of each individual filter, distribution transformer, cable, line, shunt, power transformer, and other plant parts. As a result, hundreds of models of inverters and filters and tens of models of distribution transformers, cables, and lines exist. The inverter controllers with or without dc-dc converter controllers with the power plant controller are also present in the model. To achieve the aforementioned speed-up, numerical simulation algorithms have been applied, such as numerical stiffness-based hybrid discretization, relaxation methods, differential algebraic equation clustering and aggregation, multi-order discretization, and multiple A matrix solvers with approximation or the Kron's reduction method. This model has been used to represent a PV plant that was affected by the partial reduction in power generation during the Angeles Forest 2018 event. These developments have happened in Fortran and C scripts that can be integrated within PSCAD and RSCAD software, respectively, for offline and hardware-based simulations.

High-fidelity EMT models of power grids in present and future scenarios have been developed using transient stability (TS) data available for the power grid. A process to develop such models has been published; this process is essential as utilities and system operators move toward the development of EMT models for their systems. The high-fidelity EMT model of the power grid in the present scenario was developed to replicate local measurements observed near the fault buses in the Angeles Forest 2018 event and to replicate observations within the affected PV plant upon which a high-fidelity model had been developed. In such studies, EMT-TS cosimulation capability has been established to highlight replication of the event. The EMT-TS cosimulation enables large system studies such as the impact of partial loss of generation from multiple PV plants in a local region in the Western Interconnection power grid. The future grid scenario's EMT model has been used to highlight the interactions expected between multiple PV plants and power grids when fault events happen. These interactions lead to a partial reduction in power generation from individual PV plants, as has been observed during recent events in the power grid with large local penetration of inverter-based resources (IBRs) like PV plants. This analysis has shown the need for high-fidelity EMT models of different components in the power grid when faults are analyzed, such as in planning and operational studies.

Finally, future grid scenarios with 60% and 100% penetration of IBRs in California are developed. These scenarios are analyzed with advanced control functionalities in IBRs

to evaluate stability of the power grid. The analysis has provided insights in terms of the type of voltage and frequency control needed in the power plant controller and inverter controllers to reduce the impact of faults on the power grid. This is a preliminary analysis in TS simulations and a first-of-its-kind analysis to understand the control requirements in IBRs in future power grids. Such analysis will need to be confirmed in EMT simulations once large-scale models can be developed (currently a limitation owing to a lack of models and challenges with scalability in EMT simulations).

Table of Contents:

Acknowledgement: 2
Disclaimer: 2
Executive Summary: 3
List of Figures: 7
List of Tables: 15
Background: 16
Project Objectives: 16
Abbreviations: 18
Project Results and Discussion: 20
T-1. Data collection and nondisclosure agreements (NDAs) 20
ST-1.1 PV system data collection 20
ST-1.2 PV configuration data collection 20
ST-1.3 Contingency event data collection 20
ST-1.4 Grid model 20
ST-1.5 NDAs 21
ST-1.6 Industry Advisory Board (IAB) formation 21
T-2. Develop baseline PV system model 21
ST-2.1 Model development 21
ST-2.2 Testing 23
T-3. Develop suite of dynamic PV system models 23
ST-3.1 Quasi-dynamic model in PSCAD/PSSE 23
ST-3.2 High-fidelity model in PSCAD 24
ST-3.3 Advanced model in PSCAD/PSSE 27
T-4. Evaluation and redesign dynamic models 28
ST-4.1 Evaluation of quasi-dynamic model 28
T-5. Present scenario development 30
ST-5.1 Develop dynamic (EMT-TS) model of present grid in PSCAD 30
ST-5.2 Evaluate performance and redesign in real-time simulations in a real-time simulator (like RTDS) 33
T-6. Future scenario model development 33
ST-6.1 Collect information on future PV in queue 33
ST-6.2 Upgrade present model with future model in PSCAD 34
T-7. Advanced control functionalities 34
ST-7.1 Collect data on future PV system response requirements 34
ST-7.2 Design advanced control functionalities 34
T-8. Develop suite of dynamic PV system models 35
ST-8.1 High-fidelity model in PSCAD 35
ST-8.2 Advanced model in PSCAD/PSSE 37
T-9. Evaluation and redesign dynamic models 39
ST-9.1 Evaluation of high-fidelity model 39
ST-9.2 Evaluation of advanced model 42
T-10. Present scenario development 42

ST-10.1 Incorporate suite of dynamic PV system models 42
T-11. Future scenario model development 48
ST-11.1 Upgrade present model with future model in PSCAD 48
ST-11.2 Incorporate suite of dynamic PV system models 49
ST-11.3 Test and redesign in real-time simulations in a real-time simulator (like RTDS) 49
T-12. Validation of PV system models in present scenario 49
ST-12.1 Evaluate performance of PV system models within present scenario in PSCAD/PSSE 49
T-13. Advanced control functionalities 51
ST-13.1 Incorporate designed control methods 51
ST-13.2 Evaluate performance in suite of dynamic models and redesign 53
T-14. Demonstration of future scenario 54
ST-14.1 Evaluate performance of advanced control functions 54
T-15. Advanced control functionalities 57
ST-15.1 Evaluate performance in future grid scenarios and redesign 57
T-16. Investigation of future scenarios 63
ST-16.1 Incorporate advanced control functionalities into future grid scenarios in real-time simulation 63
T-17. Demonstration of generic present grid scenario 67
ST-17.1 Develop a test case for IEEE case study 67
ST-17.2 Integrate generic PV plant in IEEE case study 68
ST-17.3 Demonstration of generic PV plant in generic grid model 70
Significant Accomplishments and Conclusion: 74
Path Forward: 76
Products: 77
Project Team and Roles: 82
Appendix: 83
References: 190

List of Figures:

Fig. 3.2-1: Overview of the advanced simulation algorithm for the large number of PV systems in the MV distribution grid. 25
Fig. 3.2-2: Comparison of the simulation of the MV distribution grid with a large number of PV systems based on the proposed simulation algorithms: (a) dc-dc boost converter inductor current (iL,pv) in one PV system, (b) errors of the inductor current (iL,pv), (c) dc link voltage ($v\mathrm{dc}$), and (d) error of the dc link voltage ($v\mathrm{dc}$). 26
Fig. 3.2-3: Comparison of the simulation of the MV distribution grid with a large number of PV systems based on the proposed simulation algorithms: (a) filter capacitor voltage ($va,\mathrm{ac},\mathrm{fil}$) phase A in one PV system, (b) dc-ac inverter output current ($ia,\mathrm{ac},\mathrm{fil}$) phase A in one PV system, (c) grid voltage (va,grid) phase A at the primary side of distribution transformer, and (d) grid current (ia,grid) phase A at the primary side of distribution transformer. 27
Fig. 4.1-1: Top traces: Real power output of inverter 1 ac side—PSCAD simulation and field data. Middle trace: Instantaneous error between the real power output of inverter 1 ac side—PSCAD simulation minus field data. Bottom trace: RMS error of the middle trace—RMS was computed over a sliding time window of 480 s. 29
Fig. 4.1-2: The dc power (top), real power (middle), and reactive power (bottom) of inverter 1 from the simulation of the baseline and quadratized models. 30
Fig. 5.1-1: Minimum spanning tree from fault bus to one affected PV plant with one-hop method. 32
Fig. 5.1-2: Voltage and current plots form the EMT simulation at the local end and the substation away from the local end on the faulted transmission line. 32
Fig. 7.2-1: Single-line diagram representation of the PSCAD model for steady state analysis. 35
Fig. 8.1-1: Simulation results for the specific PV plant-1. 36
Fig. 8.2-1: Process to generate an advanced model in PSCAD with a greater degree of automation. The automation aspects of the process are shown in bold, italicized text. 37
Fig. 8.2-2: Circuit implementation of RNN AI model for one PV system in PV plant-1. 38
Fig. 8.2-3: Advanced model's active power output (P1Labc = advanced model output; Pac = baseline model output). 38
Fig. 9.1-1: Simulation results for the specific PV plant-1. 40
Fig. 9.1-2: Simulation results for the specific PV plant-1 during steady state: (a) $P_{ac,HV}$, (b) $Q_{ac,HV}$, (c) $P_{ac,LV2}$, and (d) $Q_{ac,LV2}$. 41
Fig. 9.1-3: Simulation results for the specific PV plant-1 during capacitor switching in module 2: (a) $P_{ac,HV}$, (b) $Q_{ac,HV}$, (c) $P_{ac,LV2}$, and (d) $Q_{ac,LV2}$. 41
Fig. 9.2-1: Advanced model's active power output (P1Labc = advanced model output, Pac = baseline model output). 42
Fig. 9.2-2: Simulation results from the advanced model's integration within the specific PV plant-1. Shown are the behavior of the distribution grid voltage (left) and the PV system current (right) as expected. 42
Fig. 10.1-1: EMT simulation results from the power grid in three cases: (a) local end voltages and currents, (b) remote end voltages and currents (solid line: Case 1; dotted line: Case 2; dashed line: Case 3), (c) error plot for local end voltages (top) and current (bottom) between Cases 3 and 1, and (d) error plot for remote end voltages (top) and current (bottom) between Cases 3 and 1. 43
Fig. 10.1-2: Local end and remote end voltage and current plots from the EMT simulation of the present scenario grid model Case 3 with the Angeles Forest fault event. 44

Fig. 10.1-3: Continuous time difference between Cases 1 and 2 for the local end and remote end voltage and current plots. 44
Fig. 10.1-4: Voltage plots near one affected PV plant from the EMT simulation of the present scenario grid model for the Angeles Forest fault event....45
Fig. 10.1-5: High-fidelity model of the specific PV plant-1 developed in RSCAD. 47
Fig. 12.1-1: Simulation results from the integrated EMT high-fidelity model (grid-plant) during line-to-line fault: (a) voltages at the near end of the faulted line; (b) currents at the near end of the faulted line; (c) voltages at the remote end of the faulted line; and (d) currents at the remote end of the faulted line....50
Fig. 12.1-2: Specific PV plant response during line-to-line fault: (a) $P_{ac,HV}$; (b) $Q_{ac,HV}$; (c) $P_{ac,LV1}$; (d) $P_{ac,LV2}$; (e) $Q_{ac,LV1}$; and (f) $Q_{ac,LV2}$....51
Fig. 13.1-1: PI controller (top); MPC controller (bottom). 52
Fig. 13.1-2: Comparison of reactive power responses with MPC (vs. PI). 53
Fig. 13.2-1: PV plant's POI powers and voltage during a three-phase-to-ground fault on the transmission line connecting to the PV plant with Rf = 0.2 Ω, without and with support at the POI (left and right, respectively). 53
Fig. 13.2-2: Reactive power waveforms at the inverter level without and with support (left and right, respectively). 54
Fig. 14.1-1: Frequency plot after the event simulation in Scenario 1. 54
Fig. 14.1-2: Frequency plot for Scenario 2 after Palo Verde event simulation....56
Fig. 14.1-3: Frequency plot after Palo Verde generation loss. (a) Scenario 2A: voltage control in all and frequency control in Y% of replaced plants—stable for Y > 33; (b) Scenario 2B: both voltage and frequency controls in X% of replaced plants—stable for X > 39....57
Fig. 15.1-1: Specific PV plant-1 for different shunt configurations using min bus grid scenario: (a) Pac when shunts-2 are enabled only in module 1; (b) Pac when shunts-2 are enabled in all modules; (c) Pac when shunts-2 are enabled only in module 2; and (d) Pac when shunts-2 are disabled in all the modules....59
Fig. 15.1-2: Specific PV plant-1 for different shunt configurations using min bus grid scenario (with Vac-peak-based protection algorithm): (a) Pac when shunts-2 are enabled only in module 1; (b) Pac when shunts-2 are enabled in all modules; (c) Pac when shunts-2 are enabled only in module 2; and (d) Pac when shunts-2 are disabled in all the modules. 60
Fig. 15.1-3: Specific PV plant-1 for different shunt configurations using best-case grid scenario: (a) Pac when shunts-2 are enabled only in module 1; (b) Pac when shunts-2 are enabled in all modules; (c) Pac when shunts-2 are enabled only in module 2; and (d) Pac when shunts-2 are disabled in all the modules....61
Fig. 15.1-4: Response of the fault event in the developed WECC scenario with 100% renewable generation in California. 62
Fig. 15.1-5: Response of the generation loss event in the developed WECC scenario with 100% renewable in California....63
Fig. 16.1-1: Future scenario grid generic model in RSCAD (RTDS) for real-time simulation. 64
Fig. 16.1-2: Results comparison of the fault response on the future scenario grid generic model: local end and remote end voltages and currents from the PSCAD model (left) and RSCAD model (right). 65
Fig. 16.1-3: Results comparison of the fault response on the future scenario grid generic model: PV plant terminal voltages from the PSCAD model (left) and RSCAD model (right)....65

Fig. 16.1-4: Results of the fault response on the future scenario grid generic model: PV plant terminal voltages and output power of the PV plant during the fault condition from the RSCAD model. 66
Fig. 16.1-5: Advanced power plant controller for a PV plant in the future grid model in RSCAD....66
Fig. 17.1-1: IEEE nine-bus system diagram. 67
Fig. 17.2-1: Detailed layout of the generic PV plant....68
Fig. 17.2-2: Simulation results for the generic PV plant: (a) active power of the PV plant; (b) grid currents; and (c) three-phase voltage for one of the PV systems....69
Fig. 17.2-3: Simulation results for the generic PV plant: (a) inverter active power; (b) three-phase inverter currents; (c) dc-dc converter inductor current; and (d) dc-dc converter input PV capacitor voltage and dc-ac inverter dc capacitor voltage....69
Fig. 17.3-1: Frequency plot after a generator loss event. 70
Fig. 17.3-2: Response after a generator loss simulation in PSCAD for the IEEE nine-bus scenario with 50% renewable penetration. 71
Fig. 17.3-3: Response after fault simulation for IEEE nine-bus scenario: (a) original, (b) 50% renewable energy with Kqv = 2 for renewable plants, and (c) 50% renewable energy with Kqv = 0 for renewable plants. 71
Fig. 17.3-4: Response after fault simulation in the PSCAD model with 50% renewable penetration. 72
Fig. 17.3-5: (a) Active power response of IBR, and (b) ac voltage under single-line-to-ground fault in IEEE nine-bus system with 25% renewable penetration (and with one IBR in the IEEE nine-bus system)....72
Fig. 17.3-6: (a) Active power response of IBR1, and (b) active power response of IBR2 under single-line-to-ground fault in IEEE nine-bus system with 50% renewable penetration (and with two IBRs in the IEEE nine-bus system). 73
Fig. A1.1-1: List of PV systems in California with power rating and locations. 83
Fig. A2.1-1: Overview of the large PV plant....84
Fig. A2.1-2: Power plant controller**.** 85
Fig. A2.1-3: Multiple PV modules in the developed feeder module....85
Fig. A2.1-4: PV system in the developed PV module. 85
Fig. A2.1-5: PV array model parameters. 86
Fig. A2.1-6: Small PV plant model....86
Fig. A2.1-7: PV system model....87
Fig. A2.1-8: dc-dc converter control modes....87
Fig. A2.1-9: Inner *dq* current control in inverter. 88
Fig. A2.1-10: Outer loop control. 88
Fig. A2.2-1: Simulation results: voltage and current measured at the point of connection for one of the 36 feeder modules in the baseline large PV plant model....89
Fig. A2.2-2: Simulation results: Reactive power (high-voltage side) and reactive power (low-voltage sides) of the baseline large PV plant (based on data collected in ST-1.2) during switching events. 89
Fig. A2.2-3: Simulation results: Power measured at the POI of the PV system in the small PV plant....89
Fig. A3.1-1: Overall block diagram of quasi-dynamic quadratized inverter model....90
Fig. A3.1-2: Inverter circuit configuration....90
Fig. A3.1-3: User interface for quasi-dynamic domain inverter model that shows the parameters used to define the model. 91
Fig. A3.2-1: Configuration of a large PV plant in a medium-voltage (e.g., 34.5 kV) distribution system connected to a high-voltage (e.g., 230 kV) transmission system....93

Fig. A3.2-2: Configuration of the PV inverter module. 94
Fig. A3.2-3: Configuration of multiple PV systems through a distribution transformer. 95
Fig. A3.2-4: Nonlinear behavior of the transformer with a ferromagnetic core. 97
Fig. A3.2-5: Three-phase, single ferromagnetic core transformer. 97
Fig. A3.2-6: Measurement setup for magnetic field intensity and density nonlinear dependencies. 97
Fig. A3.2-7: (a) Relative permeability as a function of flux density and frequency and (b) *BH* loops at different frequencies. 98
Fig. A3.2-8: Small signal primary side inductance as a function of frequency. 98
Fig. A3.2-9: Transformers models: (a) lumped parameter model, (b) LC filter equivalent circuit model, and (c) transfer function model. 99
Fig. A3.2-10: Large signal measurements of the real part of magnetic permeability of the M6 steel: (a) magnetic permeability as a function of frequency at different flux densities 0.1–1.6 T; (b) magnetic permeability as a function of frequency at flux density B = 0.8 T and its approximation using transfer function. 100
Fig. A3.2-11: Comparison of the simulated transfer functions (V_O/V_I) of the transformers with 1:2 turns ratio using fixed values model, LC second-order approximation, and transfer function approximation of the magnetic permeability. 100
Fig. A3.2-12: Circuit diagram of NPC. 101
Fig. A3.2-13: Delta configuration of capacitors in LC filter. 101
Fig. A3.2-14: Without the interpolation method implementation: (a) capacitor voltages, (b) phase-*j* grid currents, and (c) phase-*j* grid voltages. 103
Fig. A3.2-15: With the interpolation method implementation: (a) capacitor voltages; (b) phase-*j* grid currents; and (c) phase-*j* grid voltages. 103
Fig. A3.2-16: FORTRAN implementation of dc-dc (left) and dc-ac (right) converters. 104
Fig. A3.2-17: PV dc-dc converter and dc-ac inverter: (a) 1.2 kV dc bus voltage, (b) 0.8 kV PV input capacitor voltage, (c) dc-dc converter inductor, and (d) distribution grid load currents 104
Fig. A3.2-18: High-fidelity PV inverter module with multirate converter/inverter controllers 107
Fig. A3.2-19: High-fidelity PV plant model with multirate power plant controller 107
Fig. A3.2-20: PV plant states during the voltage reduction: (a)1.2 kV bus voltage; (b) 0.8 kV PV voltage; (c) inductor current; (d) distribution grid voltage; (e) inverter load currents; and (f) the PV plant power. 108
Fig. A3.2-21: PV plant states during normal operation: (a) 1.2 kV bus voltage; (b) 0.8 kV PV voltage; (c) inductor current; (d) distribution grid voltage; (e) inverter load currents; and (f) the PV plant power. 108
Fig. A3.3-1: NARX model. 109
Fig. A3.3-2: CNN model. 110
Fig. A4.1-1: Example test system. 111
Fig. A4.1-2: Simulation results of the inverter module. 112
Fig. A4.1-3: Simulation results of the voltage source converter and its controller. 112
Fig. A4.1-4: Recorded data for 6/19/2013 from hour 06:00 to hour 21:00—(top) Trace 1: frequency; (middle) Trace 3: three-phase voltage magnitudes–inverter output; and (bottom) Trace 7: solar insolation. 113
Fig. A4.1-5: The magnitude and phase of phase-*a* current of inverter 1 from simulation of baseline and quadratized models. 114
Fig. A4.1-6: The magnitude and phase of phase-*a* voltage of inverter 1 from simulation of baseline and quadratized models. 114
Fig. A5.1-1: Dialogue box for a load in PSCAD. 115
Fig. A5.1-2: Real power of a load modeled in PSCAD. 115
Fig. A5.1-3: Results for different simulations. 116

Fig. A5.1-4: Spectral analysis of generator speeds. 116
Fig. A5.1-5: Location of Angles Forest fault....120
Fig. A5.1-6: Short circuit current of the remote bus in the PSSE simulation (normalized with respect to pre-fault value)....121
Fig. A5.1-7: EMT model development process from the WECC grid TS model. 122
Fig. A5.1-8: Minimum spanning tree for fault bus and the other affected PV plant considered in this analysis with one-hop....122
Fig. A5.1-9: Voltage and current plot of the remote and near end of the tripped transmission line for different cases in the order 1PD, 1HD, 1HP, 2PD, 2HD, 2HP, 3PD, and 4 PD (top left screenshot from [6]). 124
Fig. A5.1-10: Voltage at the one of the affected PV plants for different simulation cases: (a) 1PD, (b) 1HD, (3) 1HP, and (4) 3PD. 125
Fig. A5.1-11: Simulation of the fault and circuit breaker operation in the PSCAD model. 126
Fig. A5.1-12: Equivalent circuit after first breaker operation. 126
Fig. A5.2-1: Configuration of the transmission and distribution grid developed in RSCAD.....127
Fig. A6.1-1: PV plants in queue in CAISO grid. 128
Fig. A7.1-1: Mean ranking of control features based on IAB feedback. 142
Fig. A7.1-2: Percentage of times ranked in top five. 142
Fig. A8.1-1: Two-level converter with grounded midpoint circuit architecture 144
Fig. A8.1-2: Two-level converter model with midpoint ground model capacitor voltages: (a) V_{c1}, (b) V_{c2}, and (c) V_{dc}....144
Fig. A8.1-3: NPC circuit architecture. 145
Fig. A8.1-4: NPC capacitor voltages: (a) V_{c1}, (b) V_{c2} and (c) V_{dc}....145
Fig. A8.1-5: Simulation results for inverter-1. 146
Fig. A8.1-6: Simulation results for inverter-2. 147
Fig. A8.2-1: Phase-a current from a four-layer RNN model. 148
Fig. A8.2-2: General RNN model structure (implemented in C code) 149
Fig. A9.1-1: Comparison of the simulation of MV distribution grid with a large number of PV inverter modules based on the proposed simulation algorithms: (a) dc-dc boost converter inductor current (iL,pv) in one PV module, (b) errors of the inductor current (iL,pv), (c) dc link voltage ($v\mathrm{dc}$), and (d) error of the dc link voltage ($v\mathrm{dc}$).....150
Fig. A9.1-2: Comparison of the simulation of MV distribution grid with a large number of PV inverter modules based on the proposed simulation algorithms: (a) filter capacitor voltage ($va,\mathrm{ac},\mathrm{fil}$) phase A in one PV inverter module, (b) dc-ac inverter output current ($ia,\mathrm{ac},\mathrm{fil}$) phase A in one PV inverter module, (c) grid voltage (va,grid) phase A at the primary side of distribution transformer, and (d) grid current (ia,grid) phase A at the primary side of distribution transformer. 151
Fig. A9.1-3: Comparison of converter inductor current (iL,pv), dc link voltage ($v\mathrm{dc}$), and inverter output power ($P\mathrm{inv}$ and $Q\mathrm{inv}$) in the simulated system based on the numerical simulation algorithms: (a) Case 1, steady-state; (b) Case 2, power step change; and (c) Case 3, grid fault condition.....152
Fig. A9.1-4: Comparison of secondary side current ($i\mathrm{a},\mathrm{TF}$), feeder current ($i\mathrm{a},\mathrm{feeder}$), and plant current ($i\mathrm{a},\mathrm{POC}$) in the simulated system based on the numerical simulation algorithms: (a) Case 1, steady-state; (b) Case 2, power step change; and (c) Case 3, grid fault condition. 153
Fig. A9.2-1: Currents from the four-layer RNN model: (a) phase-a; (b) phase-b; and (c) phase-c. 154
Fig. A10.1-1: Comparison of an aggregated quasi-dynamic model to a detailed model for Santa Fe facility: (a) active power, reactive power, and ac-side voltage magnitude; and (b) ac-side voltage magnitude, ac-side current magnitude, and ac-side current phase angle.....155

Fig. A10.1-2: Integrating the power grid present scenario EMT model (a) with a high-fidelity model of the specific PV plant-1 (b) using a transmission line with remote ends. 155
Fig. A10.1-3: Local end and remote end voltage and current plots from the EMT simulation of the present scenario grid model for the Angeles Forest fault event (based on the upgraded EMT model). 155
Fig. A10.1-4: Simulation model for the specific PV plant-1. 156
Fig. A10.1-5: Voltage plots near PV plant -1 from the EMT simulation of the present scenario grid model for Angeles Forest fault event: (a) original model, and (b) after equivalencing the EMT model to hide sensitive WECC information. 157
Fig. A10.1-6: Voltages and currents from test simulation results of the MA high-fidelity model of the specific PV plant-1 in RSCAD. 157
Fig. A11.1-1: Process taken to update the existing TS dynamic model of power grid (26HS2) to increase renewable penetration in the dynamic model. 159
Fig. A11.1-2: Renewable power plant model (REPCA). 160
Fig. A11.1-3: Renewable energy electrical control model (REECB). 160
Fig. A11.3-1: Future scenario grid model in RSCAD (RTDS) for real-time simulation. 161
Fig. A11.3-2: Simulation results of the developed model of the future scenario of power grid in RSCAD (RTDS) for line-to-line fault: left, voltages and current measured at the local end of the fault; and right, voltages and currents measured at remote end of the fault. 161
Fig. A13.1-1: Schematic of the baseline model. 162
Fig. A13.1-2: Demonstration of a single step in the aggregation methodology. 163
Fig. A13.1-3: Voltage and reactive power measurements for aggregation of (a) a single PV system, (b) a single feeder, and (c) the entire PV plant. 164
Fig. A13.1-4: Schematic of a grid connected PV system (three-phase-to-ground) 164
Fig. A13.1-5: Top: One-line diagram of a generic PV plant connected to the power grid (with a three-phase-to-ground fault on the line connecting to the PV plant). Bottom: Equivalent one-line diagram that removes the fault resistance based on equivalencing. 165
Fig. A13.2-1: Reactive power reference generator module in PPC using MPC formulation. 166
Fig. A13.2-2: MPC-based reactive power reference generator implementation in the PSCAD. 166
Fig. A14.1-1: DSP inverter controller interaction with real time inverter model. 167
Fig. A15.1-1: PSCAD model for the PV plant representation. 167
Fig. A15.1-2: (a) Output power plots at the PV plant terminal: (1) PSSE simulation, (b) PSCAD simulation (WT model without PLL for PV plant), and (c) PSCAD simulation (RE model without PLL). 168
Fig. A15.1-3: Output power plots near the affected PV plant: (a) WT model without PLL, (b) WT model with PLL, (c) RE model without PLL, and (d) RE model with PLL. 168
Fig. A15.1-4: PV plant results for the filter size increase of two times of: (a) HV-side ac power, (b) LV-side ac power of a module, and (c) LV-side ac power of another module. 169
Fig. A15.1-5: Interchange of inverters: (a) plant with all inverter-1s; (b) plant with all inverter-2s, and (c) plant with inverter-1s and inverter-2s interchanged. 169
Fig. A15.1-6: Increase in line length for inverters (a) with original lengths, (b) with a two times increase, (c) with a three times increase, (d) inverter profile in the original case, (e) inverter profile in case with a two times increase, and (f) inverter profile in case with a three times increase 170
Fig. A15.1-7: PV plant with different switching frequencies for inverter-2: (a) 2.5 kHz (original controller gains multiplied by 0.5 and 0.5^2); (b) 5 kHz (original controller

gains multiplied by 0.5 and 0.5^2); and (c) 10 kHz (original controller gains multiplied by 0.75 and 0.75^2). 170
Fig. A15.1-8: Simulation results for Rf = 0.2 Ω with support using MPC, with support using PI, and without support: (a) POI active power, (b) POI reactive power, and (c) POI voltage. 171
Fig. A15.1-9: Simulation results for Rf = 0.1 Ω with support using MPC, with support using PI, and without support: (a) POI active power, (b) POI reactive power, and (c) POI voltage. 171
Fig. A15.1-10: Response of the generation loss event in the developed WECC scenario with 100% renewable in California for different PI controller values in REPCA. 171
Fig. A15.1-11: Response of the generation loss event in the developed WECC scenario with 100% renewable in California for different deadband values in REPCA. 172
Fig. A15.1-12: Voltage and current plots near the fault location for the EMT model case P1289. 173
Fig. A15.1-13: Differences between the voltage and current plots near the fault location for the EMT model cases: (left) between P9 and P1289 and (right) between P129 and P1289. 174
Fig. A15.1-14: Comparison of the voltage and current plots near the fault location for the EMT model cases: solid line, P1289; and dashed line, larger model with more buses added to P1289. 174
Fig. A15.1-15: Voltage plots near the PV plants in the future grid EMT model case P1289. 175
Fig. A15.1-16: Responses near the fault for EMT (solid) and EMT-TS cosimulation (dashed). 175
Fig. A15.1-17: Simulation results for the three PV plants: (a) specific PV plant-1, (b) IBR-1, and (c) IBR-2. 176
Fig. A15.1-18: The specific PV plant-1 with the future grid scenario. 177
Fig. A15.1-19: Three PV plant responses during the power grid when connected to the future grid (IBR-1 and IBR-2 operated at 125 MW): (a) specific PV plant-1, (b) IBR-1, and (c) IBR-2. 178
Fig. A15.1-20: Three PV plant responses during the power grid when connected to the future grid (IBR-1 operated at 0 MW and IBR-2 operated at 125 MW): (a) specific PV plant-1, (b) IBR-1, and (c) IBR-2. 178
Fig. A15.1-21: Two PV plant responses during the power grid when connected to the future grid, both operated at 125 MW: (a) IBR-1 and (b) IBR-2. 179
Fig. A15.1-22: Two PV plant responses during the power grid when connected to the future grid: (a) IBR-1 operated at 0 MW and (b) IBR-2 operated at 125 MW. 179
Fig. A16.1-1: Grid side voltage for PV plant modules 1 and 2. 180
Fig. A16.1-2: Active power for PV plant modules 1 and 2. 180
Fig. A16.1-3: Quasi-dynamic model of the specific PV plant-1 in RSCAD for real-time simulation. 181
Fig. A16.1-4: Quasi-dynamic model of the specific PV plant-1 integrated with the future scenario grid model in RSCAD for real-time simulation. 182
Fig. A16.1-5: Results of the high-fidelity model of specific PV plant-1 integrated with the present scenario grid model in a single rack with six PB cards in RTDS (from top left to bottom right: voltages at grid near the fault, voltages at terminal of the PV plant, active and reactive power of the PV plant, voltages at the first feeder and inverter currents at the first feeder, voltages at the 20th feeder, and inverter currents at the 20th feeder). 183
Fig. A16.1-6: Results of the high-fidelity model of specific PV plant-1 integrated with the present scenario grid model in eight racks with 40 PB cards in RTDS (from top left to bottom right: voltages at grid near the fault, voltages at terminal of the PV plant,

active and reactive power of the PV plant, voltages at the first feeder and inverter currents at the first feeder, voltages at the 20th feeder, and inverter currents at the 20th feeder) 184
Fig. A16.1-7: Results of the high-fidelity model of specific PV plant-1 integrated with the present scenario grid model in 13 racks with 65 PB cards in RTDS (from top left to bottom right: voltages at grid near the fault, voltages at terminal of the PV plant, active and reactive power of the PV plant, voltages at the first feeder and inverter currents at the first feeder, voltages at the 20th feeder, and inverter currents at the 20th feeder). 185
Fig. A17.2-1: (a) RNN model summary and (b) learning curve. 186
Fig. A17.2-2: (a) Test data vs. prediction results from RNN model and (b) zoomed-in result between 4 and 5 s. 186
Fig. A17.2-3: (a) GRU model summary and (b) learning curve. 186
Fig. A17.2-4: Test data vs. prediction results from GRU model. 187
Fig. A17.2-5: (a) Bidirectional RNN model summary and (b) learning curve. 187
Fig. A17.2-6: (a) Test data vs. prediction results from bidirectional RNN model and (b) zoomed-in result between 4 and 5 s. 187
Fig. A17.2-7: Grid side voltage for a generic PV plant. 188
Fig. A17.2-8: Active and reactive power for all PV modules. 188
Fig. A17.3-1: Frequency plot after the generation loss event from: (top) PSCAD simulation and (bottom) PSSE simulation. 189
Fig. A17.3-2: Response from TS model after three-phase self-clearing fault event at bus 4: (left) with VDL logic and (right) without VDL logic. 189

List of Tables:

Table 3.2-1: Comparison of speed-up, accuracy, and stability between different high-fidelity models....26
Table 3.2-2: Comparison of measured time and observed speed-up between different models....27
Table 5.1-1: Comparison of simulation results....33
Table 10.1-1: Characterization of the cases of EMT models....43
Table 15.1-1: Overview of different quasi-dynamic models of PV plants....58
Table 15.1-2: Overview of the response from quasi-dynamic models of PV plants during the Angeles Forest 2018 event (or similar) simulations....58
Table 17.1-1: Generator replacement scenarios.....67
Table A1.2-1: PV configuration information....83
Table A1.3-1: Contingency events data....83
Table A4.1-1: Parameters of the PV system.....111
Table A5.1-1: Summary of modal estimation from generator speeds using Prony analysis....116
Table A5.1-2: Summary of mapping of plants from EIA data to the WECC grid model....118
Table A5.1-3: Summary of the mapping task for different grid scenarios....118
Table A5.1-4: Different hybrid (EMT-TS) simulation models....119
Table A5.1-5: Events in the PSCAD simulation....126
Table A5.2-1: Quantified errors between offline and real-time simulation models....128
Table A6.1-1: Summary of mapping PV plants from WECC grid to EIA-860 data and in-queue report....129
Table A6.1-2: 2028HS case study characterization....130
Table A6.1-3: 2026HS2 case study characterization....131
Table A6.1-4: Power generation in California in the 26HS2 WECC power grid TS model....131
Table A7.2-1: A framework to implement MPC for reactive power/voltage control....143
Table A11.1-1: Information on conventional power plants that are likely to retire in the next 10 years....158
Table A11.1-2: Power generation in California in the upgraded WECC power grid TS model....158
Table A11.1-3: Power capacity in different regions....159
Table A17.2-1 Comparison of different neural networks for an advanced model of a generic PV plant....185

Background: Increased penetration and deployment of power electronics-based generation like solar photovoltaic (PV) systems has led to challenges that have not been predicted by existing dynamic models [1–3]. The traditional transient stability (TS) models or phasor-domain/positive-sequence simulation models have been unable to provide an adequate understanding of the effect of unbalanced faults on PV systems and the larger grid. Moreover, their shortcomings are further exacerbated with the introduction of smart functionalities in PV inverters and the corresponding controllers with multiple time constants (including fast frequency response). Electromagnetic transient (EMT) simulations can capture the complex interactions of converter-interfaced systems with the power grid [2,4]. However, EMT simulation of high-fidelity PV system models can be extremely time-consuming with the presence of a very large number of inverters (hundreds or thousands in 500–1,000 MW plants). The time to simulate is worsened when a high penetration of PV systems is studied in a large area to identify the effect of extreme events in bulk power systems on PV systems. Alternatively, all the PV inverters are aggregated as one inverter supplying power to the bulk power system. Whereas this method speeds up the simulation, substantial fidelity is lost with no means to identify vulnerable PV inverters within the utility-scale PV plant or aggregated distributed energy resource (DER)-PVs during extreme events. This loss of information (or fidelity) limits the ability to accurately identify the amount of loss of PV generation, such as during momentary cessation or partial shutdown.

The effect of many reported events [1–3] has been observed in a large area with several PV systems. The EMT simulation of large grids with several PV systems is a huge challenge computationally, especially if high-fidelity PV system models are used. This problem is further exacerbated with a higher penetration of PV systems in the future, but it can be overcome with a better understanding of the boundaries of EMT and TS simulations [5]. The understanding of boundaries and EMT-TS cosimulation methods research can enable studying large grids with a high penetration of PV.

The effect of extreme events on grid reliability is sensitive to the control and protection algorithms in different types of PV systems [1–3]. There is limited understanding of this impact on future grids with a combination of legacy and advanced PV systems. The advanced PV systems integrated in the future will incorporate advanced control functionalities to reduce momentary cessation, increase system inertia, and provide grid support as recommended by North American Electric Reliability Corporation (NERC) guidelines [1–3].

Project Objectives: A suite of dynamic models of PV systems has been developed in this project to accurately capture the PV system dynamics during different contingencies. The following models are included: (i) quasi-dynamic, (ii) high-fidelity EMT, (iii) advanced, and (iv) baseline. The models have the flexibility to consider different control functionalities at different controller levels. The type of contingency, PV system configuration, and PV system location with respect to the contingency event location determine the model requirements. The developed PV system models can accurately represent the dynamics during defined contingencies with greater than 98% accuracy. They also can simulate up to 326 times faster than the simulation speeds of baseline models. The developed models are evaluated in present and future scenarios, with advanced control functionalities incorporated into the PV system models in the

future scenarios. These advanced control functionalities help mitigate some of the present generation problems such as momentary cessation and future problems with high-penetration PV systems like low inertia. Evaluation of these systems is performed through EMT-TS cosimulations to study large-scale systems with high-fidelity models of PV systems (where required).

Abbreviations:

21HW2	2020–2021 Heavy Winter Case
22HS	2022 Heavy Summer Case
26HS2	2026 Heavy Summer Case
AI	artificial intelligence
CAISO	California Independent System Operator
CEC	California Energy Commission
CNN	convolutional neural network
DAE	differential algebraic equation
DER	distributed energy resource
DOE	US Department of Energy
DSP	digital signal processor
EIA	US Energy Information Administration
EMT	electromagnetic transient
GRU	gated recurrent unit
IAB	Industry Advisory Board
IBR	inverter-based resource
IID	Imperial Irrigation District
IRP	inverter-based resource performance
IRPS	inverter-based resource performance subcommittee
LADWP	Los Angeles Department of Water and Power
MA	multiple A (matrixes model)
MPC	model predictive control
MPPT	maximum power point tracking
MV	medium voltage
NARX	nonlinear autoregressive exogenous
NDA	nondisclosure agreement
NERC	North American Electric Reliability Corporation
NPC	neutral point clamped
ORNL	Oak Ridge National Laboratory
PCC	power plant controller
PES	Power & Energy Society
PG&E	Pacific Gas & Electric
PI	proportional integral
PLL	phase-locked loop
POC	point of connection
POI	point of interconnection
PPC	power plant controller
PSSE	Power System Simulator for Engineering
PV	photovoltaic
PWM	pulse width modulation
REEC[A,B,…]	renewable energy electrical control [model A, B, etc.]
RMS	root mean square
RNN	recurrent neural network
RTDS	real-time digital simulator
SCE	Southern California Edison

SDG&E	San Diego Gas and Electric
SETO	DOE Solar Energy Technologies Office
SPP	Southwest Power Pool
THD	total harmonic distortion
TRD	total rated distortion
TS	transient stability
VDL	voltage dependent current limit
WECC	Western Electric Coordinating Council

Project Results and Discussion:

T-1. Data collection and nondisclosure agreements (NDAs)

ST-1.1 PV system data collection

Information on current PV plants in California is provided in form EIA-860 and has been used to identify the major PV plants and their corresponding locations. The major PV plants have been classified as those rated higher than 100 MW. A snapshot of the data is shown in Fig. A17.3-7: in the Appendix.

ST-1.2 PV configuration data collection

To collect information on PV configurations, a data requirements document has been developed (as mentioned in Table A0-1 in the Appendix).

Based on the data requirements mentioned above for PV configurations, data from three PV plants in California have been collected. Specifics on the data obtained are withheld as they have been obtained under NDA, but the PV plants are identified in this report.

NDAs were signed with the Western Electric Coordinating Council (WECC), Southern California Edison (a utility), and a PV plant owner for grid models, access to laboratories, and plant/contingency data, respectively.

M1.1: PV system and configuration data collected

ST-1.3 Contingency event data collection

To collect information on the contingency events' data, a table had been created in the data requirements document (Table A0-1 in the Appendix). Data from the three PV plants have been collected for the April 2018 Angeles Fire disturbance, including voltage and power measured in the plants. This information has been received from the PV plant owners along with the data collected in ST-1.2.

In addition to the three specific PV plants, further data have been collected from NERC documentation on the April 2018 Angeles Fire disturbance [6]. The disturbance occurred because of a failed splice on a 500 kV transmission line in the vicinity of Angeles National Forest, causing a B-C line fault that was normally cleared within 2.6 cycles. The digital fault recorder data from both ends of the faulted circuit are collected. The data on the fault location, fault type, and voltages observed at the two ends of the transmission line have been used to validate the simulation of the fault and to evaluate the models developed.

Detailed data are available from the NERC report in 2020 on the San Fernando event [7], with information on the reduction in power from some of the plants mentioned earlier from which data have been collected.

M1.2: Contingency event data

ST-1.4 Grid model

Present and future grid models are identified from the WECC library. The models that represent the present (2022) and future (2026) grid have been identified. The future grid model has been selected based on the availability of dynamic model data in PSSE

software for a grid. The PV plants identified in the EIA-860 form are mapped to the ones modeled in the aforementioned grid models. Plants with renewable models are identified in the WECC models, and PV plants with wind aerodynamics or pitch or mechanical control are removed (because they represent wind farms). This process is used because it appears some of the PV plants have been modeled using WT4G1 models when the present grid is compared with future grid models. Another method that has been applied is the identification of similarities in bus names, generator IDs, and plant power ratings because it appears some of the PV plants may have been modeled using round rotor generator GENROU models. Finally, the summation of multiple plants in both form EIA-860 and the WECC models is used to identify similarities. This information is provided more in detail in Tasks 5 and 6.

ST-1.5 NDAs

NDAs have been signed with WECC and a PV plant owner for grid models and plant/contingency data, respectively. A contract was negotiated with Southern California Edison (SCE) to use laboratory facilities and get access to data under NDA.

ST-1.6 Industry Advisory Board (IAB) formation

The IAB was formed with 47 members from 30+ organizations, which are named in the Appendix. One example of the support provided by the advisory board was validation of the mapping of data from the EIA datasheet to the WECC grid models being used in the project. The control specifications document, which is explained more in detail under Task 7, had been distributed among the IAB members to receive feedback on the ranking of control features of interest and/or development in future PV plants. The feedback assisted with identifying critical advanced control functionalities in PV plants in future grids.

T-2. Develop baseline PV system model

ST-2.1 Model development

Detailed baseline models of large PV plant are developed. The developed models include a large PV plant (with hundreds of inverters) and a small PV plant (with tens of inverters) in two different models. The models are developed based on library components provided in PSCAD software. The components considered in the PV plant include PV arrays, boost converters, inverters, filters, distribution transformers, distribution lines, capacitor banks, power transformers, and a hierarchical control system. The hierarchical control system consists of a power plant controller (PPC) and inverter firmware. The diversity of models developed indicates the capability to cater to a wide range of user specifications.

Generic large PV plants: The overall layout of a generic large PV plant is shown in Fig. A17.3-8 in the Appendix. The developed PV plant model is connected to the 230 kV grid through a power transformer, which steps down system voltage from 230 kV to 34.5 kV distribution grid voltage. There are 36 feeders connecting to the power transformer. The PV power plant controller is shown in Fig. A17.3-9 in the Appendix. The voltages, feeder numbers, transformer parameters, and the power plant controller parameters are flexible based on user request.

Each of the 36 feeders has 7 distribution transformers connected through distribution lines, as shown in Fig. A17.3-10 in the Appendix. Multiple PV inverter modules are connected by a distribution transformer that steps down the voltage from 34.5 kV to 480 V, which is a typical secondary voltage in the grid to connect to PV inverters. The PV inverter modules connected to a distribution transformer are also termed a PV system. In this study, two PV inverter modules are present in each PV system. The number of transformers and inverters (or PV systems), the voltage of lines, and distribution line lengths can vary based on user request.

Each of the developed models of the PV inverter module (rated at 1 MW) consists of a PV array, boost converter, inverter, LCL filter, and controllers, as shown in Fig. A17.3-11. The boost converter regulates the power generated through the maximum power point tracking (MPPT) control. The inverter regulates dc bus voltage and the output reactive power to defined references. Further details on the power electronics controllers are provided in the next subtask. The PV array model in PSCAD enables the user to specify the number of series and parallel cells per module and the number of modules connected in series and in parallel. The output power of the PV array is a function of the inputs, namely irradiation and temperature. The details of the parameters that can be tuned in the PV array model are shown in Fig. A17.3-12 in the Appendix. Each of the parameters and components in the PV inverter module is customizable based on user request. The large PV plant model contains 504 inverters.

Specific PV plant: The structure of the generic large PV plant model developed earlier is extended to develop a model based on the specific PV plant information collected in Subtask 1.2. It includes multivendor inverters that can be modeled. Because the information is under NDA, the generic PV plant model is shown here.

Small PV plants: Another small PV plant model is developed, with the overview of the model shown in Fig. A17.3-13 in the Appendix. The PV plant connects to a 138 kV grid through a power transformer (138 kV/13.8 kV). A single feeder (at 13.8 kV) in the PV plant connects to five PV systems, each of which has a distribution transformer (13.8 kV/480 V). Each distribution transformer connects a 480 V grid to the three inverters, and each inverter is connected to a PV array through a dc-dc converter. The PV array rating is 0.5 MW. Each PV system is shown in Fig. A17.3-14 in the Appendix.

The difference between the controllers used in the PV system in the large and small PV plant models includes the flexibility introduced here in dc-dc converter control mode. The control modes in the dc-dc converter include the following:

- *Control mode 1:* dc voltage control mode, where the dc-link between the inverter and the dc-dc converter is controlled to generate the duty ratio.
- *Control mode 2:* MPPT control mode, where the voltage at the dc-link between the dc-dc converter and the PV array is controlled to generate MPPT power reference. The power generated by the PV array is then controlled to the MPPT power reference to generate the duty ratio.

The overview of the dc-dc boost converter controller is given in Fig. A17.3-15 in the Appendix.

The inverter controller in the PV inverter uses a traditional inner *dq* current control through a grid-following mode of operation (using a phase-locked loop [PLL] that generates the phase angle and frequency). The overview of the inner *dq* current control is shown in Fig. A17.3-16 in the Appendix. The inverter controller also uses an outer loop control that generates the reference *dq* currents for the inverter. In control mode 1, the active power control is controlled to a defined reference value to generate the reference *d* current. In control mode 2, the dc-link voltage between the inverter and the dc-dc converter is controlled to a defined reference value to generate the reference *d* current. In both control modes, the reactive power is controlled to its reference value to generate the reference *q* current. The overview of the outer loop control is shown in Fig. A17.3-17 in the Appendix.

M2.1: Baseline model development

ST-2.2 Testing

Large PV plant: The large PV plant with 504 inverters was tested in PSCAD software. The test results are shown in Fig. A17.3-18in the Appendix. The need for advanced simulation algorithms is highlighted by the computational burden imposed by the baseline model: The time required to simulate just 0.85 s of the model was nearly 1 week.

Specific PV plant: Testing of the baseline PV plant model developed based on PV plant data collected in ST-1.2 is shown in Fig. A17.3-19 in the Appendix as a representative figure. A switching event results in a change of reactive power from the plant (measured at high-voltage side) as well as individual sections of the plant (measured at low-voltage sides). The results indicate similarities with the collected field data.

Small PV plant: The test results from the small PV plant model are shown in Fig. A17.3-20 in the Appendix.

M2.2: Evaluation of baseline model

T-3. Develop suite of dynamic PV system models

ST-3.1 Quasi-dynamic model in PSCAD/PSSE

The quasi-dynamic model of the inverters consists of a digital signal processor (DSP), a controller, and an average-value model of the converter. The DSP model receives as input the data from the ac and dc side of the inverter and performs digital signal processing to prepare the data in the form required by the controller. For example, the DSP computes the positive sequence voltages and current from the three-phase voltages and current on the grid side of the ac side of the inverter. The controller model receives as inputs the processed data from the ac and dc sides of the inverter and computes the control signals to be sent to the inverter. It is basically a PI controller with several options (P-Q control, P-V_{ac} control, V_{dc}-V_{ac} control). The inverter model is a PWM inverter controlled by the outputs of the controller. This model is developed in such a way that multiple inverter systems can be connected to collector and transmission systems. The models are also designed so that multiple inverters can be

aggregated to a single inverter of capacity equal to the sum of the capacities of the individual inverters.

The overall block diagram of the inverter model is shown in Fig. A17.3-21. The inverter model circuit configuration is shown in Fig. A17.3-22. The parameters defining the converter model are shown in Fig. A17.3-23. The quasi-dynamic inverter model's equations are presented in the Appendix.

M3.1: Quasi-dynamic model development

ST-3.2 High-fidelity model in PSCAD

An example large PV plant is shown in Fig. A17.3-24 in the Appendix. The components present within the large PV plant are identified. Based on the components identified, a high-fidelity model is being developed in Fortran (and transferable to C/C++) in PSCAD. The large PV plant is composed of fifties to hundreds of PV systems (PV inverters connected to one distribution transformer) in the medium-voltage (34.5 kV) distribution system, which is connected to the high-voltage (230 kV) transmission system. The PV system consists of PV arrays, PV inverter modules (dc-dc converters and dc-ac inverters), and inverter firmware. Additionally, a PPC is present in the PV plant.

PV Inverter Module Model

The high-fidelity model of a PV inverter module consisting of a PV array, a dc-dc boost converter, an ac-dc three-phase voltage source inverter, and an LCL filter is developed. The PV inverter module is illustrated in Fig. A17.3-25 in the Appendix, and the corresponding EMT model is shown in the Appendix. Additionally, different types of inverters have been considered in the models (typically representative of inverters from different vendors and/or from different generations of inverters from the same vendor). The corresponding models developed are provided in the Appendix. The controllers used in dc-dc converters and dc-ac inverters are implemented in a multirate implementation, similar to the field implementation where the controller is implemented in 50–100 µs.

PV System Model

A number of PV inverter modules are connected to a distribution transformer in a PV system. In the high-fidelity model, up to five inverter modules may be connected. The PV system is shown in Fig. A17.3-3 in the Appendix, and the corresponding EMT model is shown in the Appendix.

PV Plant Model

The differential algebraic equations (DAEs) for distribution feeders that connect to multiple PV systems are developed based on the PI section model of the distribution lines. The DAEs that represent the dynamics of the lumped T-type model of power transformers are also incorporated into the PV plant's DAEs. Using this approach, the high-fidelity model of a generic PV plant is developed. In addition to the lumped T-type model of the transformer used in Equations **Error! Reference source not found.**)–**Error! Reference source not found.**) in the Appendix, advanced models of transformers have been developed for future use cases (such as start-up or other use cases of interest). The advanced model of a transformer is provided in the Appendix.

Simulation Algorithms

Advanced numerical algorithms to simulate high-fidelity models of large PV plants are developed, such as the following: (i) numerical stiffness-based hybrid discretization (applied to individual PV arrays and connected converters), (ii) DAEs clustering and aggregation (applied to a PV system with multiple PV inverters and/or multiple PV systems), (iii) time constant–based separation (applied to the interface between feeders and transmission lines), (iv) multi-order discretization with second-order in power system networks and first-order in power electronics components, and (v) linear solvers (such as the multiple A matrix method, discussed in detail in the Appendix, and Kron's reduction method).

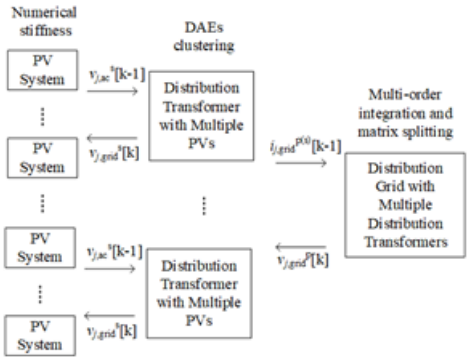

Fig. 3.2-1: Overview of the advanced simulation algorithm for the large number of PV systems in the MV distribution grid.

The proposed algorithm is applied to the state-space equations developed for the dynamics of the system. The state-space equations are based on the EMT model that are expressed as DAEs. The overview of the algorithm is shown in Fig. 3.2-1.

Simulation Results and Comparison

The proposed simulation algorithms are applied to the generic PV plant that has a medium-voltage (MV) distribution system with 52 three-phase nodes, 25 distribution transformers (and PV systems), and 125 PV inverter modules. More information on the generic PV plant can be found in the Appendix. In this project, three different types of high-fidelity models were developed for the simulation of distribution networks within a large-scale PV plant. The first type of high-fidelity model is developed by using only second-order discretization methods to form a single A matrix as in A**x**=**b** of the network equation. Once the size of a distribution network increases, the second model is not efficient because of the expensive matrix inversion process that must be performed at each simulation time step. Thus, a second type of high-fidelity model was proposed by physical modularization of feeders to reduce the size of the A matrix, resulting in multiple A matrices according to the number of feeders. Although this second model has advantages of modularization and simulation speed-up, a small capacitance is required at terminals of modules for simulation algorithm stability. This makes the second model

less accurate during fast transient studies. Therefore, the third high-fidelity model was proposed by Schur complement to reduce the matrix size while maintaining accuracy and stability. These three different types of high-fidelity models based on advanced simulation algorithms are compared in Table 3.2-1 for advantages and disadvantages regarding simulation speed, modularization, stability, and accuracy.

Table 3.2-1: Comparison of speed-up, accuracy, and stability between different high-fidelity models

	Single A matrix	Multiple A matrices	Schur complement
Simulation speed	Fast	Fastest	Faster
Modularization	Difficult	Easy	Moderate
Stability	High	Capacitors needed	High
Accuracy	High	Medium	High

Simulation results were compared for the three types of high-fidelity models based on advanced simulation algorithms and the baseline model. The measured simulation time taken for a 0.25 s simulation for the different models and observed speed-up compared with the baseline model are presented in Table 3.2-2. As seen from the results comparison in Table 3.2-2, the multiple A matrices method shows the highest simulation speed-up of 326.4 times.

Some of the states from the simulation results are illustrated to compare and evaluate the accuracy and stability of the three high-fidelity models in Fig. 3.2-2 and Fig. 3.2-3. The observed errors present less than 2% except for the simulation initialization.

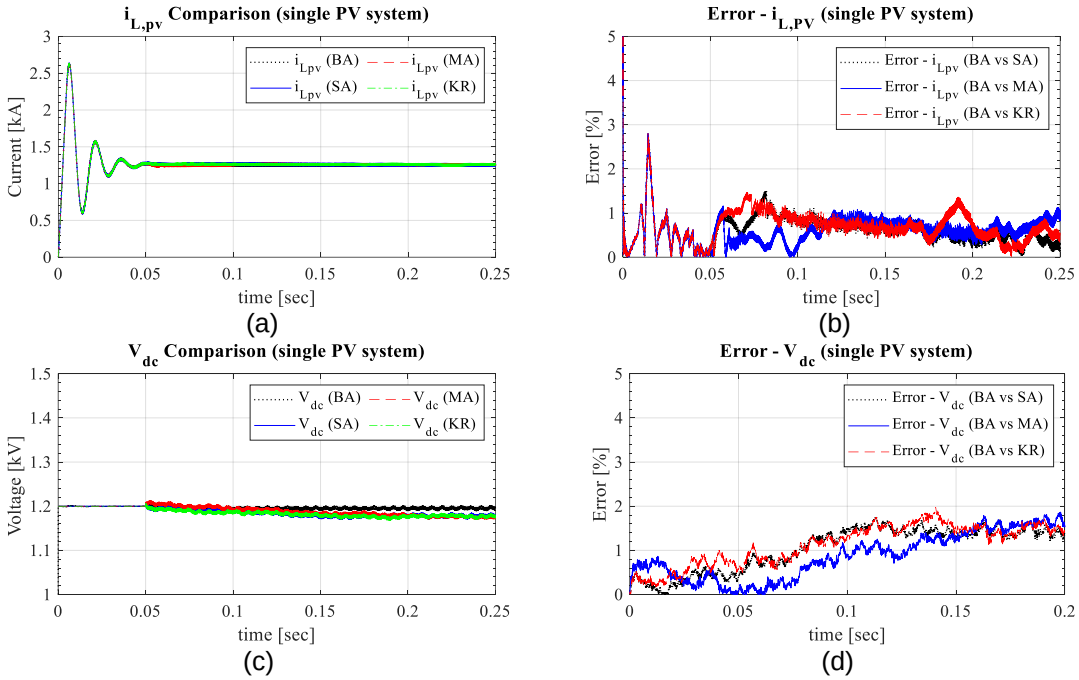

Fig. 3.2-2: Comparison of the simulation of the MV distribution grid with a large number of PV systems based on the proposed simulation algorithms: (a) dc-dc boost converter inductor current ($i_{L,\mathrm{pv}}$) in one PV system, (b) errors of the inductor current ($i_{L,\mathrm{pv}}$), (c) dc link voltage (v_{dc}), and (d) error of the dc link voltage (v_{dc}).

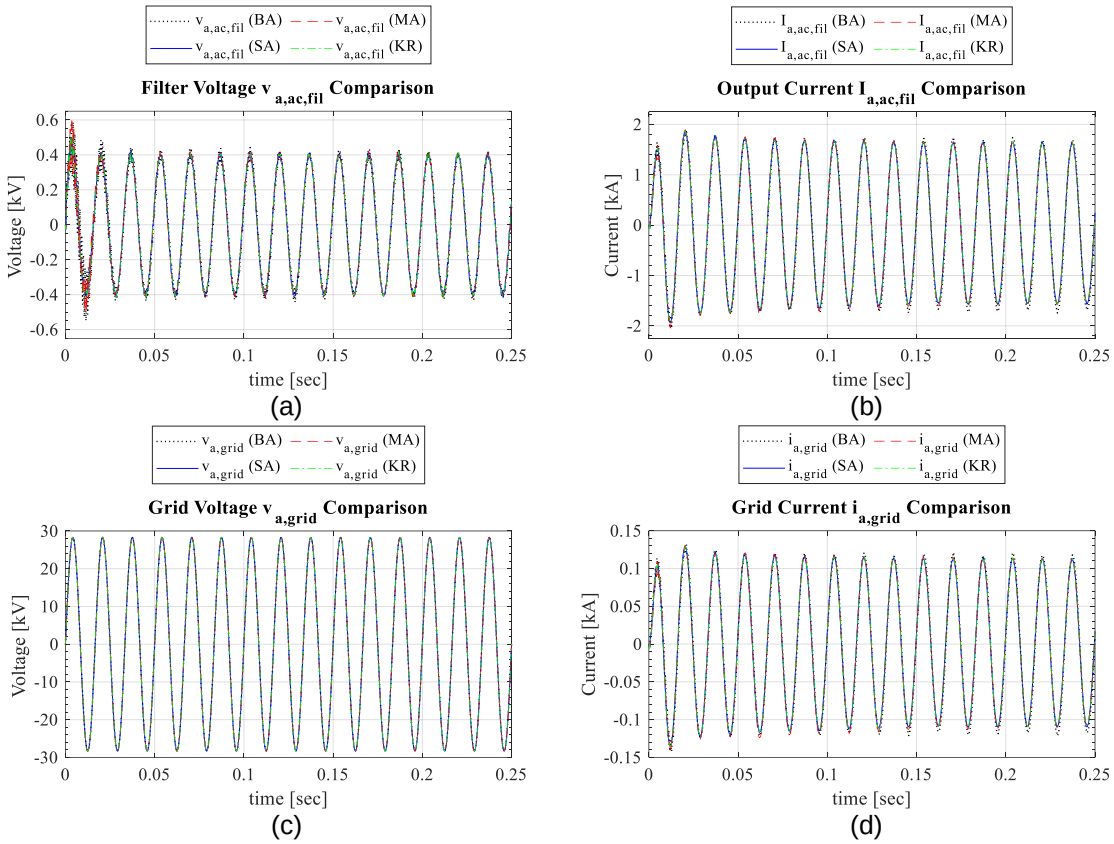

Fig. 3.2-3: Comparison of the simulation of the MV distribution grid with a large number of PV systems based on the proposed simulation algorithms: (a) filter capacitor voltage ($v_{a,\mathrm{ac,fil}}$) phase A in one PV system, (b) dc-ac inverter output current ($i_{a,\mathrm{ac,fil}}$) phase A in one PV system, (c) grid voltage ($v_{a,\mathrm{grid}}$) phase A at the primary side of distribution transformer, and (d) grid current ($i_{a,\mathrm{grid}}$) phase A at the primary side of distribution transformer.

Table 3.2-2: Comparison of measured time and observed speed-up between different models

	Baseline	Single A matrix	Multiple A matrices (matrix splitting)	Schur complement
Time taken for 0.25 s simulation	3,484 min (58 h)	155.3 min (2.58 h)	10.675 min (0.18 h)	12.74 min (0.21 h)
Speed-up	1×	22.4×	**326.4×**	**273.5×**

ST-3.3 Advanced model in PSCAD/PSSE

Different artificial intelligence (AI)-based models have been evaluated for the PV plants based on data generated from simulations of high-fidelity, small-scale PV plant models. The AI models considered were based on the following: (i) recurrent neural networks (RNNs), (ii) convolutional neural networks (CNN), and (iii) nonlinear autoregressive exogenous (NARX) models.

Dataset: The dataset considered to train the small-scale PV plant model with a single inverter included instantaneous voltages (phase), instantaneous currents, and PV power generated. The use cases considered include step changes in voltage magnitude and frequency. Hereafter, this dataset will be called dataset-1. Another dataset considered included the following use cases: ramp changes in voltage magnitude and

step change in frequency with three different changes. This dataset will be called dataset-2, hereafter.

Training Software: Whereas the Keras library in Python has been used to train the RNN and CNN models, MATLAB has been used to train the NARX model.

RNN model: The RNN model was trained on dataset-1 with different numbers of layers and units per layer and different activation functions (relu, tanh). The best results were obtained with three layers; relu activation function in the first two layers and tanh in the third layer; and 10, 20, and 1 unit, respectively, in the three layers. A comparison of the simulation results with the test dataset indicates good dynamic performance of the developed model.

CNN model: The CNN model was trained on dataset-1, and the numbers of filters, filters per layer, and layers; activation functions; and types of layers (convolution, transpose, and max pooling) were varied to identify the best CNN model. The best results were obtained with the model with three layers that contained 50 filters and 1 filter in each of the first two layers and a max pooling in the third layer. The activation functions relu and tanh were used in the first and second layers, respectively. A comparison of the simulation results with the test dataset indicates good dynamic performance of the developed model.

NARX model: The NARX model was trained on dataset-1, and the number of layers, number of delayed inputs, and closed or open loop systems were varied as parameters. Based on training and later evaluation on extrapolated datasets, the open-loop NARX models were determined to be inadequate for accurately representing the dynamics of the system. Closed-loop NARX models are more suitable for estimation applications in real-time control and monitoring.

The best performance is identified with the RNN model. The model generated from the Python code is saved and then translated to C code to integrate with PSCAD. Based on the training and test results of the AI models on dataset-1, further training and tests are performed based on dataset-2 under Task 8.

T-4. Evaluation and redesign dynamic models

ST-4.1 Evaluation of quasi-dynamic model

The evaluation and validation of the models have two components:

1. Evaluation of quasi-dynamic models
2. Comparison of the models to field data

Evaluation of quasi-dynamic models

The quasi-dynamic model was evaluated based on a small system shown in Fig. A17.3-40 in the Appendix. The system consists of a source, a distribution line, a transformer and a PV array, a converter, a converter controller, and a DSP unit for processing the feedback signals to the converter controller. This is equivalent to the aggregation of inverters in a PV plant. The Appendix lists some of the parameters in Table A17.3-1 and shows representative results in Fig. A17.3-41 and Fig. A17.3-42.

Comparison of the models to field data and corresponding PSCAD model

The field data were obtained from a 1.16 MW PV solar plant in Santa Fe. The data were collected from June 15 to September 26, 2013. The raw field data are stored in a set of COMTRADE files. The data consist of the following: frequency, magnitude, and phase angle of the three-phase ac voltages; magnitude and phase angle of the three-phase ac currents; dc voltages; dc currents; and GPS clock quality. Example data are plotted in Fig. A17.3-43 in the Appendix. These data are used to evaluate/validate the quasi-dynamic and baseline models developed. Details about the quasi-dynamic model developed are provided in the Appendix.

Model Testing and Validation: For testing and validation, the model of the Santa Fe PV plant facility (a small-scale PV plant baseline model) was developed in PSCAD. The Santa Fe PV plant is a 1.1 MW PV installation consisting of two PV arrays/inverter systems connected to one step-up transformer. The PV plant and the system and inverter parameters are shown in the Appendix. The step-up transformer is rated 1.0 MVA and 13.8 kV/480 V. Each PV array rated at 1,000 V_{DC} 0.5 MW is connected to 0.5 MVA 1,000 V_{dc}/480 V_{ac} inverter. Field data from the Santa Fe PV plant have been used to validate the baseline model. A 480 s dataset has been used for the simulation. The simulation results generated from the baseline model were compared with the field data. The comparison was performed with two metrics, absolute error and root mean square (RMS) error. The results of the simulations, shown in Fig. 4.1-1, very closely followed the field data (with average RMS error less than 5%); thus, this is a good indication that the simulated baseline model can accurately represent real PV plants. The simulation results between the baseline and quasi-dynamic models are compared to evaluate the simulation accuracy and computational speed of the quasi-dynamic domain model.

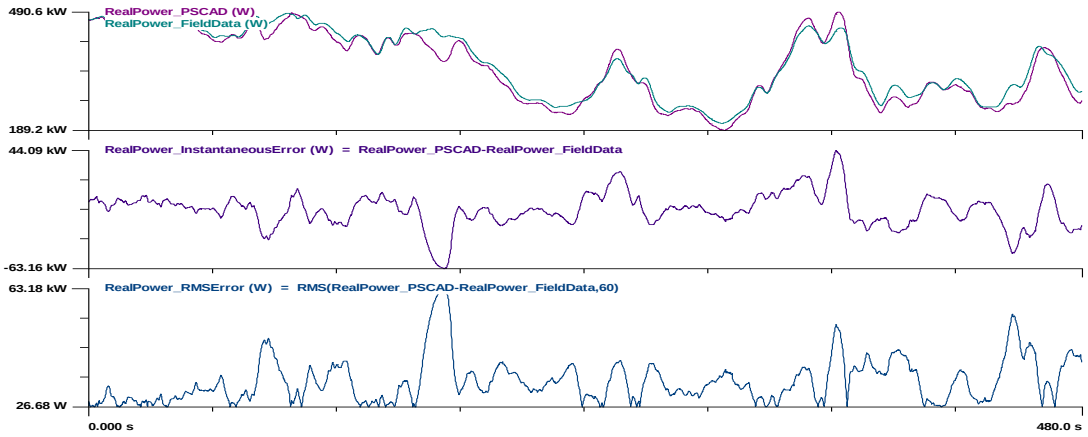

Fig. 4.1-1: Top traces: Real power output of inverter 1 ac side—PSCAD simulation and field data. Middle trace: Instantaneous error between the real power output of inverter 1 ac side—PSCAD simulation minus field data. Bottom trace: RMS error of the middle trace—RMS was computed over a sliding time window of 480 s.

It takes the PSCAD 39.2 hours to simulate the 480 s event with a 10 μs simulation time step on a personal computer with an 8th Gen Intel i7 vpro CPU. The quasi-dynamic model based on quadratized device models uses only 1,030 s to get the simulation results with a 200 μs simulation time, and the speed is about 135 times faster. The simulation results produced from the quasi-dynamic model are very similar to the ones

from the baseline model, as may be noted from the power plots in Fig. 4.1-2. The other plots are shown in the Appendix.

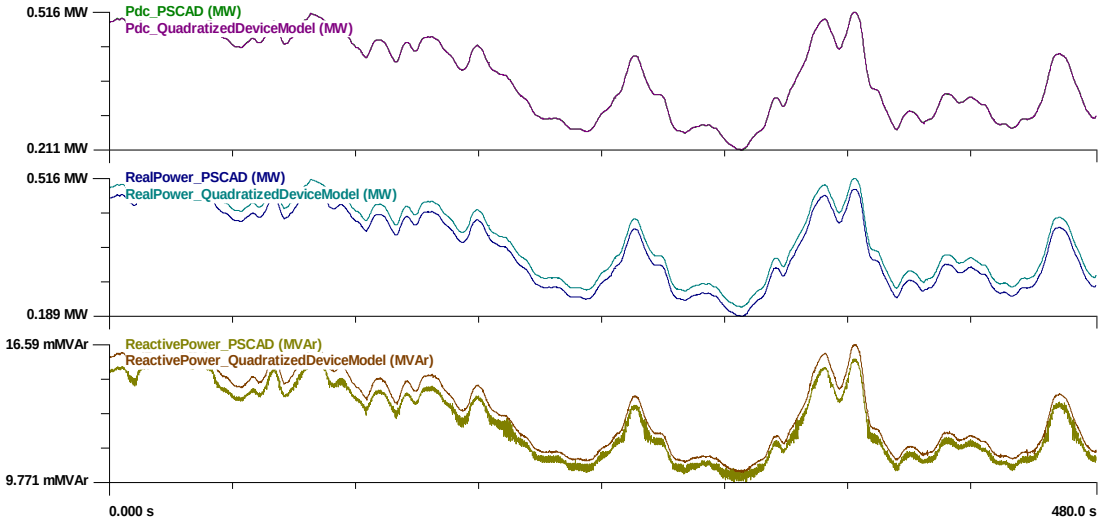

Fig. 4.1-2: The dc power (top), real power (middle), and reactive power (bottom) of inverter 1 from the simulation of the baseline and quadratized models.

T-5. Present scenario development

ST-5.1 Develop dynamic (EMT-TS) model of present grid in PSCAD

The dynamic (EMT-TS) model of the present grid requires conversion of models in a TS simulator to the EMT simulator and/or to hybrid EMT-TS simulations. Conversion tools or hybrid simulation platforms like E-Tran [8] that convert PSSE models to PSCAD or perform cosimulation between PSSE and PSCAD need to be considered. To evaluate and set up the conversion tool and the hybrid simulation platform, the tool is first evaluated on the present WECC grid scenario, the 2020–2021 Heavy Winter Case (21HW2).

Hybrid Simulation Model of Present WECC Grid Scenario:

The latest version of the present WECC grid scenario (21HW2) is used for hybrid simulation in the EMT-TS environment. Some of the major challenges faced in this type of simulation include the following:

1. The dynamic simulation parameters recommended by WECC should be used with the appropriate application programming interface (DYNAMICS_SOLUTION_PARAM_2) to avoid any error in hybrid simulation. Hybrid interface fails during simulation if this is not followed.
2. For a large number of boundary buses, updating the PSSE case file manually for hybrid simulation is challenging and time consuming. A Python-based code is used to do this task quickly and accurately.
3. By default, the number of boundary buses is limited to 20 in E-Tran. Upon request, the vendor (PSSE) helped remove this limitation, a process that required replacing the library files in the E-Tran installation folder.

4. While converting an area to PSCAD for hybrid simulation, the renewable models are converted as constant frequency voltage source in PSCAD. This PSCAD model is not able to capture dynamic behavior of the renewable models. This challenge is related to the existence of incompatible libraries in PSSE and in PSCAD, as highlighted in a previous study [9].

Before the hybrid simulation interface starts, the loads and the machines should stabilize to minimize the difference between hybrid and PSSE simulation. Also, the hybrid simulation interface should be started within the 1 s of simulation, according to the E-Tran recommendation. The initialization process is explained in detail in the Appendix. Two hybrid tests are performed to ensure the stability of the simulations.

Hybrid test I: For hybrid simulation of the present WECC grid scenario, 18 buses are selected in E-Tran for conversion from PSSE to PSCAD. Of those, 13 are completely modeled in PSCAD, and 5 are used as boundary buses between PSCAD and PSSE. The analysis and lessons learned from this hybrid test are provided in the Appendix.

Hybrid test II: Here, a larger area was converted in PSCAD with 33 boundary buses for hybrid simulation. The simulation runs without any issue, and the result is the same as that of the PSSE simulation. This creates a platform for more detailed case studies.

Mapping of PV plants: The large PV power plants (>100 MW) of California that are mentioned in EIA-860 data are identified in WECC grid scenarios. Buses and plants in WECC grid models in the California region are considered here. The WECC grid scenarios used for identifying the solar plants are the following:

1. Present grid scenario—2020–2021 Heavy Winter Cases (one that is last modified on 4/17/2020 and another last modified in 2016), 2022 Heavy Summer Case for planning (last modified on 2/28/2019)
2. Future grid scenario—2028 Heavy Summer Planning Case (last modified on 5/2/2018), 2026 Heavy Summer Planning Case

Detailed information on the methods taken to map the plants can be found in the Appendix.

Simulated Event: The Angeles Forest Event [6], which occurred in the Southern California region on April 20, 2018, is simulated and studied in a Western Electricity Coordinating Council (WECC) grid scenario [10] in this project. During this event, a splice failure caused a 500 kV transmission line fault, which affected a few PV plants in the California Independent System Operator (CAISO) region as described in the NERC and WECC report [6]. The Angeles Forest fire event is simulated in the EMT-TS platform. The fault bus location and the tripped line in this event are identified using the information from the NERC-WECC joint report [6], WECC data, and Google Maps. The fault location is shown in a map, and the fault bus voltage is 500 kV, according to the NERC-WECC report. Based on this information, the location of the “fault bus” with 500 kV bus voltage is identified as accurately as possible from the WECC scenario. Also, the tripped transmission line between the “fault bus” and “bus 1” is identified from the WECC data using the NERC-WECC report. The fault duration, breaker tripping time, and instant of the fault (phase-A voltage negative zero-crossing) are also determined from the voltage and current plots given in the same report. Using the available real

power output plots [6] and cross-referencing those with the ratings of PV plants in the vicinity of the fault, multiple plants were identified as potential candidates and were verified with the data obtained.

For simulating an EMT-TS model, first, two of the affected PV plants during the Angeles Forest event in 2018 were considered. Different simulated cases (summarized in Table 5.1-1 in the Appendix) are based on different numbers of power grid buses being considered from the fault bus to the affected PV plant(s). The graphical representation of the power grid model is considered with one-hop, which means the electrical buses between the fault bus and one of the affected PV plants are considered, and at every bus, one additional bus is considered (Fig. 5.1-1). Some of the challenges faced in the development of the model are discussed in detail in the Appendix.

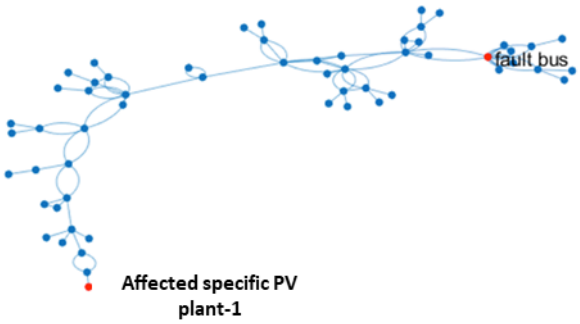

Fig. 5.1-1: Minimum spanning tree from fault bus to one affected PV plant with one-hop method.

Event Data: A self-clearing B-C line fault is simulated at the “fault bus” for 2.6 cycles at t = 1.99 s. One of the two parallel transmission lines from “fault bus” to “bus 1” is tripped at t = 2.035 s at the near end (“fault bus”) and at t = 2.042 s at the remote end (“bus 1”). Further detailed event data collection can be found in the Appendix. The voltages at the MV side of the transformer connected to the PV plants are measured. Also, the voltages and currents are measured at both the near and remote ends of the tripped transmission line.

Simulation Results:

The voltages and currents from the PSCAD simulation at the local end substation and the substation away from the local end on the faulted transmission line buses are shown in Fig. 5.1-2 (a) and Fig. 5.1-2 (b), respectively. The comparative analysis of local end data between the NERC report data and simulation results is presented in Table 5.1-1. The local end measurements from the simulation are greater than 95% accurate.

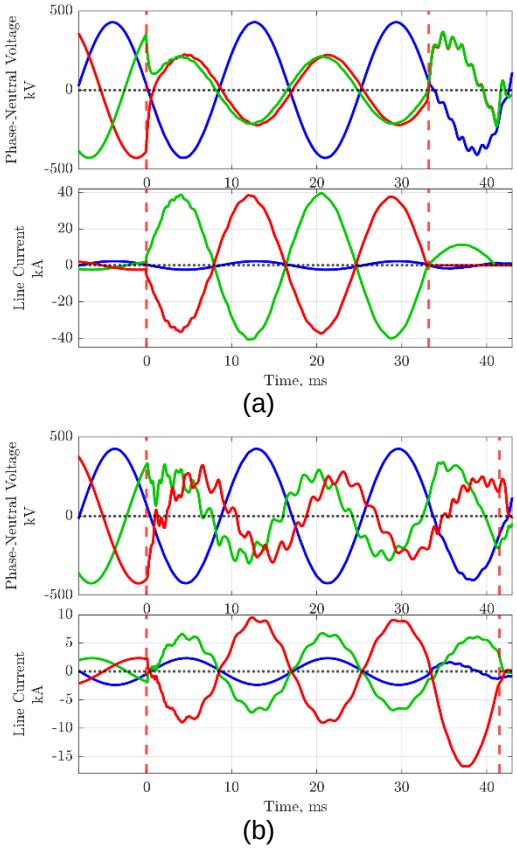

Fig. 5.1-2: Voltage and current plots form the EMT simulation at the local end and the substation away from the local end on the faulted transmission line.

The phase jump in the red curve in Fig. 5.1-2 is explained in the Appendix.

Table 5.1-1: Comparison of simulation results

Parameters	NERC report	EMT simulation
Local end voltage data		
B and C phase voltage	0.48	0.5
The average phase difference between B and C phase voltages	~15°	15°
Local end current data		
B and C phase currents	17	17
The phase difference between B and C phase currents during fault	180°	180°
C phase current after local end breaker operation*	5	5
Pre-fault and during fault current direction	same	

ST-5.2 Evaluate performance and redesign in real-time simulations in a real-time simulator (like RTDS)

Based on Case 1PD (described in Table A5.1-4 in the Appendix), a grid model was developed in RSCAD software for real-time simulation. Fig. A17.3-45 in the Appendix presents the layout of the developed model in RSCAD. The voltage levels of the transmission grid are 115 kV, 230 kV, and 500 kV. The transmission and distribution lines were developed by using Bergeron line models and PI-section line models in RSCAD library. The transformers in the grid model were developed by three-phase–two-windings or three-phase–three-windings models. Series capacitors and shunt capacitors were modeled for compensation in the grid model. The load in the grid was modeled by constant impedance of the RSCAD library model. The converted model in a real-time digital simulator (RTDS) has an error of less than 1.25%. The process to convert to a real-time simulation model and the corresponding results are discussed in detail in the Appendix.

M5.1: Real-time simulation model of present scenario without PV models

T-6. Future scenario model development

ST-6.1 Collect information on future PV in queue

The *2028 Heavy Summer WECC grid scenario* is not updated with the latest PV plants or renewable plants in the queue of CAISO. The detailed information on this scenario is provided in the Appendix, as is the summary of the generation for the *2026 Heavy Summer scenario*.

Observations:

- This WECC planning model (2026 Heavy Summer) has the highest generation (45%) from the renewable plants compared with other available planning cases. But this model still doesn't have the same renewable generation as the planned goal.
- From the in-queue PV plant list, 12 large (>100 MW) plants are identified in this planning model.
- Large (>100 MW) thermal nuclear plants are also identified in the California region from this WECC planning model. This helps to identify the conventional plants, which undergo a decrease in generation or shut down in the future.

ST-6.2 Upgrade present model with future model in PSCAD

Upgrades to the 26HS2 (2026 Heavy Summer WECC grid scenario) are discussed in later tasks. Additional analysis on the 2028 Heavy Summer WECC grid scenario is provided in the Appendix.

T-7. Advanced control functionalities

ST-7.1 Collect data on future PV system response requirements

Several studies on future grids and the study of problems in present grids with local high penetration of inverter-based resources worldwide have been reviewed to identify the list of control functionalities of interest in the faster timescale that may improve the reliability of future power grids [11–27]. Fourteen control functionalities are identified and mentioned in the Appendix. Based on the literature reviewed and analyzed, a control specifications document was developed and provided to IAB members for feedback; this document can be found in the Appendix (with the content in italics and green font). An IAB meeting was organized with more than 20 participants to describe the project's goals and the control features surveyed. The control features were documented in a control specifications document and circulated among the IAB members to rank the features of interest and/or those expected to play a major role in future grids. Based on the feedback, all control features were ranked as well as identified the number of times they were top ranked. Results are shown in Fig. A17.3-47 and Fig. A17.3-48 in the Appendix. Based on the mean ranking, the identified top features of interest can be grouped as follows: (i) providing continuity of operations and voltage/reactive power support during events, and (ii) providing frequency support during events. Based on these control features of interest, the control algorithms are being developed.

M7.1: Specifications document for PV control functionalities

ST-7.2 Design advanced control functionalities

Model predictive control (MPC) has been identified as a potential method to facilitate embedding advanced control functionalities. MPC implementation requires a system model to provide the predictive feature. Models for the advanced control functionalities of the PV plant are developed using PSCAD software with a built-in knowledge-based PV model. The objective function is defined in terms of optimizing the decision variables that need to be controlled. Constraints are defined based on the simplified system model and physical system requirements and conditions that the solution must satisfy. The model is shown in the Appendix. The equivalent single-line diagram representation of a PV plant with "N" PV modules connected to the point of connection (shown as POC) is illustrated in Fig. 7.2-1.

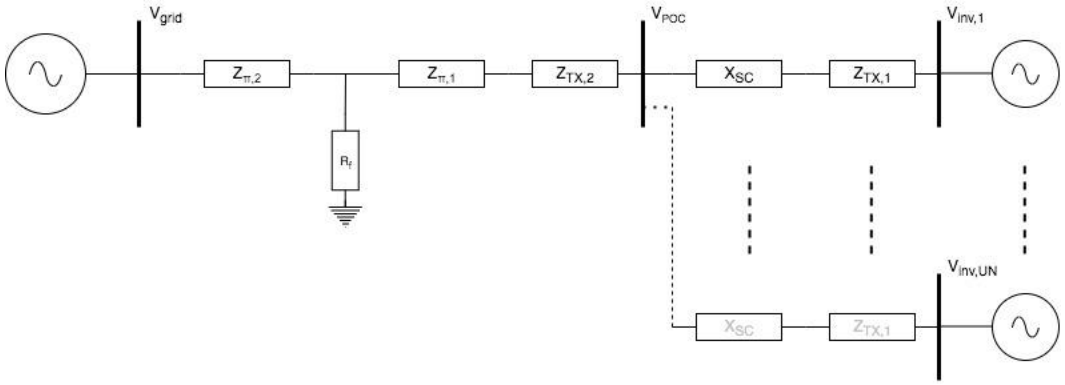

Fig. 7.2-1: Single-line diagram representation of the PSCAD model for steady state analysis.

T-8. Develop suite of dynamic PV system models

ST-8.1 High-fidelity model in PSCAD

A library of high-fidelity converter models in a PV plant were developed to include different grounding configurations (like midpoint dc-link grounding and ungrounded), different filter configurations (LC, LCL), and different converter configurations (dc-dc converter and dc-ac inverter, dc-ac inverter only with different configurations like two-level and three-level converters). More details of the library of models can be found in the Appendix.

Specific PV Plant-1 High-Fidelity Model

In addition to the generic PV plant's high-fidelity model, a high-fidelity model was developed of a specific PV plant-1 (one of the plants affected during the Angeles Forest event in California in 2018). The simulation algorithm proposed in ST-3.2 and applied to the generic PV plant's high-fidelity model was used on the high-fidelity model developed for the specific PV plant-1. Data were extracted from plant specification documents, and an individual data sheet for each component in the plant (lines, cables, transformers, inverters) was provided under NDA with the generation owner. Data included PV array specifications, converter specifications, distribution network layout, feeder lines and cables, line and cable conductors, and power and distribution transformers. Unavailable data were estimated based on (1) vendor suggestions, such as inverter controller parameters like switching frequency and controller gains; and (2) Google map images of the PV plant, which were correlated with the layout available in the plant specifications document to estimate factors such as plant feeder line length.

This plant has two types of PV systems, each comprising a distribution transformer, multiple inverters, and PV arrays. For the remainder of this document, the systems will be called PV system-1 and PV system-2. The high-voltage side of the distribution transformer in a PV system connects to the distribution grid. Typically, the inverter controllers in a plant PV system(s) use a control time step in the range of 50–100 µs, and the PPCs use a control time step in the range of 10–100 ms. In many traditional plants, active power from the inverters in the PV systems is delivered from the plant based on the solar irradiance available, and reactive power from the inverters depends on the reference sent from the PPC. The reactive power reference for each inverter

generated from the PPC may depend on the control mode chosen in PPC, such as: (i) reactive power control at point of interconnection (POI) of plants, (ii) power factor control at POI of plants, or (iii) voltage control at POI of plants. In the specific PV plant-1 model, a multirate hierarchical control system based on real code (as it would be in the controllers) is developed to represent the control time step along with control algorithms as in the field. This results in a multirate control system implementation with time steps like 50–100 µs and 10–100 ms being utilized in the inverter controller and PPC, respectively. Additionally, the hardware within the PV plant is simulated at a different time step. The PV systems use the library of developed high-fidelity converter models, and system details are in the Appendix. The models incorporate protection, changes to the filters, and multirate implementation of the inverter control system.

Distribution Grid in Specific PV Plant-1: The distribution grid consists of multiple feeders and internal buses. Its model is developed without the PV systems integrated. Advanced numerical simulation algorithms like Kron's reduction and the conventional trapezoidal discretization are applied to the model.

Simulation of Specific PV Plant-1's High-Fidelity Model: The specific PV plant with all the upgraded PV systems integrated within the distribution grid model and with the PPC is simulated at an operating condition for which data are available. The corresponding simulation results are shown in Fig. 8.1-1. The active and reactive power from the PV plant shown in Fig. 8.1-1(c)–(d) closely follow available the data, with less than 1% error observed. That is, ***greater than 98% accuracy*** is observed in the simulation results from specific PV plant high-fidelity model and ***speed-up is up to 326 times, compared with the baseline***.

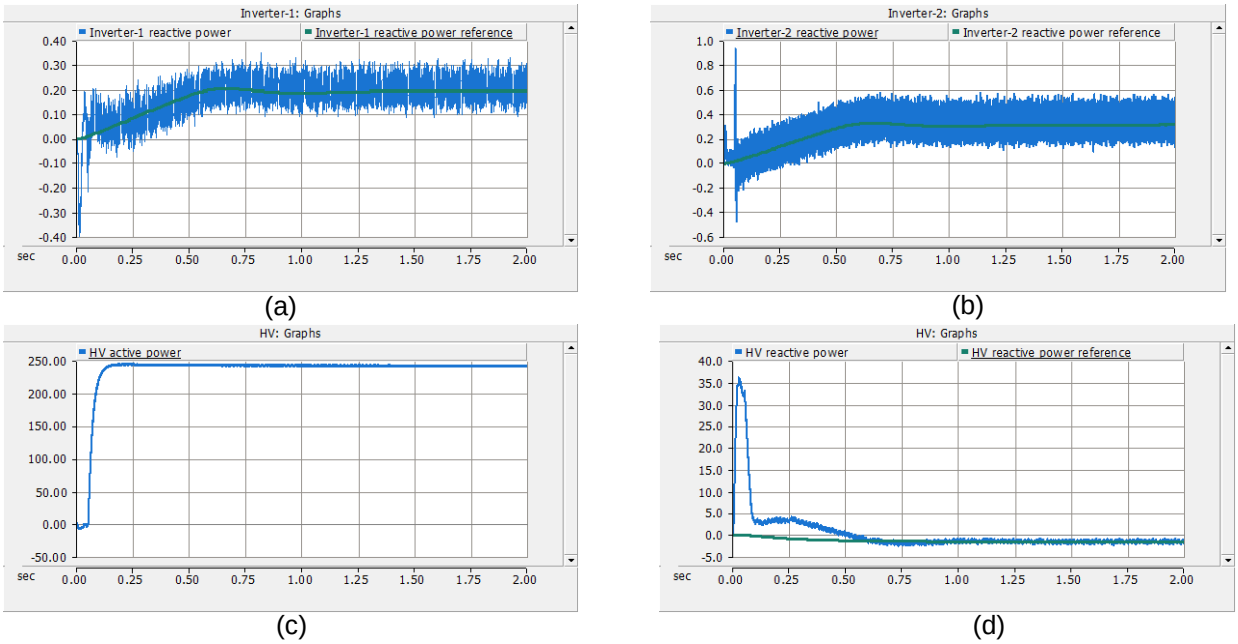

(a) (b)

(c) (d)

Fig. 8.1-1: Simulation results for the specific PV plant-1.

M8.1: High-fidelity model development

ST-8.2 Advanced model in PSCAD/PSSE

The overall process to generate the advanced model is shown in Fig. 8.2-1. In this process, the data from simulation of a dynamic model and/or field data are required for various operating conditions for the system for which the advanced model is generated. Based on the data generated and/or obtained, the RNN AI model is trained in Python. The parameters of the RNN model are varied for best fit to the available data. Thereafter, the parameters of the RNN model are extracted for the best fit. The RNN model is coded in C using the extracted parameters; this C code is integrated into PSCAD for testing during simulations. Starting with a more manual process, a greater degree of automation was introduced in the process to generate data, train the RNN model, and develop the RNN model in C, and test the RNN model in C with PSCAD. Incorporating a greater degree of automation simplifies the process to generate an advanced model for different types of PV inverters, transformers, and PV plant configurations. The goal is to generate the data from a dynamic model in PSCAD, store and process the data, train an advanced model using the data, store the advanced model with gains and biases, develop C code that can access these data, and run PSCAD-C advanced model simulations with the click of one button. Detailed information on data generation, data processing and storage, C code development, and PSCAD-C advanced model development can be found in the Appendix.

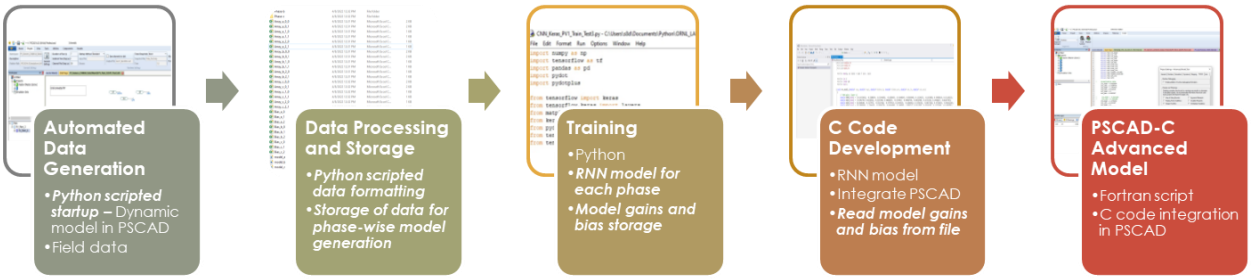

Fig. 8.2-1: Process to generate an advanced model in PSCAD with a greater degree of automation. The automation aspects of the process are shown in bold, italicized text.

The implementation of the advanced model is shown in Fig. 8.2-2. The simulation results from the advanced model compared with simulation results from the baseline (or high-fidelity) models have shown very close similarity with ***greater than 98% accuracy with respect to field data and up to 42 times speed-up***. These results are obtained from the simulation of a single PV system. One of the results, shown in Fig. 8.2-3, highlights an extremely close match between the simulation results.

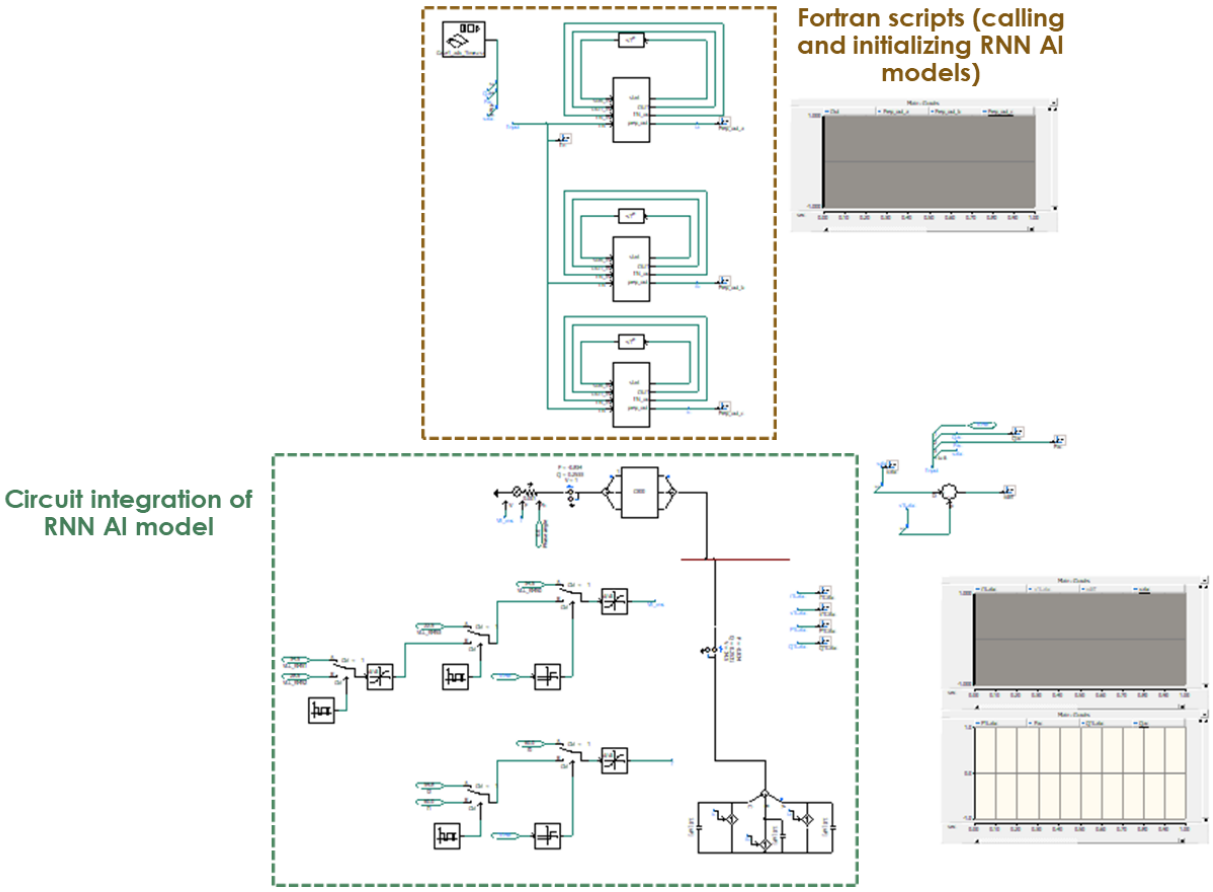

Fig. 8.2-2: Circuit implementation of RNN AI model for one PV system in PV plant-1.

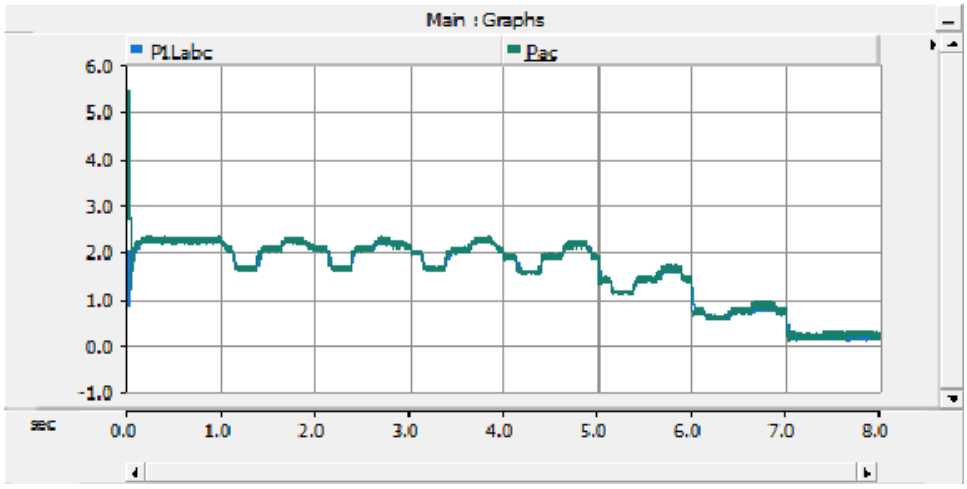

Fig. 8.2-3: Advanced model's active power output
(P1Labc = advanced model output; Pac = baseline model output).

M 2.8.2: Advanced model development

T-9. Evaluation and redesign dynamic models

ST-9.1 Evaluation of high-fidelity model

Specific PV Plant-1

A 2 s stress test is conducted on the high-fidelity model of the specific PV plant-1 with the following dynamic changes: (a) operating condition changes in PV system-1 at t = 0.5 s, 1.05 s, and 1.4 s; (b) operating condition changes in PV system-2 at t = 0.5 s, 0.85 s, 1.05 s, and 1.4 s; and (c) blocked condition at t = 1.75 s in all the inverters (that happen in the field owing to transient overvoltage at inverter terminals). The simulation results for these changes within the specific PV plant-1 are shown in Fig. 9.1-1(a)–(l), including the currents and voltages within two of the modules within the specific PV plant-1. A module within the specific PV plant-1 incorporates a distribution grid with several numbers of both types of PV systems. The distribution grid within the module connects to its own power transformer. From Fig. 9.1-1(a)–(f), it can be observed that the states (voltages, currents) within the specific PV plant-1 are stable during all the dynamic changes, and the ac-side currents change as expected during dynamic operating conditions. The total harmonic distortion (THD) and total rated distortion (TRD) of modules 1 and 2 ac-side currents, as shown in Fig. 9.1-1(g)–(j), are within the recommended limits of IEEE 519-2014. The active power also is as expected from Fig. 9.1-1(k) based on the changes introduced in the different types of PV systems.

In addition to the changes within the PV systems (and their inverters), the specific PV plant-1 is also evaluated for steady state operation and capacitor switching within the plant. The results for steady state operation of PV plant-1 are shown in Fig. 9.1-2. The active power ($P_{ac,HV}$) and reactive power ($Q_{ac,HV}$) on the high side are shown in Fig. 9.1-2(a)–(b), respectively. The active power ($P_{ac,LV2}$) and reactive power ($Q_{ac,LV2}$) on the low side of one of the modules are shown in Fig. 9.1-2(c)–(d). The results are consistent with the specific PV plant-1 results obtained from the plant owner.

The results for the capacitor switching use case in the specific PV plant-1 are shown in Fig. 9.1-3. In this use case, the capacitors in the module 2 are switched at t = 2 s, and the entire plant response was observed and compared with the results obtained from the vendor for the same use case. The $P_{ac,HV}$, $Q_{ac,HV}$, $P_{ac,LV2}$, and $Q_{ac,LV2}$ results are shown in Fig. 9.1-3(a)–(d). From the figures it is observed that the results are consistent with the specific PV plant-1 results obtained from the vendor. The $P_{ac,HV}$ result during transient is >97% accurate in comparison with the vendor data. The $Q_{ac,HV}$ differential observed during the switching of the capacitor in Fig. 9.1-3(c) is 17.3 MVAr, whereas the $Q_{ac,HV}$ differential observed during the switching of the capacitor from the vendor data is 16.5 MVAr. From these observations, it can be inferred that the $Q_{ac,HV}$ is >95% accurate.

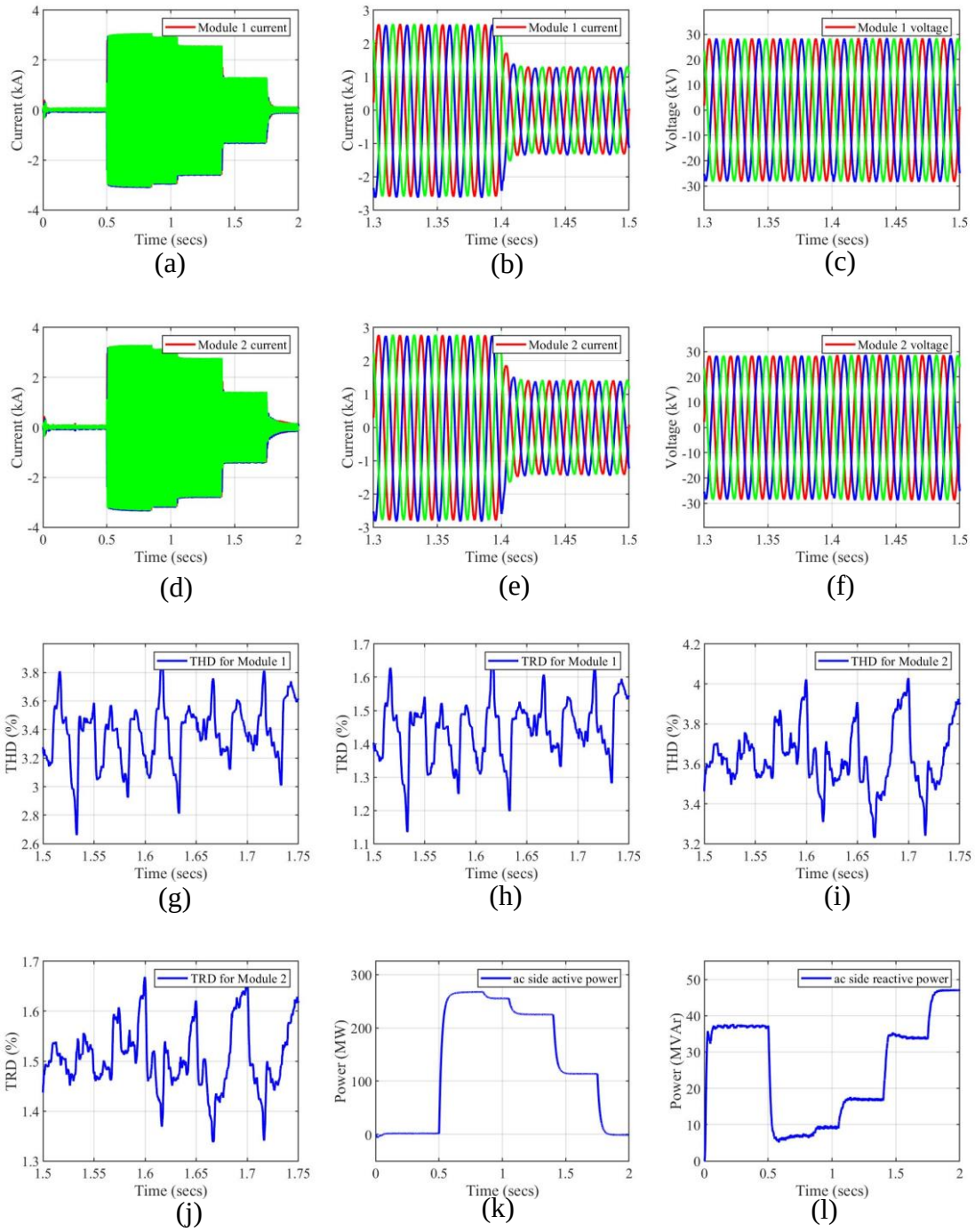

Fig. 9.1-1: Simulation results for the specific PV plant-1.

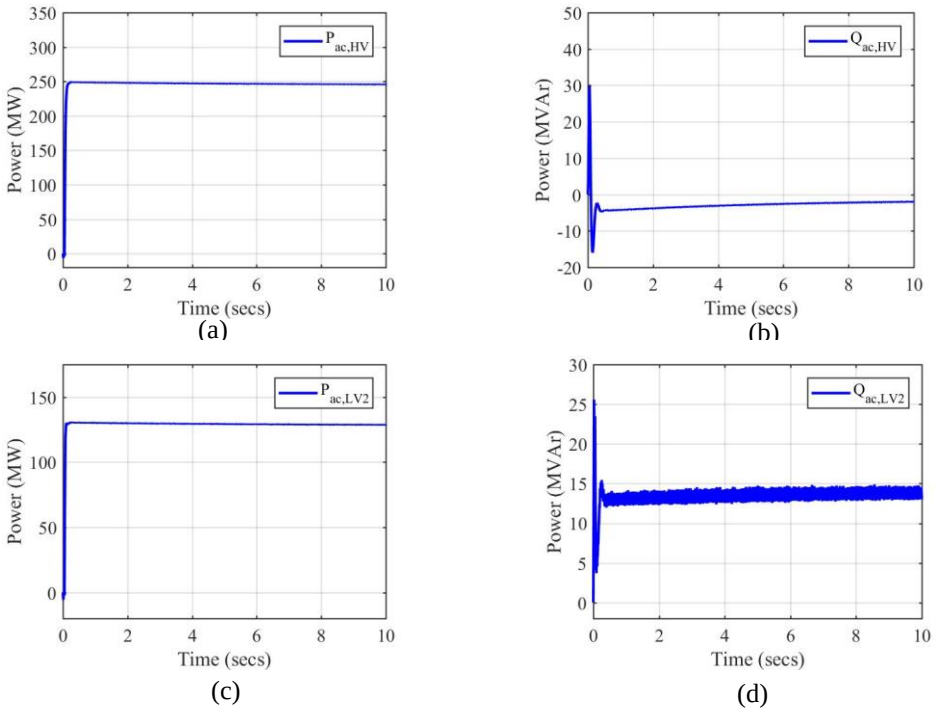

Fig. 9.1-2: Simulation results for the specific PV plant-1 during steady state: (a) $P_{ac,HV}$, (b) $Q_{ac,HV}$, (c) $P_{ac,LV2}$, and (d) $Q_{ac,LV2}$.

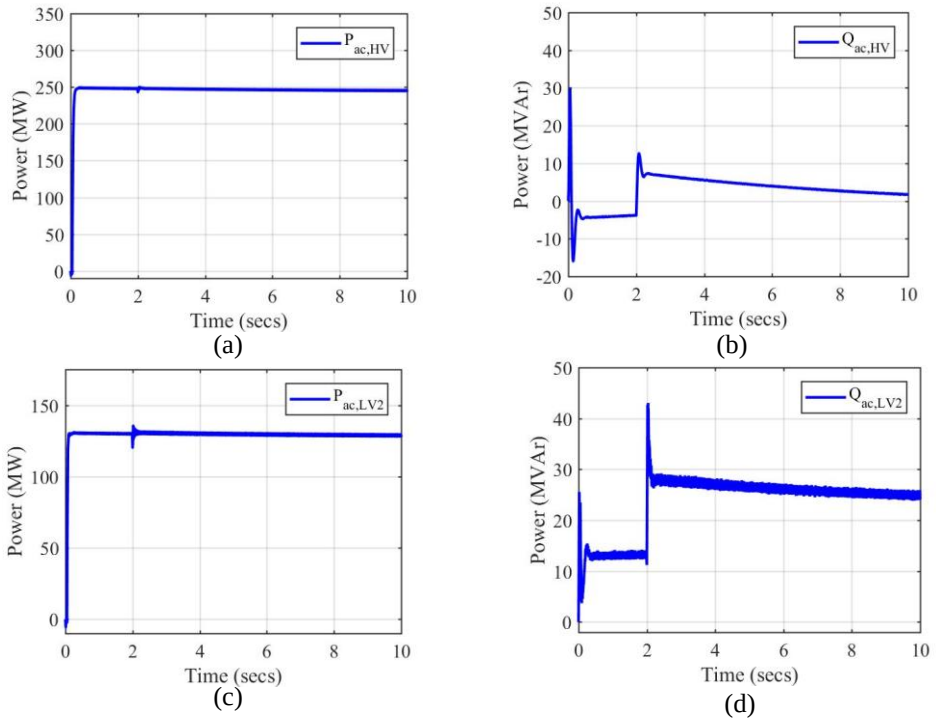

Fig. 9.1-3: Simulation results for the specific PV plant-1 during capacitor switching in module 2: (a) $P_{ac,HV}$, (b) $Q_{ac,HV}$, (c) $P_{ac,LV2}$, and (d) $Q_{ac,LV2}$.

ST-9.2 Evaluation of advanced model

PV system-2's advanced model is developed using the process discussed in ST-8.2 and integrated within PSCAD environment using C codes. The simulation results from the advanced model compared with simulation results from the baseline (or high-fidelity) models have shown very close similarity (with ***greater than 98% accuracy*** with respect to field data and ***up to 100 times speed-up***). These results are obtained from the simulation of the second PV system. One of the results, shown in Fig. 9.2-1, highlights an extremely close match between the simulation results.

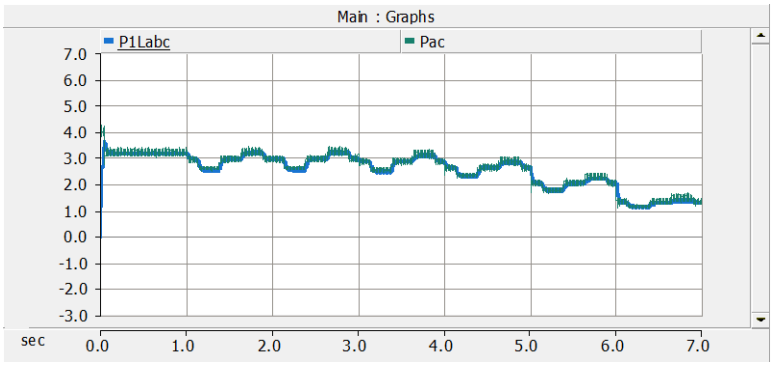

Fig. 9.2-1: Advanced model's active power output (P1Labc = advanced model output, Pac = baseline model output).

The two PV system advanced models have also been integrated with the distribution grid model of the PV plant. Some of the simulation results from one advanced model's integration within the plant are shown in Fig. 9.2-2.

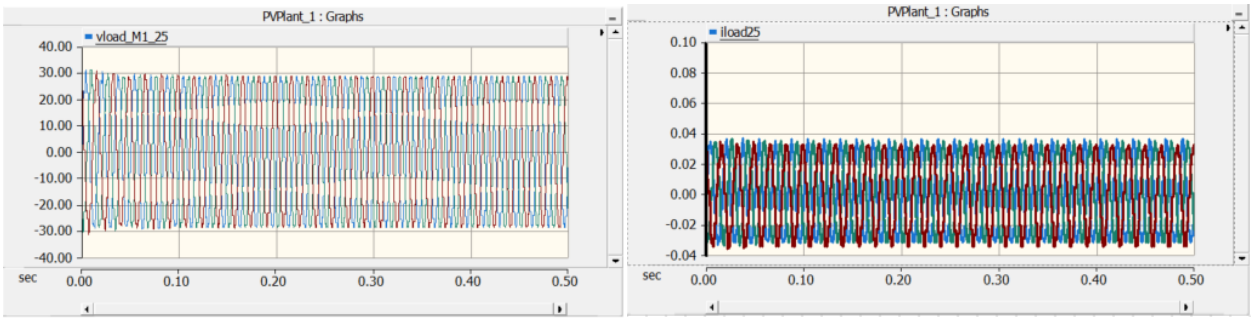

Fig. 9.2-2: Simulation results from the advanced model's integration within the specific PV plant-1. Shown are the behavior of the distribution grid voltage (left) and the PV system current (right) as expected.

T-10. Present scenario development

ST-10.1 Incorporate suite of dynamic PV system models

Electromagnetic Transient (EMT) Model of Present Grid

In addition to k-hop (k = 1, 2) models developed in ST-5.1, a zero-hop model is based on the following cases:

1. Case 1: Power grid model with the fault buses and includes path to the specific PV plant-1
2. Case 2: Power grid model with the fault buses and includes path to the specific PV plant-2

3. Case 3: Power grid model with the fault buses and includes path to both of the specific PV plants

All the EMT models contain the high-fidelity models and detailed circuit implementation of the lines, cables, shunts, and breakers near the fault location that were identified in ST-5.1 for Case 1. Additionally, they contain the exact system as in the field in the EMT model of the power grid in this case. The rest of the grid is modeled as an equivalent source with an impedance in series; the system is connected to the equivalenced part through the boundary buses. The buses and boundary buses in all the three cases are summarized in Table 10.1-1.

Table 10.1-1: Characterization of the cases of EMT models

	Case 1	Case 2	Case 3	**Common buses**
Total buses	16	24	29	11
Boundary buses	11	10	12	9

The PSCAD simulation results from all three EMT models and the continuous time error are shown in Fig. 10.1-1. The errors observed are small, except at the remote end.

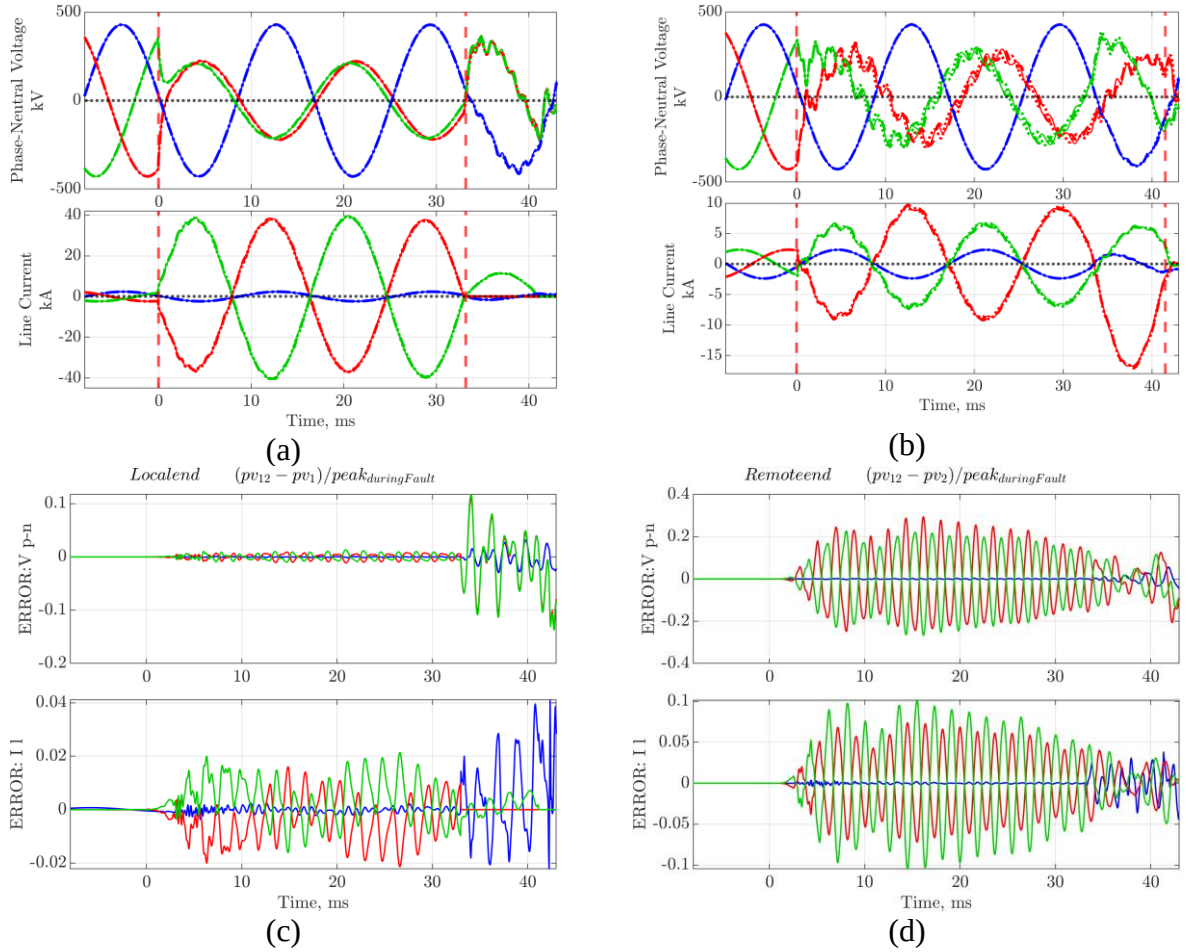

Fig. 10.1-1: EMT simulation results from the power grid in three cases: (a) local end voltages and currents, (b) remote end voltages and currents (solid line: Case 1; dotted line: Case 2; dashed line: Case 3), (c) error plot for local end voltages (top) and current (bottom) between Cases 3 and 1, and (d) error plot for remote end voltages (top) and current (bottom) between Cases 3 and 1.

Observation and Modification near the Fault Location (Remote End): Local end voltages and currents are similar for all cases during the fault. The remote end voltage has a high-frequency component, which has some phase difference among the three cases. This results in a significant difference in the voltages of the three cases in the continuous-time error plot. Using frequency spectrum analysis, the source of this high-frequency component is identified as the underground cable near the remote end bus along with the measurement devices (with filters). This underground cable and the measurement devices (with filters) are upgraded to reduce the observed high-frequency oscillations, which are not observable in the NERC report [6].

Information about the underground cable and overhead line present in faulted transmission circuits from publicly available documents is used to improve the model. Parameterization and configuration of the lines are modified. Following these changes, the voltage and current response near the fault location becomes like the NERC report data during the fault. Plots from the simulation of case 3 are shown in Fig. 10.1-2. The normalized (using peak value during the fault) continuous-time differences between Cases 1 and 2 are shown in Fig. 10.1-3, from which it may be noted that the simulation results are very similar in Cases 1 and 2. In general, the simulation results for all three cases are quite similar. These models are termed the min grid model.

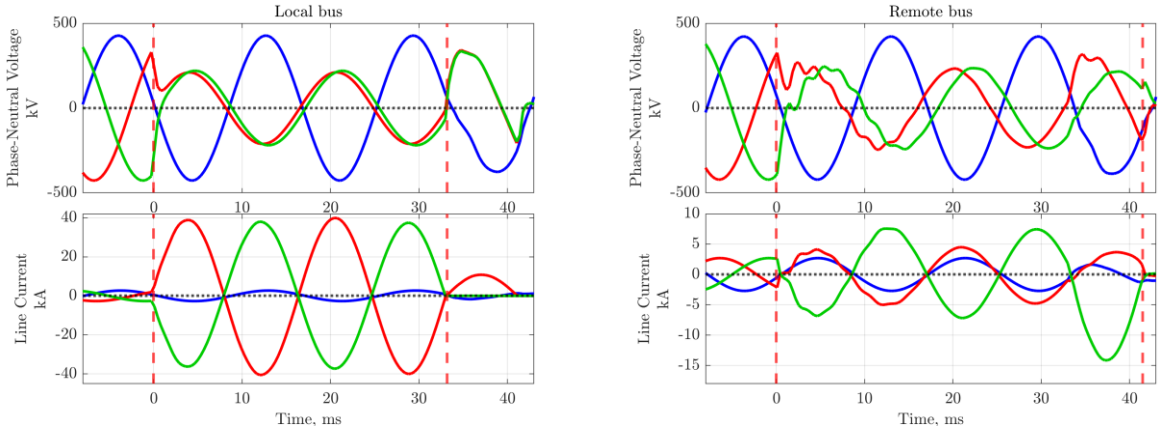

Fig. 10.1-2: Local end and remote end voltage and current plots from the EMT simulation of the present scenario grid model Case 3 with the Angeles Forest fault event.

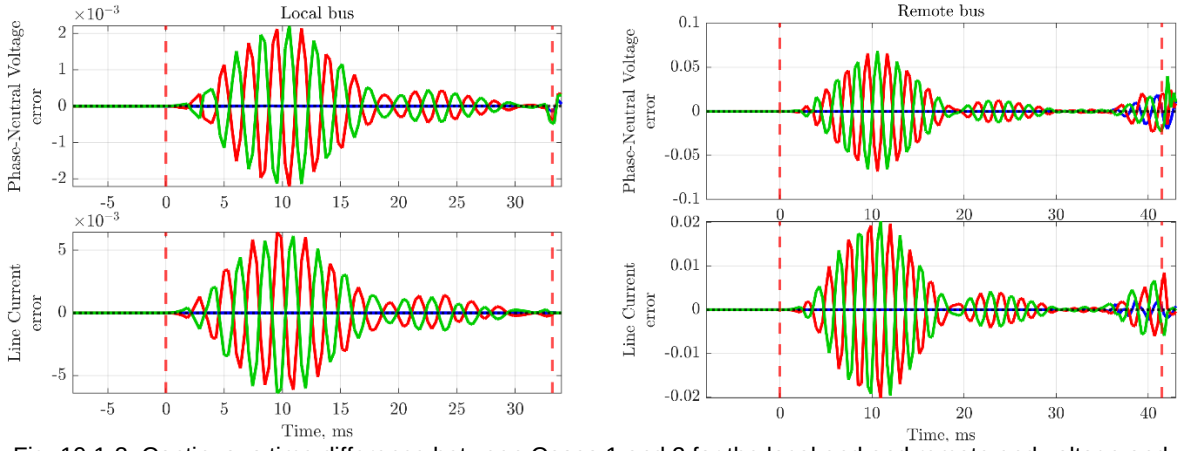

Fig. 10.1-3: Continuous time difference between Cases 1 and 2 for the local end and remote end voltage and current plots.

High-Fidelity PV Plant Model Integration with EMT Model of Power Grid in PSCAD

The EMT dynamic model of the present scenario of the power grid connecting the fault location to the specific PV plant-1 (Case 1) is integrated with the high-fidelity model of the specific PV plant-1. A modular integration approach is considered with the present grid model and the specific PV plant-1 model in separate files. Connectivity is achieved through a transmission line with remote ends that connect the models in the two files (shown in Fig. A17.3- in the Appendix). This approach eases the upgrading of individual grid or plant models separately and then integrating either of them back. To ensure successful simulation of the present scenario grid model with the specific PV plant-1's high-fidelity model, the models are run at the same time in PSCAD by creating a new simulation set in PSCAD and including both files (with the models) in that particular set with the ends of the transmission line named the same in both models.

Once the two models were integrated, the simulation results showed high-frequency oscillations and transient overvoltage at the buses near the specific PV plant-1 (similar to the ones observed in Fig. A5.1-10 in the Appendix). These were not observed in the recorded data from the fault event.

Upgrades in EMT Model of Power Grid near the Affected PV Plants: More synchronous generators, which are near the affected specific PV plant-1, are added to the developed EMT model of the present scenario of the power grid to better capture the during- and post-fault voltage response near the specific PV plant-1 buses. This upgraded EMT model has 52 buses in PSCAD (13 boundary buses and 39 in the detailed model). The voltage and current responses at the local and remote buses during the event are plotted in Fig. A17.3- in the Appendix; they remain very similar to the response observed earlier (without the upgrades described here). The voltage during the fault near the specific PV plant-1 at transmission level is shown in Fig. 10.1-4. The high-frequency oscillations and transient overvoltage are no longer observed during the fault. This model is termed the best case grid model.

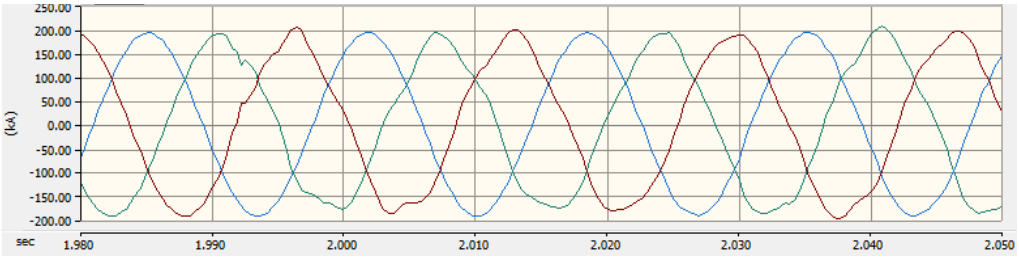

Fig. 10.1-4: Voltage plots near one affected PV plant from the EMT simulation of the present scenario grid model for the Angeles Forest fault event.

Upgrades to the Specific PV Plant-1's High-Fidelity Model: There is an overlap region introduced within the specific PV plant-1's high-fidelity model and the plant's integration into the EMT model of the power grid. The overlap region consists of power transformers and plant-level filters modeled both in the specific PV plant-1's high-fidelity model and in the circuit that integrates the high-fidelity model to the EMT model of the power grid. This introduction of an overlap region improves the model's accuracy compared with nonoverlapping models, especially in the presence of high-frequency components. An example of the overlap region in the circuit that integrates the high-

fidelity model of the PV plant is shown in Fig. A17.3- in the Appendix. In this case, the voltages measured upstream (above the power transformers) are fed to the specific PV plant-1's high-fidelity model, and the individual module's currents are fed back to the circuit model from the specific PV plant-1's high-fidelity model. In the absence of the buffer zone, the voltages measured at the terminals of the module's currents are fed to the specific PV plant-1's high-fidelity model, and the individual module's currents are still fed back to the circuit model.

Equivalencing of the EMT Model for Present Grid Scenario: To remove sensitive information in the power grid models, an equivalencing technique is also studied in this project. The zero-hop EMT model with PV-1 (Case 1) for the Angeles Forest fault simulation is modified to remove the power grid line and bus information from the model. The following methods are used to mask sensitive data with minimal alteration of the voltage response near the affected PV plant and faulted buses:

(a) The parallel lines are replaced with an equivalent single transmission line.

(b) Some E-Tran–generated equivalent lines that are parallel to the actual transmission lines in the system's EMT model are replaced with a single transmission line.

(c) Few series-connected transmission lines are equivalenced as a single line.

(d) The WECC line data are given for the π-model of the transmission lines. Some of the π-line models are replaced with equivalent T-line models to hide the exact power grid line parameters.

(e) Few buses are removed from the E-Tran–generated EMT model using Schur complement.

(f) Some transmission lines have very small susceptance and are removed because they don't change the voltage dynamics at any bus where PV plants are connected.

(g) Three winding transformers are reduced to conventional two winding transformers.

After these modifications, the voltage at the bus where the PV plant is connected is observed (plotted in Fig. A17.3- in the Appendix) and is found to be similar to the original model.

C code development for High-Fidelity Model of PV plant in RSCAD

In RSCAD, the C programing language is used for a custom component. The syntax of C in RSCAD is mostly the same as a general C language. However, the C in RSCAD has three important sections: STATIC, RAM, and CODE. In the STATIC section, declared variables may be used in both the RAM and CODE sections, and the STATIC section is executed before the start of real-time simulation. C codes in the RAM section compute constants required for the CODE section. The C code in the RAM section is executed once before the start of the real-time simulation. Thus, constants such as RLC parameters of a line, inverter parameters, PV array parameters, and matrices (upon discretization of the dynamic models) like the A matrix can be implemented in this section. C codes in the CODE section runs on the real-time hardware at every time step. Hence, codes for updating states such as **b** vector from previous states' values and/or input values and for calculating states such as **x** vector through solution of A**x**=**b** can be implemented in this section.

After developing custom components for base operations such as vector update calculation, matrix formulation, matrix inversion, and matrix multiplication, the high-fidelity models (using the multiple A [MA] matrices model) of the specific PV plant-1 is implemented by using the developed custom components in RSCAD. Several challenges were encountered during the implementation and simulation of the specific PV plant-1 in C code and integrated with RSCAD. The first challenge was completing the computations while simulating a high-fidelity model of the specific PV plant-1 in real-time in a single core with a small time step needed. The second challenge was numerical instability introduced by a short feeder line length if the time step was increased.

To resolve these challenges, the hard real-time constraints are relaxed, and all the calculations within a simulation time step can be completed within a defined solution time step. Moreover, to mitigate these issues, the high-fidelity model of the specific PV plant-1 was implemented on multiple cores using the inherent parallelism capabilities in the MA models. The PV plant's multiple radial feeders were modularized and allocated into multiple cores so that the hard, real-time constraints are met at a smaller simulation time step, compared with a single core implementation. Finally, short feeder lines typically introduce small time constants that do not enhance stability of the simulations if they are at the boundary of separation.

To address this challenge, some of the short lines' inductances are equivalenced and introduced within the feeders to increase length of the lines without compromising accuracy. For example, a line can be separated by two parallel feeder lines that include twice the inductance and resistance of the single line. The circuit model is enhanced accordingly with the capacitance of the short line. This separation in the inductances and capacitances is chosen as voltage is fed as an input to the high-fidelity model of the specific PV plant-1 in C code and the current is fed as an input to the circuit model that integrates the specific PV plant-1's high-fidelity model to the power grid. The high-fidelity MA model of the specific PV plant-1 is implemented in this process (shown in Fig. 10.1-5).

Simulation results that highlight stable simulation capability for the high-fidelity model of the specific PV plant-1 are provided in the Appendix in Fig. A10.1-6.

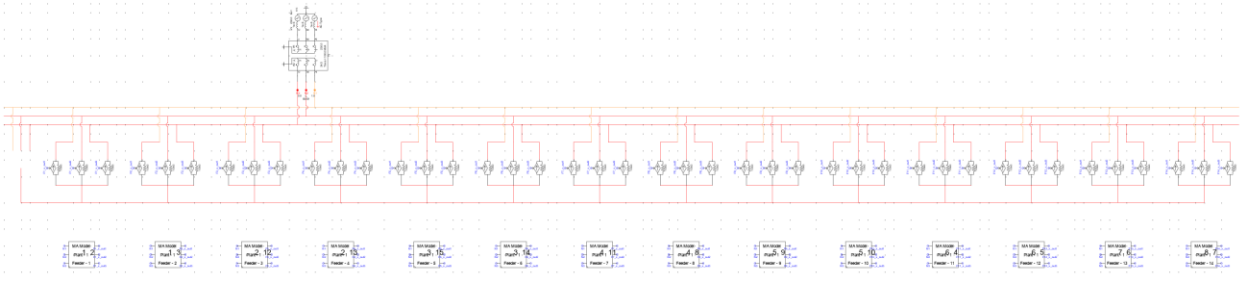

Fig. 10.1-5: High-fidelity model of the specific PV plant-1 developed in RSCAD.

T-11. Future scenario model development

ST-11.1 Upgrade present model with future model in PSCAD

The California Energy Commission plans to have 100% clean and carbon-free energy sources in the California region by 2045 [28]. As part of this process, a significant number of existing conventional power plants (e.g., thermal power plants) will retire by 2030, and renewable power sources (e.g., solar PV, wind, and hybrid plants and energy storage systems) will be integrated to the grid. To study this near-future (next 10–15 years) grid scenario with a high penetration of renewable power sources in California, a TS model is developed from an existing WECC grid scenario that has >60% of the total power generation in California from clean energy sources. This model, known as Scenario 1, was not found in existing databases. A TS model with 100% clean energy generation in the California-based WECC grid is also developed; called Scenario 2, this model is a long-future grid scenario focusing on 20–25 years from now.

Method to Upgrade the Model (Scenario 1): To obtain a model representing the future scenario (Scenario 1) of a power grid with ~60% generation from clean energy in California, the changes in the grid in California in the next 5−15 years need to be implemented in the existing model. This motivates the team to identify conventional power plants that will retire in the next 15 years, and the dynamic models of those plants are replaced with a renewable plant model in the existing 26HS2 base model. This approach is divided into the following three steps:

(a) Step 1: Collecting information on the conventional plants that will retire within the next 15 years and identifying those plants in the WECC 26HS2 scenario.

(b) Step 2: Replacing the dynamic models of the identified conventional plants with renewable plant models with same power outputs.

(c) Step 3: Analyzing stability of the modified grid models and comparing the TS simulation results between the original scenario and the modified scenarios for different past events related to line faults and generation loss.

Identification of Plants that will Potentially Retire: Different sources used to identify the retired plants are summarized in Table A17.3- in the Appendix. The exact names and power ratings are available only for a few plants that will potentially retire. The following approaches are used to identify potential plants that may retire where an exact name is missing (with references provided in the Appendix in the table):

1. Map data are found from a report by the Union of Concerned Scientists, which is marked with plants that can be retired to achieve less CO_2 emission from the power plants. This information is used to identify 11 potential plants in the WECC scenario that may retire in the future.
2. Information about plant age is found from a report by Physicians, Scientists, and Engineers for Healthy Energy. This information is used to retire 13 plants from the California region that are older than 17 years and that have power generation > 50 MW.

Upgraded Future Grid Scenario: These sources help to identify 37 plants and 81 units with total power generation of 9,653.6 MW in the WECC scenario. Replacing the dynamic model of these identified plants with a renewable plant dynamic model gives a TS dynamic model of a future grid scenario with >60% of the total generation in the

California region from renewable power sources. The summary of power generation in the modified scenario is summarized in Table A11.1-3 in the Appendix. To upgrade the dynamic TS model, a python-based automated tool is developed that is described in the Appendix (and shown in Fig. A17.3-56 in the Appendix). The quasi-dynamic model of the renewable power plants is shown in Fig. A17.3-57 and Fig. A17.3-58 in the Appendix.

ST-11.2 Incorporate suite of dynamic PV system models

High-Fidelity Model Integration in PSCAD for Future Grid Scenarios

The future scenario grid EMT dynamic model connecting the fault location to the specific PV plant-1 is integrated with the high-fidelity model of the specific PV plant-1 using the modular integration approach as discussed in ST-10.1. The future grid model (with 60% renewable penetration) and the specific PV plant-1 are in separate PSCAD files. These two models are connected through a transmission line with each remote end connecting each file. The setup for the process is discussed in Task 10 and is not repeated here.

ST-11.3 Test and redesign in real-time simulations in a real-time simulator (like RTDS)

The model of the future scenario of the power grid (with 60% penetration of renewables in California) was developed in RSCAD (RTDS) for real-time simulation. The model was originally developed in PSCAD to analyze the impact of transmission grid-level disturbances on new emerging PV plant(s). Later, simulation parameters needed for library components in RSCAD (RTDS) were extracted, such as system voltage ratings, source location/parameters, transmission lines lengths/parameters, transformer locations/ parameters, and fault type/location/fault duration. The extracted datasets are used to develop the model in RSCAD, illustrated in Fig. A17.3-59 in the Appendix. The simulation results for a line-to-line fault in the developed model of the future scenario of the power grid are illustrated in Fig. A17.3-60 in the Appendix. During the development of the model of future scenario of the power grid in RSCAD for real-time simulation, challenges were encountered. A variable resistor from 0.005 ohms to 1e6 ohms is used to represent the opening operation of the circuit breaker. However, such variable resistors do not exist in RSCAD. However, a different type of variable resistor exists that can be changed during simulation only by a slider, which is inefficient and difficult to achieve during a real-time simulation.

T-12. Validation of PV system models in present scenario

ST-12.1 Evaluate performance of PV system models within present scenario in PSCAD/PSSE

The integrated EMT model of the present scenario of the power grid with the high-fidelity model of the specific PV plant-1 is evaluated for a line-to-line fault incident that replicates the Angeles Forest disturbance scenario. The line-to-line fault is incepted at t = 1.99 s. The simulation results of the voltages and currents at the local and remote ends of the faulted line in the integrated model are shown in Fig. 12.1-1. The voltages and currents observed in Fig. 12.1-1(a) and (b), respectively, at the remote end of the faulted line are similar to the results observed in the EMT model of the power grid

(shown in section T-10). The same can also be said about the voltages and currents at the local end of the faulted lines shown in Fig. 12.1-1(c) and (d), respectively.

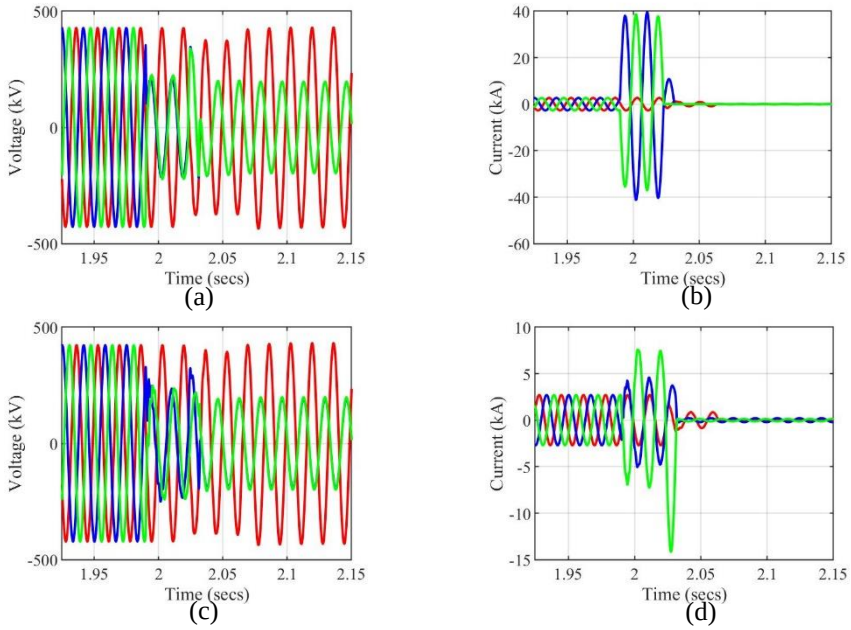

Fig. 12.1-1: Simulation results from the integrated EMT high-fidelity model (grid-plant) during line-to-line fault: (a) voltages at the near end of the faulted line; (b) currents at the near end of the faulted line; (c) voltages at the remote end of the faulted line; and (d) currents at the remote end of the faulted line.

The simulation results of active power from plant ($P_{ac,HV,}$) reactive power from plant ($Q_{ac,HV}$), active power from module-1 ($P_{ac,LV1}$), active power from module-2 ($P_{ac,LV2}$), reactive power from module-1 ($Q_{ac,LV1}$), and reactive power from module-2 ($Q_{ac,LV2}$) in the specific PV plant-1 are shown in Fig. 12.1-2(a)–(f), respectively. From the figures, it is observed that the active power from the plant reduces in response to the line-to-line fault. The reduction observed in the power arises from the transient over-voltage at some of the inverters' terminals within the plant. Accordingly, it may be observed that the active power from modules 1 and 2 also reduces but does not become zero because only some of the inverters in the plant trip. Minimal change is observed in the reactive powers in the plan and within each module. This is a ***first-of-its-kind EMT simulation to replicate a field event with trips in inverter-based resources (IBRs)*** recurrently being observed in the field.

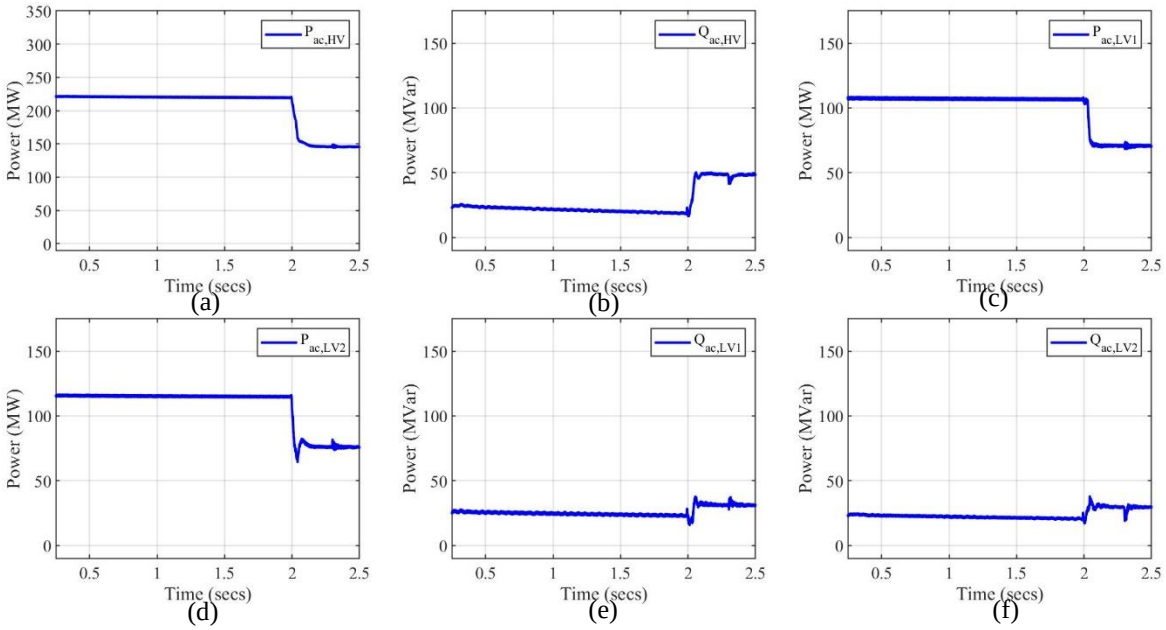

Fig. 12.1-2: Specific PV plant response during line-to-line fault: (a) $P_{ac,HV}$; (b) $Q_{ac,HV}$; (c) $P_{ac,LV1}$; (d) $P_{ac,LV2}$; (e) $Q_{ac,LV1}$; and (f) $Q_{ac,LV2}$.

ST-12.2 Redesign PV and grid models to mimic real-world data in real-time simulations in a real-time simulator (like RTDS)

To develop a real-time simulation integrated model of the present scenario of the power grid model with the high-fidelity model of the PV plant, a multicore implementation in RTDS is evaluated. Such an implementation can avoid numerical instability that may appear with hard real-time constraints if the implementation is attempted in a single core. To develop the model, resource requirements are evaluated based on the tests performed on the EMT model of the present scenario of the power grid and the high-fidelity model of the PV plant. Accordingly, the following information on resource requirement (in terms of the number of processor cards in RTDS) is gathered for the maximum parallelizable case implementation:

1. For the EMT model of the present scenario of power grid: four cards
2. For the power transformers in the PV plant: two cards
3. For the feeders in the PV plant: eight cards
4. For the PV systems (aggregation transformers + inverters + controllers) in the PV plant: 104–~156 cards

Thus, the total number of processor cards required is 118–~170 cards. These resources are available in the RTDS laboratory in SCE.

T-13. Advanced control functionalities

ST-13.1 Incorporate designed control methods

The model used in MPC for reactive power control is provided in detail in the Appendix. The MPC controls the reactive power injected by the PV modules to regulate the voltage at the point of connection (POC) during a fault instance. The initial

implementation of the MPC controller assumed a symmetrical three-phase-to-ground fault. The fault is assumed to take place between two transmission line pi sections with known positive sequence impedance. The initial simulation results, illustrated in Fig. 13.1-1, show the performance of the standard PI controller compared with the MPC controller after a rapid voltage drop caused by the three-phase fault. The results in Fig. 13.1-1 illustrate the improved stability of the MPC during and after the occurrence of the fault. The oscillations observed in the PI controller are not observed in the case with the MPC controller. The comparison shows that the MPC takes half the time to stabilize the voltage during fault and post fault when compared with the PI controller usage, thereby providing a recovery two times faster through the proposed MPC controller. The preliminary test setup uses an aggregated single-inverter switched system model of the PV plant.

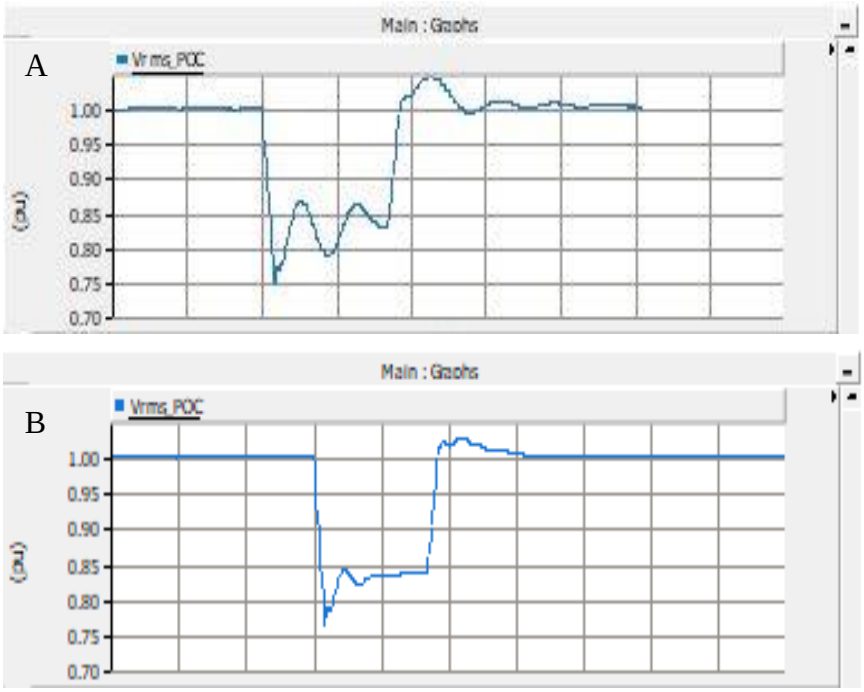

Fig. 13.1-1: PI controller (top); MPC controller (bottom).

M13.1: Control methods preliminary performance

The proposed MPC method is evaluated on the generic high-fidelity PV plant model. The generic high-fidelity PV plant model is much faster than the speed of the baseline model, which helps with debugging the model while control upgrades are performed. Whereas the baseline model takes days to simulate, the high-fidelity PV plant model is simulated within an hour. To compare the MPC with the traditional voltage control in the PPC, a PI-based voltage control is implemented. The simulation results (pre-fault and during fault) from MPC-based voltage control in the PPC and PI-based voltage control(s) in the PPC can be found in Fig. 13.1-2. Different control time steps within the PPC for the PI-based voltage control are also evaluated. Whereas most traditional PPCs use a 100 ms or slower control time step, the performance of MPC mirrors closer to the 10 ms control time step–based PI controller implementation. The 10 ms control time step implementation in a PPC has been identified as difficult for practical reasons

and is used only to highlight the enhanced dynamic performance obtained from MPC. The reactive power response observed in Fig. 13.1-2 is based on a three-phase-to-ground fault initiated at t = 0.6 s.

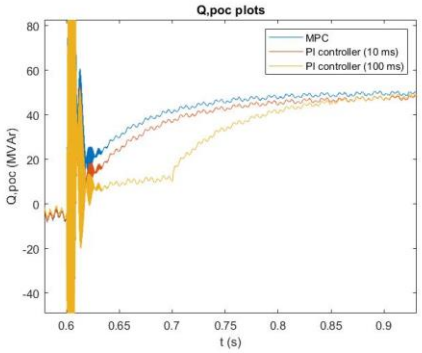

Fig. 13.1-2: Comparison of reactive power responses with MPC (vs. PI).

The main observation from the figure is that the reactive power settles down during fault faster with an MPC implementation compared with a traditional PI controller (with a 100 ms control time step). Whereas the reactive power during the fault is settling after 0.1 s in the MPC-based voltage control, it takes 0.25 s in the PI-based voltage control (with 100 ms control time step in PPC). Another observation is the stability of the MPC-based voltage control strategy during a three-phase-to-ground fault.

ST-13.2 Evaluate performance in suite of dynamic models and redesign

The updated closed-form MPC solution is implemented in PSCAD by developing a user defined module that takes the grid voltage, grid voltage angle with respect to the POI voltage, and a POI voltage reference sent by the system operator. The module and the corresponding code are illustrated in Fig. A17.3-65 and Fig. A17.3-66 in the Appendix. The simulation results from the fault simulated on a transmission line connecting to the generic PV plant are illustrated in Fig. 13.2-1 and Fig. 13.2-2. The fault resistance is 0.2 Ω. The results shown in the figures include the case with MPC-based voltage control and without any voltage control. The waveforms in the case with MPC-based voltage control demonstrate the ability of the plant to generate reactive power and the ability of the inverter to follow MPC controller commands. Comparing the case with and without voltage control, an improvement in the POI voltage can be observed in the case with voltage control. An improvement on the order of 10.15% is observed.

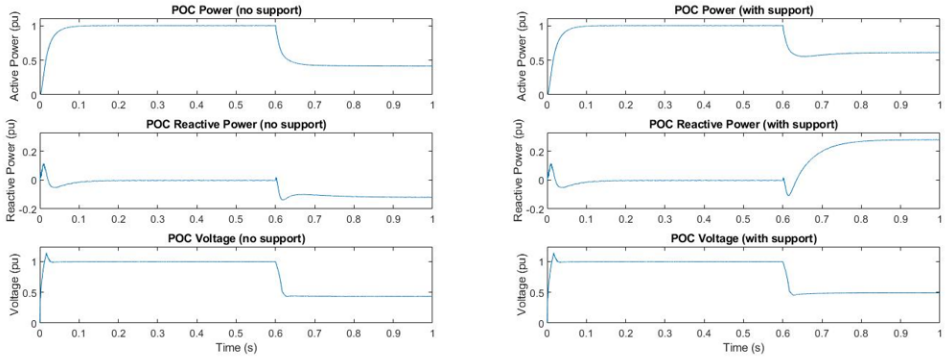

Fig. 13.2-1: PV plant's POI powers and voltage during a three-phase-to-ground fault on the transmission line connecting to the PV plant with Rf = 0.2 Ω, without and with support at the POI (left and right, respectively).

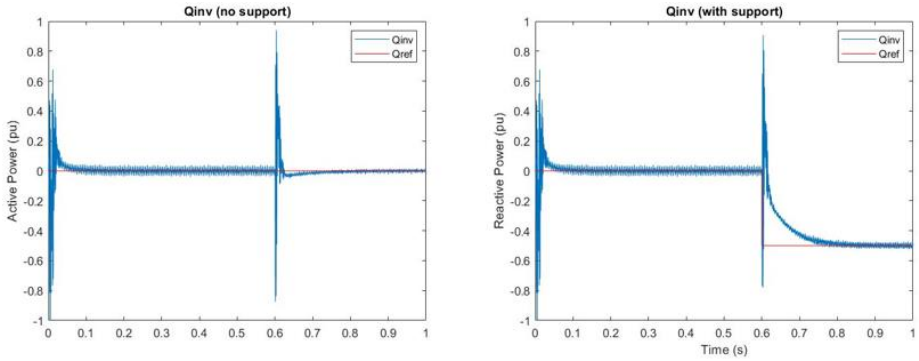

Fig. 13.2-2: Reactive power waveforms at the inverter level without and with support (left and right, respectively).

T-14. Demonstration of future scenario

ST-14.1 Evaluate performance of advanced control functions

Scenario 1(~60% of total power generation in California is from renewable)

This modified scenario represents the grid in California after 10–15 years. All the identified conventional plants listed in Table A11.1-2 in the Appendix are replaced with renewable plant models using the method described in the flowchart in Fig. A17.3-56. This scenario is further categorized in three cases based on the voltage and frequency control flags in the model of the PPC (REPCA model) used in the replaced plants.

1. Case 1A: The replaced plant models have either of the following controls in the PPCs: (1) both voltage and frequency control, or (2) only voltage control. The choice of the control in the PPC is based on existing renewable plants of similar size.
2. Case 1B: All the replaced plant models have both voltage and frequency control enabled in the PPCs.
3. Case 1C: The PPCs of the replaced plant models have neither voltage nor frequency control.

Responses of all these models after Palo Verde generation loss are shown in Fig. 14.1-1(a). The Angeles Forest event is simulated, and the corresponding results are shown in Fig. 14.1-1(b).

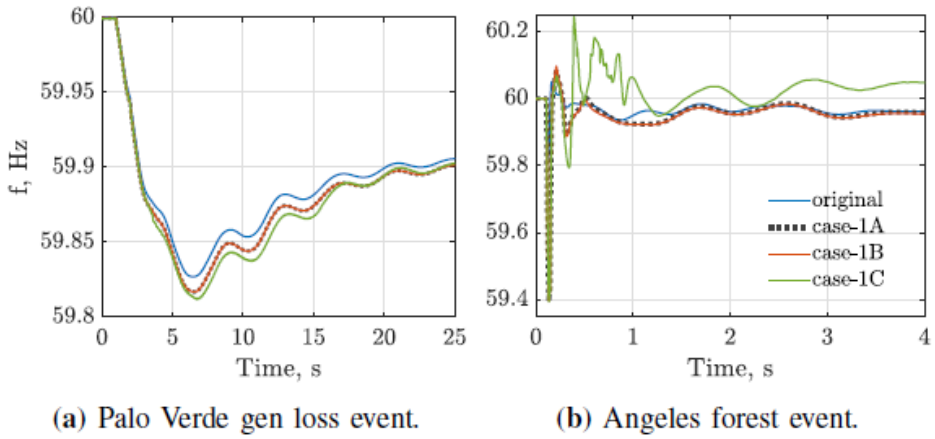

Fig. 14.1-1: Frequency plot after the event simulation in Scenario 1.

Observation: Both the system inertia and active power support for primary frequency response decreased in all the modified cases in Scenario 1 compared with the original model (shown in Fig. 14.1-1[a]), which is reflected in the frequency dynamics when loss of generation happens. The frequency drops more after the event and settled at lower frequency for the modified cases in Scenario 1 than in the original case. Post-event frequency drops most for the modified case 1C because there is no active or reactive power support from the replaced renewable plants. This is observable in Fig. 14.1-1(b).

Observation: The frequency drops more after the fault in the modified cases in Scenario 1 with ~60% renewable generation in California. Oscillatory behavior in the frequency is observed post fault in case 1C because of a lack of voltage and frequency control in the replaced renewable plants.

Scenario 2 (100% of total power generation in California is from renewable)

All the conventional plants in California are replaced with renewable plant models in the 26HS2 scenario to replicate a 100% renewable scenario in California. The conventional plants in the WECC scenario are modeled using one of the following generator models, which helps in the identification of all the conventional plants in California: (a) WECC type J generator model - GENTPJ1, and (b) round rotor generator model - GENROU.

Next, the power flow data (.raw) and dynamic data (.dyr) files are modified using the method described in ST-11.1. For this work, all the dynamic model parameters in the replaced plants are considered to be identical, which are of nominal value from the manual and used in existing active renewable plants in the 26HS2 model. However, different control strategies are considered for the replaced plant models for different cases, which are discussed next in detail.

Effect of lag time constant in PPC: For the 100% renewable scenario, both voltage and frequency controls are enabled in all the replaced plants, and k_{qv} is set to 0. With these changes, the system is stable after Palo Verde generation loss simulation in PSSE only when the lag time constant in the reactive power control of the PPC is set to a very small value (T_{fv} = 0.005 s). As shown in Fig. 14.1-2(a), when this constant is assigned a practical value (T_{fv} = 0.05 s) from existing plants in the WECC grid model, oscillations in frequency dynamics are observed initially and divergence of the frequency is observed thereafter.

Observation: For the PPC, T_{fv}_= 0.005 s is very small, so a part of the controller may need to be present in the inverter controller.

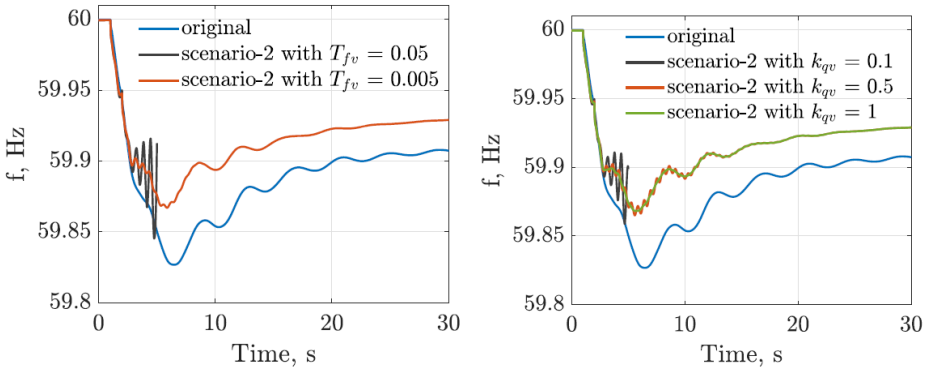

(a) $k_{qv} = 0$ and different T_{fv}. **(b)** $T_{fv} = 0.05$ and different k_{qv}.

Fig. 14.1-2: Frequency plot for Scenario 2 after Palo Verde event simulation.

Effect of voltage control through reactive current gain in electrical control (inverter controller): For the 100% renewable scenario, the k_{qv} in the replaced renewable plant control is set to 0.5. This scenario is stable after Palo Verde generation loss simulation in PSSE even with a lag time constant (T_{fv}) of 0.05 s, as shown in Fig. 14.1-2(b). The drop in the frequency after generation loss is less compared with the original scenario because active power support is present in all the replaced models, and conventional plants did not have governor support in the original scenario. It is also observed that a smaller k_{qv} results in oscillation in the post-event frequency dynamics, which might cause instability in the system. This shows that for a grid with high renewable penetration, voltage control reactive current control in the inverter controllers in renewable plants may be necessary to ensure stability.

Effect of voltage and frequency control in PPC: For the following cases, the reactive current gain (k_{qv}) is set to 0.5 and the lag time constant (T_{fv}) is 0.05:

1. *Case 2A:* In the PPC of all the replaced plants, the voltage control is enabled. Frequency controls are also enabled for the largest 30%, 33%, and 40% of the replaced plants. Evaluation of the Palo Verde generation loss indicates that the case is stable only when at least 33% of the replaced plants incorporate frequency control in the PPC. The comparison of the frequency on the generation loss in the original scenario and Case 2A of Scenario 2 is shown in Fig. 14.1-3(a). The case with 33% of the replaced plants incorporates frequency control in the PPC and has similar inertial and initial primary frequency response to the original scenario (but does not have the settling down value in the primary frequency response).

   Observation: For 100% renewable in the power grid in California, only voltage control in PPC and voltage control through reactive current in inverters do not ensure stability after a large generation loss. Frequency control is also required for the plants, which can provide active power support after a generation loss.

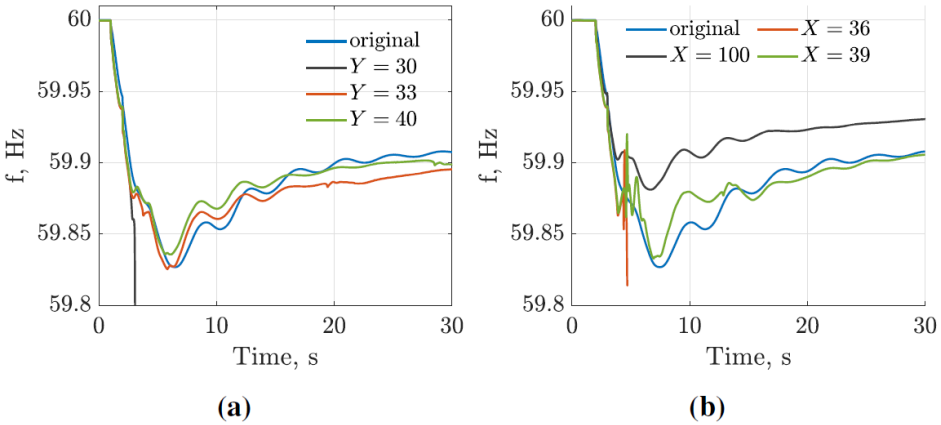

Fig. 14.1-3: Frequency plot after Palo Verde generation loss. (a) Scenario 2A: voltage control in all and frequency control in Y% of replaced plants—stable for Y > 33; (b) Scenario 2B: both voltage and frequency controls in X% of replaced plants—stable for X > 39.

2. *Case 2B:* In this case of Scenario 2, a different percentage of the replaced plants is enabled with both voltage and frequency control in the PPC, and the rest of the replaced plants have none of the voltage and frequency control in the PPC. All the replaced plants incorporate reactive current control in the inverter controller. After the Palo Verde generation loss simulation, the system is stable when at least 39% of the replaced plants have both voltage and frequency controls. The frequency upon loss of generation in different subcases of Case 2B is shown in Fig. 14.1-3(b), which displays that at least 39% of the replaced plants need both voltage and frequency control in the PPC.

   Observation: For a power grid in California with 100% renewable-based generation, voltage and frequency controls are required in the PPC in at least 39% of the upcoming plant to ensure stability after a large generation loss. Also, voltage control at inverter through reactive current injection in the electrical control needs to be enabled with proper gain (k_{qv}) value. This active power support helps reduce frequency drop, and the frequency settles at a higher value compared with the case without support. Additional control features may be necessary as more details emerge on the renewable penetration scenarios in the future power grid.

T-15. Advanced control functionalities

ST-15.1 Evaluate performance in future grid scenarios and redesign

Different Models Studied in Present Grid Scenario for Angeles Forest Fault Simulation

Objective: During the Angeles Forest fault event, one affected PV plant observed transient subcycle ac undervoltage at the 230 kV bus. In the WECC planning model, quasi-dynamic models are used for the plant and control of this PV plant. However, in the E-Tran–converted PSCAD model, the PV plant is represented as a constant ac voltage source. So different PV plant models are developed and evaluated in PSCAD for fault events' simulation.

Existing PV Plants' TS Models in the WECC Grid Scenarios: The following models are present in present and future grid scenarios:

1. *WECC present grid model scenario (2022 Heavy Summer scenario)*

The affected PV plant is one unit with 250 MW rating. The following dynamic models are used for the plant: (a) plant model, WT4G1; and (b) control model, WT4E1. The voltage

control is enabled through reactive power control; active power control is present, and there is no frequency control.

2. WECC future grid model scenario (2026 Heavy Summer scenario)

The affected PV plant is four units with a total 250 MW rating. The following dynamic models are used for the plant: (a) plant model, REGCA1; (b) electrical control model, REECA1; and (c) plant model REAX4BU1, PLNTBU1. The reactive power control and constant active power control are present.

Quasi-Dynamic EMT Model of PV Plant: Controllable current sources are used for the PV plants to replicate the dynamic model from WECC data. For generating the current references for the controllable source, either a fixed triangular signal or the output from PLL are used as the angle.

Additional Developed Quasi-Dynamic Models: The developed quasi-dynamic models of the PV plant are summarized in Table 15.1-1. Thereafter, the Angeles Forest fault is simulated for all the PV plant models. The comparison of the responses observed in response to three-phase and line-to-line faults in the same location as the Angeles Forest fault event is discussed in Table 15.1-2.

Table 15.1-1: Overview of different quasi-dynamic models of PV plants

Models	**Used cases**	
	Three-phase fault	**Line-to-line fault**
TS model	Simulate a fault event in TS and compare the response in EMT model	NA
EMT with WT and no PLL		Angeles Forest fault replication and compare different PV plant model in EMT simulation
EMT with WT and PLL	Observe the effect of PLL modeling	
EMT with RE and no PLL	Model the PV plant using the dynamic data from the future grid	
EMT with RE and PLL		

WT = Wind Turbine model; RE = Renewable model.

Table 15.1-2: Overview of the response from quasi-dynamic models of PV plants during the Angeles Forest 2018 event (or similar) simulations

Models	**Used cases**	
	Three-phase fault	**Line-to-line fault**
TS model	Active power drop is very small during the fault, and it increases after the fault clearance. Reactive power increases during fault	NA
EMT with WT and no PLL	Power outlet response is similar to that of the TS model; however, the power outlet dynamics are different from those of the TS simulation	Active power drops, and reactive power increases during the fault
EMT with WT and PLL	After the fault clearance, the response is different from that of the case without PLL	
EMT with RE and no PLL	Change in power output is small compared with the WT model	Output powers during the fault are different from those of the three-phase fault
EMT with RE and PLL	After the fault clearance, the response is different from the case without PLL. Output power takes more time to settle after the fault clearance	

Sensitivity Analysis on High-Fidelity EMT Model of PV Plant in Present Grid Scenario

In this section, different configurations within the specific PV plant-1 and with different types of power grid models (min grid model and best case grid model) are analyzed.

This analysis assists with understanding the interaction between power grid and different components in an affected PV plant.

Sensitivity Analysis in Shunt Operation (within Specific PV Plant-1): The combination of shunts ON and OFF in different modules of the specific PV plant-1 is considered and analyzed with the plant connecting to the min grid model. The simulation results and active powers on the high-voltage side of the PV plant are shown in Fig. 15.1-1. In this analysis, it is observed that the operation of shunts affects the behavior of the plants during faults. For example, with only shunt-2 operation in module-1 or module-2, partial loss of power produced from the PV plant is observed. In the case with shunt-2 operation in both modules, no loss of power is observed. In the case with no shunt-2 operation in both modules, complete loss of power is observed. Where a peak-voltage-based protection scheme was used, the results were different in some cases and similar in other cases. For example, with only shunt-2 operation in module-2, in contrast to the partial power loss, complete power loss is observed. The results with only shunt-2 operation in both modules has similar results. The results are shown in Fig. 15.1-2.

This analysis shows that operation of shunts within the specific PV plant affected during the Angeles Forest 2018 event can play a role in avoiding the observed power generation reduction

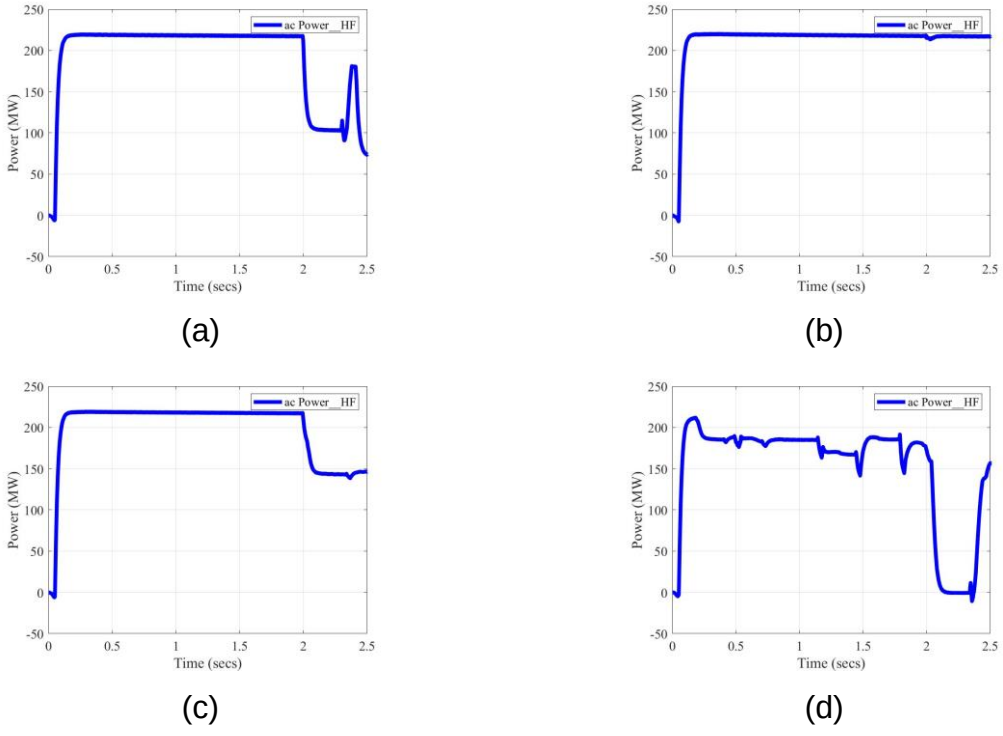

Fig. 15.1-1: Specific PV plant-1 for different shunt configurations using min bus grid scenario: (a) Pac when shunts-2 are enabled only in module 1; (b) Pac when shunts-2 are enabled in all modules; (c) Pac when shunts-2 are enabled only in module 2; and (d) Pac when shunts-2 are disabled in all the modules.

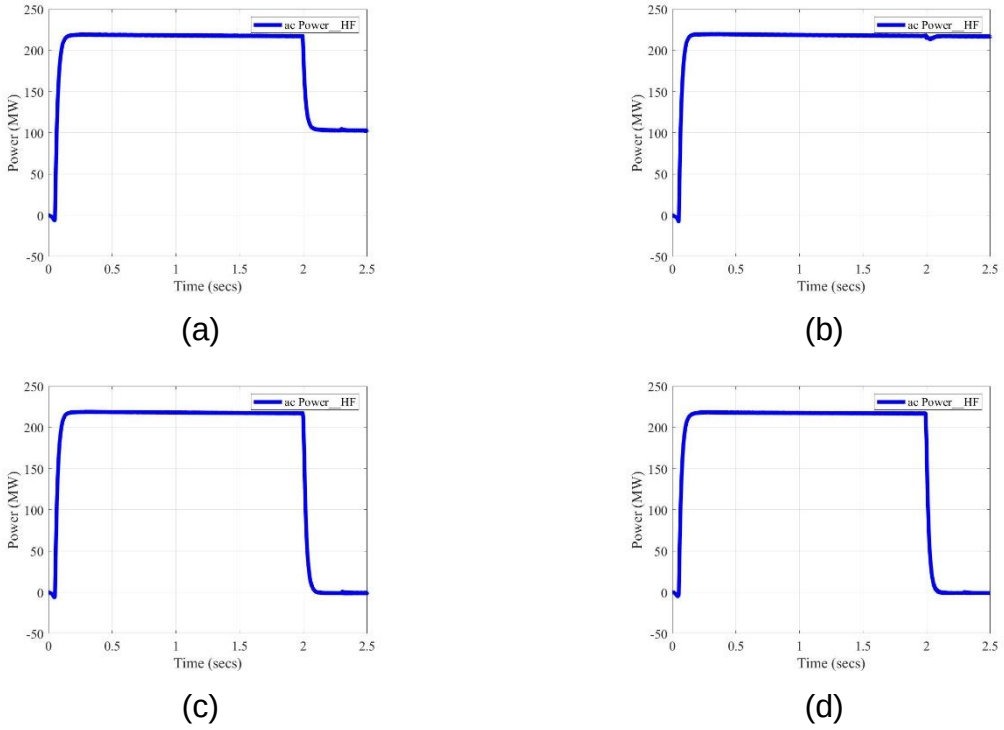

Fig. 15.1-2: Specific PV plant-1 for different shunt configurations using min bus grid scenario (with Vac-peak-based protection algorithm): (a) Pac when shunts-2 are enabled only in module 1; (b) Pac when shunts-2 are enabled in all modules; (c) Pac when shunts-2 are enabled only in module 2; and (d) Pac when shunts-2 are disabled in all the modules.

Sensitivity Analysis in Inverters: In this analysis, the following changes are considered within the inverters in the specific PV plant:

- Inverter-1 and inverter-2 filter size increase for 2, 5, and 10 times
- Interchange of inverters in the PV plant
- Change in the line lengths of inverter-1 and inverter-2 that were affected during the Angeles Forest event for 2 and 3 times
- Change in either the switching frequency (2.5 kHz, 5 kHz, and 10 kHz) or controller gains (inner current control, PLL, and outer current controller gains) in inverter-2

The simulation results from this sensitivity analysis to observe the active power at the terminals of the plant are shown in the Appendix (Fig. A15.1-4 to Fig. A15.1-7). From the sensitivity analysis, it is observed that the inverter hardware used plays an important role in the response within the plant, as does changing the filter in the inverter. The distribution grid and/or PV plant controller have limited effect on the specific fault case studied.

Sensitivity Analysis with Power Grid Model used in Analysis in the Present Grid Scenario

The combination of shunts ON and OFF in different modules in the affected specific PV plant-1 with best case grid scenario is considered in this section. The corresponding simulation results and active powers on the high-voltage side of the PV plant are shown

in Fig. 15.1-3. A comparison of the response observed in this figure to Fig. 15.1-1 indicates that interaction with other components near the PV plant is observable. That is, the assumption that the power generation reduction in a PV plant is due only to its internal components is not correct, but it is, in general, dependent on all the components present in the region. In this case, the best case grid model has multiple synchronous generators along with additional lines and transformers present in the region (that are not present in the min grid model). Hence, another worthwhile deduction is that the analysis of understanding the impact of faults during planning (as part of contingency analysis) needs to consider high-fidelity inverter-based resource models in a wider region that encompasses the fault and the power grid model of the wider region.

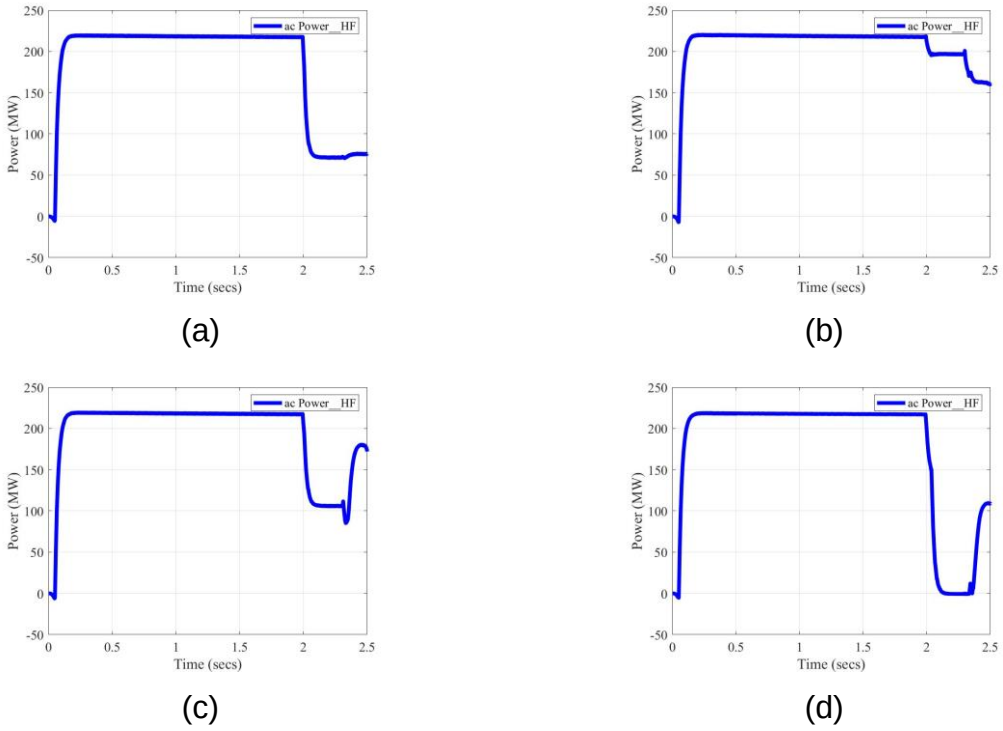

Fig. 15.1-3: Specific PV plant-1 for different shunt configurations using best-case grid scenario: (a) Pac when shunts-2 are enabled only in module 1; (b) Pac when shunts-2 are enabled in all modules; (c) Pac when shunts-2 are enabled only in module 2; and (d) Pac when shunts-2 are disabled in all the modules.

Advanced Controller in High-Fidelity Model of PV Plants and Comparison

Further analysis of the advanced controller based on MPC is demonstrated in Fig. A15.1-8 and Fig. A15.1-9 in the Appendix, which display that MPC response is faster than that of conventional PI controllers. Benefits of advanced voltage control functionalities in PV plant are demonstrated in future grid scenarios, especially with 100% penetration of renewables in California.

Future Grid TS Model Development with 100% Renewable in California

The sensitivity analysis on the controller gains in PPC and inverter controllers to include both voltage and frequency control in PPC and voltage control through reactive current in inverters assisted with fine-tuning the gains. In addition to the generation loss tests performed in Section T-14, three-phase faults are analyzed in this section.

Response after a Fault Event: A self-clearing three-phase fault for t = 0.043 s is simulated at the local end bus of the Angeles Forest fault event. The responses from the PSSE simulation are shown in Fig. 15.1-4. The grid reaches the pre-disturbance states after the contingency. As shown in the figure, the terminal voltage at one plant drops during the fault, and the reactive power support helps to recover the voltage.

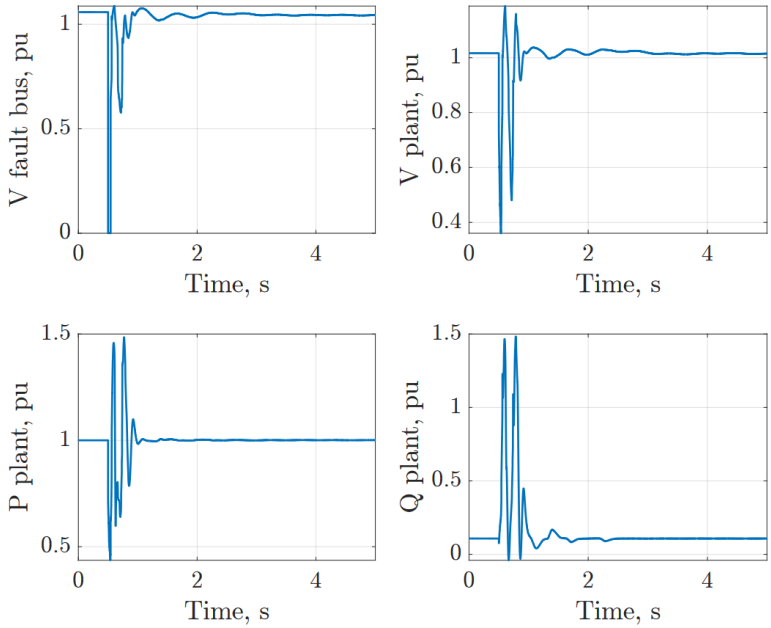

Fig. 15.1-4: Response of the fault event in the developed WECC scenario with 100% renewable generation in California.

Response after a Generation Loss Event: Next, the Palo Verde generation loss event is simulated in PSSE for the developed WECC grid scenario. As shown in Fig. 15.1-5, the frequency and voltage of one bus in California indicate that the system is stable after this contingency. Low-frequency electromechanical oscillations are visible in the dynamic behavior. The generation loss leads to a reduced post-disturbance steady-state frequency, as expected from the primary frequency response.

For the 100% renewable scenario in California, to ensure stability of the WECC system following a fault and generation loss event, the following are recommended:

1. PPC: Both voltage and frequency controls are required.
2. Inverter control: The reactive power control, fast dynamic voltage control, and reactive current injection during voltage deviation should be enabled. In active power control, the frequency-dependent control may not be necessary.

Additional sensitivity analysis is performed on the controller gains (PI controller gains in PPC and on deadbands) in the Appendix. This analysis helps fine-tune the gains used in the IBRs in the future power grid.

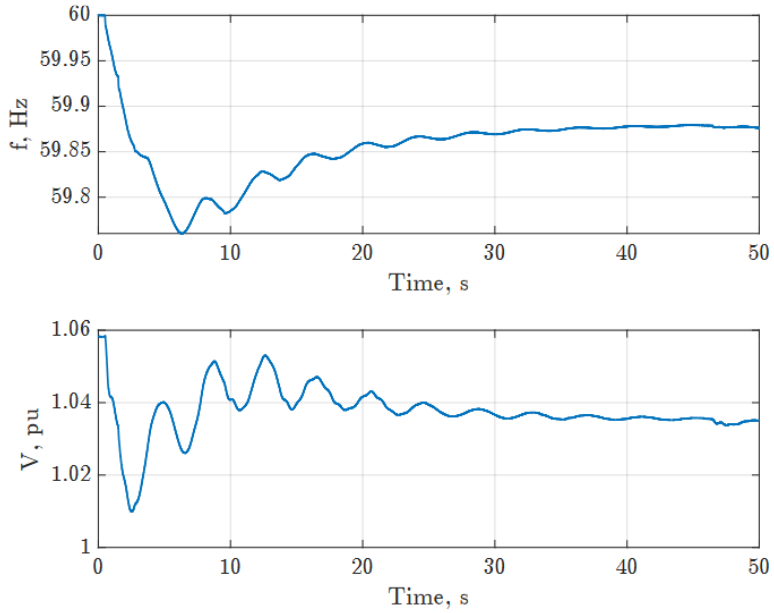

Fig. 15.1-5: Response of the generation loss event in the developed WECC scenario with 100% renewable in California

M15.1: Preliminary results from control benefits provided in future grid

M15.2: EMT-TS cosimulation boundaries in various grid scenarios (present, future)

The EMT model of the future power grid with >60% and 100% penetration of renewables in California is developed.

T-16. Investigation of future scenarios

ST-16.1 Incorporate advanced control functionalities into future grid scenarios in real-time simulation

Development of Future Scenario Grid Model in RSCAD

A generic model of the future scenario grid, based on the WECC planning model, was developed in RSCAD for real-time simulation. The future grid model was originally developed in PSCAD to analyze the impact of transmission grid-level disturbances on a large PV plant. From that model in PSCAD, simulation parameters needed for library components in RSCAD were extracted such as system voltage ratings, source location/parameters, transmission lines lengths/parameters, transformer locations/parameters, breaker parameters, and fault type/location/duration. The extracted datasets were used to develop the generic model in RSCAD for real-time simulation, shown in Fig. 16.1-1.

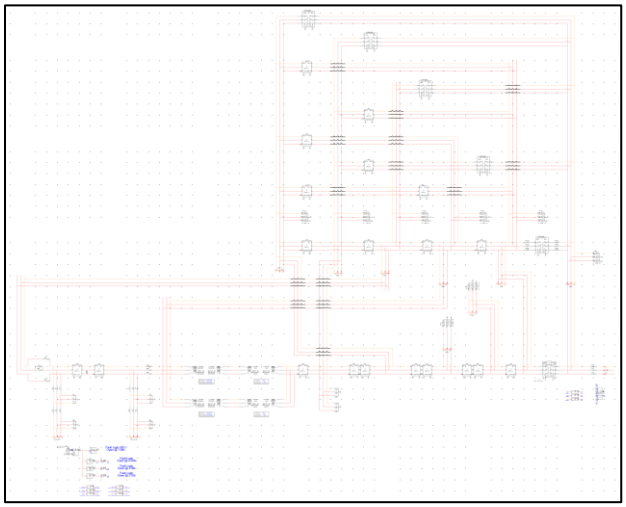

Fig. 16.1-1: Future scenario grid generic model in RSCAD (RTDS) for real-time simulation.

To validate the model in RSCAD, voltages and currents during a fault were compared with the results from the corresponding PSCAD model. The voltages and currents were measured at both near and remote ends of the fault line. Before and during the fault, the results (presented in Fig. 16.1-2) from the developed grid model in RSCAD are matched with the ones from PSCAD. The post-fault results from the fault line are not important because the line is taken out of service.

Voltages at the bus to which one of the affected PV plants from the Angeles Forest 2018 event is connected were also compared between the two models. In both models, the PV plant model is not connected. They match well, as observed in Fig. 16.1-3.

The high-fidelity PV plant model of the affected PV plant was integrated with the developed future grid model in RSCAD. The response of the PV plant with the current PPC and inverter protection scheme to an external fault was analyzed in RSCAD. Before the fault, output active power from the PV plant is at 230 MW. During the fault, the active power starts to reduce and reaches around 200 MW between 0.0167 and 0.05 s. The results are shown in Fig. 16.1-4. This indicates that some inverters in the PV plant are affected by the fault, highlighting the value proposition of developing high-fidelity PV plant dynamic models, as shown in the previous quarters. Additionally, an interesting observation was noted in the PV plant's behavior once the fault line is taken out of service and the plant attempts to recover—there is a further dip in the active power. Although this is out of the scope of the current research, it may be considered for analysis in the future.

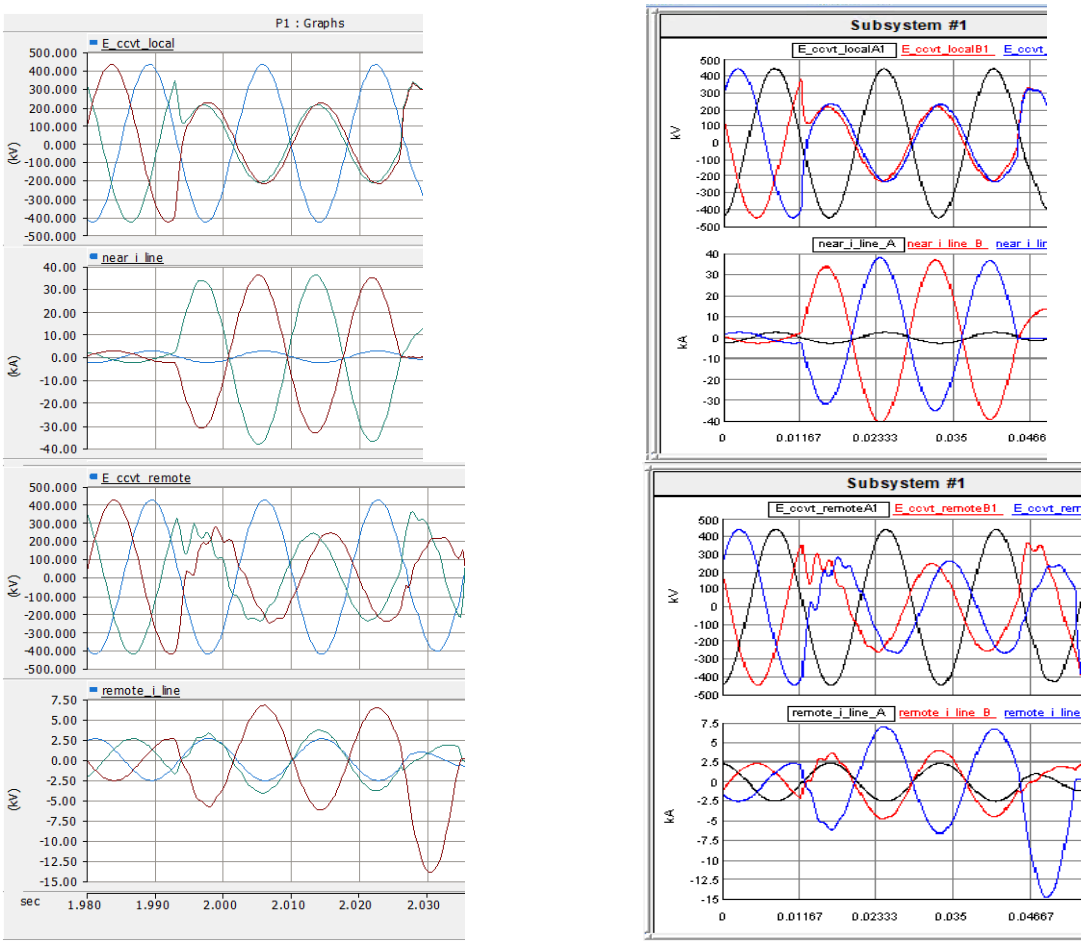

Fig. 16.1-2: Results comparison of the fault response on the future scenario grid generic model: local end and remote end voltages and currents from the PSCAD model (left) and RSCAD model (right).

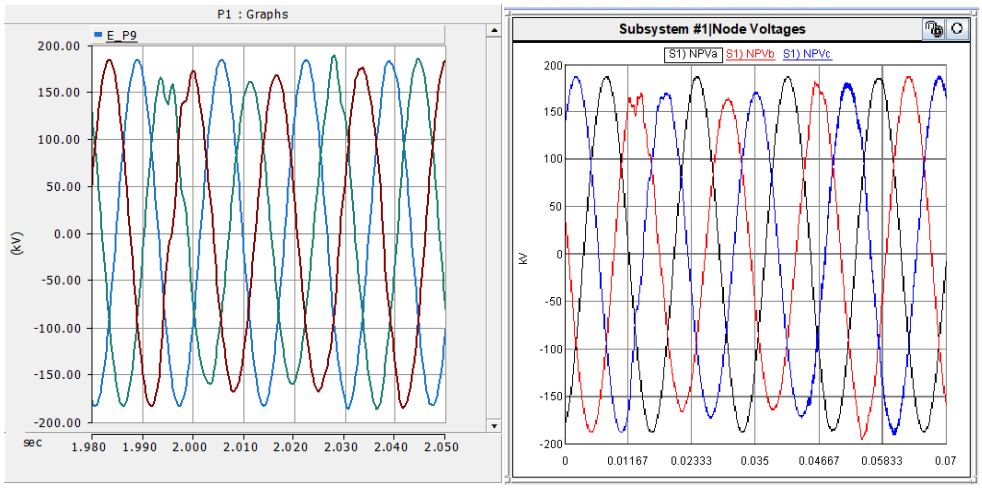

Fig. 16.1-3: Results comparison of the fault response on the future scenario grid generic model: PV plant terminal voltages from the PSCAD model (left) and RSCAD model (right).

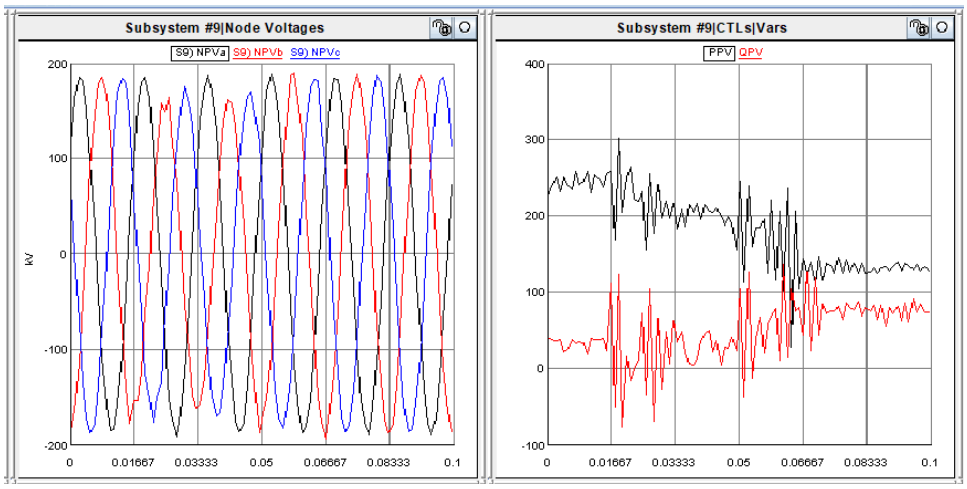

Fig. 16.1-4: Results of the fault response on the future scenario grid generic model: PV plant terminal voltages and output power of the PV plant during the fault condition from the RSCAD model.

An advanced PPC, based on expected control modes, was developed in RSCAD within the high-fidelity model of the PV plant that connects to the future grid model. The advanced PPC model was developed in PSCAD to analyze the impact of the PPC on fault response of large PV plants. From the originally developed model in PSCAD, simulation parameters (e.g., controller, limiter, integrator) needed for library components in RSCAD were extracted. The extracted datasets were used to develop the same PPC model in RSCAD for real-time simulation (illustrated in Fig. 16.1-5).

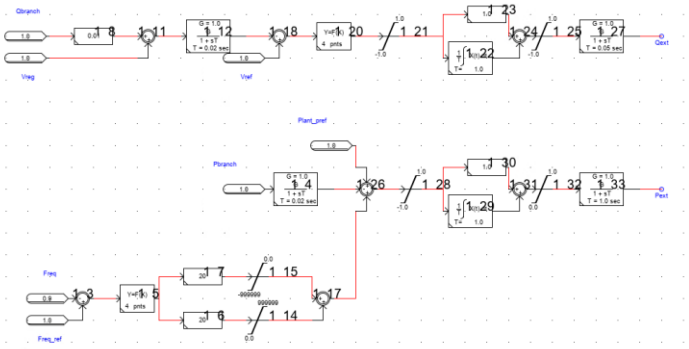

Fig. 16.1-5: Advanced power plant controller for a PV plant in the future grid model in RSCAD.

Advanced Model of a PV Plant

The advanced model of the PV system has been upgraded with a smaller time step considered to improve the dynamics captured with respect to the high-fidelity model of the PV plant. It also helps with enhancing the stability of the simulations. Additional capacitance is incorporated within the distribution grid at the terminals of the PV system. Other updates considered to improve the stability of the advanced model are listed below:

- The buffer zone between the distribution grid model and the transmission grid based on the transformer has been removed from the distribution grid.
- Additional capacitance has been introduced at the shunt locations.
- The transformers for the different inverters and internal control reference have been updated.
- The capacitance at each PV location has been adjusted to the minimum required added capacitance.

The simulation results of the PV plant with advanced models of PV systems are shown in the Appendix.

T-17. Demonstration of generic present grid scenario

ST-17.1 Develop a test case for IEEE case study

The IEEE nine-bus model is developed in both TS and EMT simulation platforms. The line diagram is shown in Fig. 17.1-1. The generator-3 is represented by two units generating 15 MW and 70 MW, respectively.

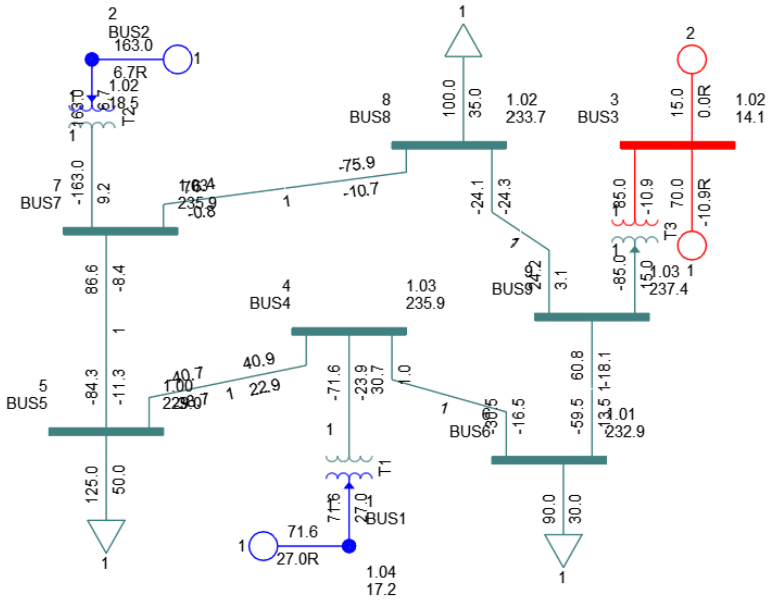

Fig. 17.1-1: IEEE nine-bus system diagram.

The existing synchronous generators are replaced with renewable plant models to develop various scenarios, summarized in Table 17.1-1.

Table 17.1-1: Generator replacement scenarios.

Scenario	Description
Original	All synchronous generators (SGs)
25% renewable	Generator-1 renewable
50% renewable	Generator-2 renewable
75% renewable	Both generator-1 and generator-2 renewable

For the renewable plants, the REGCA, REECB, and REPCA models are used for the plant, electrical control, and plant power control, respectively. E-Tran is used to convert the PSSE model into PSCAD for EMT simulation. For the PV plant, controllable current sources are used with the controller models. The PSCAD models use PLL for converting the real and imaginary current references into three phase currents. For the PPC, a provision enables and disables the voltage and frequency controls.

M17.1: IEEE nine-bus use case (generic present grid scenario)

ST-17.2 Integrate generic PV plant in IEEE case study

Generic PV Plant

The symmetric generic PV plant developed earlier and rated at 125 MW is upgraded to incorporate different types of inverters, different lengths of feeders, and other changes. It consists of five feeders, each with five PV systems; each PV system consists of a transformer and either a 1 MW PV inverter module or a 2.5 MW PV inverter module. Each PV inverter module contains PV arrays connected to a dc-ac inverter (two-level voltage source converter) through a dc-dc converter. The detailed layout of the generic PV plant is shown in Fig. 17.2-1.

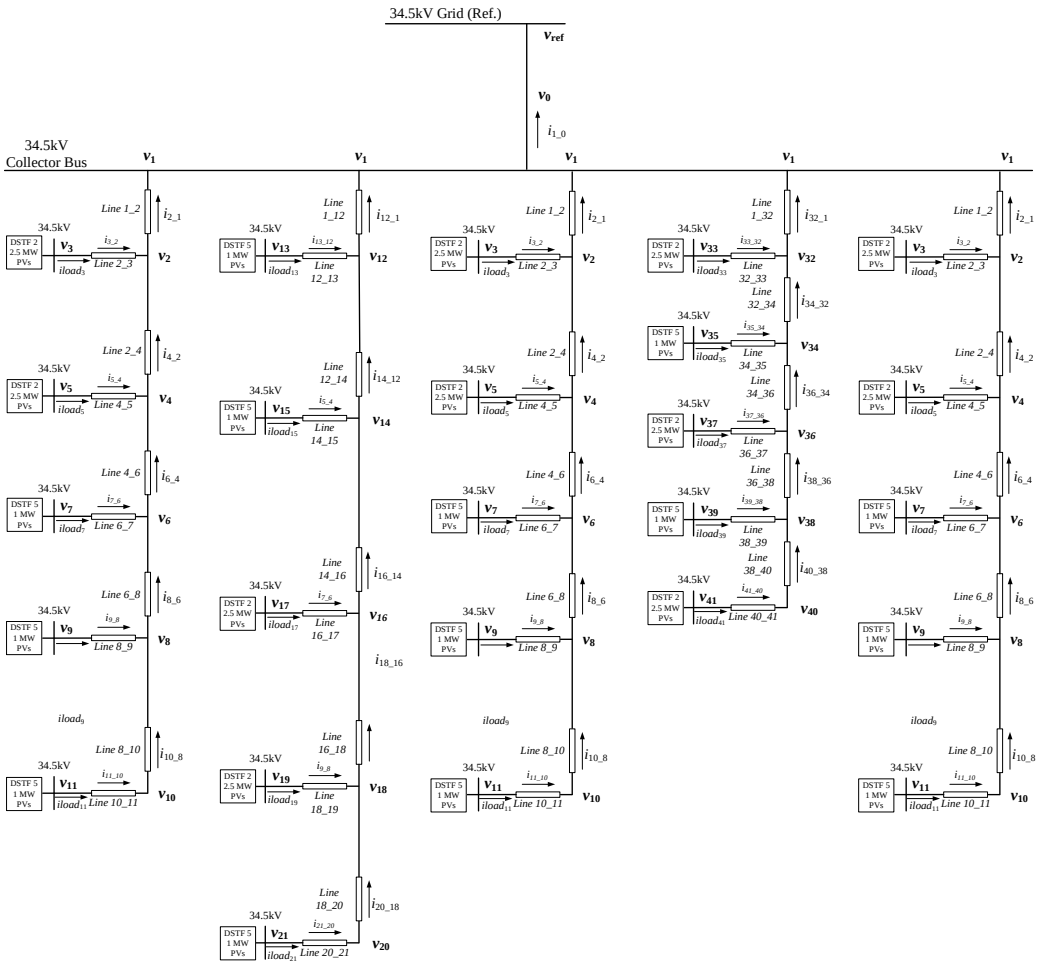

Fig. 17.2-1: Detailed layout of the generic PV plant.

PV Inverter Module Upgrades in Generic PV Plant: As the first step, a model is developed of a 2.5 MW PV inverter module, and it is tested stand-alone. The model of the PV array has been changed to deliver 2.5 MW output power. In addition to the PV array rating updates, protection schemes in the dc-ac inverter control are also included in both the 2.5 MW and 1 MW PV inverter module's models. The PV inverter module's model is tested at different operating conditions. From the simulation results for steady-state operation (shown in Fig. 17.2-2), it is observed that the active power, three-phase

grid currents, and PV system voltages are as expected. The simulation results for the generic PV plant during a step change in active power and the PV system's internal variables are shown in Fig. 17.2-3.

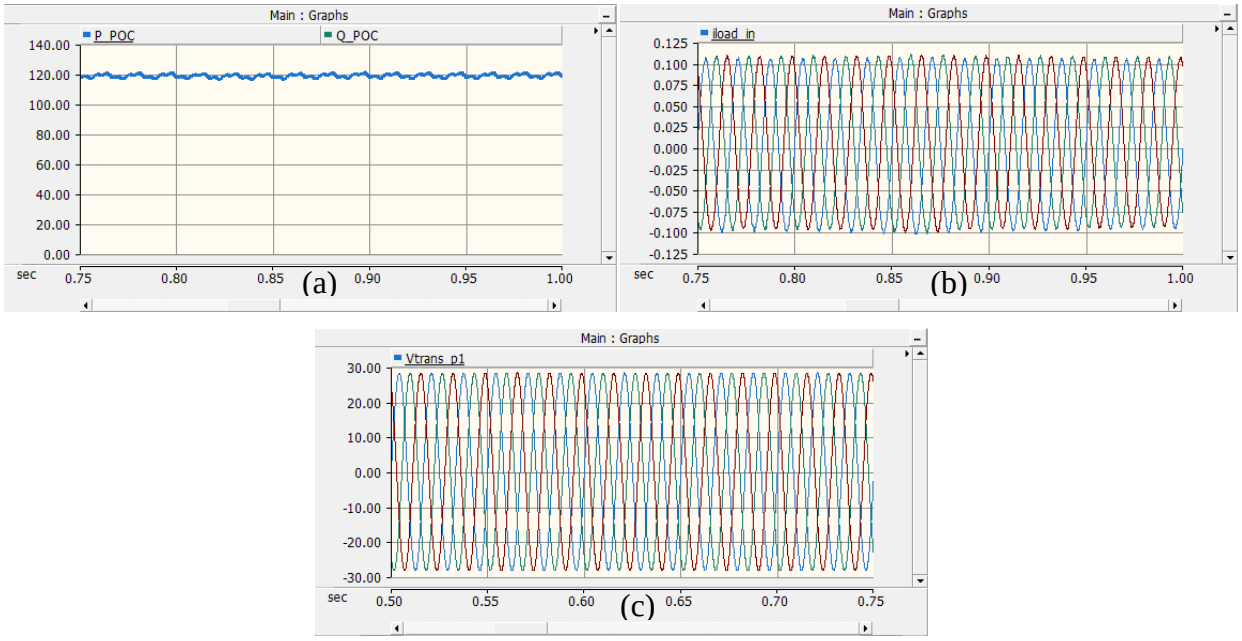

Fig. 17.2-2: Simulation results for the generic PV plant: (a) active power of the PV plant; (b) grid currents; and (c) three-phase voltage for one of the PV systems.

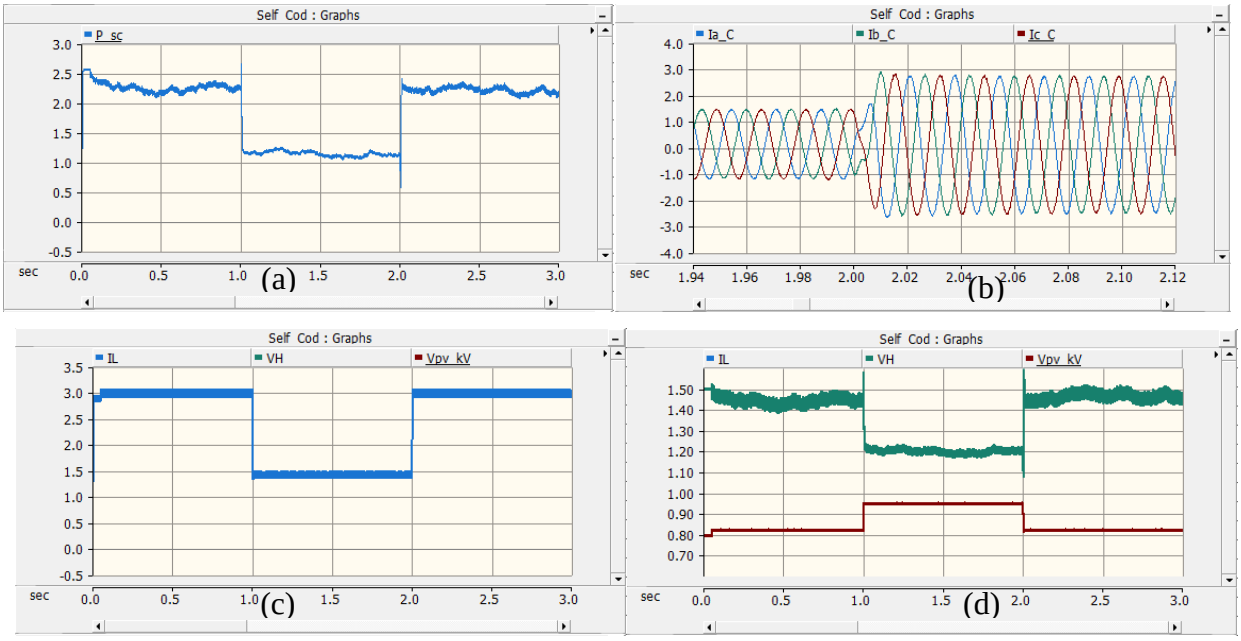

Fig. 17.2-3: Simulation results for the generic PV plant: (a) inverter active power; (b) three-phase inverter currents; (c) dc-dc converter inductor current; and (d) dc-dc converter input PV capacitor voltage and dc-ac inverter dc capacitor voltage.

IEEE Nine-Bus System with High-Fidelity Model of the Generic PV Plant in 25% Renewable Penetration Scenario: A high-fidelity EMT dynamic model of the generic PV plant is connected to one of the nodes in the IEEE nine-bus system. The generic PV plant is an asymmetric PV plant with both 1 MW and 2.5 MW PV inverters.

Advanced Model of Generic PV Plant: An advanced model for the generic PV plant is evaluated and shows good results for slower timescale dynamics, as noted in the Appendix.

M17.2: Generic present grid scenario with PV system model

ST-17.3 Demonstration of generic PV plant in generic grid model

IEEE Nine-Bus System with Quasi-Dynamic Models and Different Renewable Penetration Scenarios

Generation loss and fault events are studied for all the developed scenarios.

Generator loss event: To simulate a generation loss event, unit 2 of generator-3 is tripped, and the frequency response is plotted as shown in Fig. 17.3-1.

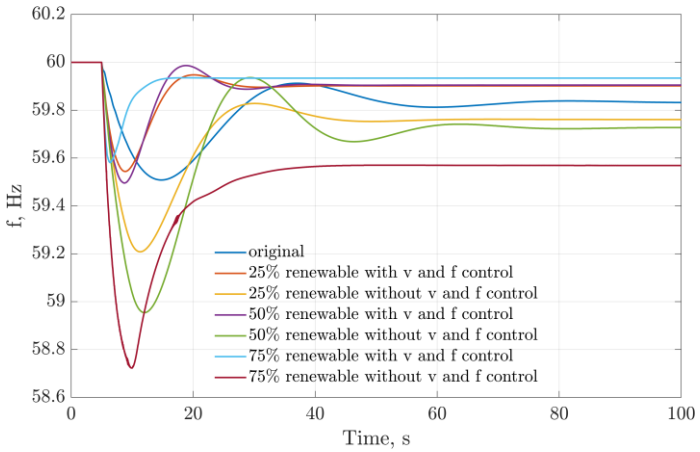

Fig. 17.3-1: Frequency plot after a generator loss event.

Observation: After the generation loss event, the frequency drops more when the frequency and voltage control are disabled in the PPC. With frequency and voltage control the frequency drop is almost the same as that of the original scenario (with no renewables); however, the steady state frequency is lower for the original scenario.

EMT and TS Simulations in IEEE Nine-Bus System with 50% Renewable Penetration: A generator loss event is also simulated in the PSCAD model for the IEEE nine-bus scenario with 50% renewable penetration. The responses are shown in Fig. 17.3-2.

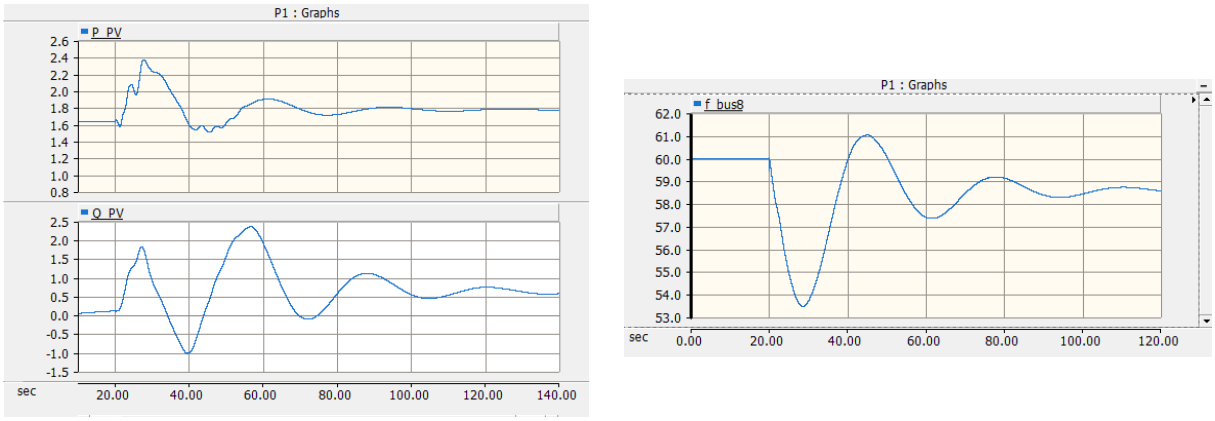

Fig. 17.3-2: Response after a generator loss simulation in PSCAD for the IEEE nine-bus scenario with 50% renewable penetration.

Observation: The frequency drop after the event in EMT simulations is much higher than that of the TS simulation models.

Fault event: A self-clearing fault event is simulated for all the developed models. The responses are shown in Fig. 17.3-3 and Fig. 17.3-4 for TS and EMT simulations, respectively.

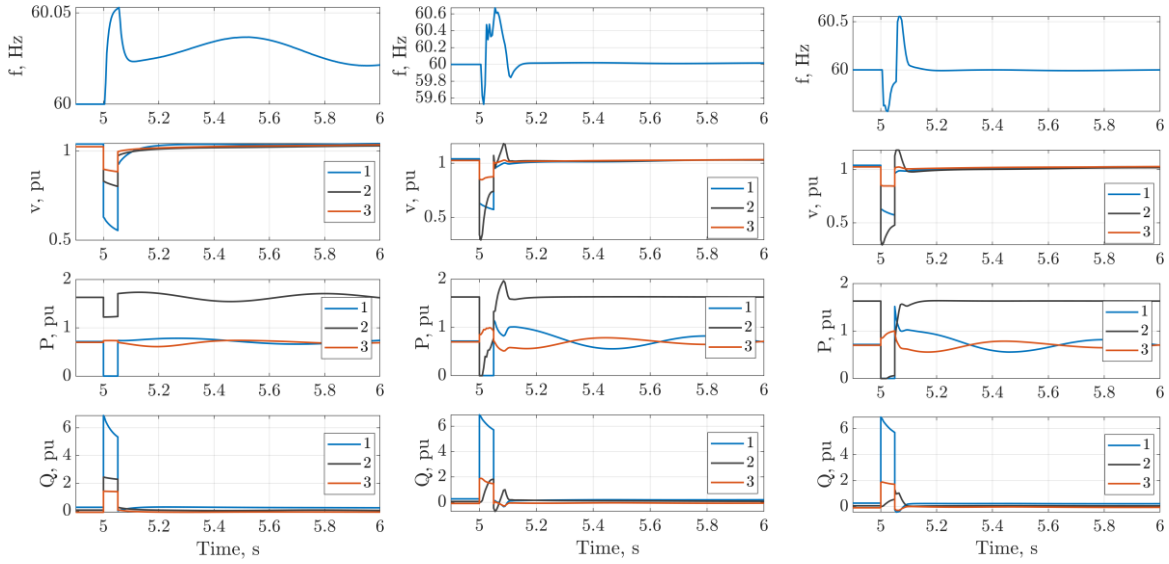

Fig. 17.3-3: Response after fault simulation for IEEE nine-bus scenario: (a) original, (b) 50% renewable energy with Kqv = 2 for renewable plants, and (c) 50% renewable energy with Kqv = 0 for renewable plants.

Observation: During fault, the reactive power support is smaller when Kqv = 0.

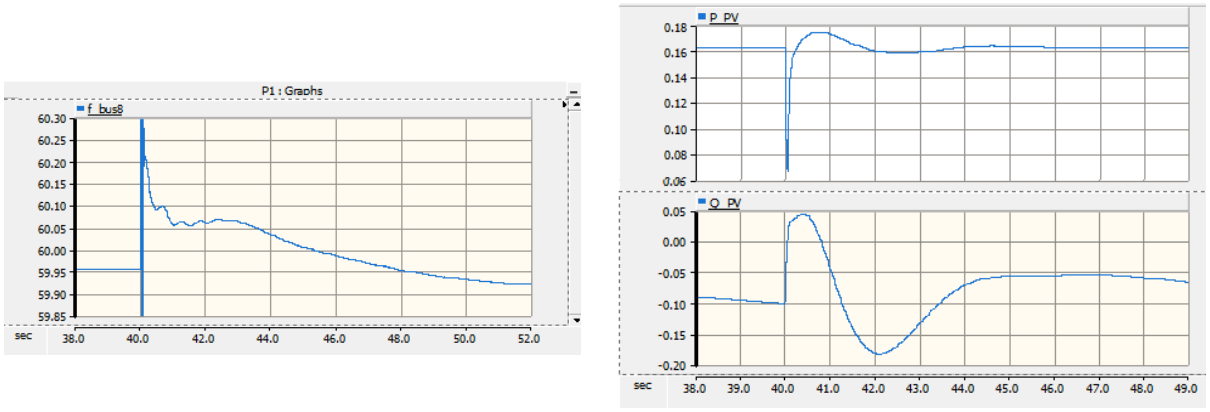

Fig. 17.3-4: Response after fault simulation in the PSCAD model with 50% renewable penetration.

Observation: Frequency reaches predisturbance value more slowly in the EMT simulation. The reactive power response is also slower in EMT simulations compared with the reactive power response in the TS simulation.

A similar analysis is completed with the IEEE nine-bus system with 75% renewables penetration; this analysis is provided in the Appendix.

IEEE Nine-Bus System with High-Fidelity Dynamic Models and Different Renewable Penetration Scenarios

The high-fidelity model of the generic PV plant is incorporated in the IEEE nine-bus in two different scenarios: (1) 25% renewable penetration with one IBR present, and (2) 50% renewable penetration with two IBRs present. A single-line-to-ground fault is simulated in the IEEE nine-bus system in both these scenarios. The corresponding simulation results are shown in Fig. 17.3-5 and Fig. 17.3-6. These results indicate the partial reduction in power generation from the IBRs during the event, similar to observations in real-world events.

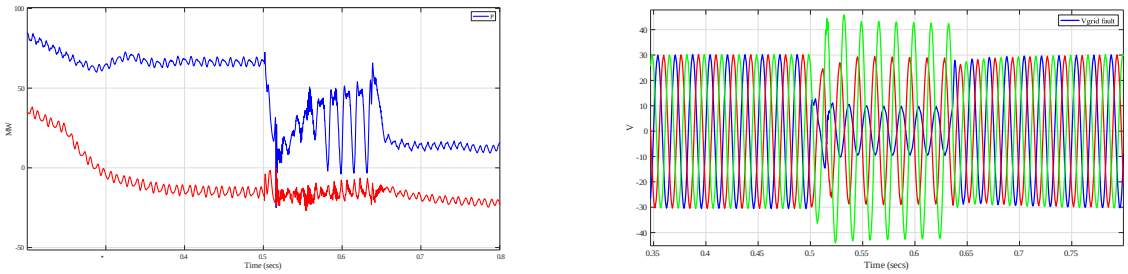

(a) (b)

Fig. 17.3-5: (a) Active power response of IBR, and (b) ac voltage under single-line-to-ground fault in IEEE nine-bus system with 25% renewable penetration (and with one IBR in the IEEE nine-bus system).

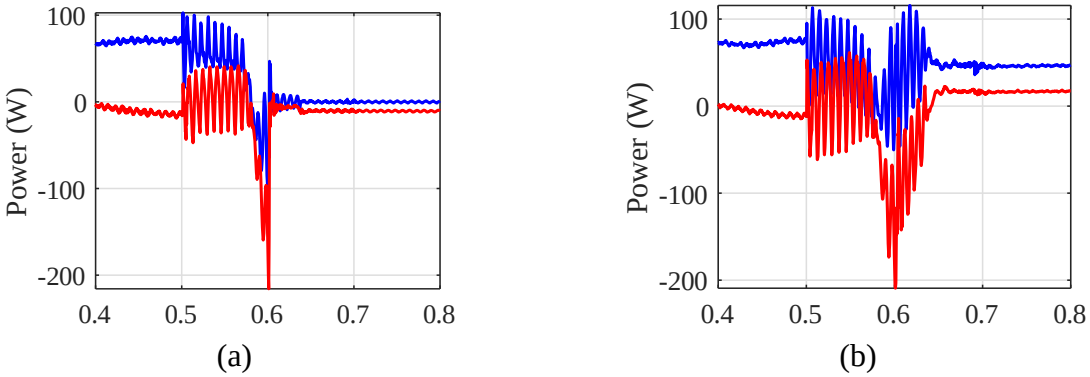

Fig. 17.3-6: (a) Active power response of IBR1, and (b) active power response of IBR2 under single-line-to-ground fault in IEEE nine-bus system with 50% renewable penetration (and with two IBRs in the IEEE nine-bus system).

Significant Accomplishments and Conclusion: An extremely challenging problem of modeling the dynamics of large-scale PV plants is being considered in this project along with increased fidelity of models. Four types of high-fidelity models (including a baseline model), quasi-dynamic model, and advanced models are being developed. These models have speed-up of up to 326 times with accuracy greater than 95%. In previous developments, aggregation and/or simplified representations of the PV plants have been considered in planning studies. Methods and tools to simulate several large-scale PV plants in high-penetration renewable scenarios are also being considered. Some of the challenges in hybrid, EMT, and TS simulations are being studied and documented as a knowledge base for the user community. Fault sequence re-creation in the Angeles Forest event has been documented. Future grid scenario models with >60% and ~100% renewables in California have been developed. Preliminary tests indicate stability challenges that require grid-forming control features when the renewables are ~100% of the generation in California. Control features of interest in the future grid to mitigate challenges that may be observed with a higher penetration of power electronics have been identified through literature review, IAB (and industry) feedback, and brainstorming within the project team. Finally, generic grid models for multiple representative future grid scenarios in TS and EMT simulators have been developed to represent 25%, 50%, and 75% renewables penetration.

Presentations, publications, committees, and mentorship:

- Eleven invited presentations have been completed—one each at 2020 NERC Inverter-Based Resource Performance (IRP) Task Force meeting, Southwest Power Pool (SPP) Technology Expo 2021, IEEE GreenTech Conference panel session 2021, NERC IRP working group 2022, IEEE Power & Energy Society (PES) Day, ACM Internal Conference on Principles of Advanced Discrete Simulation (PADS) 2022, SPP Engineering Planning Summit 2022, NERC IRP subcommittee (IRPS) meeting 2022, SPP Technology Expo 2023; and two at US Department of Energy (DOE) Solar Energy Technologies Office (SETO) workshops in 2021 and 2022.
- Eleven conference papers have been published (including one invited paper), and two more are being drafted.
- Ten presentations in conferences have been completed, with one more due in 2024.
- One tutorial and one panel session at IEEE PES GM and one special session at IEEE ECCE have been organized—these are prestigious conferences for PES and PELS, respectively.
- Workshop organized in 2023 in collaboration with DOE SETO and OE and NERC. Panel session organized in IEEE PES GM 2023 in collaboration with DOE SETO.
- Four journal papers are either being drafted or have been submitted.
- Participation in NERC IRPS to help with guidelines for EMT simulations needed for planning and/or post-mortem analysis by reliability coordinators or transmission planners (independent system operators or utilities). Participation in

NERC EMT Task Force that has recently started. Support to CIGRE C4-60 working group on “Generic EMT-Type Modelling of Inverter-Based Resources for Long-Term Planning Studies.” IAB meeting organization to provide project updates.

- An estimated five doctoral students are supported in science, technology, engineering, and mathematics (STEM) fields.

Path Forward: The research completed in this project needs to be taken forward in multiple paths:

1. Extend the applicability of the simulation algorithms to larger power grids with a large number of IBRs and generalize the EMT simulation platform.
2. Analyze larger power grids with a large number of IBRs during events using the developed simulation platform for post-event automated analysis to provide insights on the upgrades that would have prevented the impact on IBRs observed during events (the simulation platform also can be used in operations for real-time situational awareness).
3. Analyze future grid scenarios with large penetration of IBRs with high-fidelity EMT models to understand the reliability, stability, and operation of future power grids.
4. Building on the highly successful EMT simulation workshop organized at DOE's Oak Ridge National Laboratory (ORNL) in collaboration with DOE and NERC, continue engagement with industry and academia to create a consortium for EMT simulations to research and develop solutions in EMT and to assist industry with understanding the use of EMT.

Products:

Publications

1. Jongchan Choi, Suman Debnath, “Electromagnetic Transient (EMT) Simulation Algorithm for Evaluation of Distribution Grids with Photovoltaic (PV) Distributed Generation Systems,” Kansas Power & Energy Conference, pp. 1–6, 2021.
2. Sayan Samanta, Nilanjan Ray Chaudhuri, Suman Debnath, David Piper, “Simulation and Postmortem Analysis of Angeles Forest Disturbance Event,” IEEE Conference on Innovative Smart Grid Technologies (ISGT 2022), pp. 1–5, 2022.
3. Kaiyu Liu, A. P. Sakis Meliopoulos, Obadolagbonyi Osamuyi, Siyao Cai, “Quasi-Dynamic Domain Modeling and Simulation of Voltage Source Converters,” IEEE ISGT 2022, pp. 1–5, 2022.
4. Suman Debnath, Phani Marthi, Jongchan Choi, “Applied Mathematics Challenge: Simulation of Power Electronics in Future Power Grid,” ACM Internal Conference on Principles of Advanced Discrete Simulation (PADS) 2022, pp. 126–133, 2022.
5. Sayan Samanta, Suman Debnath, Nilanjan Ray Chaudhuri, “Development of TS Model of Future WECC Grid to Replicate High Renewable Generation in California,” IEEE ISGT 2023, pp. 1–5, 2023.
6. Omar Abu-Rub, Phani Marthi, Suman Debnath, Maryam Saeedifard, “Model Predictive Voltage Control of Large-Scale PV or Hybrid PV-BESS Plants,” IEEE Conference on Technologies for Sustainability (SusTech) 2023, pp. 75–79, 2023.
7. Phani Marthi, Jongchan Choi, Suman Debnath, “Interpolation Methods to Enable Fast and Accurate EMT Simulation of PV Inverters,” IEEE 24th Workshop on Control and Modeling for Power Electronics (COMPEL), pp. 1–8, 2023.
8. Jongchan Choi, Phani Marthi, Suman Debnath, Md Arifujjaman, Nicole Rexwinkel, Farzad Khalilpour, Andrew Arana, Huzaifa Karimjee, “Hardware-based Advanced Electromagnetic Transient Simulation for a Large-scale PV Plant in Real Time Digital Simulator,” IEEE Energy Conversion Conference and Exposition (ECCE) 2023, pp. 1–8, 2023.
9. Suman Debnath, Phani Marthi, Qianxue Xia, “AI-Based EMT Dynamic Model of PV Systems,” IEEE ISGT-LA 2023, pp. 1–5, 2023.
10. Suman Debnath, Phani Marthi, Jongchan Choi, Sayan Samanta, Nilanjan Chaudhuri, Andrew Arana, Huzaifa Karimjee, David Piper, Md Arifujjaman, “EMT Simulation of Large PV Plant & Power Grid for Disturbance Analysis,” IEEE ISGT-LA 2023, pp. 1–5, 2023.
11. Misael Martinez, Phani Marthi, Suman Debnath, “A High-Fidelity Electromagnetic Transient Model of Inverter-based Resources Integrated to an IEEE-9 Bus System for Benchmarking Studies,” IEEE ISGT 2024 (accepted).
12. Misael Martinez, Phani Marthi, Suman Debnath, “A High-Fidelity Electromagnetic Transient Model of 50% Renewables in IEEE-9 Bus System for Benchmarking Studies,” IEEE ECCE 2024 (draft).

13. Phani Marthi, Sayan Samanta, Suman Debnath, Nilanjan Chaudhuri, “Behavior of Multiple PV Plants in Futuristic Power Grids During Events,” IEEE PES GM 2024 (submitted).
14. Jongchan Choi, Suman Debnath, Phani Marthi, “Advanced Electromagnetic Transient Numerical Simulation Algorithms for Large-scale Photovoltaic Power Plants,” IEEE Transactions on Sustainable Energy (submitted).
15. Sayan Samanta, Suman Debnath, Phani Marthi, Jongchan Choi, Nilanjan Chaudhuri, Md Arifujjaman, David Piper, “EMT Models of Grids and PV Plants to Study Partial Generation Loss During a Fault Event,” IEEE Transactions on Power Delivery (submitted).
16. Sayan Samanta, Suman Debnath, Nilanjan Chaudhuri, “Development and Stability Analysis of TS Model of WECC Grid with 100% Renewable in California,” IEEE ECCE 2024 (draft).
17. Suman Debnath, Phani Marthi, Jongchan Choi, Sayan Samanta, Nilanjan Chaudhuri, Andrew Arana, Huzaifa Karimjee, David Piper, Md Arifujjaman, “EMT Simulation of Large PV Plant & Power Grid to Understand Fault Events in Grids,” IEEE Transactions on Power Systems (submitted).
18. Jongchan Choi, Suman Debnath, Phani Marthi, “Hardware-based Advanced Electromagnetic Transient Simulation of Large-scale PV Plant & Power Grid in Real Time Digital Simulator,” IEEE Transactions on Industrial Electronics (submitted).

Presentations (Public Release of Data/Information)

1. Suman Debnath, “High Penetration Power Electronics Grid: Challenges, Opportunities, Ongoing Research,” presented in NERC inverter-based resource performance task force, Sept. 2020.
2. Suman Debnath, “High Penetration Power Electronics Grid: Challenges, Opportunities, Ongoing Research,” presented in Southwest Power Pool (SPP) Tech Expo 2020, Oct. 2020.
3. Suman Debnath, “High Penetration Power Electronics Grid: Advanced Simulation and Solutions,” invited talk in IEEE GreenTech Conference panel session, April 2021.
4. Phani Marthi, Jongchan Choi, Suman Debnath, “Electromagnetic Transient (EMT) Simulation Algorithm for Evaluation of Photovoltaic (PV) Generation Systems,” presented in IEEE Kansas Power & Energy Conference (KPEC), April 2021.
5. Suman Debnath, Garth Irwin, Marcelo Elizondo, “Advanced Simulation of Power Electronics, Use of Real-Codes, and Hybrid Simulation,” presented at IEEE Power & Energy Society (PES) General Meeting (GM) Conference, August 2021.
6. Suman Debnath, “High-Fidelity Electromagnetic Transient (EMT) Modeling of Power Electronics in Future Grid,” presented at IEEE ECCE, October 2021.

7. Suman Debnath, “Library of Advanced Dynamic Models of Large-Scale PV Plants,” presented at DOE Workshop on Power System Modeling, November 2021.
8. Suman Debnath, “Advanced Dynamic Models of Large-Scale PV and PV-Grids,” presented at NERC inverter-based resource performance working group, December 2021.
9. Suman Debnath, “Simulation Algorithms & Models to Simulate Future Power Grid with Large-Scale Power Electronics in T&D Systems,” presented at IEEE PES Day 2022, April 2022.
10. Sayan Samanta, Nilanjan Ray Chaudhuri, Suman Debnath, David Piper, “Simulation and Postmortem Analysis of Angeles Forest Disturbance Event,” presented at IEEE ISGT 2022, April 2022.
11. Kaiyu Liu, A. P. Meliopoulos, Osamuyi Obadolagbonyi, Siyao Cai, “Quasi-Dynamic Domain Modeling and Simulation of Voltage Source Converters,” presented at IEEE ISGT 2022, April 2022.
12. Suman Debnath, “Data Requirements for EMT and PV Plant Simulations: Challenges and Requirements,” presented at DOE Workshop on Addressing Data Challenges for Utilities and Power Systems, June 2022.
13. Suman Debnath, “Applied Mathematics Challenge: Simulation of Power Electronics in Future Power Grid,” invited talk at ACM PADS 2022, June 2022.
14. Phani Marthi, Suman Debnath, “Future modeling of inverter-based resources and advanced computing technologies,” presented at SPP Engineering Planning Summit 2022, July 2022.
15. Suman Debnath, “High-Performance Computing: Lessons Learnt and Way Forward for Power & Energy Society,” presented at IEEE PES GM 2022, July 2022.
16. Suman Debnath, “Event Replication: EMT Simulation of High-Fidelity Power Grid-PV Plant Models,” presented at NERC inverter-based resource performance subcommittee (IRPS), December 2022.
17. Sayan Samanta, Suman Debnath, Nilanjan Ray Chaudhuri, “Development and Stability Analysis of Future Grid Models for California with High Renewable Penetration,” presented at IEEE ISGT 2023, January 2023.
18. Omar Abu-Rub, Phani Marthi, Suman Debnath, Maryam Saeedifard, “Model Predictive Voltage Control of Large-Scale PV or Hybrid PV-BESS Plants,” presented at IEEE SusTech 2023, April 2023.
19. Phani Marthi, Jongchan Choi, Suman Debnath, “Interpolation Methods to Enable Fast and Accurate EMT Simulation of PV Inverters,” presented at IEEE COMPEL 2023, June 2023.
20. Suman Debnath, “Role of EMTP simulations to capture accurate T&D interactions driven by power electronic components,” presented at IEEE PES GM panel session 2023, July 2023.

21. Suman Debnath, “High-Fidelity PV Plant and Plant-Grid EMT Simulations: Angeles Forest,” presented at IEEE PES GM panel session 2023, July 2023.
22. Suman Debnath, Jongchan Choi, “High Fidelity Modeling of Large-Scale PV plant (IBR) for EMT Simulations,” presented at EMT workshop 2023, August 2023.
23. Nilanjan Ray Chaudhuri, Phani Marthi, “EMT Simulation of PV Plant,” presented at EMT workshop 2023, August 2023.
24. Jongchan Choi, Phani Marthi, Suman Debnath, Md Arifujjaman, Nicole Rexwinkel, Farzad Khalilpour, Andrew Arana, Huzaifa Karimjee, “Hardware-Based Advanced Electromagnetic Transient Simulation for a Large-Scale PV Plant in Real-Time Digital Simulator,” presented at IEEE ECCE 2023, Oct. 2023.
25. Suman Debnath, Phani Marthi, Qianxue Xia, “AI-Based EMT Dynamic Model of PV Systems,” presented at IEEE ISGT-LA 2023, Nov. 2023.
26. Suman Debnath, Phani Marthi, Jongchan Choi, Sayan Samanta, Nilanjan Chaudhuri, Andrew Arana, Huzaifa Karimjee, David Piper, Md Arifujjaman, “EMT Simulation of Large PV Plant & Power Grid for Disturbance Analysis,” presented at IEEE ISGT-LA 2023, Nov. 2023.

Events Organized

1. **IEEE PES GM Tutorial 2021:** Advanced Simulation of Power Electronics, Use of Real-Codes, and Hybrid Simulation.
2. **IEEE ECCE Special Session 2021 (co-organized with DOE EERE SETO):** Power Electronics Dominated Grids: Dynamic Modeling and Simulation for Reliable and Resilient Operation of Future Grids.
3. **IEEE PES GM Panel Session 2023 (co-organized with DOE EERE SETO):** Power Electronics-Dominated Power Grid: EMT Simulations, Modeling.
4. **EMT Workshop at ORNL (co-organized with DOE EERE SETO, DOE OE AGM, and NERC) in August 2023:** EMT Simulation Workshop had 90+ registered participants and attendees (https://emtworkshop.ornl.gov/).
5. **IAB Meetings:** Four IAB meetings held in April 2020, January 2021, March 2022, and September 2022 with up to 30 participants each.

Technical Products (Models)

1. Baseline PV plant model (PSCAD)
2. Quasi-dynamic PV plant model (PSCAD)
3. Three types of high-fidelity PV plant models (PSCAD)
4. Three TS models of future power grids for scenarios of 60% and 100% renewables in CA (PSSE)
5. Equivalent EMT model of present and future grids (PSCAD)
6. Advanced model of PV plant (PSCAD)

7. High-fidelity model of PV plant (RSCAD)
8. Advanced model of PV plant (RSCAD)
9. EMT model of present grid and future grid (RSCAD)
10. Three EMT models of IEEE nine-bus for different scenarios of renewable penetration (PSCAD)
11. Three TS models of IEEE nine-bus for different scenarios of renewable penetration (PSSE)

Media Reports/Articles

1. https://potomacofficersclub.com/news/ornl-researchers-use-new-analysis-method-to-study-power-grid-faults/
2. https://www.utilitydive.com/news/national-lab-ornl-doe-models-interveter-faults-emt-analysis/691067/
3. https://www.ornl.gov/news/ornl-demonstrates-power-new-modeling-approach-understand-faults-modern-electric-grid
4. https://electrek.co/2023/08/17/heres-what-us-utilities-need-to-do-to-prevent-faults-on-the-grid/
5. https://www.ourmechanicalcenter.com/archives/3722
6. https://www.solarpowerworldonline.com/2023/08/doe-research-explores-reliability-inverter-based-resources-power-grid/
7. https://www.power-grid.com/td/transmission/ornl-sce-demonstrate-new-modeling-approach-to-understand-faults-in-an-ibr-heavy-electric-grid/
8. https://www.nacleanenergy.com/energy-efficiency/ornl-demonstrates-power-of-new-modeling-approach-to-understand-faults-in-the-modern-electric-grid
9. https://emtworkshop.ornl.gov/

Key Collaborations Formed

1. **NERC:** ORNL partnered with NERC and DOE to organize the EMT Simulation Workshop in August 2023. ORNL supported multiple NERC documents like EMT guidelines and supported activities in the NERC IRPS and EMT TF, resulting in documents released from NERC such as “Reliability Guidelines: Electromagnetic Transient Modeling for BPS Connected Inverter-Based Resources—Recommended Model Requirements and Verification Practices,” March 2023. https://www.nerc.com/comm/RSTC_Reliability_Guidelines/Reliability_Guideline-EMT_Modeling_and_Simulations.pdf.
2. **NextEra/Florida Power & Light:** Assistance provided with data needed for research in the project.

Project Team and Roles: List all participants along with their individual roles and/or intellectual contribution (e.g., DOE personnel, students, collaborating organizations).

Oak Ridge National Laboratory: Suman Debnath has been involved in (1) managing the technical developments, finances, and contracts in the project; and (2) development of a high-fidelity dynamic model of PV plants in PSCAD and RTDS, future grid and generic present grid scenarios' development, and advanced modeling tasks. Jongchan Choi has been involved with development of a high-fidelity dynamic model of PV plants, quasi-dynamic model of PV plant, present grid model, and future grid model in RTDS. Phani Marthi has been involved with development and testing of a high-fidelity dynamic model of PV plants in PSCAD and the integration of PV plants with present and future grid scenarios in PSCAD. Qianxue Xia has been involved with the advanced model of the PV plant. Misael Martinez has been involved with the incorporation of a new PV system introduced within the generic PV plant and integrating a high-fidelity model of PV plants within the IEEE nine-bus case study.

Pennsylvania State University: Nilanjan Ray Chaudhuri has been involved in managing the overall project developments and overviewing the mapping and hybrid simulation tasks at PSU. Sayan Samanta has been involved in (1) developing generic present grid and future grid scenarios, (2) upgrading future grid scenarios and developing IEEE nine-bus case study, and (3) developing quasi-dynamic models of PV plants in PSCAD.

Southern California Edison (SCE): David Piper has provided advice and information on the fault sequence during the event studied in EMT and EMT-TS model development. Md Arifujjaman has been involved with contractual negotiations, providing feedback on the control specifications and performance, and reviewing ongoing modeling exercises. Nicole Rexwinkel and Farzad Khalilpour have assisted with the real-time simulation lab's remote access and testing simulators.

Others: Harvey Scribner (SPP), Austin White (Oklahoma Gas & Electric), and Ebrahim Rahimi (CAISO) have been involved in reviewing control specifications and ongoing modeling exercises and in reviewing results observed from the project. Huzaifa Karimjee and Andrew Arana have supported with data needed in this project.

Georgia Institute of Technology: Maryam Saeedifard has been involved in managing overall project developments at Georgia Tech. A P Meliopoulos has been cohandling technical developments related to modeling exercises. Omar Abu-Rub has been involved with advanced control functionalities and inverter control hardware-in-the-loop testing tasks. Osamuyi Obadolagbonyi, Siyao Cai, and Zhengrong Chen have been involved with development of preliminary quasi-dynamic model using winIGS.

Appendix:

T-1. Data collection and NDAs

ST-1.1 PV System Data Collection

Utility Name	Plant Name	State	County	Status	Technology	Nameplate Capacity (MW)	Summer Capacity (MW)	Winter Capacity (MW)	Operating Month	Operating Year
AV Solar Ranch 1 LLC	AV Solar Ranch One	CA	Los Angeles	OP	Solar Photovoltaic	253	241.5	241.5	8	2014
CD Arevon USA, Inc.	Mount Signal Solar Farm V	CA	Imperial	OP	Solar Photovoltaic	252.3	252.3	252.3	11	2018
Consolidated Edison Development Inc.	Panoche Valley Solar Farm	CA	San Benito	OP	Solar Photovoltaic	240	240	240	1	2018
Consolidated Edison Development Inc.	Great Valley Solar Portfolio Holdings, LLC	CA	Fresno	OP	Solar Photovoltaic	205.3	200	150	4	2018
Southern Power Co	RE Tranquillity	CA	Fresno	OP	Solar Photovoltaic	205.3	200	200	7	2016
Southern Power Co	RE Garland	CA	Kern	OP	Solar Photovoltaic	185	185	185	11	2016
63SU 8me, LLC	Springbok Solar Farm 2	CA	Kern	OP	Solar Photovoltaic	155	155	155	9	2016
Topaz Solar Farms LLC (BHE Renewables)	Topaz Solar Farm	CA	San Luis Obispo	OP	Solar Photovoltaic	151.2	151.2	151.2	6	2013
CSOLAR IV West LLC	Imperial Solar Energy Center West	CA	Imperial	OP	Solar Photovoltaic	148.7	148.7	148.7	4	2016
Southern Power Co	Campo Verde Solar	CA	Imperial	OP	Solar Photovoltaic	147.4	139	139	10	2013
Mojave Solar LLC	Mojave Solar Project	CA	San Bernardino	OP	Solar Thermal without Energy Storage	140	137.5	100	12	2014
Mojave Solar LLC	Mojave Solar Project	CA	San Bernardino	OP	Solar Thermal without Energy Storage	140	137.5	100	12	2014
NRG Energy Services	Ivanpah 2	CA	San Bernardino	OP	Solar Thermal without Energy Storage	133.4	133.4	133.4	12	2013
NRG Energy Services	Ivanpah 3	CA	San Bernardino	OP	Solar Thermal without Energy Storage	133.4	133.4	133.4	12	2013
NRG Energy Services	Ivanpah 1	CA	San Bernardino	OP	Solar Thermal without Energy Storage	133	133	133	12	2013
California Flats Solar 130, LLC	CA Flats Solar 130, LLC	CA	San Luis Obispo	OP	Solar Photovoltaic	130	130	130	11	2017
Topaz Solar Farms LLC (BHE Renewables)	Topaz Solar Farm	CA	San Luis Obispo	OP	Solar Photovoltaic	129.8	129.8	129.8	4	2013
CSOLAR IV South LLC	Imperial Solar Energy Center South	CA	Imperial	OP	Solar Photovoltaic	128.9	128.9	128.9	11	2013
Genesis Solar LLC	Genesis Solar Energy Project	CA	Riverside	OP	Solar Thermal without Energy Storage	125	125	125	3	2014
Genesis Solar LLC	Genesis Solar Energy Project	CA	Riverside	OP	Solar Thermal without Energy Storage	125	125	125	11	2013
Topaz Solar Farms LLC (BHE Renewables)	Topaz Solar Farm	CA	San Luis Obispo	OP	Solar Photovoltaic	112.5	112.5	112.5	10	2014
EDF Renewable Asset Holdings, Inc.	Catalina Solar LLC	CA	Kern	OP	Solar Photovoltaic	110	110	110	12	2012
CD Arevon USA, Inc.	Quinto Solar PV Project	CA	Merced	OP	Solar Photovoltaic	108	105.1	76.8	11	2015
Consolidated Edison Development Inc.	Wistaria Ranch Solar	CA	Imperial	OP	Solar Photovoltaic	106.7	100	100	12	2018
62SK 8me, LLC	Springbok Solar Farm 1	CA	Kern	OP	Solar Photovoltaic	105	105	105	7	2016
Sustainable Power Group, LLC	Antelope Expansion 2	CA	Los Angeles	OP	Solar Photovoltaic	105	105	105	12	2018
Topaz Solar Farms LLC (BHE Renewables)	Topaz Solar Farm	CA	San Luis Obispo	OP	Solar Photovoltaic	102.1	102.1	102.1	1	2014
Southern Power Co	Henrietta Solar Project	CA	Kings	OP	Solar Photovoltaic	102	102	102	8	2016
Imperial Valley Solar, LLC	Imperial Valley Solar, LLC	CA	Imperial	OP	Solar Photovoltaic	101	101	101	11	2013
RE Astoria 2 LLC (Recurrent Energy)	RE Astoria	CA	Kern	OP	Solar Photovoltaic	100	100	100	12	2016
RE Mustang LLC (Recurrent Energy)	RE Mustang LLC	CA	Kings	OP	Solar Photovoltaic	100	100	100	8	2016
Terra-Gen Operating Co-Solar	SEGS VIII	CA	San Bernardino	OP	Solar Thermal without Energy Storage	92	88	64	12	1989
Terra-Gen Operating Co-Solar	SEGS IX	CA	San Bernardino	OP	Solar Thermal without Energy Storage	92	88	64	9	1990
Topaz Solar Farms LLC (BHE Renewables)	Topaz Solar Farm	CA	San Luis Obispo	OP	Solar Photovoltaic	90.3	90.3	90.3	11	2014
NRG Renew Operation & Maintenance, LLC	California Valley Solar Ranch	CA	San Luis Obispo	OP	Solar Photovoltaic	86.5	86.5	86.5	1	2013
Sustainable Power Group, LLC	Solverde 1	CA	Los Angeles	OP	Solar Photovoltaic	85	81	78	12	2016
Southern Power Co	Stateline Solar	CA	San Bernardino	OP	Solar Photovoltaic	75.9	76	76	12	2015
RE Astoria 2 LLC (Recurrent Energy)	RE Astoria 2	CA	Kern	OP	Solar Photovoltaic	75	75	75	12	2016
Sunpin Holdings, LLC	Colgreen North Shore Solar Farm	CA	Riverside	OP	Solar Photovoltaic	74.8	74.8	74.8	12	2018
NRG Renew Operation & Maintenance, LLC	California Valley Solar Ranch	CA	San Luis Obispo	OP	Solar Photovoltaic	70	70	70	10	2013
NRG Solar Alpine	Alpine Solar	CA	Los Angeles	OP	Solar Photovoltaic	66	66	66	2	2013
Imperial Valley Solar, LLC	Imperial Valley Solar, LLC	CA	Imperial	OP	Solar Photovoltaic	64.6	64.6	64.6	12	2013
Solar Star California XIX, LLC (BHE Renewables)	Solar Star 1	CA	Kern	OP	Solar Photovoltaic	64.5	62.9	62.9	4	2014
Southern Power Co	North Star Solar	CA	Fresno	OP	Solar Photovoltaic	62.5	60	60	6	2015
Consolidated Edison Development Inc.	Great Valley Solar Portfolio Holdings, LLC	CA	Fresno	OP	Solar Photovoltaic	60	60	46	12	2017
Five Points Solar Park, LLC	Five Points Solar Park	CA	Fresno	OP	Solar Photovoltaic	60	60	50	9	2016
RE Barren Ridge 1, LLC	RE Barren Ridge 1	CA	Kern	OP	Solar Photovoltaic	60	60	60	8	2016
Regulus Solar, LLC	Regulus Solar Project	CA	Kern	OP	Solar Photovoltaic	60	60	60	11	2014

Fig. A17.3-7: List of PV systems in California with power rating and locations.

ST-1.2 PV Configuration Data Collection

Table A0-1: PV configuration information

PV plant	Power rating of plant	Voltage level plant connects	PV plant information such as single line diagrams, nameplate ratings (voltage, power), test data, manufacturer, configuration, algorithms, etc.								
			Converters	Inverters	Transformers	Filters	Capacitor banks	Cables	Control config.	Control algorithms	Others (e.g., breakers)

ST-1.3 Contingency Event Data Collection

Table A0-1: Contingency events data

PV plant	Status before event	Status post event	Data availability at substation or power plant controller (PCC) (voltages, currents, power measured, frequency measured, etc.)	Data availability within the plant (voltages, currents, power measured, frequency measured, etc.)

ST-1.4 IAB Formation

The members in the IAB are affiliated with 8minute Solar Energy, Western Area Power Administration, Florida Power & Light, Hatch, Hitachi Energy, Jacksonville Electric Authority, Western Energy Board, Western Electric Coordinating Council, Electric Reliability Council of Texas, General Electric, Commonwealth Edison, PacifiCorp, REnewable Power Plant Solutions, Eaton, Vestas, Midcontinent Independent System Operator, Terabase Energy, Siemens, Tennessee Valley Authority, California Independent System Operator, Southwest Power Pool, Oklahoma Gas & Electric, Solectria, Pacific Gas & Electric (PG&E), Solar Energy Industries Association, Powersim Inc, Central Municipal Power Agency/Services, City of Tallahassee Utilities, Enel Group, Independent System Operator New England, Trimark Associates Inc., and Omaha Public Power District.

T-2. Develop baseline PV system model

ST-2.1 Model development

Large PV Plants

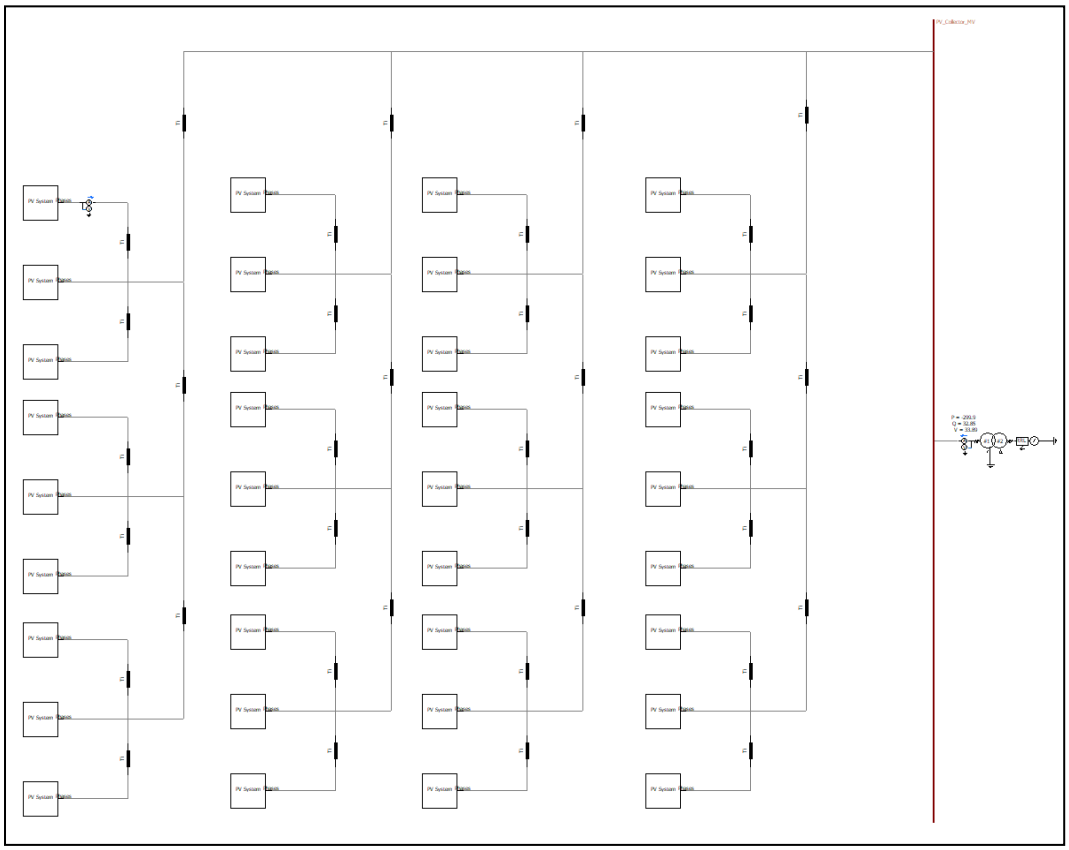

Fig. A17.3-8: Overview of the large PV plant.

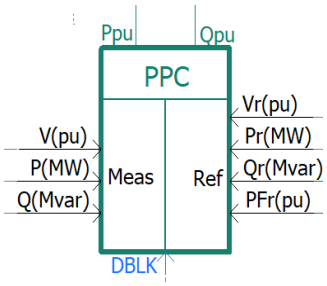

Fig. A17.3-9: Power plant controller.

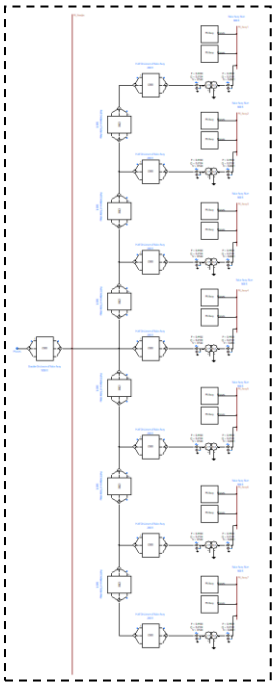

Fig. A17.3-10: Multiple PV modules in the developed feeder module.

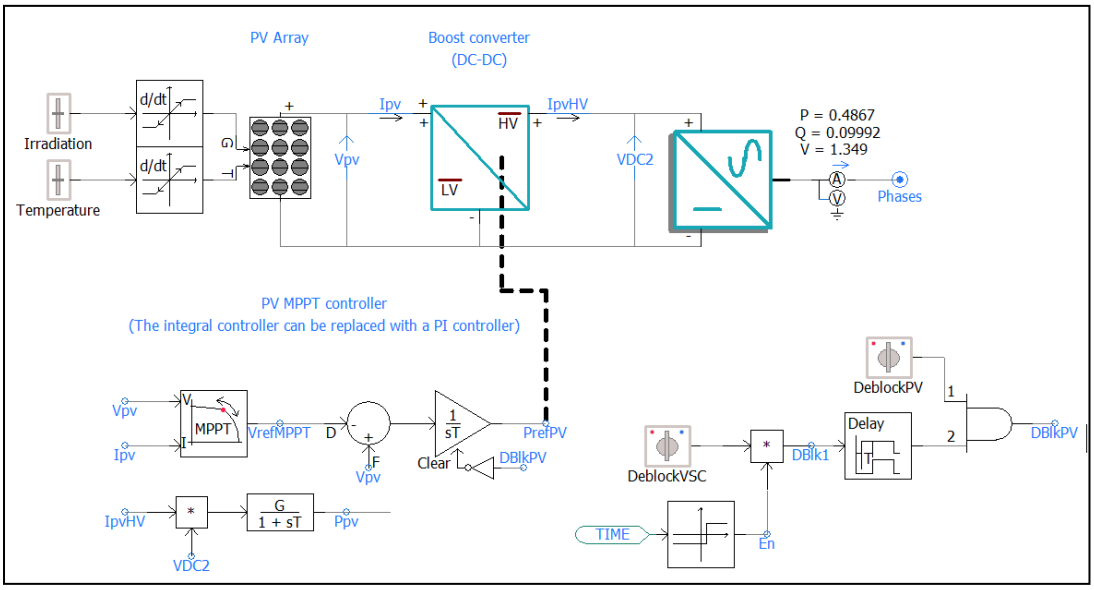

Fig. A17.3-11: PV system in the developed PV module.

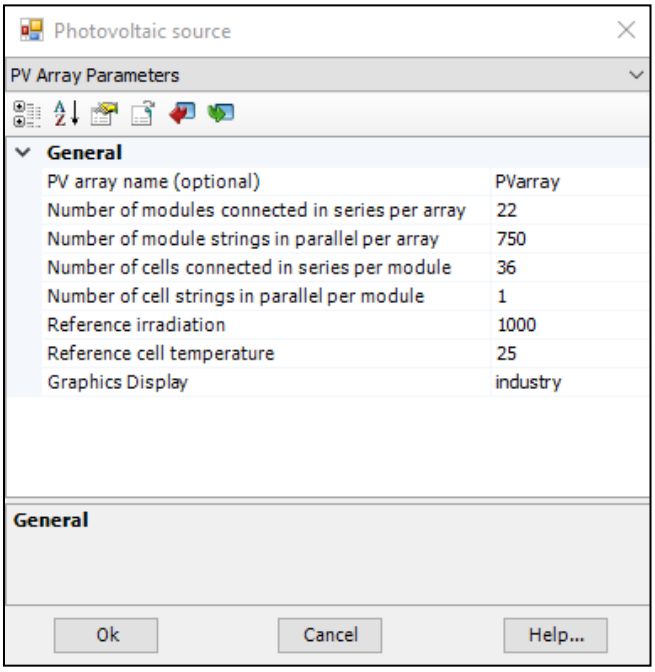

Fig. A17.3-12: PV array model parameters.

Small PV Plants:

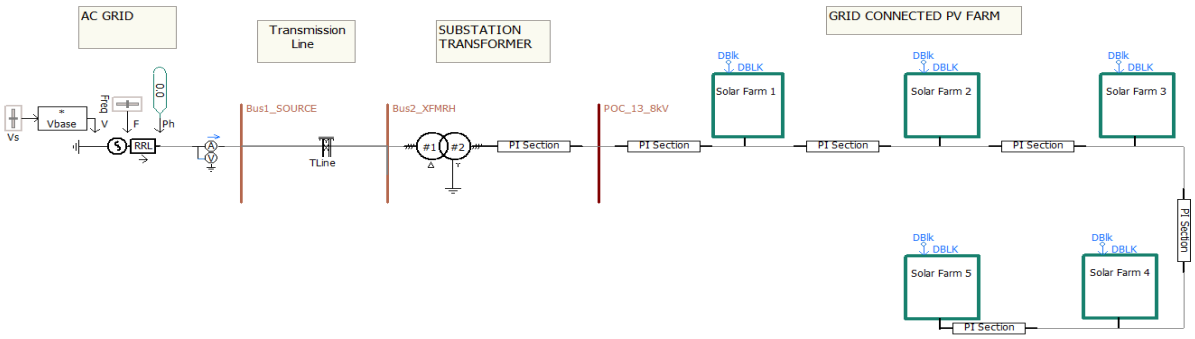

Fig. A17.3-13: Small PV plant model.

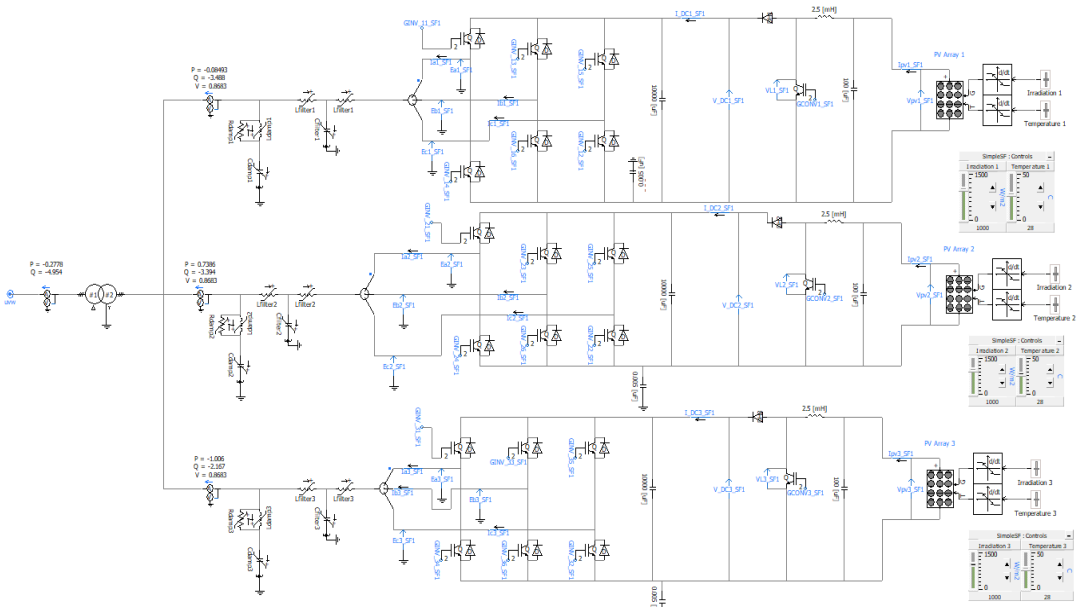

Fig. A17.3-14: PV system model.

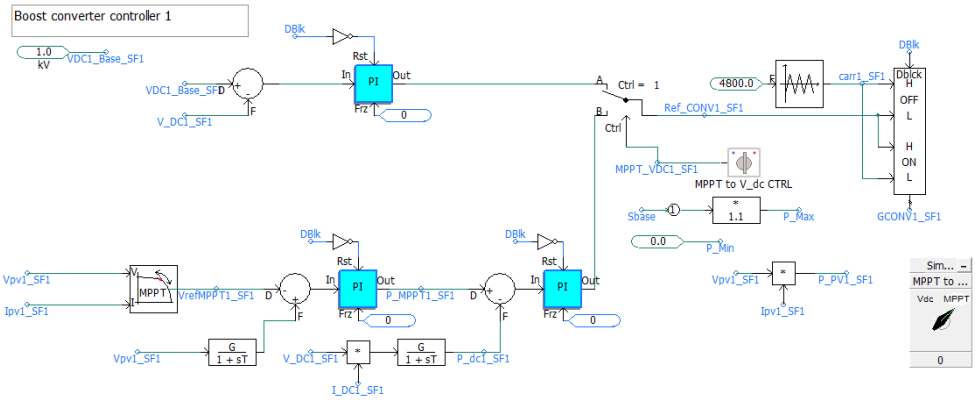

Fig. A17.3-15: dc-dc converter control modes.

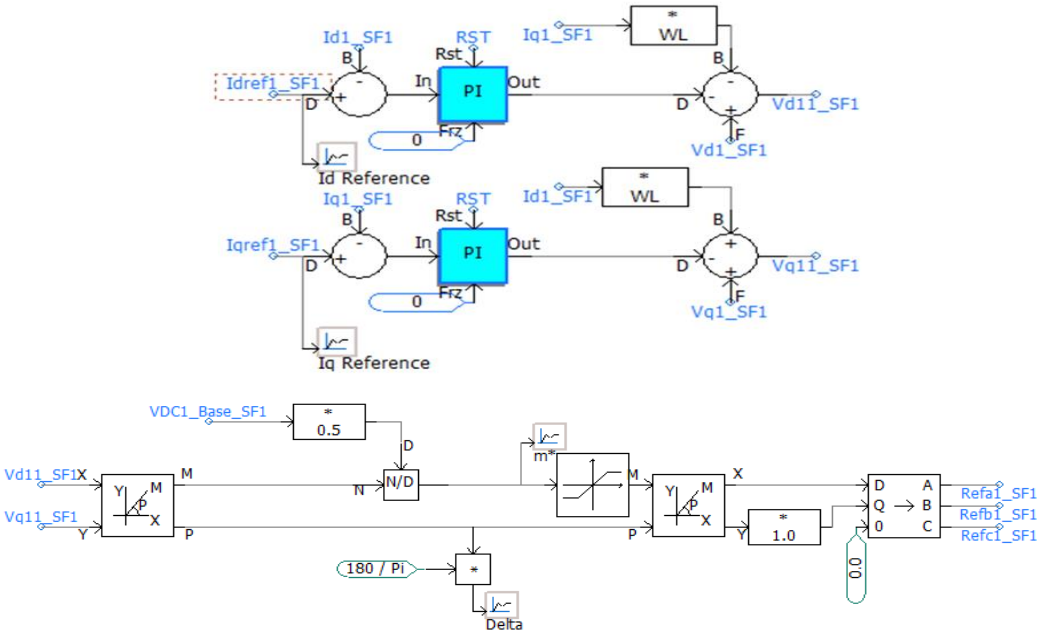

Fig. A17.3-16: Inner *dq* current control in inverter.

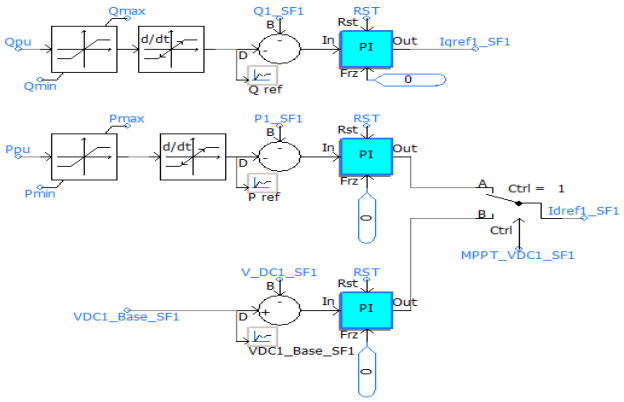

Fig. A17.3-17: Outer loop control.

ST-2.2 Testing

Large PV Plant:

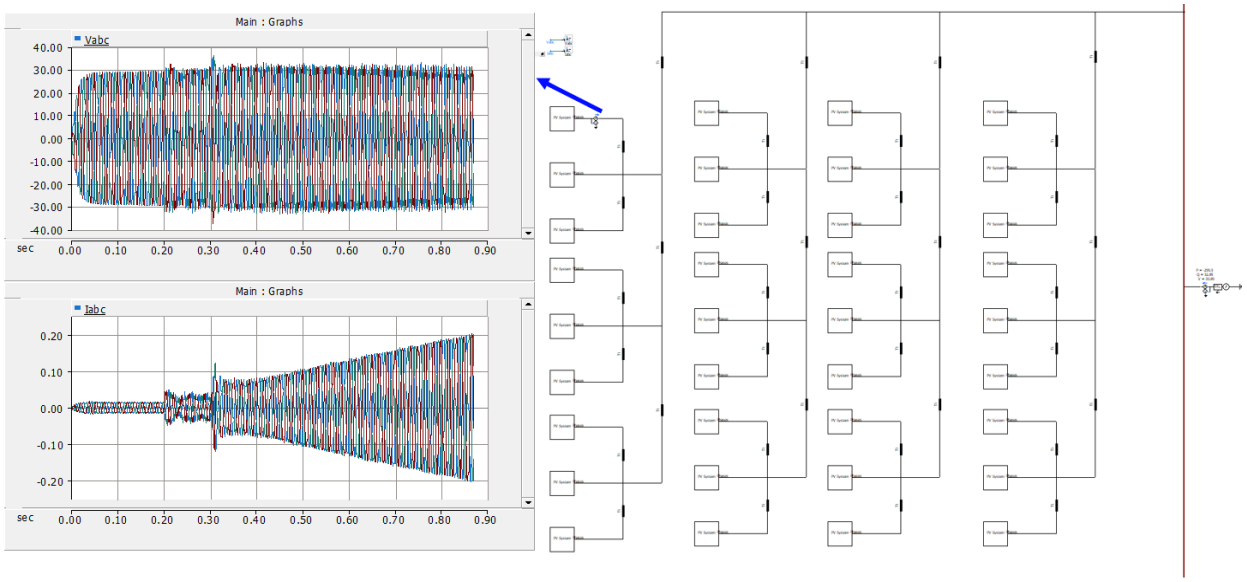

Fig. A17.3-18: Simulation results: voltage and current measured at the point of connection for one of the 36 feeder modules in the baseline large PV plant model.

Specific PV Plant:

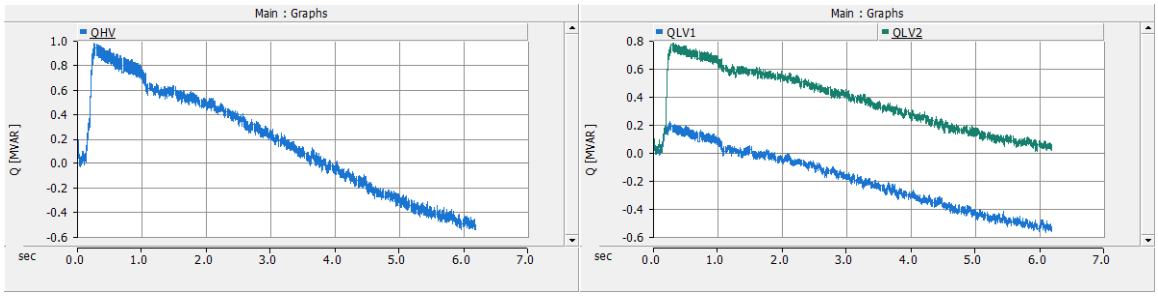

Fig. A17.3-19: Simulation results: Reactive power (high-voltage side) and reactive power (low-voltage sides) of the baseline large PV plant (based on data collected in ST-1.2) during switching events.

Small PV Plant:

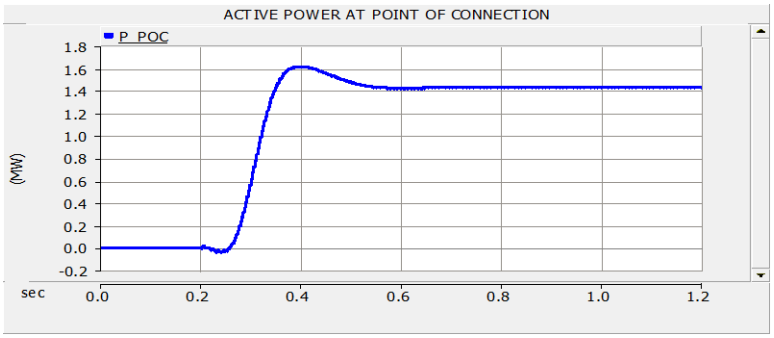

Fig. A17.3-20: Simulation results: Power measured at the POI of the PV system in the small PV plant.

T-3. Develop suite of dynamic PV system models

ST-3.1 Quasi-dynamic model in PSCAD/PSSE

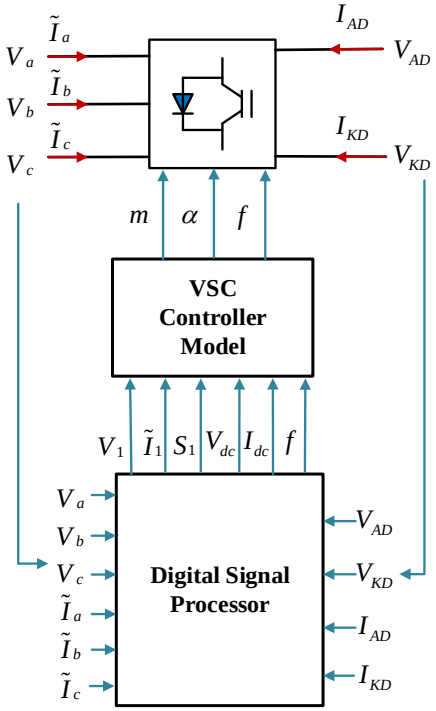

Fig. A17.3-21: Overall block diagram of quasi-dynamic quadratized inverter model.

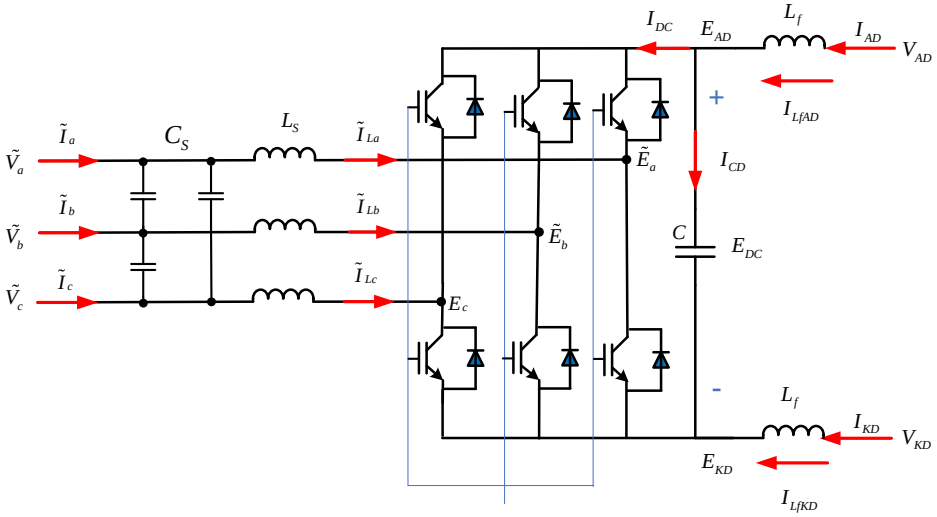

Fig. A17.3-22: Inverter circuit configuration.

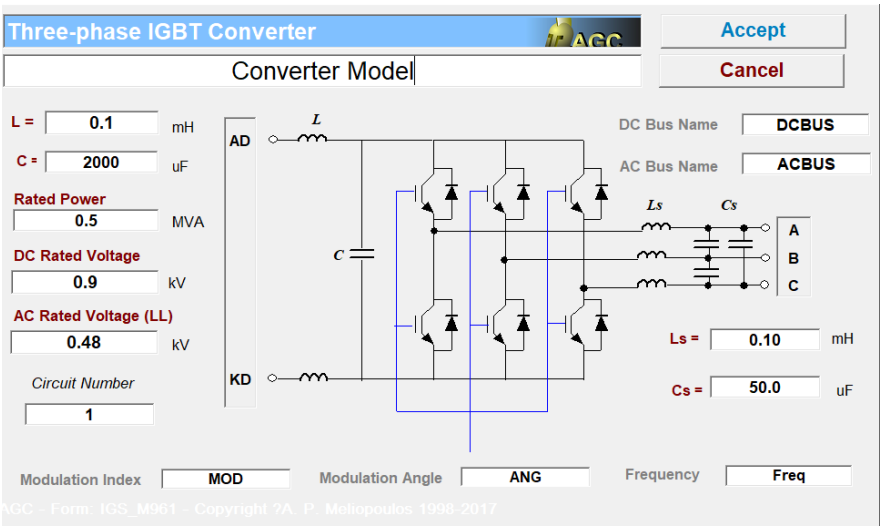

Fig. A17.3-23: User interface for quasi-dynamic domain inverter model that shows the parameters used to define the model.

The compact inverter model is given by equations (A3.1-1) to (A3.1-20):

$$I_{AD} = I_{LfAD} \tag{A17.3-1}$$

$$I_{KD} = I_{LfKD} \tag{A17.3-2}$$

$$\tilde{I}_a = \tilde{I}_{La} + j4\pi f C_s \tilde{V}_a - j2\pi f C_s \tilde{V}_b - j2\pi f C_s \tilde{V}_c \tag{A17.3-3}$$

$$\tilde{I}_b = \tilde{I}_{Lb} - j2\pi f C_s \tilde{V}_a + j4\pi f C_s \tilde{V}_b - j2\pi f C_s \tilde{V}_c \tag{A17.3-4}$$

$$\tilde{I}_c = \tilde{I}_{Lc} - j2\pi f C_s \tilde{V}_a - j2\pi f C_s \tilde{V}_b + j4\pi f C_s \tilde{V}_c \tag{A17.3-5}$$

$$I_m = 0 \text{ (Terminal m)} \tag{A17.3-6}$$

$$I_\alpha = 0 \text{ (Terminal } \alpha) \tag{A17.3-7}$$

$$I_f = 0 \text{ (Terminal } f) \tag{A17.3-8}$$

$$0 = V_{AD} - E_{AD} - L_f \frac{dI_{LsAD}}{dt} \tag{A17.3-9}$$

$$0 = V_{KD} - E_{KD} - L_f \frac{dI_{LsKD}}{dt} \tag{A17.3-10}$$

$$0 = E_{DC} - E_{AD} + E_{KD} \tag{A17.3-11}$$

$$0 = I_{LfAD} - I_{DC} - C\frac{dE_{DC}}{dt} \tag{A17.3-12}$$

$$0 = I_{LfKD} + I_{DC} + C\frac{dE_{DC}}{dt} \tag{A17.3-13}$$

$$0 = \tilde{V}_a - \tilde{E}_a - j2\pi f L_s \tilde{I}_{La} \tag{A17.3-14}$$

$$0 = \tilde{V}_b - \tilde{E}_b - j2\pi f L_s \tilde{I}_{Lb} \tag{A17.3-15}$$

$$0 = \tilde{V}_c - \tilde{E}_c - j2\pi f L_s \tilde{I}_{Lc} \tag{A17.3-16}$$

$$0 = \frac{m}{2\sqrt{2}} E_{DC} e^{j\alpha} + L_s \frac{d\tilde{I}_{La}}{dt} - \tilde{E}_a \quad \text{(A17.3-17)}$$

$$0 = \frac{m}{2\sqrt{2}} E_{DC} e^{j\left(\alpha - \frac{2\pi}{3}\right)} + L_s \frac{d\tilde{I}_{Lb}}{dt} - \tilde{E}_b \quad \text{(A17.3-18)}$$

$$0 = \frac{m}{2\sqrt{2}} E_{DC} e^{j\left(\alpha + \frac{2\pi}{3}\right)} + L_s \frac{d\tilde{I}_{Lc}}{dt} - \tilde{E}_c \quad \text{(A17.3-19)}$$

$$0 = \mathrm{Re}\left(\tilde{E}_a \tilde{I}_{La}^* + \tilde{E}_b \tilde{I}_{Lb}^* + \tilde{E}_c \tilde{I}_{Lc}^*\right) + E_{DC} I_{DC} \quad \text{(A17.3-20)}$$

The state of the system is:

$\mathbf{x}^{\mathrm{T}} = (V_{AD}, V_{KD}, \tilde{V}_a, \tilde{V}_b, \tilde{V}_c, m, \alpha, f, E_{AD}, E_{KD}, E_{DC}, I_{LfAD}, I_{LfKD}, \tilde{I}_{La}, \tilde{I}_{Lb}, \tilde{I}_{Lc}, \tilde{E}_a, \tilde{E}_b, \tilde{E}_c, I_{DC})$.

The above equations are quadratized and cast into three sets of equations.

ST-3.2 High-fidelity model in PSCAD

Components in the PV Plant and Parameter Requirements

The components present in the (PV plant and the models needed (along with parameters needed) in the high-fidelity model are as follows:

1. PV systems
   - *PV array*: A PV array is composed of parallel-connected PV strings, each consisting of series-connected PV modules. Each PV module consists of series/parallel–connected solar cells. In the high-fidelity model being developed, an equivalent electrical circuit is used to represent the PV array model. The equivalent electrical circuit uses a *N*-point current-voltage characteristics model extrapolated to different irradiances and temperatures. The current-voltage characteristics curve depends on the individual solar cell's characteristics and the numbers of series/parallel cells present in a module, modules present in a string, and strings present in an array.
   - *Power inverter module (boost converter/grid-connected inverter)*: Power electronics interfaces are required to connect the PV array to the grid such as a dc-dc boost converter and a dc-ac grid-connected inverter. The dc-dc boost converter is optional (and may not be present in a facility). Additionally, filters are connected between the dc-ac grid inverter and the distribution transformer. The dc-dc converter and inverter are being modeled using switching models. Detailed information on transformer models follows. The parameters required to model the power electronics include power ratings, voltage ratings, filter component parameters, and transformer parameters. The specific information for the power electronics model is estimated from the information provided on the plants and information collected.

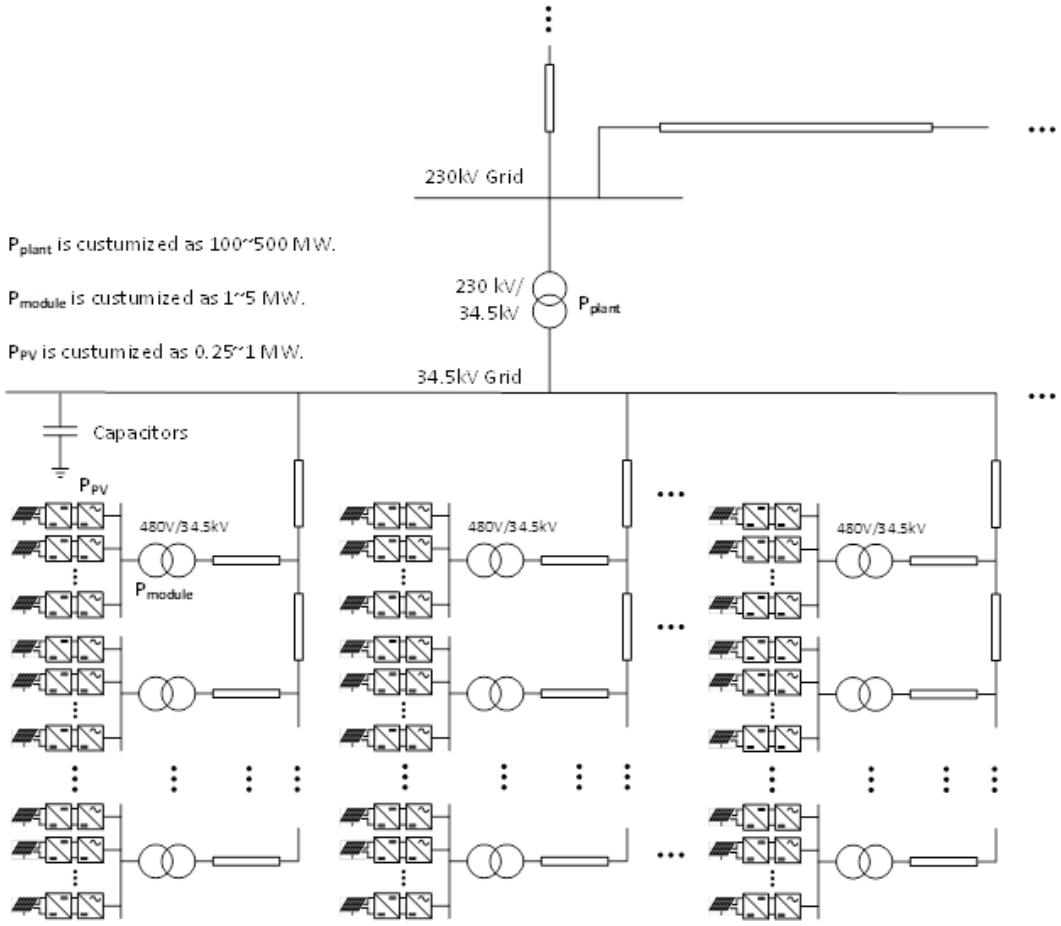

Fig. A17.3-24: Configuration of a large PV plant in a medium-voltage (e.g., 34.5 kV) distribution system connected to a high-voltage (e.g., 230 kV) transmission system.

- *Inverter firmware*: Control functionalities in the inverter firmware have been described under Task 2 and are not repeated here. Additionally, future features are introduced in the inverter firmware such as fast frequency support (inertial) or fast dynamic voltage support. Further details on features in the inverter firmware that may improve reliability of future power grids are provided under Task 7. Parameters of the control features are estimated based on information obtained on the plants in Task 1.
- Several PV inverter modules with their inverter firmware may be present in a PV system.

2. Medium-voltage distribution system

- *Breakers:* The breakers may be present at individual PV systems and/or in distribution feeders and/or at the collectors. The breakers will form an important part of the model because the shutdown of the plant and/or part of the plant will happen through control of the breaker. Specific data on presence of breakers are identified from plant information.
- *Distribution lines:* The distribution lines are typically modeled by a PI-section model consisting of LC sections. Therefore, line parameters such as self- and

mutual-series inductance and parallel capacitance are required to model the distribution line. Specific data for the distribution line parameters are estimated based on typical parameters for stated distribution lines' voltage and power ratings.

- *Capacitor banks:* Some plants have capacitor banks at the distribution feeders and/or the collector. Capacitor bank models will be based on information obtained on the plants.

3. High-voltage transmission system

- *Power transformers:* Transformers that convert medium-voltage to high-voltage in the substations are considered in the model. Typical transformer parameters include leakage reactance, magnetizing parameters, losses such as conduction and hysteresis/eddy, and others. Data on transformers are estimated based on typical parameters for stated transformers' voltage and power ratings.
- *Transmission line:* The transmission lines may be modeled by three different types: PI section, Bergeron line model, and frequency-dependent model. The chosen model depends on goals of the study, length of the lines, and model fidelity needed. Line parameters or conductor specifications are required to model the transmission. Specific information for the transmission line model is identified by estimation from typical transmission lines' stated voltage and power ratings.
- *Power plant controller*: Several control modes and parameters will be present in a PPC, such as droop characteristics in reactive power control (or power factor control or voltage control) or frequency support. Some features are present in existing PV plants, and other features may improve the reliability of future power grids. Detailed description of features that may improve reliability are provided in Task 7. Parameters of the control features are being estimated based on information obtained on the plants in Task 1.

PV Inverter Module Model

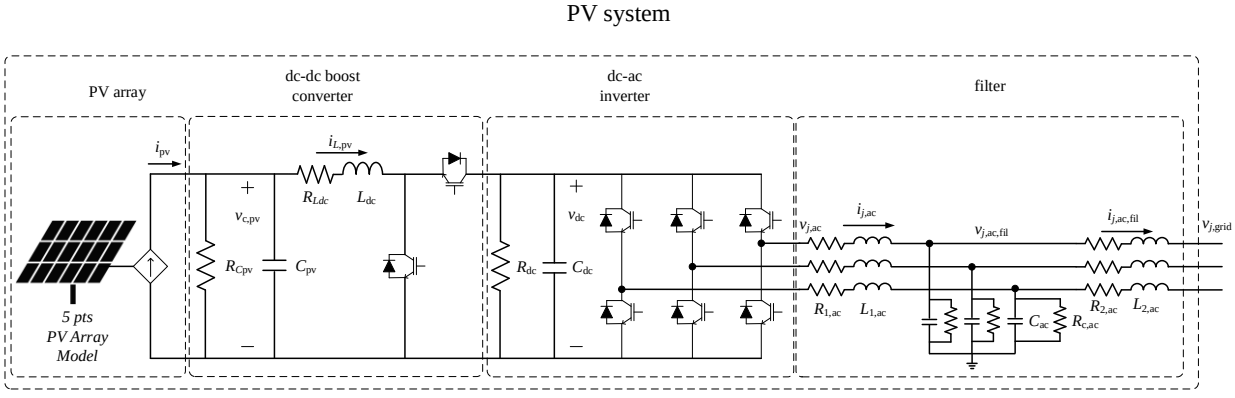

Fig. A17.3-25: Configuration of the PV inverter module.

The EMT model of the PV system shown in Fig. A17.3-25 can be expressed by DAEs **Error! Reference source not found.**) to **Error! Reference source not found.**):

$$C_{pv}\frac{dv_{c,pv}}{dt} = -\left(\frac{v_{c,pv}}{R_{C,dc}}\right) - i_{L_{pv}} + i_{pv} \quad \text{(A17.3-21)}$$

$$L_{pv}\frac{di_{L_{pv}}}{dt} = -R_{L,dc}i_{L_{pv}} + v_{c,pv} - v_{dc}\left\{S_{2,dc}(1-S_{1,dc}) + (1-S_{2,dc})(1-S_{1,dc})\,sgn\left(i_{L_{pv}}\right)\right\} \quad \text{(A17.3-22)}$$

$$C_{dc}\frac{dv_{dc}}{dt} = -\frac{v_{dc}}{R_{dc}} + i_{L,pv}\left\{S_{2,dc}(1-S_{1,dc}) + (1-S_{2,dc})(1-S_{1,dc})\,sgn(i_{L,pv})\right\} - i_{j,ac}\left\{S_{1,j,ac}(1-S_{2,j,ac}) + (1-S_{2,j,ac})(1-S_{1,j,ac})\,sgn(-i_{j,ac})\right\} \quad \text{(A17.3-23)}$$

$$L_{1,ac}\frac{di_{j,ac}}{dt} = -R_{1,ac}i_{j,ac} + \frac{v_{dc}}{2}\left\{S_{1,j,ac}(1-S_{2,j,ac}) - S_{2,j,ac}(1-S_{1,j,ac}) - (1-S_{2,j,ac})(1-S_{1,j,ac})(2\,sgn(i_{j,ac})-1)\right\} - v_{j,ac,fil} \quad \text{(A17.3-24)}$$

$$C_{ac}\frac{dv_{j,ac,fil}}{dt} = -\frac{v_{j,ac,fil}}{R_{c,ac}} + i_{j,ac} - i_{j,ac,fil} \quad \text{(A17.3-25)}$$

$$L_{2,ac}\frac{di_{j,ac,fil}}{dt} = -R_{2,ac}i_{j,ac,fil} + v_{j,ac,fil} - v_{j,grid}^{s} \quad \text{(A17.3-26)}$$

PV System Model

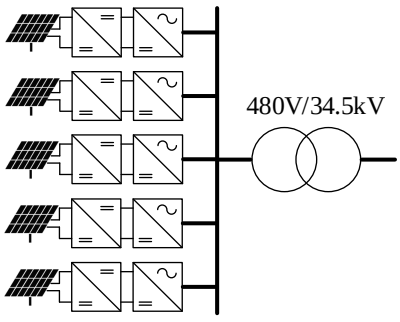

Fig. A17.3-3: Configuration of multiple PV systems through a distribution transformer.

The dynamics of the PV system are provided by the following DAEs, in addition to DAEs **Error! Reference source not found.**) to **Error! Reference source not found.**):

$$v_{j,grid}^{p(s)} = \frac{n_s}{n_p} v_{j,grid}^{p} \tag{A17.3-27}$$

$$L_{1s} \frac{d\sum_k i_{j,ac,fil}^{k}}{dt} + L_{1p}^{(s)} \frac{di_{j,grid}^{P(s)}}{dt} = -R_{1s} \sum_k i_{j,ac,fil}^{k} - R_{1p}^{(s)} i_{j,grid}^{p(s)} + v_{j,grid}^{(s)} - \frac{n_s}{n_p} v_{j,grid}^{p} \tag{A17.3-28}$$

$$v_{j,grid}^{p(s)} = \frac{n_s}{n_p} v_{j,grid}^{p} \tag{A17.3-29}$$

$$L_{1s} \frac{d\sum_k i_{j,ac,fil}^{k}}{dt} + L_{1p}^{(s)} \frac{di_{j,grid}^{P(s)}}{dt} = -R_{1s} \sum_k i_{j,ac,fil}^{k} - R_{1p}^{(s)} i_{j,grid}^{p(s)} + v_{j,grid}^{(s)} - \frac{n_s}{n_p} v_{j,grid}^{p} \tag{A17.3-30}$$

$$L_m^s \frac{d\sum_k i_{j,ac,fil}^{k}}{dt} + \left(L_{1p}^{s} + L_m^s\right) \frac{di_{j,grid}^{P(s)}}{dt} = R_{1p}^{(s)} i_{j,grid}^{p(s)} + \frac{n_s}{n_p} v_{j,grid}^{p} \tag{A17.3-31}$$

Transformer Model

High-fidelity transformer models of distribution and power transformers may be needed to capture the high-frequency response of transformers during start-up transients or in use cases where high-frequency components in voltages/currents are observed. Two of the common types of distribution transformers in PV systems include the three-phase, three-ferromagnetic-core transformer and the three-phase, single ferromagnetic core transformer (distribution transformer). All aforementioned transformers exhibit nonlinear behavior, which must be studied to develop a high-frequency, high-fidelity model of the transformer. The nonlinear behavior of these transformers may be identified in the following: ac resistance, magnetic field intensity–flux density dependence, and magnetic flux density–frequency dependence. Fig. A17.3-26 shows these nonlinear characteristics.

For the purposes of setting up the model, the three-phase single ferromagnetic core transformer shown in Fig. A17.3-27 is studied. The absence of the data on the nonlinear characteristics of the magnetic field intensity and density of the distribution transformer has led to the experimental setup shown in Fig. A17.3-28. The setup is used to characterize the nonlinearities in a single-phase transformer that have been shown in Fig. A17.3-26(b) and Fig. A17.3-26(c).

Existing data on the nonlinear behavior of the grain-oriented silicon steel is used in the distribution transformers (Fig. A17.3-29). To further extrapolate this data to introduce

higher frequency characteristics, characterization of the silicon steel used in the distribution transformer needs to be performed up to approximately several kHz.

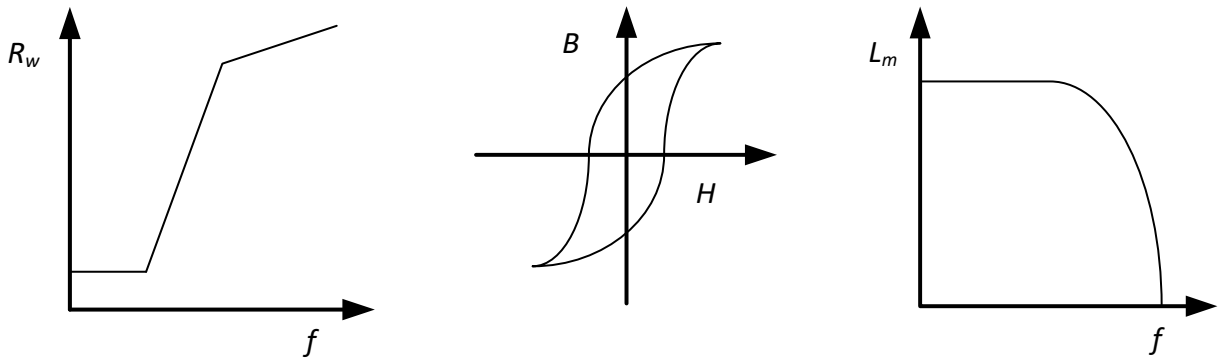

Fig. A17.3-26: Nonlinear behavior of the transformer with a ferromagnetic core.

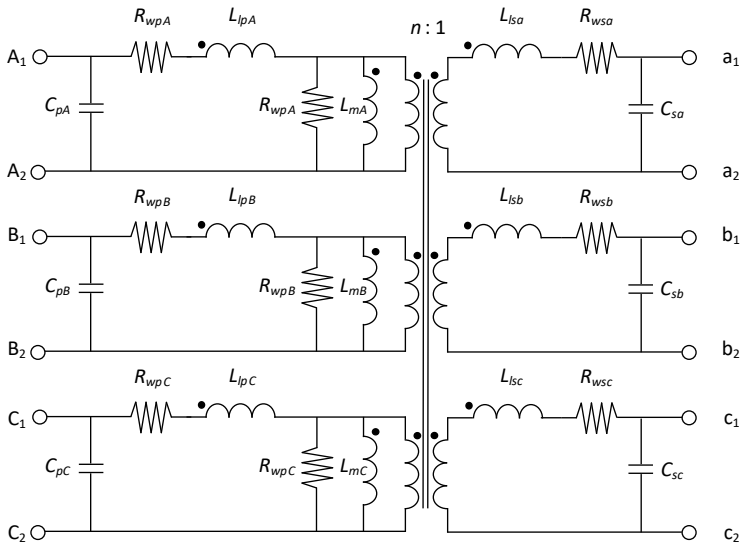

Fig. A17.3-27: Three-phase, single ferromagnetic core transformer.

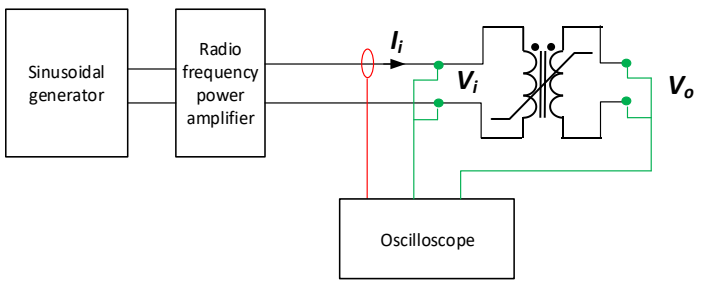

Fig. A17.3-28: Measurement setup for magnetic field intensity and density nonlinear dependencies.

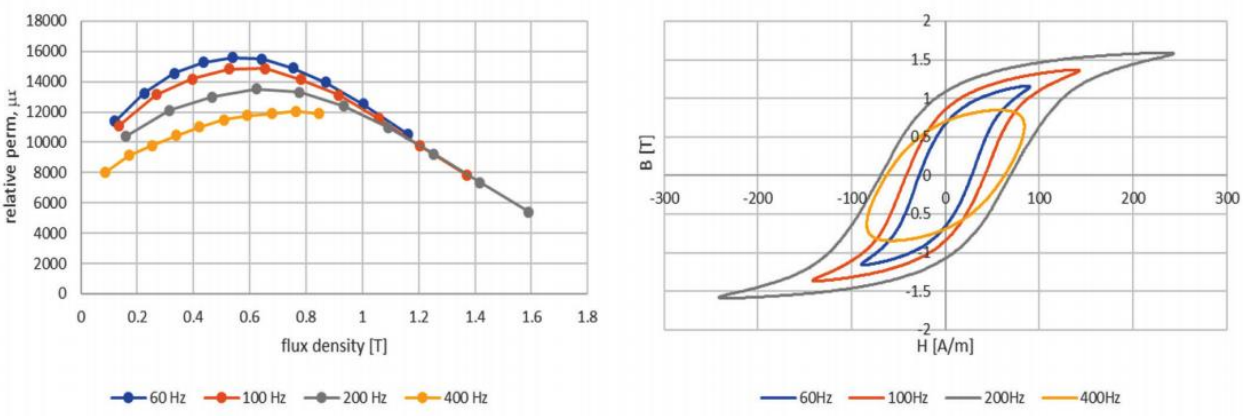

(a) (b)

Fig. A17.3-29: (a) Relative permeability as a function of flux density and frequency and (b) *BH* loops at different frequencies.

The small signal analysis of the transformer built with 0.35 mm grain-oriented steel is performed. The impedance of the transformer is measured up to 1 MHz. The primary-side inductance as a function of frequency is shown in Fig. A17.3-30. It may be observed that the inductance decreases with an increase in frequency.

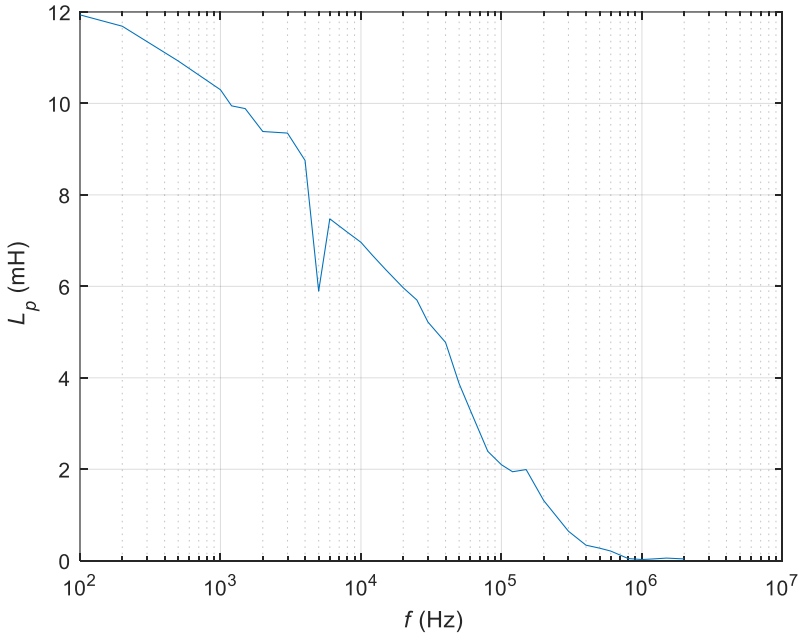

Fig. A17.3-30: Small signal primary side inductance as a function of frequency.

The conventional dynamic model of a transformer is based on the lumped T-type model shown in Fig. A17.3-31(a). This dynamic model does not consider that the permeability of magnetic material varies with frequency, and as a result, inductance varies with frequency. In these models, inductance is a constant calculated based on a constant permeability. As can be seen from Fig. A17.3-29(a) and Fig. A17.3-30, the relative permeability and inductance are not constants over a frequency range. Because these

variations are not captured by the lumped T-type model, certain high-frequency behavior of transformers may not be adequately captured.

To incorporate this behavior in the dynamic models, an updated model as shown in Fig. A17.3-31(b) and (c) may be used. In Fig. A17.3-31(b), the nonlinear magnetic material is approximated using a second- order filter (LC). The primary and secondary sides' inductances are modeled. Unfortunately, the mutual inductance is not frequency-dependent, thus discrepancies in permeability and inductance estimation at medium-range frequencies may occur. Additionally, some magnetic materials may not be modeled using the low pass filter approach. Another approach is to use the transfer function to model the nonlinear magnetic material, as shown in Fig. A17.3-31(c).

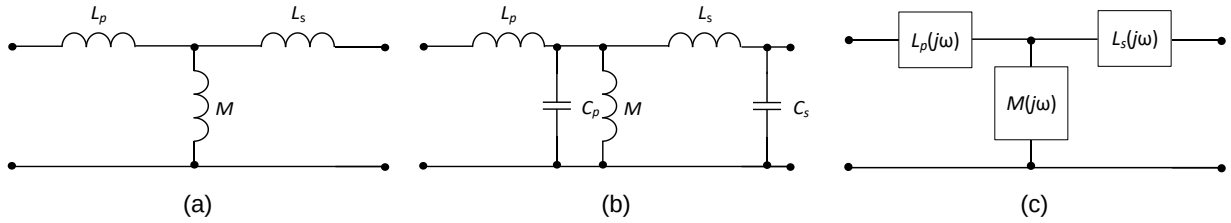

Fig. A17.3-31: Transformers models: (a) lumped parameter model, (b) LC filter equivalent circuit model, and (c) transfer function model.

The large signal measurements of the magnetic permeability of the M6 steel using a Brockhaus MPG200 measuring unit are shown in Fig. A17.3-32. The approximation of the relative series M6 steel permeability using the least mean square algorithm to generate the dependence of relative permeability as a function of frequency at B = 0.8 T is given by

$$\mu_{rs} = \frac{8693.1}{1 + {}^{f}/_{600}} \qquad \text{(A17.3-32)}$$

The choice of B = 0.8 T arises from the typical flux density where the transformers operate.

Implementation of the series-relative magnetic permeability approximation, given by equation (A17.3-33) into the simulation of the transformer in the form of transfer functions shown in Fig. A17.3-31, allows for capturing the frequency dependence of the mutual inductance in the transformer and its corresponding influence on the response. The simulated transfer functions (V_O/V_I) of the transformers with 1:2 turns ratio using a fixed values model, LC second-order approximation, and transfer function approximation of the magnetic permeability are shown in Fig. A17.3-33. In comparison to the transfer functions of the simulated transformers, the LC approximation underestimates the transfer function of the transformer, and the fixed inductance model overestimates the transfer function. Therefore, for some magnetic materials at higher frequencies, the LC approximation may underestimate the response of the transformer, and as a result may damp higher-frequency components much more than the transformer actually would damp those components. Conversely, a fixed-value model will underdamp the high-frequency components.

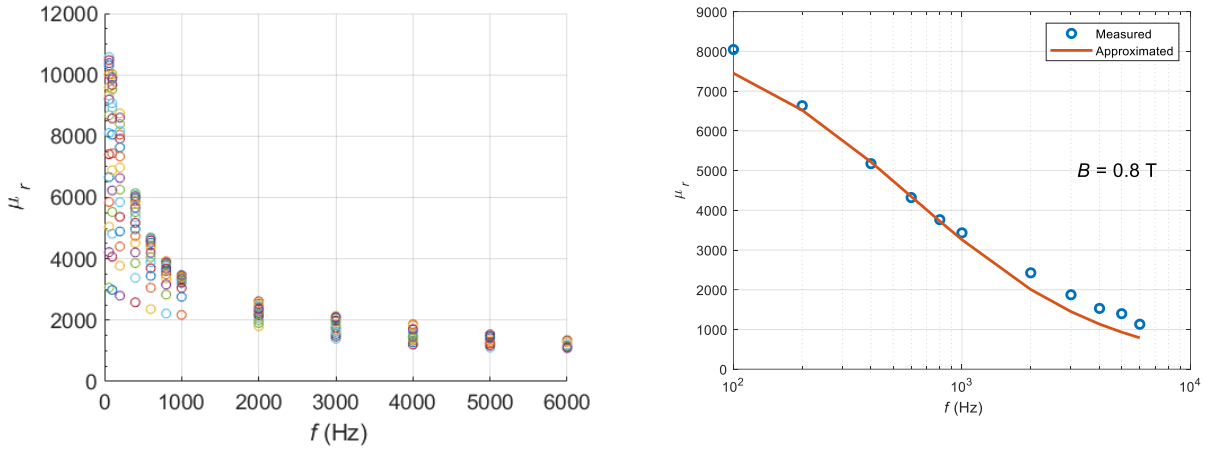

(a) (b)

Fig. A17.3-32: Large signal measurements of the real part of magnetic permeability of the M6 steel: (a) magnetic permeability as a function of frequency at different flux densities 0.1–1.6 T; (b) magnetic permeability as a function of frequency at flux density B = 0.8 T and its approximation using transfer function.

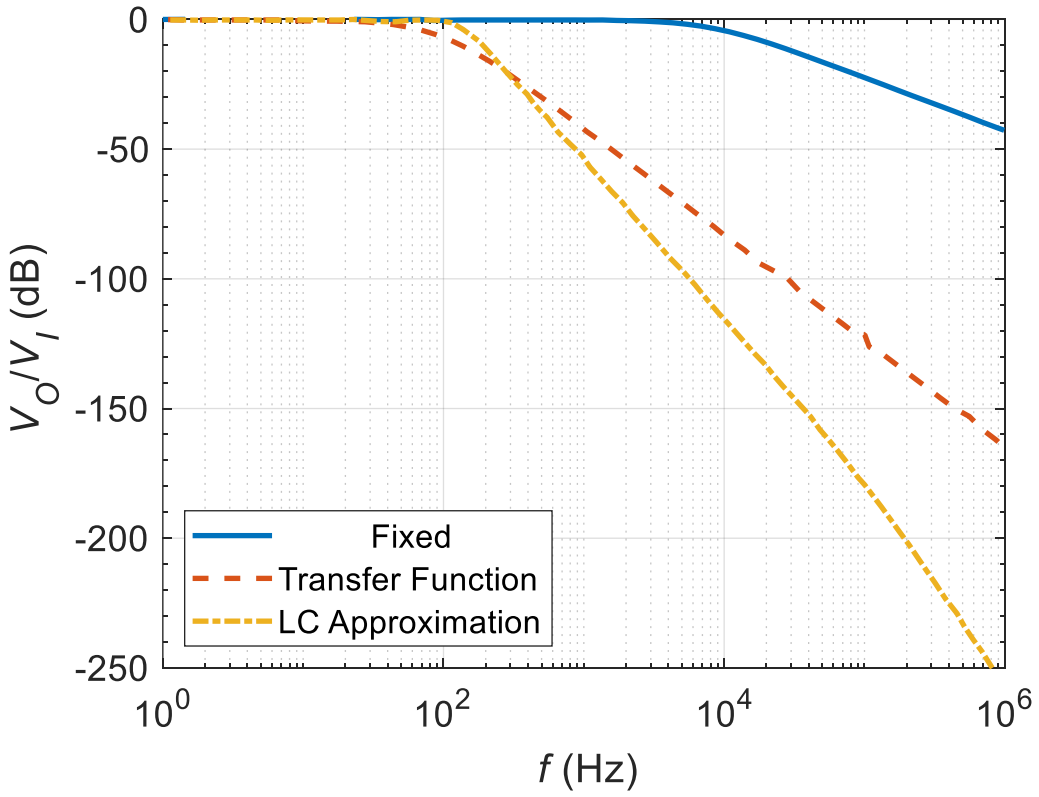

Fig. A17.3-33: Comparison of the simulated transfer functions (V_O/V_I) of the transformers with 1:2 turns ratio using fixed values model, LC second-order approximation, and transfer function approximation of the magnetic permeability.

Different Inverter Models (from different vendors): In addition to two-level inverters, the three-level NPC has been modeled. The overall circuit diagram of the NPC is shown in Fig. A17.3-34. The NPC is directly connected to the PV modules on the direct current side.

One of the main differences between a two-level voltage source converter and the NPC is the number of voltage levels the circuit can synthesize. In the case of NPC, it is three (-Vdc/2, 0, +Vdc/2), and in the case of two-level voltage source converter, it is two (Vdc, -Vdc). This is possible owing to the diode bridge clamped to capacitors C_1 and C_2 in Fig. A17.3-34. In this model, the NPC is connected to the grid via the LC filter. The capacitors in the LC filter are delta configured, as shown in Fig. A17.3-35.

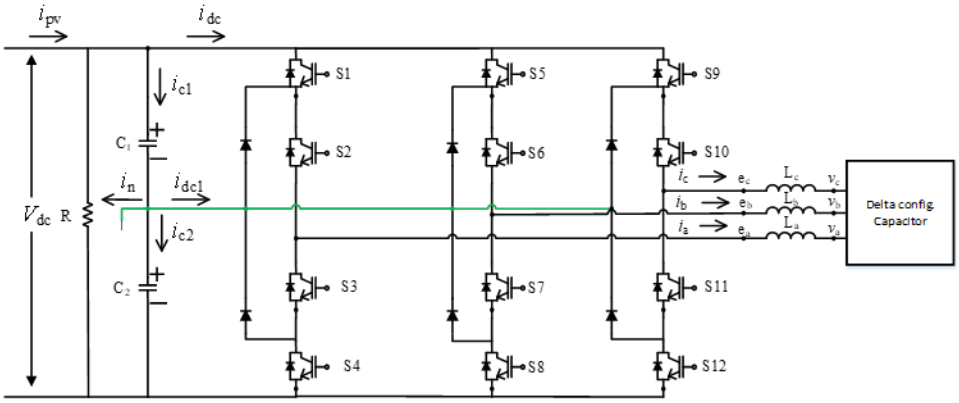

Fig. A17.3-34: Circuit diagram of NPC.

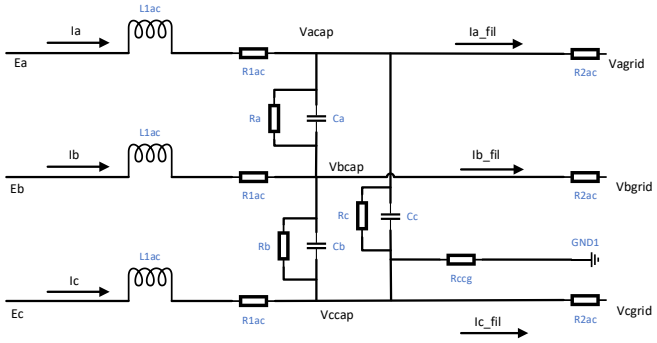

Fig. A17.3-35: Delta configuration of capacitors in LC filter.

Based on Fig. A17.3-34, the dc-link capacitor voltage dynamics, the phase-*j* inductor currents' dynamics through the inductor, and the phase-*j* ac filter capacitor voltage dynamics through delta-configured capacitors are given in equations **Error! Reference source not found.** to **Error! Reference source not found.**.

$$i_{pv} = \frac{v_{dc}}{R} + i_{c1} + i_{dc}\ ;\ C_1\frac{dV_{c1}}{dt} = \ i_{pv} - \frac{v_{dc}}{R} - i_{dc} \qquad \text{(A17.3-13)}$$

$$i_{c1} = i_{c2} + i_{dc1} + i_n; i_{c2} = i_{c1} - i_{dc1} - i_n\ ; \qquad \text{(A17.3-34)}$$

$$C_2\frac{dV_{c2}}{dt} = \ i_{pv} - \frac{v_{dc}}{R} - i_{dc} - \ i_{dc1} - i_a - \ i_b - i_c \qquad \text{(A17.3-35)}$$

$$\begin{aligned} i_{dc} = {} & (S1)(S2)(1-S3)(1-S4)i_a + (S5)(S6)(1-S7)(1-S8)i_b \\ & + (S9)(S10)(1-S11)(1-S12)i_c \\ & + (1-S1)(1-S2)(1-S3)(1-S4)sgn(i_a)i_a \\ & + (1-S5)(1-S6)(1-S7)(1-S8)sgn(i_b)i_b \\ & + (1-S9)(1-S10)(1-S11)(1-S12)sgn(i_c)i_c \end{aligned} \qquad \text{(A17.3-16)}$$

with $sgn(x) = \begin{cases} -1 & x < 0 \\ 0 & x > 0 \end{cases}$

$$i_{dc1} = (S2)(S3)(1-S1)(1-S4)i_a + (S6)(S7)(1-S5)(1-S8)i_b + (S10)(S11)(1-S9)(1-S12)i_c \quad \text{(A17.3-17)}$$

$$L_j \frac{di_j}{dt} = e_j - v_j;\ j \in (a,b,c) \quad \text{(A17.3-36)}$$

$$i_a = \frac{V_a - V_b}{R_a} + C_a \frac{d(V_a - V_b)}{dt} + \frac{V_a - V_c}{R_c} + C_c \frac{d(V_a - V_c)}{dt} + \frac{V_a - V_{agrid}}{R2ac} \quad \text{(A17.3-19)}$$

$$i_b = \frac{V_b - V_c}{R_b} + C_b \frac{d(V_b - V_c)}{dt} + \frac{V_b - V_a}{R_a} + C_a \frac{d(V_b - V_a)}{dt} + \frac{V_b - V_{bgrid}}{R2ac}$$

$$i_c = \frac{V_c - V_b}{R_b} + C_b \frac{d(V_c - V_b)}{dt} + \frac{V_c - V_a}{R_a} + C_a \frac{d(V_c - V_a)}{dt} + \frac{V_c - V_{cgrid}}{R2ac} + \frac{V_c}{R_{ccg}}$$

From the system of DAEs given in equations **Error! Reference source not found.** to **Error! Reference source not found.**, the current dynamics and phase-*j* capacitor voltage dynamics in **Error! Reference source not found.**–**Error! Reference source not found.** are discretized using the backward Euler method, and the capacitor dynamics in **Error! Reference source not found.**–**Error! Reference source not found.** are discretized using the forward Euler method. The discretization is based on the numerical stiffness exhibited by the states represented in the dynamics. The model is being tested and evaluated.

Event-Driven Interpolation Method

The developed NPC models along with the controller are implemented in a PSCAD Fortran environment. The key challenge identified in this work is to ensure the capacitor voltages across capacitors C_1 and C_2 in Fig. A17.3-34 are accurately simulated when operated at higher simulation time steps. When the NPC models are simulated at 1 µs in a PSCAD Fortran environment, it was observed that the capacitor voltages are not accurately simulated. The minimum time step to ensure accurate simulation of capacitor voltages was 0.01 µs, which is a time-consuming process. Therefore, an event-driven interpolation method has been proposed and implemented on capacitor voltages and associated states. With the implementation of the proposed method, the capacitor voltages are simulated at 1 µs in a PSCAD Fortran environment. The main step in the proposed interpolation method is to identify the time duration at which the switching signals change for the non-integer values of a simulation time step.

Simulation Results

The capacitor voltages, grid voltages, and currents without the proposed interpolation method in the NPC model are shown in Fig. A17.3-36. Capacitor voltages, grid voltages, and currents with the proposed interpolation method are shown in Fig. A17.3-37. Comparing capacitor voltages from Fig. A17.3-36(a) and Fig. A17.3-37(a), it is observed that by implementing the event-driven interpolation method, the capacitor voltages are more stable and accurate (and similar to the PSCAD library models). Also,

from Fig. A17.3-36(b)–(c) and Fig. A17.3-37(b)–(c), it can be observed that the grid voltages and currents are stable and accurate.

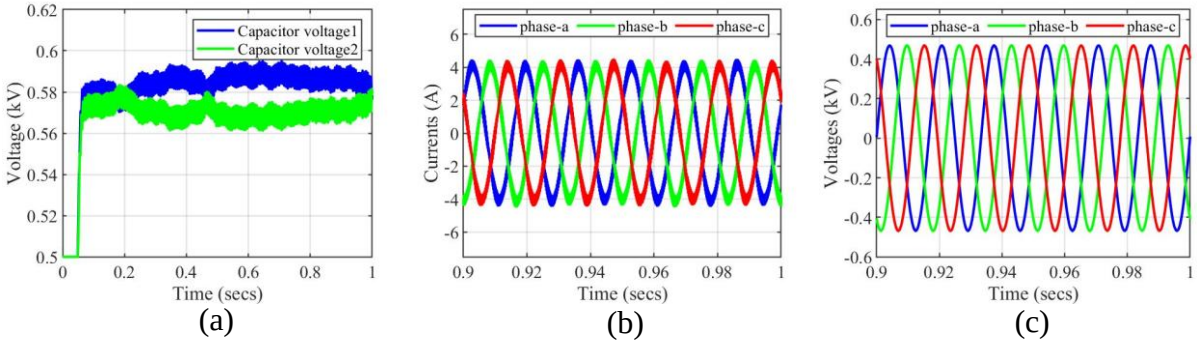

Fig. A17.3-36: Without the interpolation method implementation: (a) capacitor voltages, (b) phase-*j* grid currents, and (c) phase-*j* grid voltages.

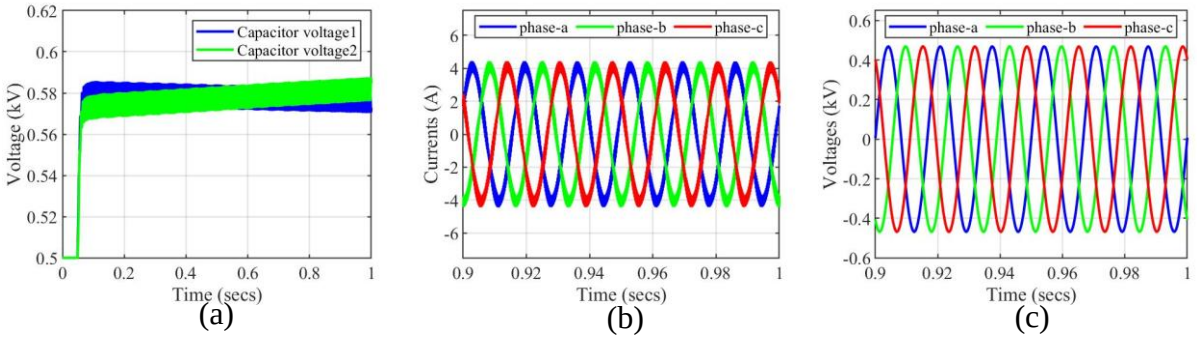

Fig. A17.3-37: With the interpolation method implementation: (a) capacitor voltages; (b) phase-*j* grid currents; and (c) phase-*j* grid voltages.

Multirate Control of Two-Level PV Inverter Model

The goal of implementing multirate control in the two-level PV inverter model is to transition from a single time step to a multiple time step PV inverter model. Transitioning to a multirate control will ensure that the functioning of digital controllers simulated in PSCAD/EMTDC software is emulated as in practical controller implementations (where it is sampled at a rate different from that of the simulation time step). In this subtask, the dc-dc converter control, dc-ac converter control, and custom developed high-fidelity EMT dynamic model of a two-level inverter model are simulated at 100 µs, 100 µs, and 1 µs, respectively. In the baseline two-level PV inverter model, all the components are simulated at 1 µs. The multirate control is implemented using FORTRAN in a PSCAD environment, whereas the baseline two-level PV inverter model is implemented using generic library models in a PSCAD environment. The multirate implementation of a dc-dc converter and a dc-ac converter control is shown in Fig. A17.3-38. A similar concept is implemented on the two-level converter and NPC.

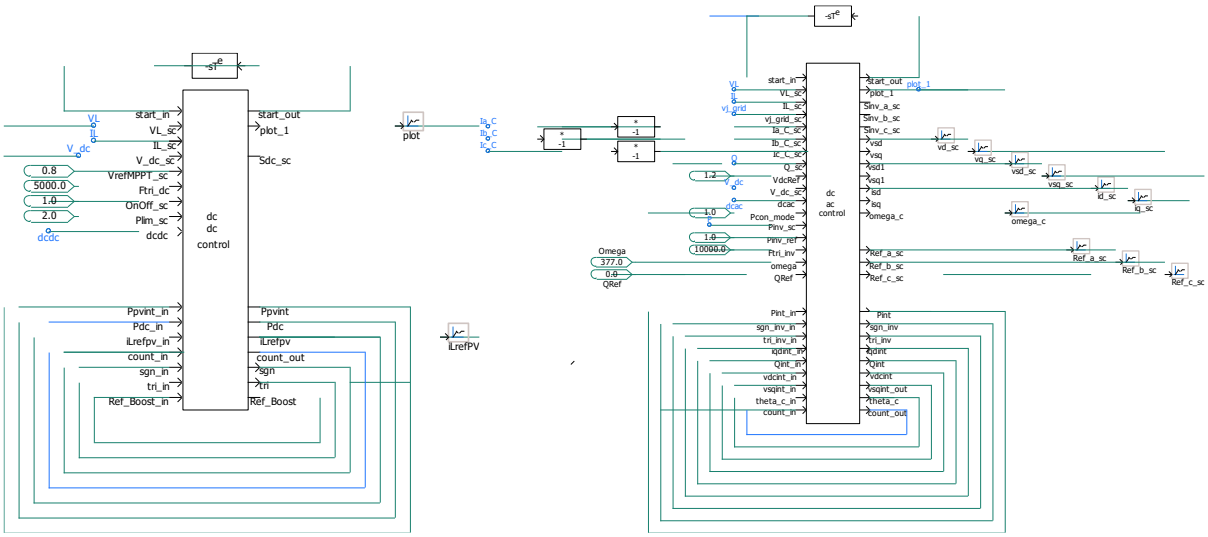

Fig. A17.3-38: FORTRAN implementation of dc-dc (left) and dc-ac (right) converters.

Simulation Results: The quantities such as dc bus voltage, dc-dc converter input capacitor voltage, dc-dc converter current, and distribution grid load currents in the PV system are shown in Fig. A3.2-17. The results indicate stable system operation.

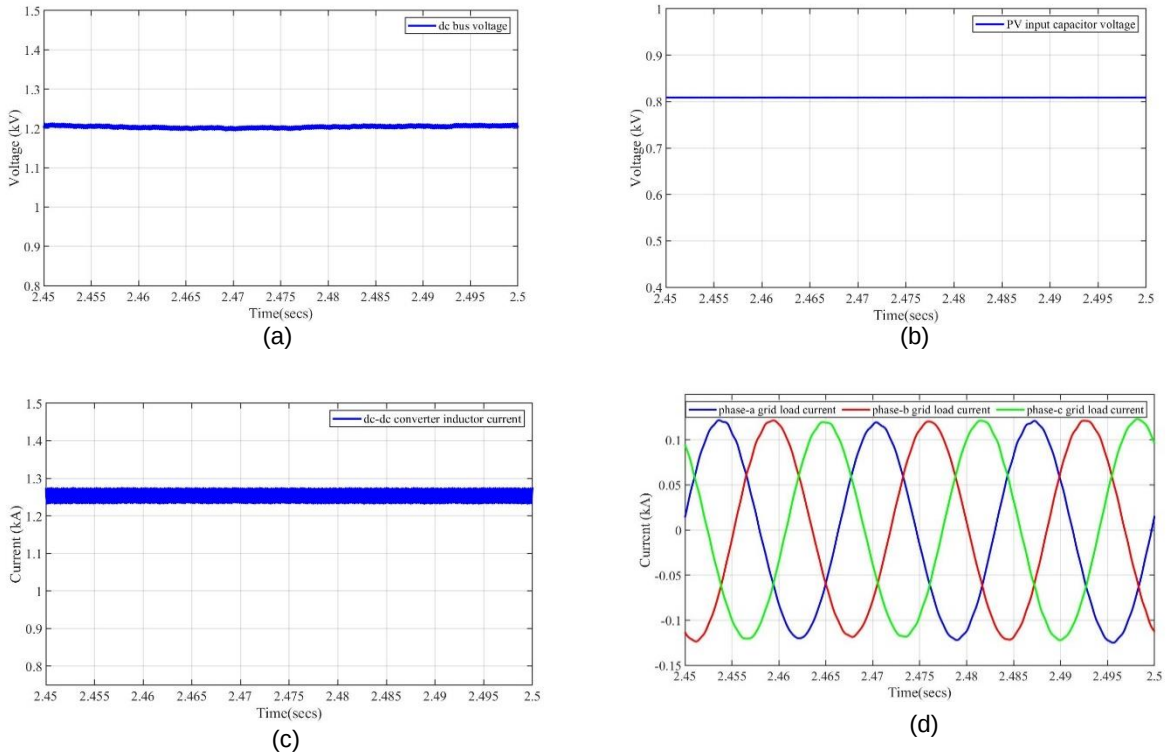

Fig. A17.3-17: PV dc-dc converter and dc-ac inverter: (a) 1.2 kV dc bus voltage, (b) 0.8 kV PV input capacitor voltage, (c) dc-dc converter inductor, and (d) distribution grid load currents.

Multiple A Matrix Method

EMT simulation time for a large grid increases as the number of nodes in the grid increases. Because the size of the A matrix (upon separation, discretization, and linearization) can create a bottleneck in the computation as the size of the grid increases, a matrix splitting method is applied to decrease the size of the A matrix by dividing the MV distribution system into multiple subsystems with similar dynamics. For example, the MV distribution system can be divided into six subsystems consisting of five radial feeders and a collector bus (called a multiple A matrixes method). When dividing the MV distribution system into subsystems to split the A matrix, a single time step delay is introduced in the transferred states between the subsystems. To prevent numerical instability from the single delayed states, small capacitors are added to the terminal nodes of each subsystem to reduce a rapid change with the delayed states.

Kron's Reduction Method

EMT simulation time for a large distribution system increases as the number of nodes in the grid increases. Because the A matrix size can create a bottleneck in the computation, the Schur complement technique was applied to decrease the size of the inverted matrix. This avoids the single time step delay with the multiple A matrix case study shown earlier. Therefore, no additional capacitors are needed to prevent numerical instability from the single time step delay. A general form of A**x**=**b** for a distribution grid can be expressed by an arrowhead matrix, also known as a bordered matrix. The A matrix is filled with the first row of border, the first column of border, and diagonal block terms. The rest of the A matrix is filled with 0 element.

$$\begin{bmatrix} A_{11} & A_{12} & \dots & A_{1n} \\ A_{21} & A_{22} & \dots & 0 \\ \vdots & \vdots & \ddots & \vdots \\ A_{n1} & 0 & \dots & A_{nn} \end{bmatrix} \begin{bmatrix} \boldsymbol{x_1} \\ \boldsymbol{x_2} \\ \vdots \\ \boldsymbol{x_n} \end{bmatrix} = \begin{bmatrix} \boldsymbol{b_1} \\ \boldsymbol{b_2} \\ \vdots \\ \boldsymbol{b_n} \end{bmatrix}$$

Where, $A_{11} = \begin{bmatrix} a_{11} & \cdots & a_{1k} \\ \vdots & \ddots & \vdots \\ a_{k1} & \cdots & a_{kk} \end{bmatrix}, A_{ii} = \begin{bmatrix} a_{11} & \cdots & a_{1m} \\ \vdots & \ddots & \vdots \\ a_{m1} & \cdots & a_{mm} \end{bmatrix}, A_{1j} = \begin{bmatrix} a_{11} & \cdots & a_{1m} \\ \vdots & \ddots & \vdots \\ a_{k1} & \cdots & a_{km} \end{bmatrix}, A_{j1} = \begin{bmatrix} a_{11} & \cdots & a_{1k} \\ \vdots & \ddots & \vdots \\ a_{m1} & \cdots & a_{mk} \end{bmatrix}, \boldsymbol{x}_i = \begin{bmatrix} x_1 \\ \vdots \\ x_{k\ or\ m} \end{bmatrix}, \boldsymbol{b_i} = \begin{bmatrix} b_1 \\ \vdots \\ b_{k\ or\ m} \end{bmatrix}.$

To partition the A matrix that needs to be inverted, it can be rewritten by each row as shown in the following equations. The size of the partitioned matrix depends on the diagonal blocks that are determined by the radial feeder in the grid model.

$$A_{11}\boldsymbol{x_1}(kbyk * kby1) + A_{12}\boldsymbol{x_2}(kbym * mby1) + \cdots + A_{1n}\boldsymbol{x_n}(kbym * mby1) = \boldsymbol{b_1}(kby1) \quad \text{(A17.3-20)}$$

$$A_{21}\boldsymbol{x_1}(mbyk * kby1) + A_{22}\boldsymbol{x_2}(mbym * mby1) = \boldsymbol{b_2}(mby1) \quad \text{(A17.3-21)}$$

$$A_{n1}\boldsymbol{x_1}(mbyk * kby1) + A_{nn}\boldsymbol{x_n}(mbym * mby1) = \boldsymbol{b_n}(mby1) \quad \text{(A17.3-22)}$$

Equations **Error! Reference source not found.**) and **Error! Reference source not found.**) can be re-arranged for $\boldsymbol{x_2}$, then $\boldsymbol{x_2} = {A_{22}}^{-1}(\boldsymbol{b_2} - A_{21}\boldsymbol{x_1})$ and $\boldsymbol{x_n} = {A_{nn}}^{-1}(\boldsymbol{b_n} - A_{n1}\boldsymbol{x_1})$, respectively.

Substituting $\boldsymbol{x_2}$ and $\boldsymbol{x_n}$ in equation **Error! Reference source not found.**) yields

$$A_{11}\boldsymbol{x_1} + A_{12}{A_{22}}^{-1}(\boldsymbol{b_2} - A_{21}\boldsymbol{x_1}) + \cdots + A_{1n}{A_{nn}}^{-1}(\boldsymbol{b_n} - A_{n1}\boldsymbol{x_1}) = \boldsymbol{b_1} \quad \text{(A17.3-23)}$$

Equation **Error! Reference source not found.**) is solved for

$\boldsymbol{x_1} = \left(A_{11} - A_{12}{A_{22}}^{-1}A_{21} - A_{1n}{A_{nn}}^{-1}A_{n1}\right)^{-1}\left(\boldsymbol{b_1} - A_{12}{A_{22}}^{-1}\boldsymbol{b_2} - A_{1n}{A_{nn}}^{-1}\boldsymbol{b_n}\right)$. Once $\boldsymbol{x_1}$ is solved, then $\boldsymbol{x_2}$ and $\boldsymbol{x_n}$ can be solved from equations **Error! Reference source not found.**) and **Error! Reference source not found.**) with the solved $\boldsymbol{x_1}$.

Generic PV Plant Model with Multirate Control

The multirate control of the two-level inverter PV model is implemented in the generic PV plant. In this generic plant, the two-level inverter PV model consists of dc-dc converter control and dc-ac converter control simulated at 100 µs, and the PPC simulated at 1 s based on their respective control time steps. The electrical circuits in the PV plant model are simulated at 1 µs time step. The multirate controllers incorporated with the high-fidelity PV plant model are illustrated in Fig. A3.2-18 and Fig. A3.2-19. The dc-dc converter control consists of outer loop MPPT control and inner loop inductor current control that generate reference for the dc-dc converter switch. The dc-ac converter control consists of an outer voltage loop that generates current references for the inner loop dq current control. The phase modulation references are generated from the inner loop dq current control. The PPC consists of a fixed reactive power control loop, POC voltage control loop, and power factor control loop. This implementation mimics the real-code integration from the controllers, similar to the approach discussed in IEEE/CIGRE B4-82 on “Use of Real-Code in EMT Models.”

Simulation Results

The developed multirate control is tested in a generic PV plant that consists of 125 two-level PV inverter units with the rating of 125 MW. The use case identified for testing the developed multirate control is reduction of distribution grid voltage to 0.8 pu for a duration of 0.3 s. The following requirements are considered during testing of the PV plant model: (a) during the grid event resulting in voltage reduction, stable operation of the PV plant is feasible, and (b) the two-level PV inverter ceases to operate if the voltage of the dc bus goes beyond 1.5 pu.

The 1.2 kV bus voltage, 0.8 kV PV voltage, inductor current, distribution grid voltage, the inverter load currents, and the PV plant power under grid event and normal operating condition are shown in Fig. A3.2-20 and Fig. A3.2-21, respectively. From Fig. A3.2-20, the following observations are made during the voltage magnitude reduction: (a) the generated active power from the PV plant is reduced to 100 MW; (b) the 1.2 kV dc bus is maintained; (c) the inductor current is reduced to 0.8 kA; and (d) the PV voltage is maintained at approximately 0.915 kV. From Fig. A3.2-21, it is observed that the PV plant is in a stable mode of operation.

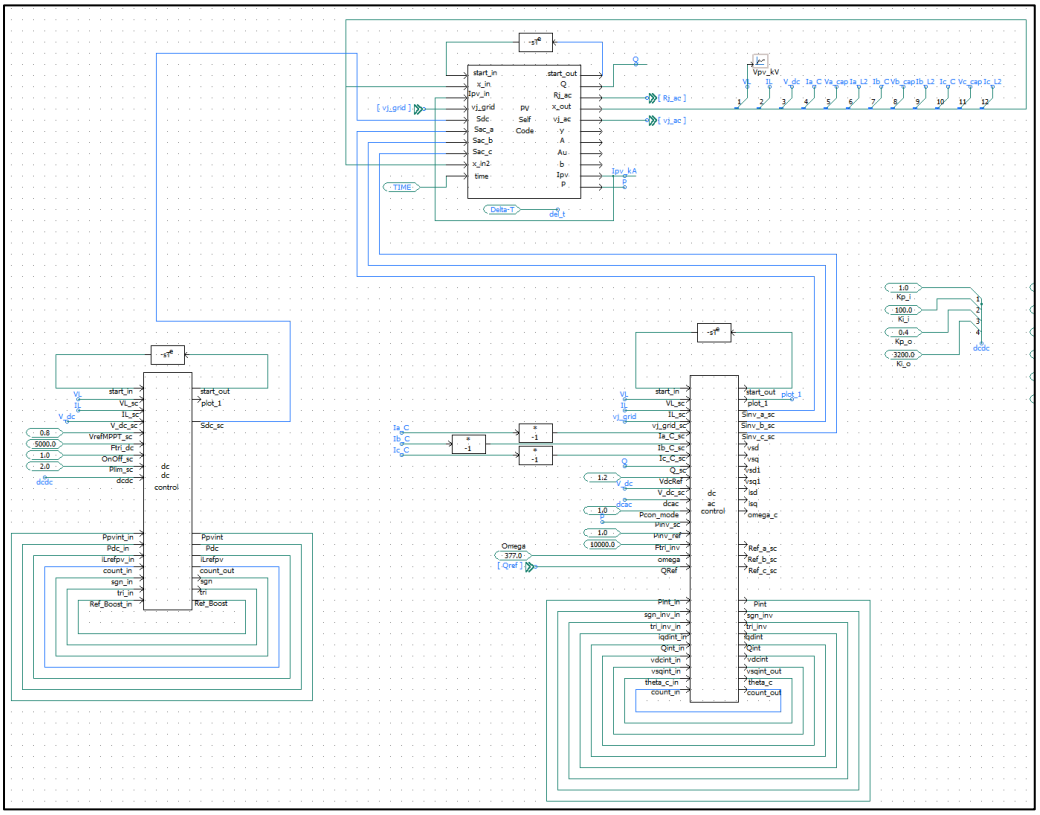

Fig. A17.3-18: High-fidelity PV inverter module with multirate converter/inverter controllers.

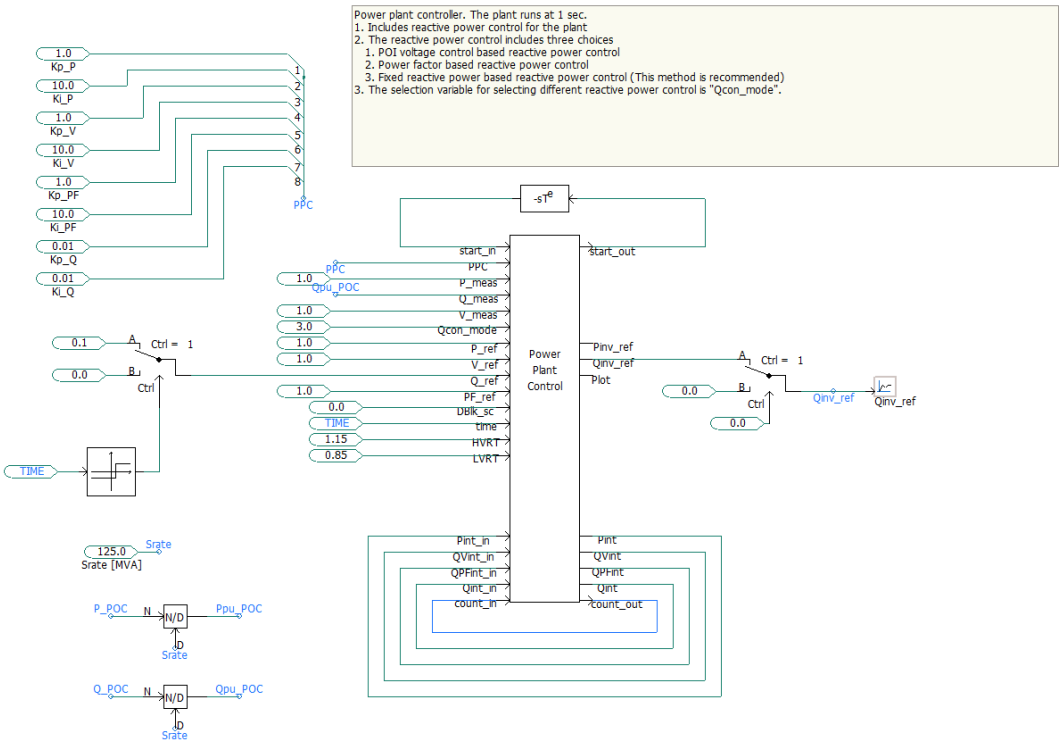

Fig. A17.3-19: High-fidelity PV plant model with multirate power plant controller.

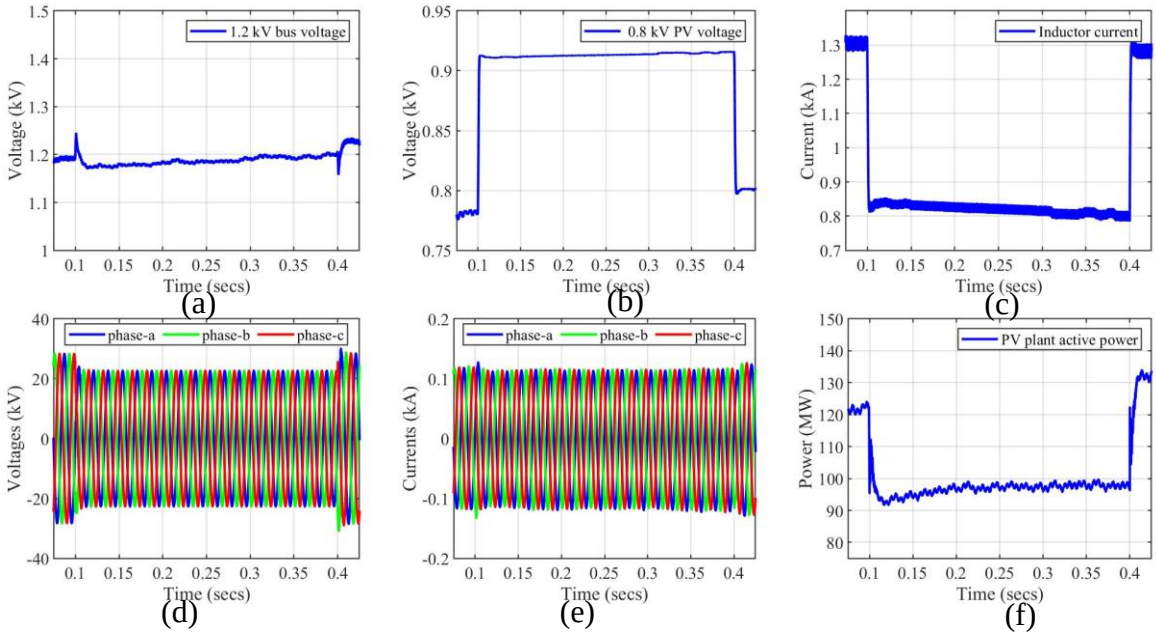

Fig. A17.3-20: PV plant states during the voltage reduction: (a)1.2 kV bus voltage; (b) 0.8 kV PV voltage; (c) inductor current; (d) distribution grid voltage; (e) inverter load currents; and (f) the PV plant power.

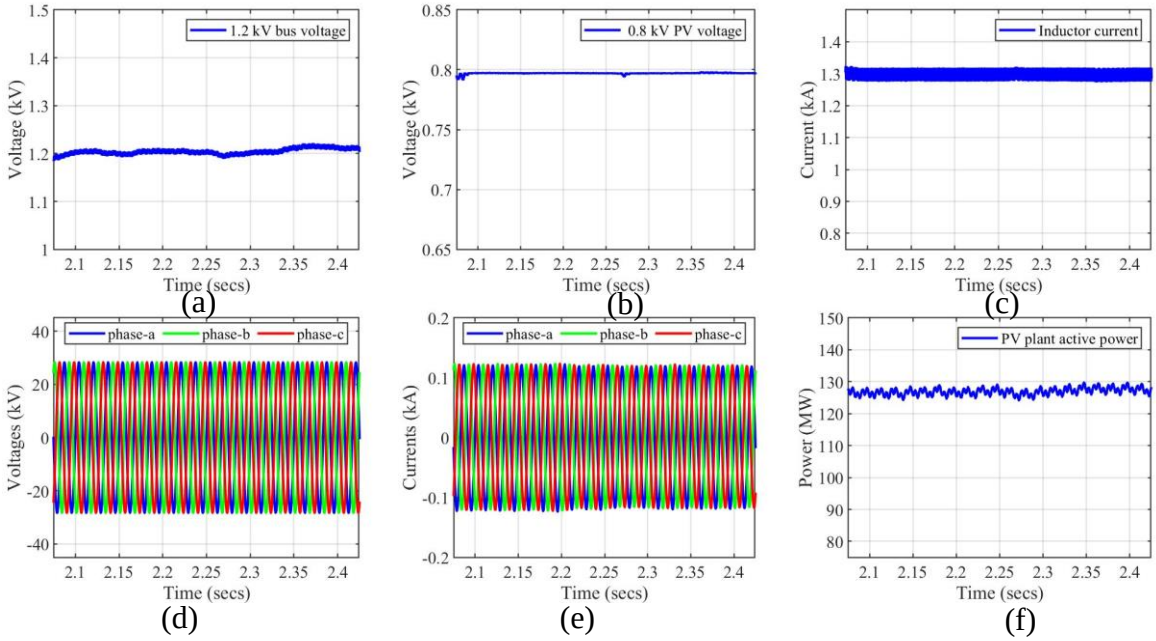

Fig. A17.3-21: PV plant states during normal operation: (a) 1.2 kV bus voltage; (b) 0.8 kV PV voltage; (c) inductor current; (d) distribution grid voltage; (e) inverter load currents; and (f) the PV plant power.

High-Fidelity Model for Specific PV Plant with Multirate Control

Along with a generic PV plant high-fidelity model, a high-fidelity model for the specific PV plant (from an actual plant in California) is developed in PSCAD. To develop the specific PV plant model, parameters of the PV plant such as overall layout, number of feeders, number of medium voltage lines, transformer parameters, inverter parameters,

PV array parameters, and other factors, were extracted and estimated. Based on the extracted parameters, a single A matrix model of the specific PV plant is developed. Because the PV plant consists of many feeders and inverters, modularization is applied to the plant model.

ST-3.3. Advanced model in PSCAD/PSSE

Whereas NARX-based models can be trained in MATLAB, the CNN-based models can be trained using the Keras package in Python. The architecture of the NARX model is shown in Fig. A3.3-39, and the architecture of the CNN model is shown in Fig. A3.3-2.

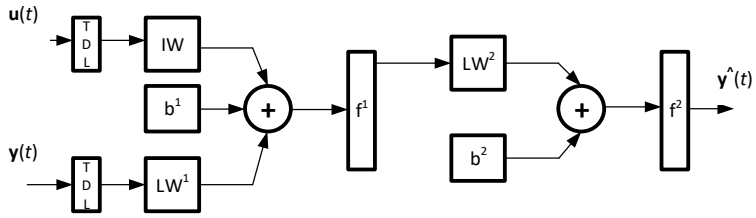

Fig. A3.3-39: NARX model.

NARX Model: The NARX model, an RNN model, consisting of a linear combination of inputs processed through a sigmoid activation function with two hidden layers is being considered. The number of hidden layers, the number of delayed inputs and outputs feeding into the model, and the activation function can vary.

CNN Model: A CNN model (shown in Fig. A3.3-2) consisting of convolutions, dropouts, and transpose of convolution is being considered for representing the dynamics of the PV plant. The activation function being considered is a rectified linear unit. The units considered such as convolution and transpose of convolution, activation function, and number of layers can vary.

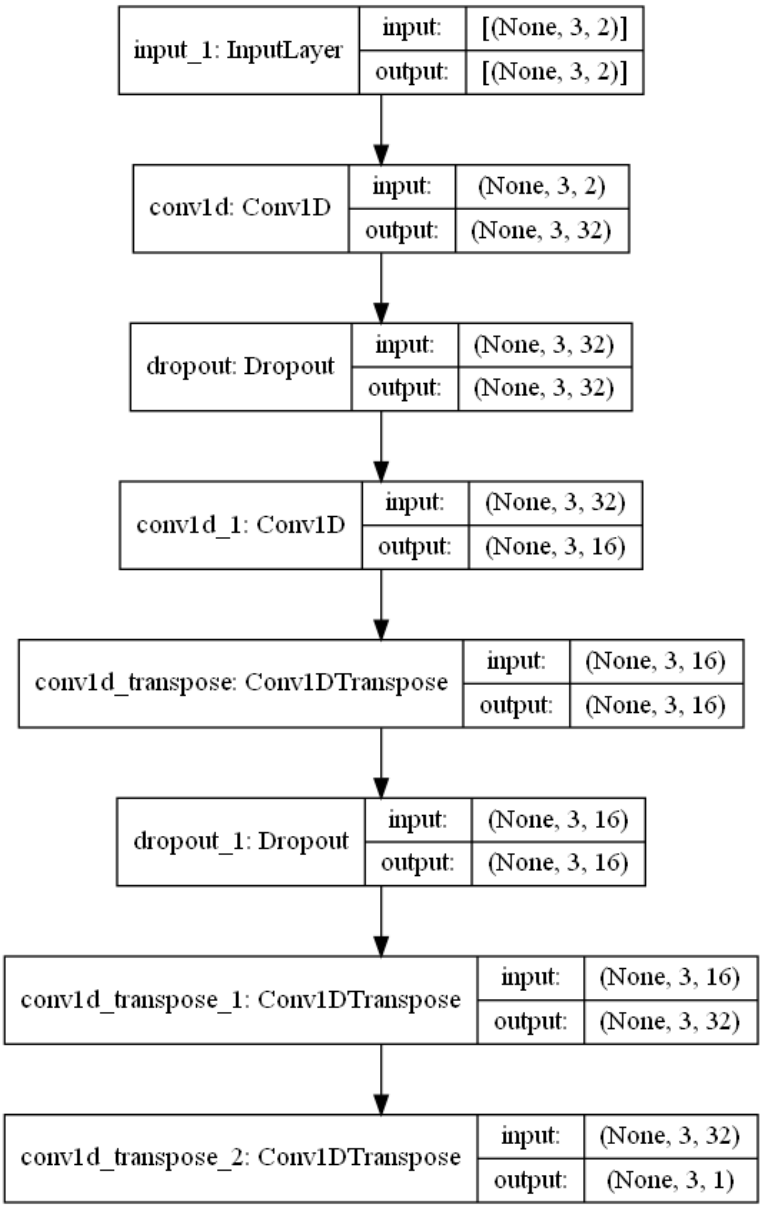

Fig. A3.3-2: CNN model.

T-4. Evaluation and redesign dynamic models

ST-4.1. Evaluation of quasi-dynamic model

A schematic of the test system is shown in Fig. A17.3-40. Representative results are provided in this section. An event of PV module output increase (solar irradiation input increase) from 0.2 MW to 0.35 MW starting at time 1.2 s and completed at time 1.5 s is simulated. The irradiation increase is considered as a ramp function. The output power, voltage, and current of the inverter module are shown in Fig. A17.3-41, and the simulation results of the ac-side of the converter and its controller are shown in Fig. A17.3-42. The output power from the inverter module increases from 0.2 MW to 0.35 MW.

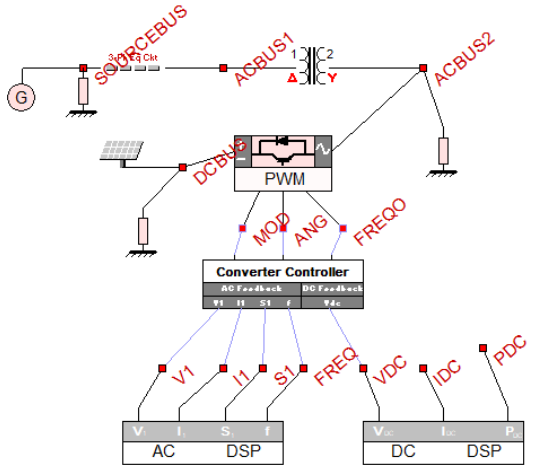

Fig. A17.3-40: Example test system.

Table A17.3-1: Parameters of the PV system.

ac-dc converter					
	Device name	**ac bus name**	**dc bus name**	**Rated ac/dc voltage (kV)**	**Rated power (MVA)**
1	Converter	ACBUS4	DCBUS	0.9/0.48	0.5
		ac capacitance (μF)	**ac inductance (mH)**	**Cut off frequency (Hz)**	**dc capacitance (μF)**
		31.66	0.20	2,000.0	16,000.0
Converter controller					
#	**Device name**	**Control setting**	**dc voltage reference (kV)**	**Reactive power reference (MVar)**	**Switching method**
1	Controller	Q-Vdc control	0.9	0.1	SPWM

SPWM = Sinusoidal PWM.

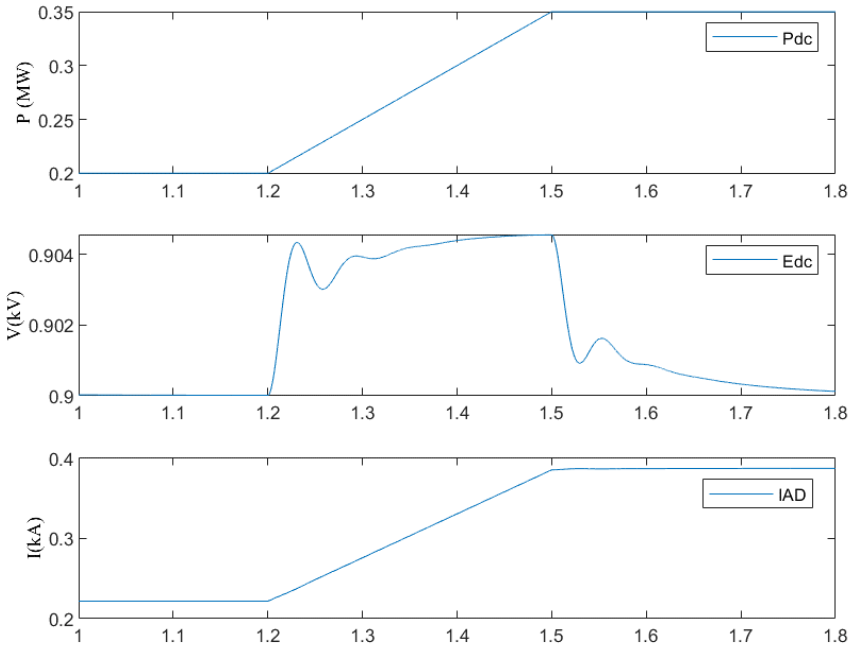

Fig. A17.3-41: Simulation results of the inverter module.

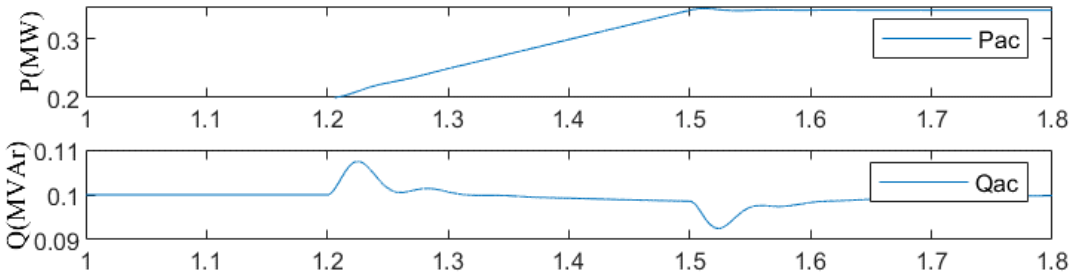

Fig. A17.3-42: Simulation results of the voltage source converter and its controller.

Comparison of the models to field data and corresponding PSCAD model

Field data from the Santa Fe facility are collected for 104 days. A sample of part of one day's data is shown in Fig. A17.3-43, including the irradiation level in the last trace of the figure.

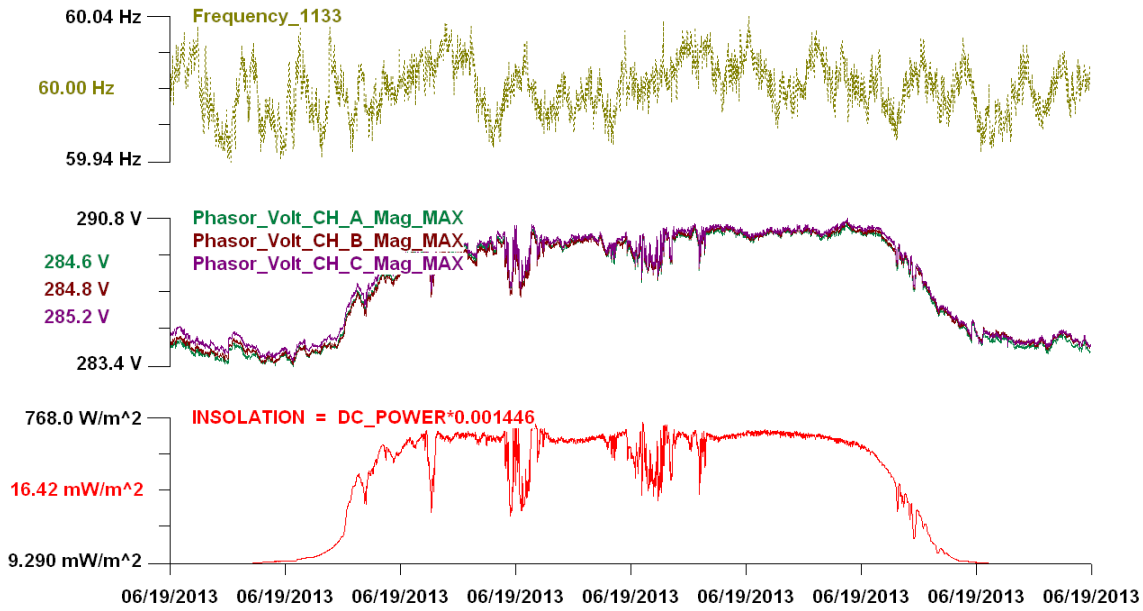

Fig. A17.3-43: Recorded data for 6/19/2013 from hour 06:00 to hour 21:00—(top) Trace 1: frequency; (middle) Trace 3: three-phase voltage magnitudes–inverter output; and (bottom) Trace 7: solar insolation.

These data are used to evaluate and validate the model. Specifically, the Santa Fe facility model has been developed in PSCAD. The PV plant is made up of two PV arrays/inverter systems connected to the same step-up transformer, which is rated 1.0 MVA and 13.8 kV/480 V. Each PV array rated 1,000 Vdc, 0.5 MW is connected to a 0.5 MVA, 1,000 Vdc/480 Vac inverter. The control of the inverter has been set at maximum power tracking.

A 480 s dataset with solar insolation and temperature inputs obtained from field data is used for simulation. The simulation results are compared to evaluate the simulation accuracy and computational speed of the quasi-dynamic domain model.

The magnitude and phase of the phase-*a* current and voltage simulation results are shown in Fig. A4.1-5 and Fig. A4.1-6. The errors of the current magnitude and voltage magnitude between the simulation of the baseline and quadratized models are about 5.0% and 0.05%. The error of the current magnitude is caused by the error of the active power. The phase angle differences of current and voltage between the simulation of the baseline and quadratized models are about 0.2° and 0.1°.

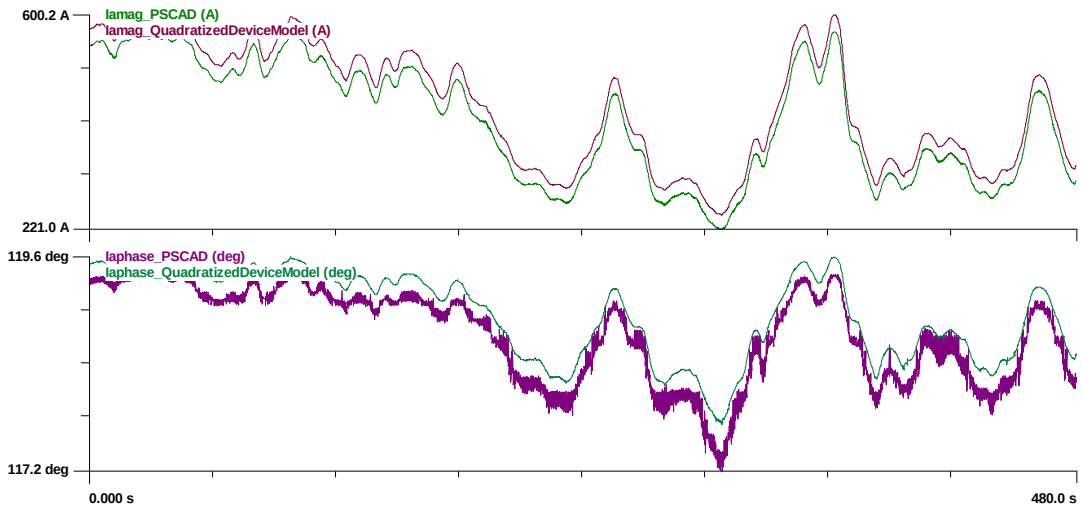

Fig. A17.3-5: The magnitude and phase of phase-*a* current of inverter 1 from simulation of baseline and quadratized models.

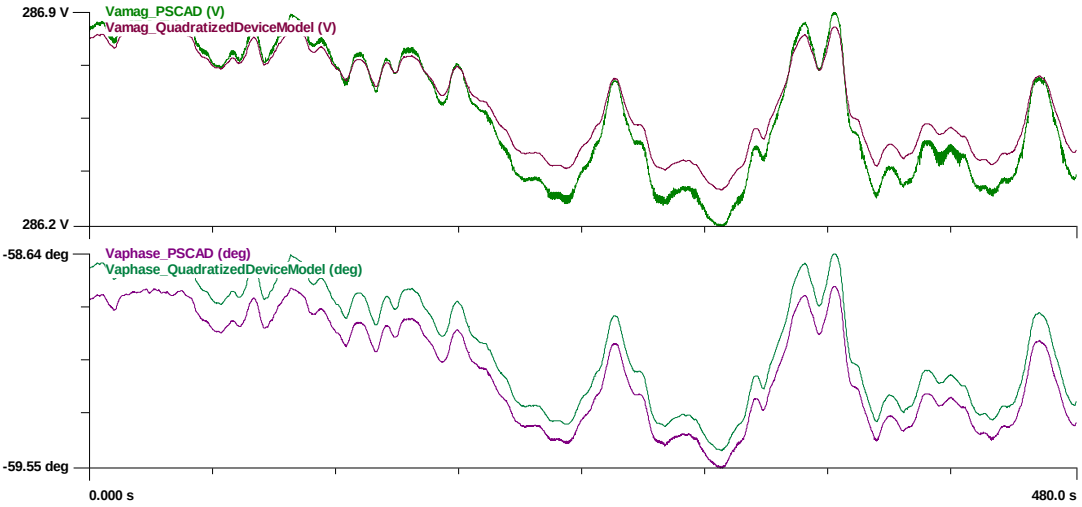

Fig. A17.3-6: The magnitude and phase of phase-*a* voltage of inverter 1 from simulation of baseline and quadratized models.

T-5. Present scenario development

ST-5.1. Develop dynamic (EMT-TS) model of present grid in PSCAD

Initialization Process: The PSSE load flow solution is used to set the initial RLC values of load. As shown in Fig. A17.3-, the power in the dialogue box corresponds to 1 pu voltage. The initial load RLC values are held for 0.2 s to give the PSCAD simulation adequate time to reach steady state. After 0.2 s, the “hold signal” in load parameters can be set to “1” to match the selected load characteristics. For this WECC scenario, the load characteristics are chosen as the following (in all the simulators):

1. Real part of the load is modeled as a constant current load.
2. Reactive part of the load is modeled as a constant impedance load.

For this scenario, the loads are initialized at t = 0.2 s, then the machines are initialized at t = 0.5 s (with exciters and governors initialized at 0.6 s and 0.7 s, respectively). Finally, the hybrid simulation interface starts at t = 1 s. In Fig. A17.3-, the real power drawn by a load in the WECC grid is shown during the hybrid simulation. When the hybrid interface starts, a small oscillation can be observed in real power, but this is negligible compared with the value of the power and does not affect the hybrid simulation.

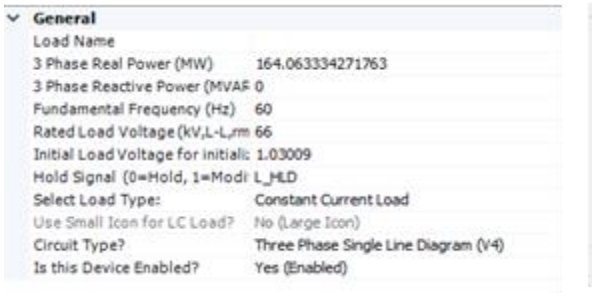

Fig. A17.3-1: Dialogue box for a load in PSCAD.

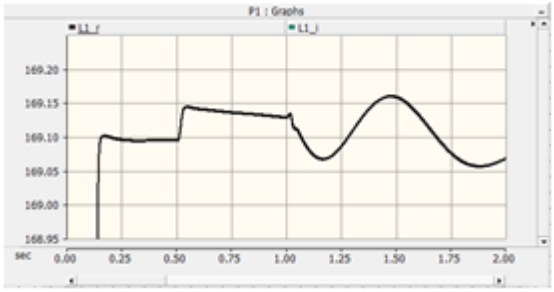

Fig. A17.3-2: Real power of a load modeled in PSCAD.

Hybrid test I: For hybrid simulation of the present WECC grid scenario, 18 buses are selected in E-Tran for conversion from PSSE to PSCAD. Among those 18 buses, 13 buses are completely modeled in PSCAD, and 5 buses are used as boundary buses between PSCAD and PSSE.

Next, a self-clearing three-phase fault is created in one bus, which is modeled in PSCAD. The results are compared in PSSE only, PSCAD only, and hybrid simulations. The generator speed is measured, the results are shown in Fig. A17.3-, and the corresponding power spectral analysis is shown in Fig. A17.3-. In addition, Prony analysis was used to estimate modal frequency and damping ratios from these signals, as summarized in Table A17.3-2.

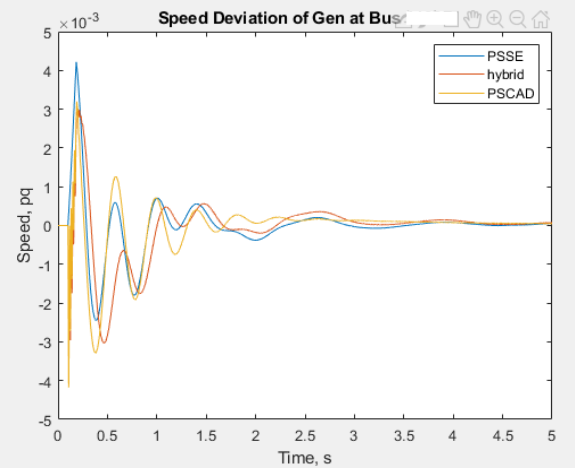

Fig. A17.3-3: Results for different simulations.

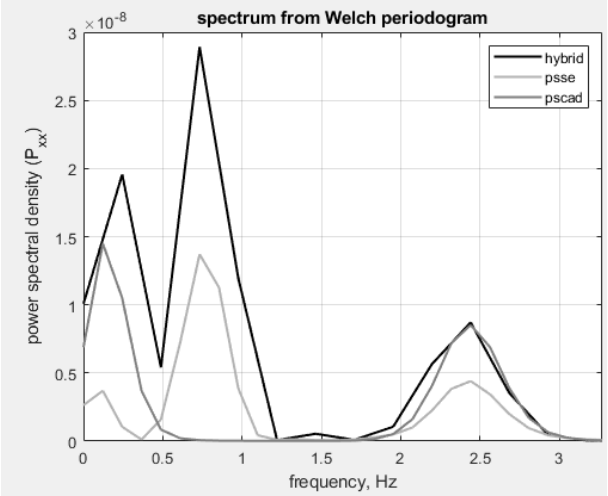

Fig. A17.3-4: Spectral analysis of generator speeds.

Table A17.3-2: Summary of modal estimation from generator speeds using Prony analysis

Frequency of mode (Hz) (Hybrid)	Damping	Frequency of mode (Hz) (PSSE)	Damping	Frequency of mode (Hz) (PSCAD)	Damping
0.7434	0.3524	0.7215	0.1782	—	—
2.5137	0.1041	2.2182	0.1982	2.3442	0.1283

Following are a few key observations from this hybrid simulation:

1. The modal frequency estimated from Prony analysis closely corresponds to the peaks in power spectral density.
2. The inter-area mode with 0.7434 Hz frequency observed from PSSE is not observed in PSCAD simulation because PSCAD considers only a small area of the WECC model (and hence, inter-area oscillations may not be observed).
3. The hybrid simulation reasonably retains the identity of the inter-area mode.

Methods used to map the solar plants in WECC:

Identifying PV plants from US Energy Information Administration (EIA) data in the WECC model cannot be performed using any standard approach. Therefore, the following assumptions and methods are used for identifying these plants:

1. The plants with renewable models (i.e., REGCAU1, WT4G1) in California region are identified in the dynamic data (.dyr file) of the WECC model. These models contain the dynamics of both solar and wind plants. Then, the possible wind plants are removed from the list by using the following attributes:
    - The plants include aerodynamic, pitch control, or mechanical models.
    - The bus name contains “WIND” or “WND.”

    The remaining plants include both REGCAU1 and WT4G1 models. Then, comparing the bus name of the WECC model and “utility name,” “plant name,” and “generator ID” in EIA data, the PV plants are identified. Next, the power ratings of plants in WECC and EIA data are compared. In most of the instances, the power ratings match exactly in both datasets. But there are also the following cases:
    - The differences in dates when the WECC model was developed and the EIA data were released. So it is possible that a few plants have undergone expansions.
    - Also, some plants have lower power ratings in the WECC model owing to possible retirements.

    These cases have been identified, and related comments have been documented for future reference.
2. In the WECC model, a few adjacent plants are found and collectively form a single solar farm or a collection of similarly named solar farms under the same utility name (also in the same county) in the EIA data sheet. In those cases, the sum of power ratings is comparable in the EIA data and the WECC model.
3. Few plants are identified from the location (county) and power rating information. All of those have renewable models in the dynamic data of the WECC model, and their power ratings are almost the same as the EIA data.
4. For a few plants in the EIA data, only buses with similar names were identified in the WECC model. But no plants with similar power ratings were found near that bus.

Using these methods, the aim was to map all the plants above 100 MVA from the EIA data to the WECC grid model. The identified plants were categorized into the following four types:

1. **Type 1**: Exact bus name match; renewable model is used for generator; power rating almost the same in EIA and WECC data (< 5%); color coded as green
2. **Type 1a**: Renewable model is used for generator; either exact bus name match or exact power ratings in EIA and WECC data; color coded as green
3. **Type 2**: Best match from power rating, location, and renewable model plant; color coded as yellow

4. **Type 3**: Only bus name found; no plants with similar power rating were found; color coded as blue
5. **Type 4**: Not identified; color coded as red

The results from this mapping exercise are summarized in Table A17.3-3.

Table A17.3-3: Summary of mapping of plants from EIA data to the WECC grid model

	Present scenario (21HW2ap) (last modified on 4/17/2020)		**Future scenario (28HS1ap) (last modified on 5/2/2018)**	
Type	*No. of plants*	*Total power in EIA data*	*No. of plants*	*Total power in EIA data*
Type 1,1a	30 (26 + 4)	6355 MW	28 (23 + 5)	5900 MW
Type 2	2	234 MW	2	235 MW
Type 3	1	105 MW	2	348 MW
Type 4	0	0 MW	1	305 MW
Total	33	6695 MW	33	6695 MW

The mapping task was repeated for different WECC grid scenarios (including future grid scenarios). The summary of this task is shown in Table A17.3-4.

Table A17.3-4: Summary of the mapping task for different grid scenarios

Scenario No.	**Grid scenario name**	**Last update**	**Identified plants (total 33)**	**PV connection status**	**Renewable model type [no. of plants]**	**Comments**
1	21HW1	2016	22	connected	REGCAU1 [29]	Old version of the scenario. Most plants are missing or modeled as wind plants
2	21HW2	4/17/2020	32	disconnected	REGCA1 [28]	Renewable model is REGCA1. For other scenario, REGCAU1 is used.
3	22HS1	2/28/2019	28	connected	REGCAU1 [30]	
4	28HS1	5/2/2018	30	connected	REGCAU1 [10]	

Simulated Grid Model: For developing a dynamic (EMT-TS) model of the present grid scenario in PSCAD, the 2022 Heavy Summer (22HS) scenario is used. This is the only current grid scenario with a dynamic model available in the WECC database where the majority of the PV plants are “in-service” and correctly mapped with EIA or queue data. Different cases are simulated and are summarized in Table A5.1-4. Two affected PV plants during the Angeles Forest 2018 event, named specific PV plant-1 and specific PV plant-2, are considered in these studies.

Table A17.3-4: Different hybrid (EMT-TS) simulation models

Case no.	Methods used to decide the boundary buses	Simulated cases	No. of buses in PSCAD and boundary
1	(a) Fault bus and one of the affected PV plants are considered. (b) All the buses in the minimum weighted spanning tree from the fault bus to the PV plant are found using Matlab-based graph tools (c) Next, one hop of the neighboring buses is taken for each of the buses in the minimum spanning tree (d) All the buses in steps (c) and (d) are now modeled in the PSCAD model	Case 1PD: PSCAD simulation (with GFortran compiler) and the PV plants are disconnected Case 1HP: Hybrid simulation (with Intel compiler) and the PV plants are modeled in PSSE Case 1HD: Hybrid simulation (with Intel compiler) and the PV plants are disconnected	Boundary = 23 PSCAD = 35 Dummy buses = 20 Total buses without dummy = 58
2	(a) Fault bus and another affected PV plant are considered (b), (c), and (d) are the same as previous	Cases 2PD, 2HP, and 2HD are simulated where the events are the same as Case 1	Boundary = 24 PSCAD = 41 Dummy buses = 17 Total buses without dummy = 65
3	Everything is the same as Case 1, except instead of one hop, two hops of neighboring buses are taken for each of the buses in the minimum spanning tree	Case 3PD: PSCAD-only simulation with PV disconnected (with GFortran compiler)	Boundary = 45 PSCAD = 70 Dummy buses = 29 Total buses without dummy = 115
4	Everything is the same as Case 2, except instead of one hop, two hops of neighboring buses are taken for each of the buses in the minimum spanning tree	Case 4PD: PSCAD-only simulation with PV disconnected (with GFortran compiler)	Boundary = 41 PSCAD = 77 Dummy buses = 29 Total buses without dummy = 118

Challenges in Model Conversion:

The PV plants are modeled in the WECC scenario using REGCAU1, REECBU1, and REPCAU1 for grid interface, electrical controls, and plant controls, respectively. After converting these PV plants in PSCAD using E-Tran, these are modeled as constant voltage and frequency sources. Because these voltage sources are not a correct representation of the PV plants, they are either disconnected from the PSCAD model (as in the cases of PD and HD) or modeled in PSSE (as in the case of HP).

For Cases 3 and 4, a few generators are correctly represented in PSCAD during E-Tran conversion, and the following models are used for those machines: GENROU for machine model; ESST4B, AC7B, for exciter model; GGOV1, WSIEG1 for governor model; and PSS2B for stabilizer model.

Finally, the shunt switched devices are modeled as constant power shunt work devices, and their switching state does not change with terminal voltage. Shunt devices are included in the EMT model whenever it is necessary for studying the event.

Challenges in Boundary Bus Selection:

In the WECC scenario, long multisection lines contain some dummy buses that are not allowed in the boundary of EMT-TS simulation during E-Tran conversion. When one neighboring bus around the minimum spanning tree is selected for hybrid simulation, the dummy buses are removed from the boundary by adding the next neighboring buses.

Settings in Hybrid Simulation:

During E-Tran conversion, negative resistances are converted to a voltage source (infinite bus) in the converted system. In the network equivalent, negative resistances are converted to zero for Case 1 and 2, and both negative resistances and impedances are converted to positive counterparts for Cases 3 and 4. In simulation settings, the load initialization time is kept at t = 0.2 s, and the simulation time step is 50 µs. In simulation Cases 1 and 2, there are no machine models in PSCAD, so the machine initialization time is made very small (t = 0.225 s), and the hybrid interface starts at t = 0.25 s.

Event Data Collection

(a) WECC grid scenario:

The TS model of the WECC grid scenario of the 2022 Heavy Summer case is used to replicate this event. This is the best available WECC planning model of recent years to replicate this event, where

- the dynamic models of most of the PV plants are included as renewable models, and
- most of the renewable plants are operational and have a generation level comparable to the condition at the time of this event.

(b) Identification of the fault location:

Using map information from the NERC report [6] and the information on substations and transmission lines from California Energy Commission (CEC) online data [31], the local end 500 kV substation is identified near the fault location. In Fig. A5.1-5, the fault location is shown. It should be noted that the fault location is toward the south of this local end substation.

Fig. A17.3-5: Location of Angles Forest fault

(c) Identification of the faulted transmission line:

The local end substation is identified in the WECC grid planning model. For cross-correlation, bus name, rating (500 kV), and utility name (Southern California Edison [SCE]) are used from CEC online data [31].

- *Known information:*
  - The fault location is toward the south of the local end substation.
  - The fault current at the remote end of the faulted transmission line is approximately 3–3.5 times the pre-fault current, as shown in Fig. 1.4 from the NERC report [6].

- The current direction of pre-fault and fault current with respect to the bus voltage is identified.

➢ *Process of identification:*

- All the 500 kV transmission lines are identified that are connected to the local end substation both in the WECC grid planning model [10] and the CEC online information [32].
- The map data of the transmission lines from CEC [31] are also used to identify which lines are toward the south of the local end substation.
- Using the phasor-based TS model of the WECC grid planning case, a low impedance balanced fault for 2.6 cycles is simulated in PSSE at the local end bus (the unbalanced fault simulation is not possible because of the limitation of the TS model). The short circuit current is observed at the other ends of the possible faulted 500 kV lines. At one bus, which is toward the south of the local end bus, the short circuit current is found to be 3.2–4.3 times the pre-fault current, as shown in Fig. A5.1-. A similar variation in the current is observed in the NERC report [6], as shown in Fig.1.4.

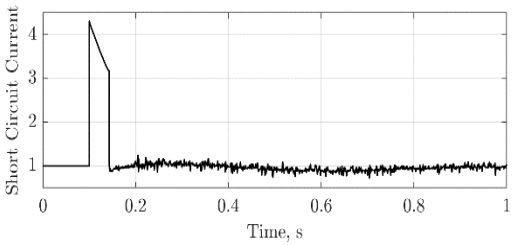

Fig. A17.3-6: Short circuit current of the remote bus in the PSSE simulation (normalized with respect to pre-fault value).

- In the NERC report, an underground cable is mentioned in the faulted 500 kV circuit, which is identified using the CEC map information [32].

The likely faulted transmission line is identified using all the information from the NERC report, CEC map data, and short circuit analysis.

(d) Identification of the affected PV plants

Data available from affected PV plants in the San Fernando disturbance event and the corresponding analysis [33] provided valuable insights on the affected PV plants in the Angeles Forest disturbance event. As shown in Fig. 1.10 from the NERC report [6], although multiple plants undergo partial generation loss during the event, two major plants that lost maximum generation are considered in our study: PV plant-1, power rating 250 MW; and PV plant-2, power rating 550 MW.

2. EMT model development and simulation

(a) EMT Model Development from WECC Grid TS Model

The TS model of the WECC planning case is not sufficient for understanding the impact of unbalanced faults on the PV plants in the grid. Hence E-Tran [9] software is used for the conversion of one portion of the TS model to the EMT model in PSCAD, which is more detailed to enable the analysis of this event. The EMT model development from the WECC grid TS model is summarized in Fig. A5.1-.

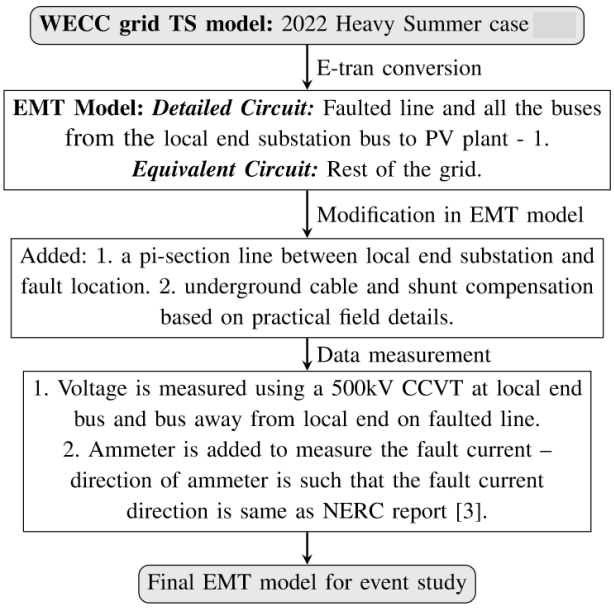

Fig. A17.3-7: EMT model development process from the WECC grid TS model.

- Boundary between the detailed and equivalent models in PSCAD:

MATLAB graph tools are used to find the minimum weighted spanning tree (Fig. A5.1-8) from the local end substation bus to the affected specific PV plant-1 bus. All the buses in this minimum spanning tree are converted in detail in PSCAD using E-Tran. The rest of the system is replaced by equivalent constant voltage sources with series impedance to retain the short circuit characteristics. The proposed approach is premised on the fact that the region with the shortest electrical distance between the fault location and the affected PV plants is the smallest portion that needs to be modeled in detail in the EMT platform to analyze the fault event. This, however, can be expanded at the cost of computational complexity.

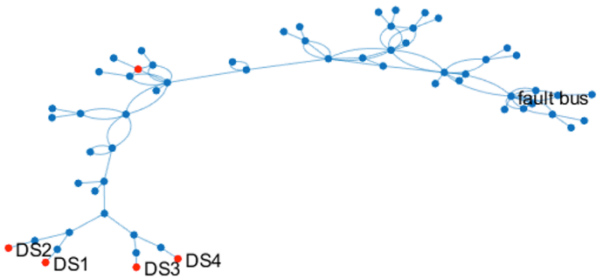

Fig. A17.3-8: Minimum spanning tree for fault bus and the other affected PV plant considered in this analysis with one-hop.

- Modification of the EMT model:
  - Because the location of the fault is not exactly at the local end substation, a small transmission line is added as a pi section model between the fault location and the local end substation.
  - Circuit breakers are added at the local and the substation away from the local end of the faulted line.
  - The underground portion of the line in the faulted 500 kV circuit is replaced with an underground cable in the EMT model. Also, as mentioned in the NERC report [6], the shunt compensation is modeled at one end of the underground cable. More details are collected from [34].

- Two current transformers are connected on the fault line, to measure the remote and local end currents. The current transformers' directions are away from the buses, which match the current directions from the NERC report [6].
- Two 500 kV capacitor coupled voltage transformers are modeled to measure the bus voltages at each end of the faulted line.

A self-clearing B-C line fault is simulated at the "fault bus" for 2.6 cycles at t = 1.99 s. One of the two parallel transmission lines from "fault bus" to "bus 1" is tripped at t = 2.035 s at the near end ("fault bus") and at t = 2.042 s at the remote end ("bus 1"). The voltages at the MV side of the transformer connected to the PV plants are measured. Also, the voltages and currents are measured at both the near and remote ends of the tripped transmission line.

Simulation Results with Different Cases:

The simulation results along with some screenshots from the NERC-WECC report [6] are shown in Fig. A17.3-44, including the voltage and the current of the tripped line for different simulation cases. It is observed that some oscillations are present in the remote end voltage of the screenshot obtained from [6], which is not observed in the simulation studies. As mentioned in [6], these oscillations are caused by the resonance between the charging capacitance of the cable section of the faulted line and large shunt reactors that were placed as shunt compensation—none of these are present in the WECC planning model.

Next, the voltages at POI are shown in Fig. A17.3- for one of the affected PV plants during the Angeles Forest event in 2018. It is observed that Cases 1PD and 1HD are almost similar, but results from Cases 1HP and 3PD differ from the other cases—especially in the post-fault scenario (see response around t = 2.055 s). The results from other solar plants will be included in future reports.

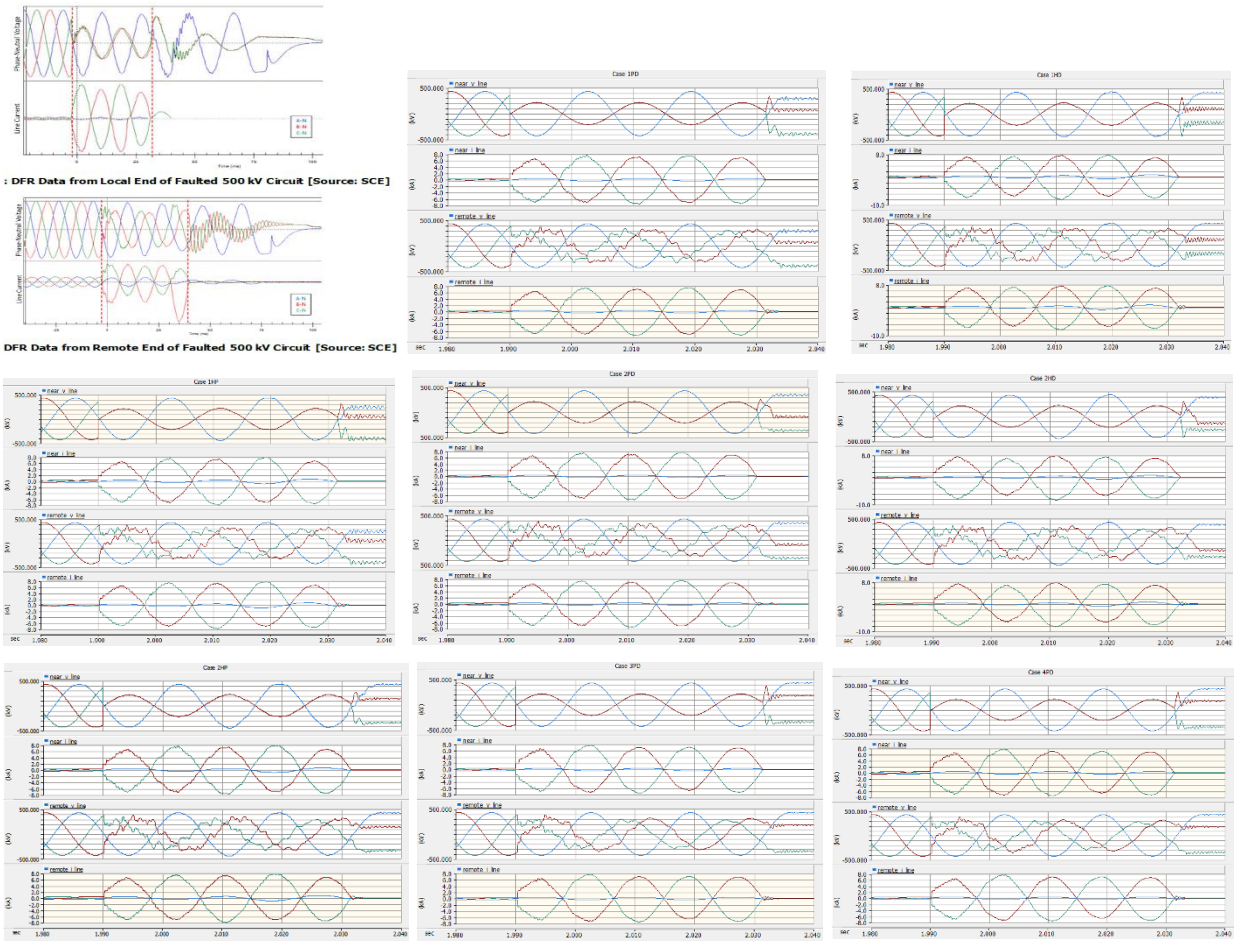

Fig. A17.3-44: Voltage and current plot of the remote and near end of the tripped transmission line for different cases in the order 1PD, 1HD, 1HP, 2PD, 2HD, 2HP, 3PD, and 4 PD (top left screenshot from [6]).

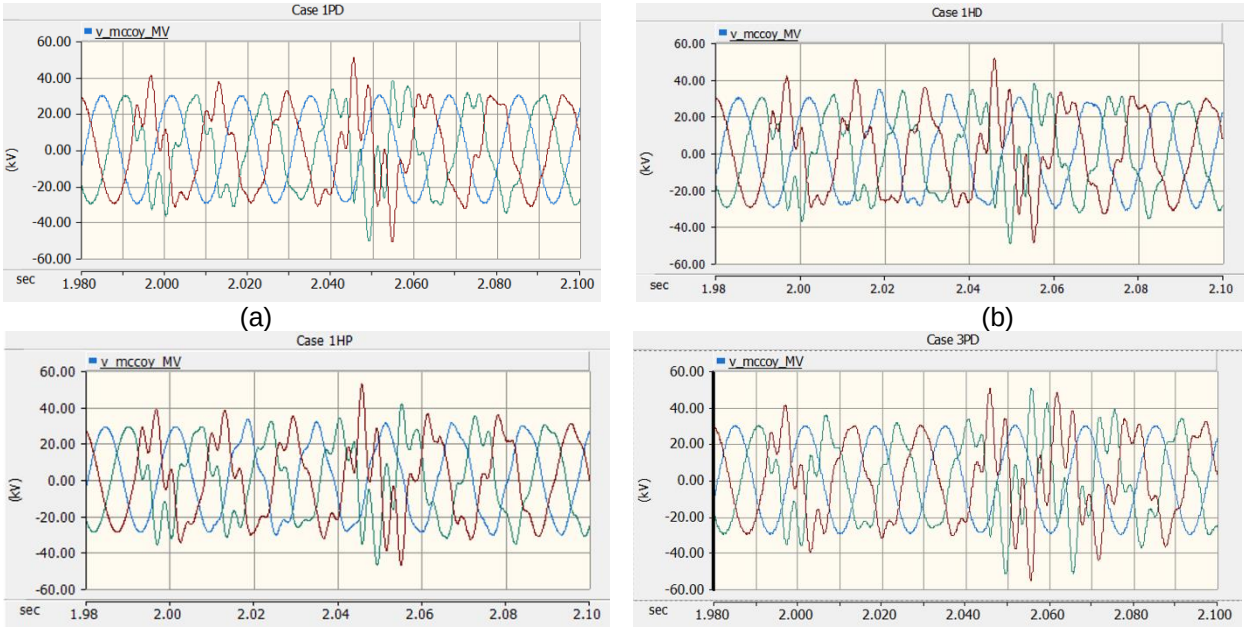

Fig. A17.3-10: Voltage at the one of the affected PV plants for different simulation cases: (a) 1PD, (b) 1HD, (3) 1HP, and (4) 3PD.

Fault Simulation with Upgrades in the 1PD Case:

In this event, a line-to-line fault occurs after the splice failed. From the NERC report [6], it is observed that the A-phase (blue) voltage and current are almost uninterrupted during the fault and the B (red) and C phase (green) voltages at the local end are almost at a similar phase, which indicates a B-C phase L-L fault.

To replicate this event, the B-C phase fault is simulated in the EMT model at the fault location close to the local end substation, as shown in Fig. A5.1-. The length of the small pi section line close to the local end substation is estimated by matching the phase difference between B and C phase voltages at the local end as shown in Fig. 1.3 in the NERC report [6]. In this phase-to-phase fault, the top phase conductor touches the middle phase. This indicates that the fault resistance is very low, which is chosen as 1 μΩ. According to the NERC report [6], the fault is cleared within 2.6 cycles, which is approximately 42 ms. To remove the faulted line in the EMT simulation, circuit breakers at the ends of the line are operated. From the digital fault recorder data at the local and the substation away from the local end on the faulted transmission lines of the faulted line, it appears that the three phases of the circuit breakers are operated independently. The sequence of events during the simulated fault is summarized in Table A17.3-.

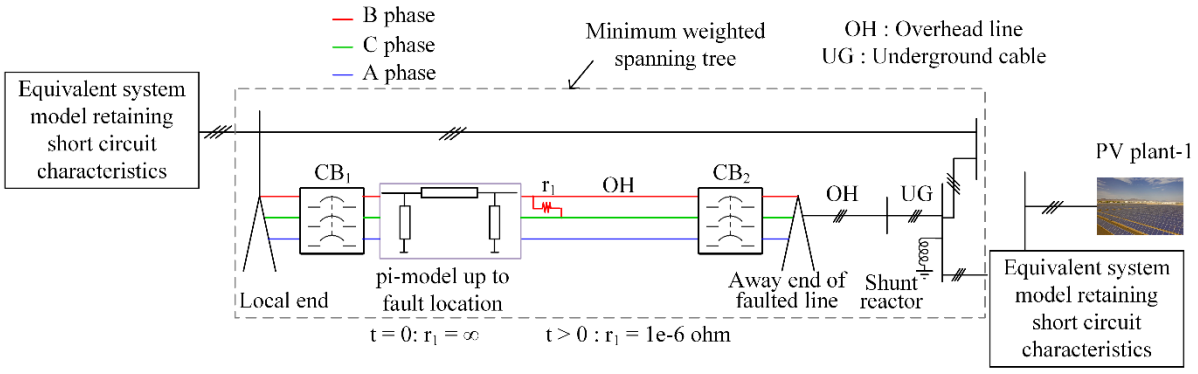

Fig. A17.3-11: Simulation of the fault and circuit breaker operation in the PSCAD model.

Table A17.3-5: Events in the PSCAD simulation

Time	Event
0 ms	B-C line-to-line fault
33 ms	A and B phase opened in CB1
42 ms	C phase of CB1 opened; B, C phases of CB2 opened

Explanation of jump in B phase current at the bus away from the local end on the faulted line

An unusual jump in the B phase current at the remote end substation is observed in the NERC data after the first breaker operation took place at the local end of the faulted transmission line. During the postmortem analysis in the PSCAD simulation, similar results are observed at the bus away from the local end of the faulted line. When the first breaker operation took place at the local end, the A and B phases were disconnected at the local end at t = 33 ms, but the C phase is still connected for another half cycle. At the substation away from the local end on the faulted transmission line, all the phases are still connected to the bus, and at the fault location, the line-to-line fault between the B and C phases is still present. As shown in the equivalent circuit in Fig. A5.1-12, during t = 33 − 42 ms, the fault current in the B phase can flow only through one end on the faulted transmission line, unlike the fault current in the C phase, which gets divided among both ends. This results in an unusual increase in B phase current to satisfy Kirchhoff's current law at the fault location.

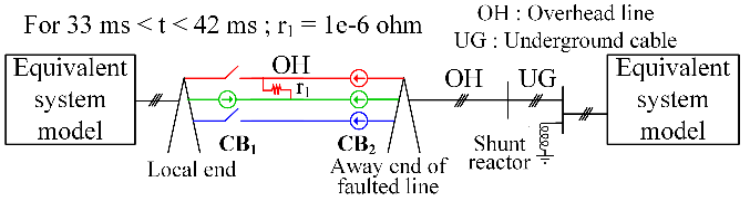

Fig. A17.3-12: Equivalent circuit after first breaker operation.

The following work is submitted to the Innovative Smart Grid Technologies (ISGT 2022) conference: S. Samanta, N. R. Chaudhuri, S. Debnath, and D. Piper, "Simulation and Postmortem Analysis of Angeles Forest Disturbance Event," *2022 IEEE PES Innovative Smart Grid Technologies (ISGT)*, 2022.

ST-5.2. Evaluate performance and redesign in real-time simulations in a real-time simulator (like RTDS)

The RTDS model of the present grid developed with the 1PD case is shown in Fig. A17.3-45.

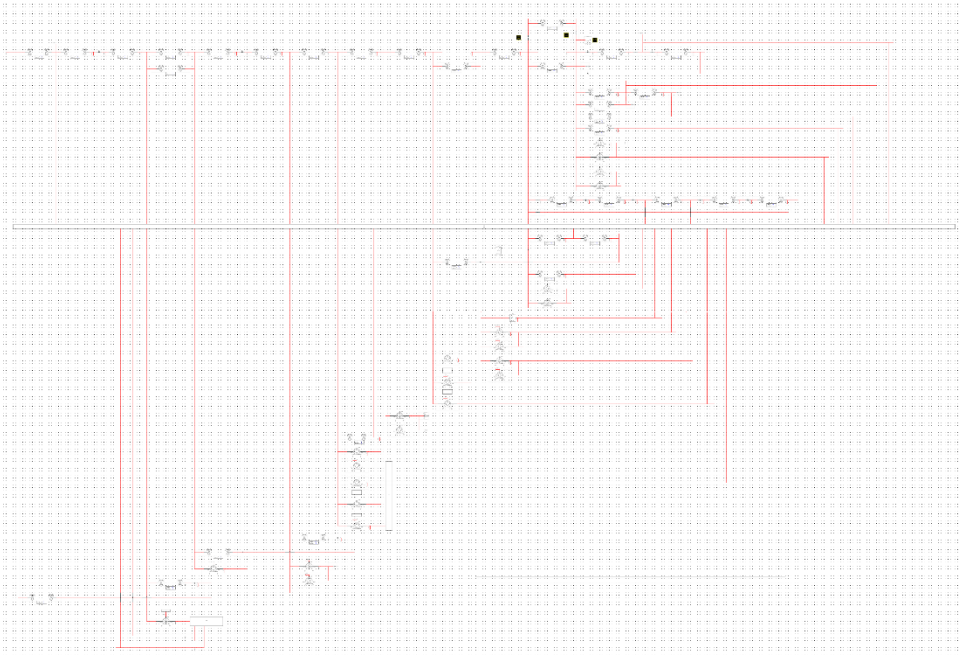

Fig. A17.3-45: Configuration of the transmission and distribution grid developed in RSCAD.

A process of simulation model conversion from off-line to real-time simulation was developed to evaluate performance and redesign in real-time simulation in a real-time simulator. Following are the steps of the process:

Step 1: Data extraction

- Source model and terminal conditions (voltage, angle, active power, reactive power)
- Line model parameters (resistance, inductance, capacitance) and length
- Transformers and parameters
- Controls (for faults and breakers) and meters

Step 2: Feasibility check

- Processors required in RTDS
- Number of nodes in the model
- Number of components in the model
- Reduction techniques applied if needed (to enable real-time simulation)

Step 3: Component development

- Components such as sources, lines, transformers, and breakers

- Library models used
- User defined model developed if needed

Step 4: Run and evaluate performance

- Real-time simulation by RTDS
- Results comparison between offline and real-time simulation models
- Quantifying errors for results
- Fine-tune if needed

The errors between the PSCAD and RSCAD models were quantified to identify the differences between offline and real-time simulation models. These errors are shown in Table A17.3-5. All the measured errors are less than 1.25%.

Table A17.3-5: Quantified errors between offline and real-time simulation models

Average Error (%)			
	Phase		
	a	*b*	*c*
Near end voltage	1.1859	0.8883	0.9213
Near end current	0.6263	0.6763	0.6864
Remote end voltage	1.1500	1.0102	1.0234
Remote end current	1.0485	0.6617	0.6742
Specific PV plant voltage	1.2436	1.0170	1.0881

T-6. Future scenario model development

ST-6.1. Collect information on future PV in queue

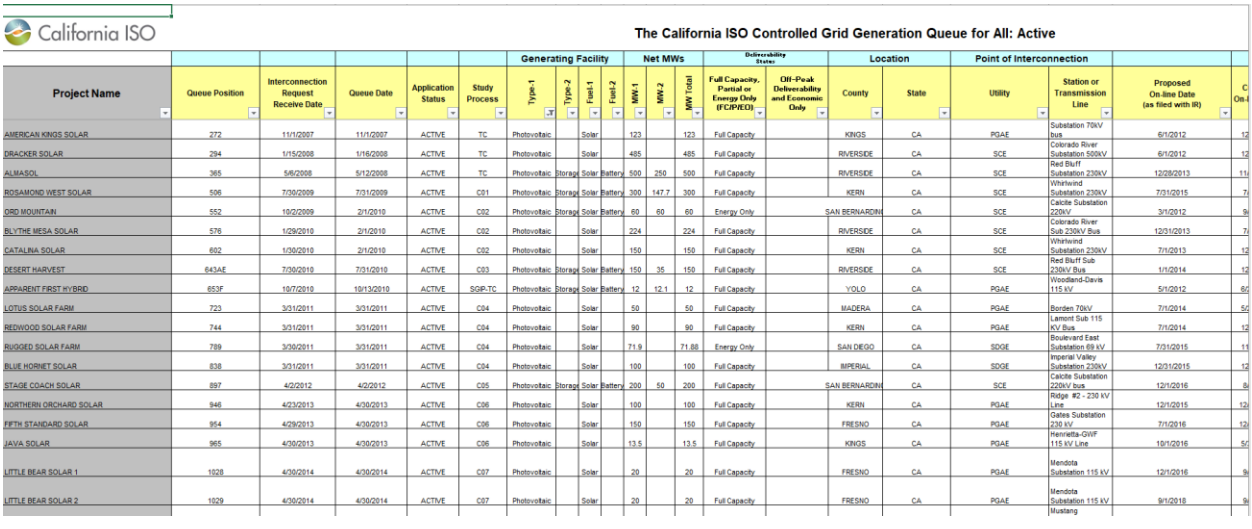

California ISO — The California ISO Controlled Grid Generation Queue for All: Active

Project Name	Queue Position	Interconnection Request Receive Date	Queue Date	Application Status	Study Process	Generating Facility: Type-1	Type-2	Fuel-1	Fuel-2	Net MWs: MW-1	MW-2	MW Total	Deliverability Status: Full Capacity, Partial or Energy Only (FC/PE/EO)	Off-Peak Deliverability and Economic Only	Location: County	State	Point of Interconnection: Utility	Station or Transmission Line	Proposed On-line Date (as filed with IR)	C On-
AMERICAN KINGS SOLAR	272	11/1/2007	11/1/2007	ACTIVE	TC	Photovoltaic		Solar		123		123	Full Capacity		KINGS	CA	PGAE	Substation 70kV bus	6/1/2012	12
DRACKER SOLAR	294	1/15/2008	1/16/2008	ACTIVE	TC	Photovoltaic		Solar		485		485	Full Capacity		RIVERSIDE	CA	SCE	Colorado River Substation 500kV	6/1/2012	12
ALMASOL	365	5/6/2008	5/12/2008	ACTIVE	TC	Photovoltaic	Storage	Solar	Battery	500	250	500	Full Capacity		RIVERSIDE	CA	SCE	Red Bluff Substation 230kV	12/28/2013	11
ROSAMOND WEST SOLAR	506	7/30/2009	7/31/2009	ACTIVE	C01	Photovoltaic	Storage	Solar	Battery	300	147.7	300	Full Capacity		KERN	CA	SCE	Whirlwind Substation 230kV	7/31/2015	7
ORD MOUNTAIN	552	10/2/2009	2/1/2010	ACTIVE	C02	Photovoltaic	Storage	Solar	Battery	60	60	60	Energy Only		SAN BERNARDINO	CA	SCE	Calcite Substation 220kV	3/1/2012	9
BLYTHE MESA SOLAR	576	1/29/2010	2/1/2010	ACTIVE	C02	Photovoltaic		Solar		224		224	Full Capacity		RIVERSIDE	CA	SCE	Colorado River Sub 230kV Bus	12/31/2013	7
CATALINA SOLAR	602	1/30/2010	2/1/2010	ACTIVE	C02	Photovoltaic		Solar		150		150	Full Capacity		KERN	CA	SCE	Whirlwind Substation 230kV	7/1/2013	12
DESERT HARVEST	643AE	7/30/2010	7/31/2010	ACTIVE	C03	Photovoltaic	Storage	Solar	Battery	150	35	150	Full Capacity		RIVERSIDE	CA	SCE	Red Bluff Sub 230kV Bus	1/1/2014	12
APPARENT FIRST HYBRID	653F	10/7/2010	10/13/2010	ACTIVE	SGIP-TC	Photovoltaic	Storage	Solar	Battery	12	12.1	12	Full Capacity		YOLO	CA	PGAE	Woodland-Davis 115 kV	5/1/2012	6/
LOTUS SOLAR FARM	723	3/31/2011	3/31/2011	ACTIVE	C04	Photovoltaic		Solar		50		50	Full Capacity		MADERA	CA	PGAE	Borden 70kV	7/1/2014	5/
REDWOOD SOLAR FARM	744	3/31/2011	3/31/2011	ACTIVE	C04	Photovoltaic		Solar		90		90	Full Capacity		KERN	CA	PGAE	Lamont Sub 115 KV Bus	7/1/2014	12
RUGGED SOLAR FARM	789	3/30/2011	3/31/2011	ACTIVE	C04	Photovoltaic		Solar		71.9		71.88	Energy Only		SAN DIEGO	CA	SDGE	Boulevard East Substation 69 kV	7/31/2015	11
BLUE HORNET SOLAR	838	3/31/2011	3/31/2011	ACTIVE	C04	Photovoltaic		Solar		100		100	Full Capacity		IMPERIAL	CA	SDGE	Imperial Valley Substation 230kV	12/31/2015	12
STAGE COACH SOLAR	897	4/2/2012	4/2/2012	ACTIVE	C05	Photovoltaic	Storage	Solar	Battery	200	50	200	Full Capacity		SAN BERNARDINO	CA	SCE	Calcite Substation 220kV bus	12/1/2016	8
NORTHERN ORCHARD SOLAR	946	4/23/2013	4/30/2013	ACTIVE	C06	Photovoltaic		Solar		100		100	Full Capacity		KERN	CA	PGAE	Ridge #2 - 230 kV Line	12/1/2015	12
FIFTH STANDARD SOLAR	954	4/29/2013	4/30/2013	ACTIVE	C06	Photovoltaic		Solar		150		150	Full Capacity		FRESNO	CA	PGAE	Gates Substation 230 kV	7/1/2016	12
JAVA SOLAR	965	4/30/2013	4/30/2013	ACTIVE	C06	Photovoltaic		Solar		13.5		13.5	Full Capacity		KINGS	CA	PGAE	Henrietta-GWF 115 kV Line	10/1/2016	5/
LITTLE BEAR SOLAR 1	1028	4/30/2014	4/30/2014	ACTIVE	C07	Photovoltaic		Solar		20		20	Full Capacity		FRESNO	CA	PGAE	Mendota Substation 115 kV	12/1/2016	9
LITTLE BEAR SOLAR 2	1029	4/30/2014	4/30/2014	ACTIVE	C07	Photovoltaic		Solar		20		20	Full Capacity		FRESNO	CA	PGAE	Mendota Substation 115 kV	9/1/2018	9
																		Mustang		

Fig. A17.3-46: PV plants in queue in CAISO grid.

The existing plants from the EIA data sheet were mapped to the WECC grid, as summarized in Table A17.3-3 and Table A17.3-4. Because the future scenario was last modified in 2018, a few recent plants are not included, resulting in a higher number of

Types 3 and 4 identified in the table. The data on PV plants in queue in CAISO have been identified based on the publicly available information from “PublicQueueReport.” These data are used to identify the corresponding models in the grid models. A snapshot of the data are provided in Fig. A17.3-46. Seventy PV plants in the queue list are from the California region. The number mentioned as “Queue Position” in the queue report is the same as the bus names in the WECC model. Identification of the queue PV plants was started first with the future grid scenario (last updated on 5/2/2018). Recently, a few more plants were identified in the present grid scenario that was updated later (4/17/2020).

Twelve PV plants have been identified from the in-queue PV plants. All of the identified plants have renewable models and power ratings that are the same in the WECC model and the queue report. The future WECC grid scenario was last updated in 2018 (and as a result is not up to date), which is the probable cause for such a large number of unidentified plants.

The solar plants in the WECC future grid scenario (i.e., 28 Heavy Summer scenario) were previously mapped with the large (above 100 MW) solar plants in EIA-860 data. Next, the unmapped renewable plants in the WECC scenario are identified from the in-queue report, smaller plants in EIA-860 data, and resources found on CAISO sites.

First, the wind plants are eliminated from the renewable plants using the following:

1. Plant model: mechanical and aerodynamic models are used only for wind plants.
2. If “WIND” or “WND” is used in the bus names, these are wind plants.
3. Wind plants with a name similar to the bus name and power rating are found after a Google search.

Next, the rest of the renewable plants are identified by the plant names and power ratings. The identified plants are divided into the following four categories:

1. Exact match: Both power rating and name are matched between WECC data and supporting reports.
2. Partially identified: The names of the plants are the same as the existing report, but total power ratings are different.
3. Unidentified: Plants are unidentified using the above-mentioned methods.
4. Withdrawn: Plants are withdrawn according to the queue report.

The findings are summarized in Table A17.3-6.

Table A17.3-6: Summary of mapping PV plants from WECC grid to EIA-860 data and in-queue report

Type	Category	No. of plants
1	Exact match	63
2	Partially identified	9
3	Unidentified	33
4	Withdrawn	3
	Total	108

The objective of this task is to identify a WECC grid planning model for the future grid where

- a dynamic model is available,
- the PV plants are modeled with a renewable plant model in the dynamic model, and
- most of the PV plants should be in service in the planning model.

To that end, the following WECC planning cases are found from all the available models in the WECC database [31] for further identification of large (100 MW) PV/wind/energy storage system (ESS) and hydro plants:

- 2026 Heavy Summer case (updated on 2021): future grid scenario
- 2028 Heavy Summer case (updated on 2018): future grid scenario

Following is a summary of the generation for the ***2028 Heavy Summer*** *scenario*.

Observations:

- Although it's a future planning model for 2028, the generation from the renewable plants is only **28%** because the model is not updated with all the plants from the in-queue PV plant list. Only 3 large (>100 MW) renewable plants are identified in this 2028 planning model from the in-queue PV plants.
- It should be noted that **11%** of the power is from hydro plants if we consider only the total power rating of the large (>100 MW) plants.
- This planning model is the first version of this case, so it is expected that the next version of this planning case will be updated with more information about the renewable plants.

The overview of the characteristics of 2028 Heavy Summer WECC grid scenarios are shown in Table A6.1-2.

Table A6.1-2: 2028HS case study characterization

Maximum Power (Pmax)			
Utility	**Total nameplate rating of plants above 100 MW**		
	Plants modeled as renewable gen, MW	**Hydro, MW**	**Unidentified 100 MW plants, MW**
IID	830		
	0	0	830 (100%)
LADWP	12,000		
	1,460 (12%)	1,800 (15%)	8,740 (73%)
SANDIEGO	5,600		
	2,000 (36%)	0	3,600 (64%)
SOCALIF	37,000		
	9,000 (24%)	1,300 (4%)	26,700 (72%)
PGANDE	38,000		
	3,300 (9%)	7,600 (20%)	27,100 (71%)
Total	93,430		
	15,760 (17%)	**10,700 (11%)**	**66,970 (72%)**

Following is a summary of the generation for the ***2026 Heavy Summer***. This model has the following characteristics:

(a) The dynamic model data for the plants and controllers are available.

(b) The PV plants are largely modeled as renewable plants. The effect of the renewable plants on stability of the power grid can be assessed with this model.

(c) A majority (>85%) of the renewable plants are in operation (i.e., not offline) in the planning scenario. This helps with studying the effect of a high renewable penetration.

The overview of the characteristics of 2026 Heavy Summer WECC grid scenarios are shown in Table A6.1-3.

Table A6.1-3: 2026HS2 case study characterization

Maximum Power Generation				
Utility	**Total nameplate rating of plants above 100 MW**			
	Solar/wind/ESS plants above 100 MW	**Hydro, MW**	**Others (natural gas, nuclear, geothermal, biomass, etc.), MW**	**Unidentified 100 MW plants**
IID	1,070			200
	430 (47%)	0	640 (53%)	
LADWP	9,500			1,800
	1,450 (15%)	1,800 (19%)	6,250 (65%)	
SANDIEGO	4,510			2,000
	2,660 (59%)	0	1,850 (41%)	
SOCALIF	31,000			5,500
	10,500 (34%)	500 (2%)	20,000 (64%)	
PGANDE	30,460			4,350
	2,860 (10%)	7,600 (25%)	20,000 (65%)	
Total	72,690			
	15,900 (22%)	**9,700 (13%)**	**48,090 (65%)**	

The 26HS2 scenario, last modified on 2/16/2021, is the best available future grid scenario in the WECC data library. It has ~45% of the total generation from the clean energy sources in the California region (including the utilities SCE, San Diego Gas and Electric [SDG&E], Pacific Gas and Electric [PG&E], Imperial Irrigation District [IID], and Los Angeles Department of Water and Power [LADWP]). The details of generation from each type of plant are provided in Table A17.3-4.

Table A17.3-4: Power generation in California in the 26HS2 WECC power grid TS model

Utility name	% of total power in California from this utility	% of power from renewable plants	% of generations from others
IID	3	35	65
LADWP	12	43	57
SDGE	7	30	70
SOCALIF	31	49	51
PG and E	47	45	55
Total	100	**45**	55

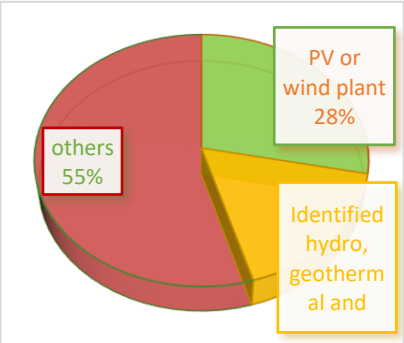

ST-6.2 Upgrade present model with future model in PSCAD

Based on the mapping exercise, the following observations were made:

1. Both WT4G1 (10 plants from type-1) and REGCA1 (65 plants from type-1,2,4) are used for the PV plant dynamic model.
   - Possible reasons: In 21HW2, all the PV plants were modeled using REGCAU1, which was last updated in 2020. In contrast, 28HS was last updated in 2018, and this is the first version of the scenario. Dynamic models are expected to be updated in future versions, where more plants might be identified.
2. There are one battery storage and nine hybrid plants (PV and storage), which are identified. These 10 plants are modeled using REGCA1.

Upgrades will be necessary based on the renewable penetration of interest studied.

T-7. Advanced control functionalities

ST-7.1. Collect data on future PV system response requirements

The following survey is designed to seek your guidance and opinions on requirements from control systems in PV plants in future power grids with high penetration of power electronics-based generation.

Project Introduction

The operation and hardware in the traditional power grids had been designed for operations with a significant percentage of synchronous generators or machine-based loads and with a very small percentage of power electronics-based generators or loads. As the penetration of power electronics-based generation like solar PV plants rise, significant upgrades in these existing or upcoming plants and/or in the operation of grids may be needed. The upgrades arise from new challenges that may be posed due to the inherent physical properties of power electronics. These properties include higher bandwidth, increased sensitivity to external grid events, no physical inertia capability, reduced short circuit current capability, among others, as compared to traditional synchronous generators. Some of these properties also provide benefits like higher bandwidth or improved controllability that may help in providing faster active or reactive power support or fast frequency support, among others. Some of the challenges that have been observed in regions with local high penetration of PV plants include power reductions in response to external grid disturbances like normally cleared bulk power system (BPS) faults[1,2,3,4]. These reductions may pose significant risks to BPS performance and reliability. The power reductions in the recent events[2,3,4] have primarily happened due to momentary cessation, partial inverter

[1] *North American Electric Reliability Corporation. 1200 MW Fault Induced Solar Photovoltaic Resource Interruption Disturbance Report.*
[2] *North American Electric Reliability Corporation. 900 MW Fault Induced Solar Photovoltaic Resource Interruption*
Disturbance Report.
[3] *North American Electric Reliability Corporation. April and May 2018 Fault Induced Solar Photovoltaic Resource Interruption Disturbances Report.*
[4] *North American Electric Reliability Corporation and Western Electric Coordinating Council. July 2020 San Fernando Solar PV Reduction Disturbance Report.*

tripping, or shutdown (including tripping of the plant) observed in the existing PV plants. Some of these challenges arise from the increased sensitivity of power electronics to external disturbances that result in phenomena like ac over-voltage (including sub-cycle transient), ac under-voltage, ac over-current, dc reverse current, phase-locked loop (PLL) loss of synchronism, among others. In addition to the challenges observed in operation of grids during the faults, there have also been challenges observed in the post-fault recovery period. The challenges include slow recovery to pre-fault operating condition of the PV plant, lack of voltage support to aid in recovery of the grid post-fault, inability to provide frequency support to reduce rate of change of frequency and/or primary frequency response as some of the PV plants remain disconnected, among others.

*These challenges observed today are in regions with up to 50% peak penetration of power electronics-based generation locally[4]. As the grid modernizes and reduces the carbon footprint, the **mean** penetration of power electronics-based generation is expected to rise significantly in the interconnections (and not just locally). The rise in the penetration of power electronics-based generation is expected to further exacerbate the problems observed in the today's power grid (like the studies performed in Great Britain, Ireland, France, and Germany[5]). Some of the other reliability challenges that may be observed, if the control systems and hardware are not upgraded in existing and upcoming power electronics-based generation, arise from reduction in inertia, primary frequency response capability, and secondary frequency response capability. Moreover, further challenges will be observed with reduced short circuit ratio (SCR) in the system, unless upgrades are performed to increase the system strength. As the frequency response capability and the system strength (based on SCR) reduce, there'll be new set of control features needed in the next-generation power electronics-based generation like PV plants.*

In this project, the project team will study the impact of next-generation control features in PV plants on the performance of BPS as the control features improve the performance of the PV plants during faults.

Control Features of Interest

The power electronics-based generations will include advanced smart functionalities[6] like voltage support, ride-through (eg, NERC PRC-024-2[7]), frequency-watt functions, unbalancing/ harmonic control methods, grid-forming control methods, among others. The studies will explore the resilience of PV plants with advanced functionalities (and some without the functionalities) in high-penetration PV scenarios during extreme events. The studies will evaluate the performance of the grid in these scenarios.

---

[5] *The Massive InteGRATion of power Electronic devices (MIGRATE), https://www.h2020-migrate.eu/_Resources/Persistent/b955edde3162c8c5bf6696a9a936ad06e3b485db/19109_MIGRATE-Broschuere_DIN-A4_Doppelseiten_V8_online.pdf*

[6] *"IEEE Standard for Interconnection and Interoperability of Distributed Energy Resources with Associated Electric Power Systems Interfaces," in IEEE Std 1547-2018 (Revision of IEEE Std 1547-2003), vol., no., pp.1-138, 6 April 2018*

[7] *North American Electric Reliability Corporation, Standard PRC-024-2 "Generator Frequency and Voltage Protective Relay Settings".*

Based on the challenges observed in the grid and recommendations studied[2,3,4,5,6,7,8,9,10,11], the following include some of the features (in the fast timescale) of interest from inverters and PV plants:

1. *Eliminate momentary cessation or reduce to the maximum extent feasible*
2. *Eliminate inverter tripping or reduce to the maximum extent feasible through the following*
    a. *For example, use of IEEE 1547-2018 or Figure A.1 of NERC recommendations[9] to avoid inverter trips during transient over-voltages or under-voltages*
    b. *Avoid dc reserve current trips during transient over-voltages*
    c. *Avoid trips associated with phase locked loop (PLL) loss of synchronism*
3. *Recover to pre-fault operating condition (active power) within 1 s of fault clearance*
4. *Provide reactive power support (or fast dynamic voltage support[7]) provided during small disturbance and after clearing the disturbance*
    a. *For example, use of Table A.3 in NERC recommendations[9]*
5. *Provide reactive current support provided during large disturbance and after clearing the disturbance*
    a. *For example, use of Table A.4 in NERC recommendations[9]*
6. *Provide negative sequence current injection and/or unbalance support during faults[10]*
7. *Provide fast frequency support (inertial response timeframe) during grid events that lead to frequency changes*
8. *Provide primary frequency response during grid events that lead to frequency changes*
    a. *For example, use of Table A.2 in NERC recommendations[9]*
9. *Damp power oscillations and sub-synchronous control interactions[12,13]*
10. *Form and maintain grids without the need for synchronous generators (like grid-forming mode of operation)*
    a. *One of the definitions[10] includes the following features: creating system voltage, contributing to fault level, sink for harmonics, sink for unbalance, contributing to inertia, system survival, preventing adverse control interactions*
    b. *Another definition[5] includes the following features: behaves as a voltage source, be synchronized, supports islanding, compatible with other connected devices, takes care of overcurrent limitations.*
11. *Switching between grid-forming and grid-following modes of operation*

---

[8] Australian Energy Market Operator, "Power System Requirements," July 2020 Reference Paper.
[9] North American Electric Reliability Corporation, Reliability Guideline "BPS-Connected Inverter-Based Resource Performance," September 2018.
[10] European Network of Transmission System Operators for Electricity (ENTSO-E) Technical Group on High Penetration of Power Electronic Interfaced Power Systems, "High Penetration of Power Electronic Interfaced Power Sources and the Potential Contribution of Grid Forming Converters," January 2020.
[11] North American Electric Reliability Corporation, Reliability Guideline "Improvements to Interconnection Requirements for BPS-Connected Inverter-Based Resources," September 2019.
[12] Midcontinent Independent System Operator (MISO), "Reliability Integration Impact Assessment," July 2019.
[13] John Schmall, Electric Reliability Council of Texas (ERCOT), "IBR Damping Support Revision Request Update," August 2020.

12. *Power quality support (including harmonics support)*
13. *Black start capability*
14. *Any system strength[8] related control measures*

Amongst fast timescale characteristics, we would like to identify the top priority items for generator owners/operators, inverter manufacturers, and grid operators. Please rate the functionalities in the faster timescale to indicate the prioritization from 1-14, with "1" indicating top priority and "14" indicating the least priority. Multiple features can be provided the same priority number if they are expected to be introduced simultaneously. Based on the prioritization and expected timeline of each functionality, the corresponding top features will be incorporated in our studies. Please feel free to add further features of interest (if any) in the faster timescales.

More details on the functionalities in the faster timescale, please refer to the "Addendum" document.

An addendum document was also provided. The contents of the addendum document are below for reference.

Addendum Document to Control Specification Document

This document supplements the "Control Specifications" document and describes in detail the features mentioned in the "Control Specifications" document. In this document, the following characteristics of the feature are explained:

1. *Control Functionality: The control function needed to implement the feature of interest.*
2. *Brief Description: A brief description of the control functionality is provided.*
3. *Risk in Future Grids if not met: The impact of not incorporating the feature of interest in future grids is assessed and described here.*
4. *Probability of Occurrence: The likelihood of the occurrence of the risk mentioned above is assessed and described here.*
5. *Timescale of Interest: The timescale of the implementation of the control functionality and the corresponding dynamics is mentioned here. It also includes the likely location of the control feature.*
6. *Current State of the Art: The state of the control functionality in today's PV power plants is described here.*
7. *Specifications: The requirements from the control functionality to provide the feature of interest is mentioned here.*

Please use this document as a support your decision on ranking the features of interest and feel free to add comments on the features/functionalities discussed in this document.

Feature	*Elimination of momentary cessation or inverter tripping [11–17]*
Control Functionality	*Use of ride through like voltage ride through (VRT) and frequency ride through (FRT).*
Brief Description	*During faults, inverters should not enter momentary cessation or trip, but rather ride-through. During ride-through conditions, the inverter controls its output and ignores signals sent by the plant-level controller. Based on the specific operating*

	conditions, it maintains a combination of active and reactive power injection. Reduction in power may be noted from IEEE 1547-2018 for present operating conditions (and it may change in future based on penetration of power electronics-based generations or based on local utility's requirements or based on finalized IEEE P2800). Once the voltage recovers and the inverter enters a normal operating range, it responds to signals from the plant controller again.
Risk in Future Grids if not met (impact)	*Momentary cessations or inverter tripping may lead to fast changes in frequency that may lead to further instability challenges in low inertia grids.*
Probability of Occurrence	*Very likely*
Timescale of Interest	*Milliseconds to seconds (inverter firmware)*
Current State of the Art	*Some of the PV power plants today have momentary cessation incorporated for maintaining stability of inverter firmware and/or for safety of equipment (like semiconductor devices and their corresponding current/voltage limitations). Some of the plants may have construed momentary cessation as a ride-through feature and/or conservatively utilized the definitions of existing grid codes (eg, IEEE 1547-2014 or 1547-2018). New inverters entering the market are expected to meet PRC-024-2 standards.*
Specifications	*When the measured voltage sent to the plant controller falls below a predetermined level (e.g., 0.9 pu), the plant ramp rate controller freezes, sending commands based on when the inverters enter ride-through mode (where command values from the plant controller are ignored and each inverter uses its terminal conditions for control). The use of momentary cessation may be removed to prevent unnecessary tripping and cessation.* *Voltage protection functions in the inverters should be set based on physical equipment limitations to protect the inverter itself and should not be set based solely on the PRC-024-2 VRT characteristic or IEEE 1547-2018 or other characteristics (eg, IEEE P2800). Within the "no trip" region of the curve, the inverters are expected to ride through and continue injecting current to the BPS. The region outside the curve should be interpreted as a "may trip" zone and not a "must trip" zone and protection should be set as wide as possible while still ensuring the reliability and integrity of the inverter-based resource.* *Inverters should ride through momentary loss of synchronism caused by phase jumps, distortion, etc., during grid events, such as faults. Inverters riding through these disturbances should continue to inject current into the grid and, at a minimum, lock the phase-locked loop (PLL) to the last synchronized point and continue injecting current to the grid at that calculated phase until the PLL can regain synchronism upon fault clearing.* *For example, in IEEE 1547-2018, rate of change of frequency (ROCOF) ride-through requirements under abnormal operating performance are classified as: Category I (0.5 Hz/sec), Category II (2 Hz/sec), and Category III (3 Hz/sec). Under high penetration level of renewables, category III is applied.*

Feature	*Fast post-fault recovery upon fault clearance [11–14]*
Control Functionality	*Ramp rate interaction with inverter response needs to be mitigated during post-fault operation.*
Brief Description	*Once the voltage recovers post fault, the inverters need to ramp up to pre-fault power conditions as soon as possible without interaction with the ramp rates in the power plant controller.*
Risk in Future Grids if not met (impact)	*Slow rate of return to pre-fault operating conditions may lead to fast changes in frequency. The changes in frequency may lead to further instability challenges in low inertia grids.*
Probability of Occurrence	*Very likely*
Timescale of Interest	*Milliseconds to seconds (inverter firmware, power plant controller)*
Current State of the Art	*Most inverters and PV power plants take time (~ minutes) to return to pre-fault operating conditions based on ramp rates.*
Specifications	*If the inverter enters momentary cessation, it should recover active current injection to pre-disturbance levels within a specific time (e.g., within 1 seconds). Once voltage recovers to the aforementioned pre-determined level, the plant controller will again begin sending commands for the inverters to follow. Ramp rates then become controlled by the plant controller again. The plant controller and inverter controls should be coordinated to ensure that active current injection returns to pre-disturbance levels unimpeded by any interaction with the ramp rate limits of the plant controller.* *Active and reactive current oscillations in the post-disturbance period that are positively damped or after momentary cessation having a maximum duration of 0.5 s shall be acceptable in response to phase angle changes.*

Feature	*Provide reactive power/fast dynamic voltage support [11, 18]*
Control Functionality	*Dynamic voltage regulation in power plants.*
Brief Description	*A PV system should automatically react/respond in real-time on/to voltage deviations by producing and consuming reactive power.*
Risk in Future Grids if not met (impact)	*Voltage fluctuation, stability problems*
Probability of Occurrence	*Likely*
Timescale of Interest	*Seconds (power plant controller)*
Current State of the Art	*The ability of reactive power absorption is limited, and voltage ride throughs are not relaxed enough to mitigate reliability/stability challenges that arise with the increasing penetration level of inverter-based resources.*
Specifications	*Apply droop control or similar advanced control features in the power plant controller that can respond fast to provide dynamic voltage support (with reaction time of the order of less than 500 ms, ramp time of 1-30 s, overshoot M*

	5%). The plant should be able to operate in three modes: voltage regulation, power factor regulation, and reactive power control (one at a time with seamless transition). The plant should be able to produce or absorb reactive power at nearly zero MW production (STATCOM mode).

Feature	*Provide reactive current support [6, 9, 13–15]*
Control Functionality	*Dynamic voltage-reactive current control at inverters.*
Brief Description	*Under large disturbances, the power plant controller cedes control to the inverters and they are required to provide dynamic voltage control.*
Risk in Future Grids if not met (impact)	*Stability challenges during faults (or other grid events that can be classified as large disturbance)*
Probability of Occurrence	*Very likely*
Timescale of Interest	*Milliseconds (inverter firmware)*
Current State of the Art	*The inverters typically have the capability to provide voltage control using reactive current. However, it may not be actively considered in older installations to maximize transfer to active power.*
Specifications	*If the voltage variation is beyond a pre-set limit (eg, 1.1 pu or 0.9 pu), the power plant controller cedes control to local individual inverters. These inverters are expected to provide dynamic voltage-reactive current control based on measurements at the individual inverter terminals. The response time is expected to be much faster (with reaction time of the order of less than 16 ms, rise of 100 ms). It is also expected to continue injection of current post-disturbance to stabilize the voltage in the system and be an enabler for smooth transition to the control by power plant controller.*

Feature	*Provide fast frequency response during frequency changes [9, 13, 14]*
Control Functionality	*Inertial response*
Brief Description	*PV systems should have the capability to arrest the decline in frequency in the grid through improving the rate of change of frequency.*
Risk in Future Grids if not met (impact)	*Large frequency deviations during contingency events. Stability problems.*
Probability of Occurrence	*Very likely*
Timescale of Interest	*Milliseconds to a few seconds (inverter firmware)*
Current State of the Art	*There is limited capability to provide inertial or fast frequency response support. This may be related to relatively lower penetration of inverter-based resources.*
Specifications	*Use of synchronous generator or virtual synchronous generator or virtual oscillator or predictive control algorithms.*

Feature	*Provide primary frequency response during frequency changes (grid events) [6, 9, 13, 14]*
Control Functionality	*Primary frequency response*
Brief Description	*PV systems should have sufficient frequency response capability to overcome small and large frequency deviations during contingency events.* *Large PV systems should operate in curtailed mode to have enough room to increase their output in response to a frequency decline below the defined limit.* *Knowing/predicting the PV system capacity limits would help for more economic operation while providing the needed frequency response.*
Risk in Future Grids if not met (impact)	*Large frequency deviations during contingency events. Stability problems.*
Probability of Occurrence	*Very likely*
Timescale of Interest	*Seconds (inverter firmware/power plant controller)*
Current State of the Art	*There is limited fast response frequency capability installed in existing PV plants.*
Specifications	*Primary frequency response through synchronous generator or virtual synchronous generator or virtual oscillator or predictive control algorithms.*

Feature	*Damp power oscillations and sub-synchronous control interactions [16–18]*
Control Functionality	*Power oscillation damping (POD) that may be similar to power system stabilizer*
Brief Description	*With increased PV penetrations, the volatility and uncertainty of power generated from PV plants may adversely impact the power system stability, for example increasing the risk of oscillations. It may happen due to connection to weak grids. Power oscillation dampers are a relatively new grid supporting function for solar farms.*
Risk in Future Grids if not met (impact)	*Stability problems and system protection.*
Probability of Occurrence	*Likely*
Timescale of Interest	*Seconds (power plant controller)*
Current State of the Art	*No known large PV plant provides today in US.*
Specifications	*Most ancillary service capacity is procured in the day-ahead market. Real-time service and prediction ahead are needed to identify the economic level for spinning and non-spinning services. [35]*

Feature	*Form and maintain grids without the need for synchronous generators [6, 19, 20]*
Control Functionality	*Grid-forming mode of operation*
Brief Description	*The inverter should be able to form the grid in the absence of conventional synchronous generators and be able to provide some of the characteristics of synchronous generators in addition to its inherent beneficial characteristics.*
Risk in Future Grids if not met (impact)	*Stability problems (voltage, frequency) as the frequency response (inertial, primary frequency response) capabilities and short circuit strength (SCR) of the grid reduces.*
Probability of Occurrence	*Very likely in high-penetration PV scenario in regions with low SCR and less likely in other regions/scenarios*
Timescale of Interest	*Milliseconds to seconds (inverter firmware, power plant controller)*
Current State of the Art	*Grid-forming mode of operation is present in research, without any adoption in industry that has been shown yet.*
Specifications	*There are multiple definitions of grid-forming mode of operation. A few of them are placed here.* *One of the definitions of grid-forming mode of operation is providing the following features: creating system voltage, contributing to fault level, sink for harmonics, sink for unbalance, contributing to inertia, system survival, preventing adverse control interactions.* *Another definition includes the following features: behaves as a voltage source, be synchronized, supports islanding, compatible with other connected devices, takes care of overcurrent limitations.* *These features will be incorporated into the inverter controller.*

Feature	*Switching between grid-forming and grid-following modes of operation [21]*
Control Functionality	*Mode switching*
Brief Description	*The inverter should be able to inject maximum available power to the grid while operating in grid following mode (current source mode) and be able to operate in grid forming mode (voltage source mode) as per the need to support the gird.*
Risk in Future Grids if not met (impact)	*Stability and power quality impacts.*
Probability of Occurrence	*Very likely in high-penetration PV scenario in regions and times with low SCR and less likely in other regions/scenarios*
Timescale of Interest	*Seconds to minutes (power plant controller)*
Current State of the Art	*There is ongoing research on operating inverters in grid-forming and grid-following modes of operation, without any observed field implementations.*
Specifications	*Mode switching is a function that may need to be incorporated in the power plant controller of the PV plant to change the mode of operation of the inverters in the PV plant based on the operating condition. This may also need prediction*

	of the SCR by the power plant controller and/or grid operator to detect the change in mode needs.

Feature	*Maintaining power quality that includes harmonics support [6, 9, 13, 22]*
Control Functionality	*Power quality support*
Brief Description	*Supporting the utilization of electric energy without interference or interruption, improve the power quality in grid with the compensation of harmonic components.*
Risk in Future Grids if not met (impact)	*Fluctuating power and distorted voltages.*
Probability of Occurrence	*Likely*
Timescale of Interest	*Milliseconds (inverter firmware)*
Current State of the Art	*Restricted to demonstrations, mostly at research level of small and medium size PV systems.*
Specifications	*Incorporate provisions to provide harmonics current support through inverter-based generators. Also, introduce negative-sequence current injection, where needed, to improve the stability of the bulk power system under stressed operating conditions (like transmission line faults).*

Feature	*Black start, soft connect and reconnect operation [6, 9, 20]*
Control Functionality	*Start-up and shut-down control, seamlessly connect and reconnect to the grid under any operating condition*
Brief Description	*A PV system should have the ability to restart a grid after a blackout. Black start is needed after intentional islanding.*
Risk in Future Grids if not met (impact)	*Loss of generation and synchronization.*
Probability of Occurrence	*Likely*
Timescale of Interest	*Seconds to minutes (inverter firmware, power plant controller)*
Current State of the Art	*There is no black-start capable PV plant that has been observed in US today.*
Specifications	*A PV system needs to seamlessly start up, shut down, connect and reconnect to the grid under any operating condition. A proper synchronization algorithm needs to be included. Avoid any significant disturbance in the grid operation. Avoid unintentional islanding or start-up without addressing safety concerns.*

Following is an overview of the results from the survey with IAB.

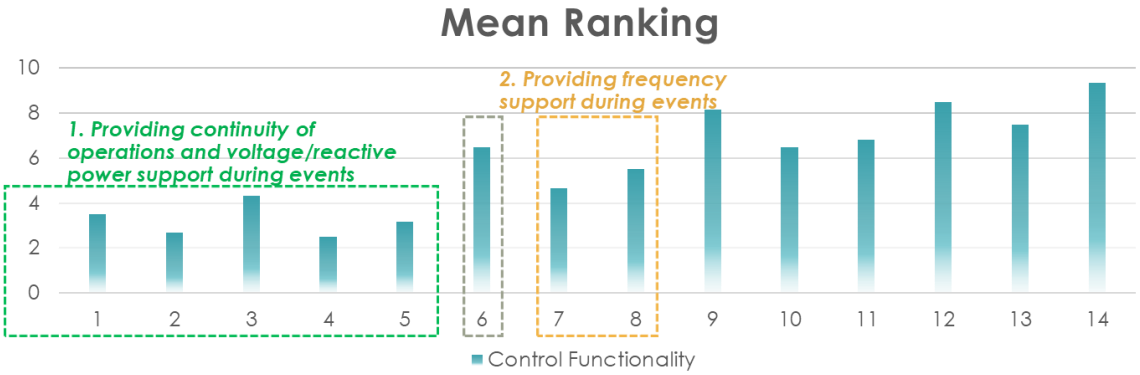

Fig. A17.3-47: Mean ranking of control features based on IAB feedback.

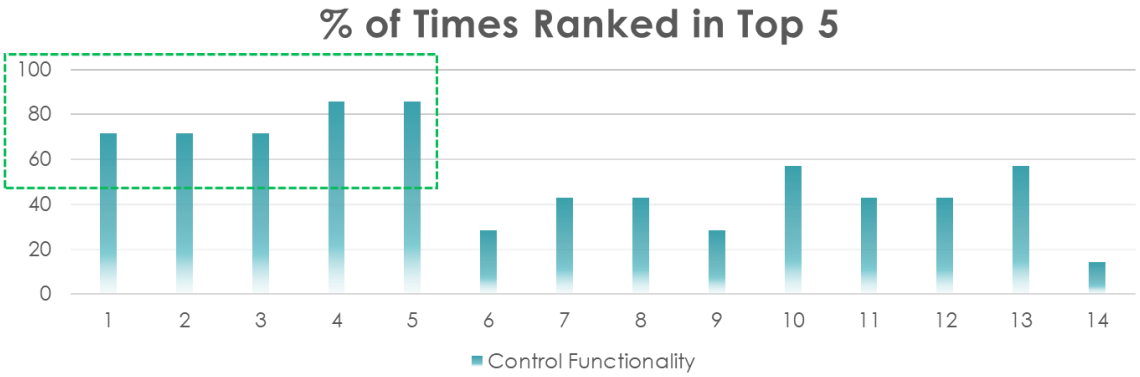

Fig. A17.3-48: Percentage of times ranked in top five.

ST-7.2. Design advanced control functionalities

A general format of the objective function used to provide advanced functionalities based on discrete-time models is expressed by:

$$\underset{x}{minimize}\ J(\boldsymbol{x})$$

$$subject\ to: \quad \boldsymbol{x}[k+1] = f(\boldsymbol{x}(k), \boldsymbol{u}(k))$$

$$\boldsymbol{x}(0) = x_0$$

$$\boldsymbol{u}(k) \in U, \forall k\ \epsilon\ [0, N]$$

$$\boldsymbol{x}(k) \in U, \forall k\ \epsilon\ [0, N]$$

$$g_1(\boldsymbol{x}) \leq 0$$

$$g_2(\boldsymbol{x}) = 0$$

$J(\boldsymbol{x})$ is the objective function that can be generally defined as follows:

$$J(\boldsymbol{x}) = \sum_{i=1}^{N} w_{x_i}\left(x_i^{ref} - x_i\right)^2 + \sum_{i=1}^{N} w_{u_i}\Delta u^2$$

where x_i is the i[th] controlled variable, x_i^{ref} is the i[th] reference variable, u_i is the i[th] manipulated variable, w_{x_i} is the weighting coefficient of x_i (reflecting importance of x_i),

controlled variable, w_{u_i} is the weighting coefficient of u_i (reflecting importance of u_i), $g_1$are inequality constraints, and g_2 are equality constraints.

Table A17.3-7 highlights a high-level framework on how to use MPC to achieve dynamic reactive power voltage control.

Table A17.3-7: A framework to implement MPC for reactive power/voltage control

Specific functionality	Reactive power/voltage control
Brief description (What is to be controlled?)	A PV system should automatically react/respond in real-time on/to voltage deviations by producing and consuming reactive power
Current literature/state of the art	Conventionally, PV systems are designed with active power control. Reactive power control is avoided owing to inverter losses, transmission line losses, and transformer losses
Objective function parameters	Possible decision variables may include voltage at POC, measured reactive power at POC, or phase of currents to inject or demand a pre-established reactive power. In the implementation below, only the voltage at POC is considered
Application	Limited research exists in this field

Based on an equivalencing technique for the inverter terminal voltage in a PV plant to the POC voltage, the following relationship is obtained for the simplified model of the plant to be used in the MPC:

$$V_m[t+1] = V_m[t] + Z_0 * I_m[t]$$
$$V_k[t+1] = V_k[t] + Z_0/UN * I_m[t]$$
$$I_k[t] = UN * I_m[t]$$

Voltage across terminal V_k is connected directly to the POC and is included in the objective function. A simple objective function can be constructed as

$$\underset{V_k}{minimize}\, J(\boldsymbol{x}) = \sum_{i=1}^{N} w_{x_i}\left(V_i^{ref} - V_{k_i}\right)^2$$

$$subject\ to: \quad V_k[t+1] = V_k[t] + Z_0/UN * I_m[t]$$
$$I_k[t] = UN * I_m[t]$$
$$\boldsymbol{x}(0) = x_0$$
$$\boldsymbol{x}(k) \in U, \forall k\ \epsilon\ [0, N$$

The model developed in the MPC-based reactive power voltage regulation is based on steady state analysis.

T-8. Develop suite of dynamic PV system models

ST-8.1. High-fidelity model in PSCAD (ORNL)

In addition to the high-fidelity models of two-level and three-level converters with LCL and LC filters developed in ST-3.2, additional high-fidelity models are developed for the converters with midpoint grounded.

Two-Level Converter with Midpoint Ground: The two-level converter model with the grounded midpoint is shown in Fig. A8.1-1. The need to develop a separate model for a two-level converter with the grounded midpoint arises from the incorporation of two capacitors (C_1 and C_2) through the midpoint ground. To ensure stable voltages across C_1 and C_2 (V_{c1} and V_{c2}) and stable operation of the two-level converter with a grounded midpoint, the dynamics of inductor current i_j need to consider the individual capacitor voltages, where phase-j ϵ (a, b, c), are given by

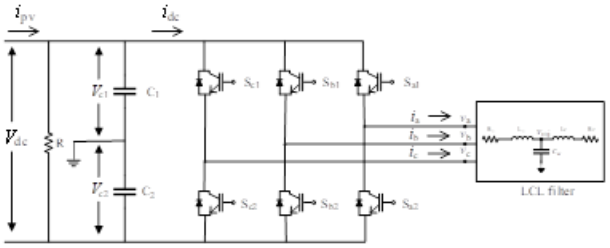

Fig. A17.3-49: Two-level converter with grounded midpoint circuit architecture

$$\left(\frac{L_1}{h}+R_1\right)i_j[k]+v_{mj}[k] = \frac{L_1}{h}i_j[k-1]+\left[S_{j1}(1-S_{j2})V_{c1}-S_{j2}(1-S_{j1})V_{c2}\right] \quad (17.3\text{-}37)$$

The two capacitor voltages are incorporated in the dynamics.

Simulation Results: The capacitor voltages V_{c1}, V_{c2}, and V_{dc} from the simulation of the high-fidelity "two-level converter with grounded midpoint" model are shown in Fig. A8.1-2(a)–(c). The corresponding results from the baseline PSCAD library-based two-level converter model with grounded midpoint are also shown. From these figures, it can be observed that the capacitor voltages V_{c1}, V_{c2}, and V_{dc} are stable and are reproduced in the developed high-fidelity model with >98% accuracy in comparison with the baseline PSCAD model.

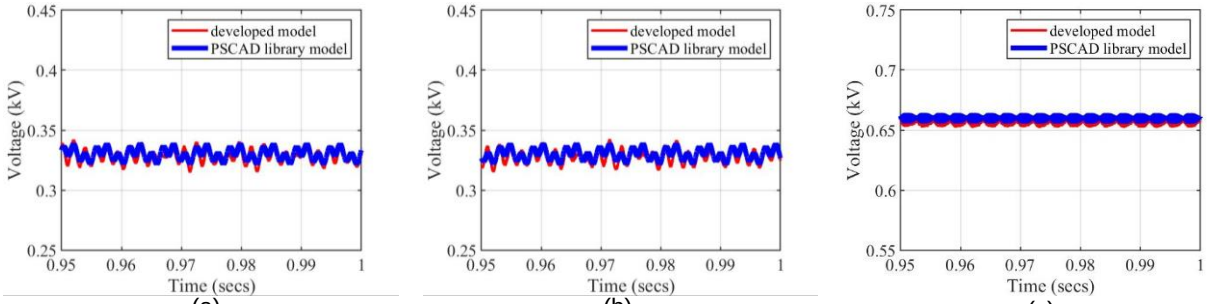

Fig. A17.3-50: Two-level converter model with midpoint ground model capacitor voltages: (a) V_{c1}, (b) V_{c2}, and (c) V_{dc}.

NPC Converter with Midpoint Grounding: The NPC converter architecture with midpoint grounding is shown in Fig. A8.1-3. The updated inductor current i_j includes the two capacitor voltages across C_1 and C_2, where phase-$j \in (a, b, c)$, are given by

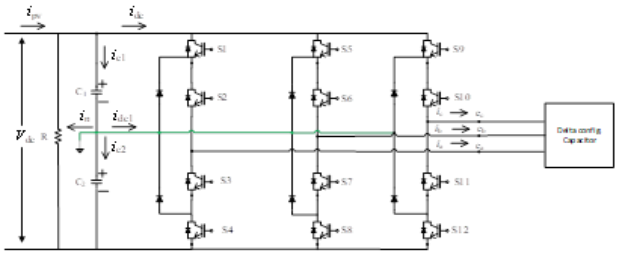

Fig. A17.3-51: NPC circuit architecture.

$$\left(\frac{L_{1ac}}{h} + R_{1ac}\right) i_j[k] + v_{jcap}[k] = \frac{L_{1ac}}{h} i_j[k-1] + [(S1)(S2)(1-S3)(1-S4)V_{c1} + (S2)(S3)(1-S1)(1-S4)V_{c2}] - v_j[k] \quad (17.3\text{-}38)$$

Simulation Results: The stable capacitor voltages V_{c1}, V_{c2}, and V_{dc} from the simulation of the high-fidelity NPC (with midpoint grounded) model are shown in Fig. A8.1-4(a)–(c). The corresponding results from the baseline PSCAD library-based NPC model are also shown. From these figures, it can be observed that the capacitor voltages V_{c1}, V_{c2}, and V_{dc} are stable and are reproduced in the developed high-fidelity model with >98% accuracy in comparison with the baseline PSCAD model.

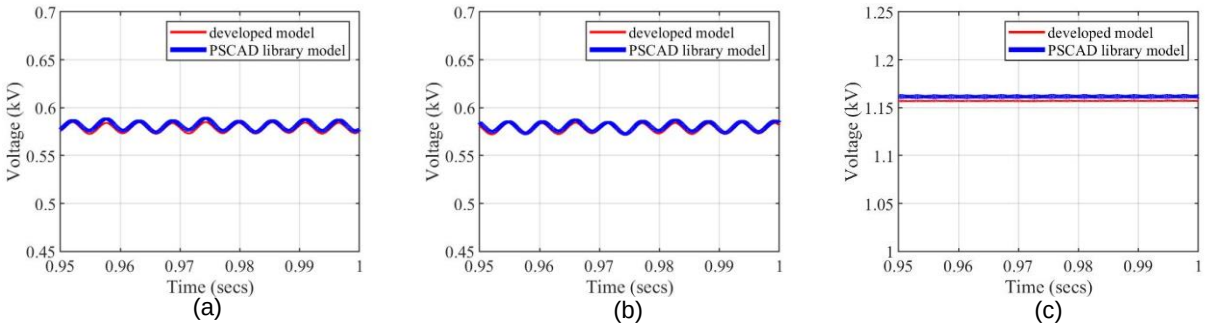

Fig. A17.3-52: NPC capacitor voltages: (a) V_{c1}, (b) V_{c2} and (c) V_{dc}.

Specific PV Plant-1 High-Fidelity Model

PV System-1: Several upgrades are included in PV system-1's inverters (in addition to the model available from the library), as follows:

a) The ac load side over-current protection, ac phase over-voltage protection, and dc link over-voltage protection are included.

b) Blocked condition is implemented in the inverter.

c) The transformer configuration is upgraded to reflect the configuration in the plant (with changes in the DAEs and the discretized model).

d) The filters are tuned based on parameters available and to meet the THD and TRD limits prescribed by the respective inverter manufacturers.

e) Multirate inverter control is implemented in the system.

The simulation results for the upgraded inverter-1 module for different operating conditions are shown in Fig. A8.1-5. The inverter ac-side currents during different dynamic operating conditions, the THD and TRD of the inverter ac-side currents, dc-link voltage, and distribution bus voltages are shown in the figure. Fig. A8.1-5(a) shows the inverter ac-side currents for different dynamic events. The different dynamic events include change in PV power operating conditions, which may be noted from the changes observed in the currents until t = 1.5 s. At t = 1.5 s, an overvoltage condition is introduced in the ac distribution voltage. The zoomed-in inverter ac-side currents during a specific change in operating condition are shown in Fig. A8.1-5 (b). The THD and TRD of the inverter ac-side currents are shown in Fig. A8.1-5(c)–(d). From the figures, it is observed that the THD and TRD are within the limits prescribed by the inverter manufacturers. The dc link voltage is accurately tracking its reference as observed in Fig. A8.1-5(e), whereas from Fig. A8.1-5(f), the change in the ac distribution voltage given at t = 1.5 s owing to an overvoltage event can be observed. This overvoltage leads to the protection features within the inverter being triggered as expected. This then leads to the zero currents observed in Fig. A8.1-5(a) after t = 1.5 s.

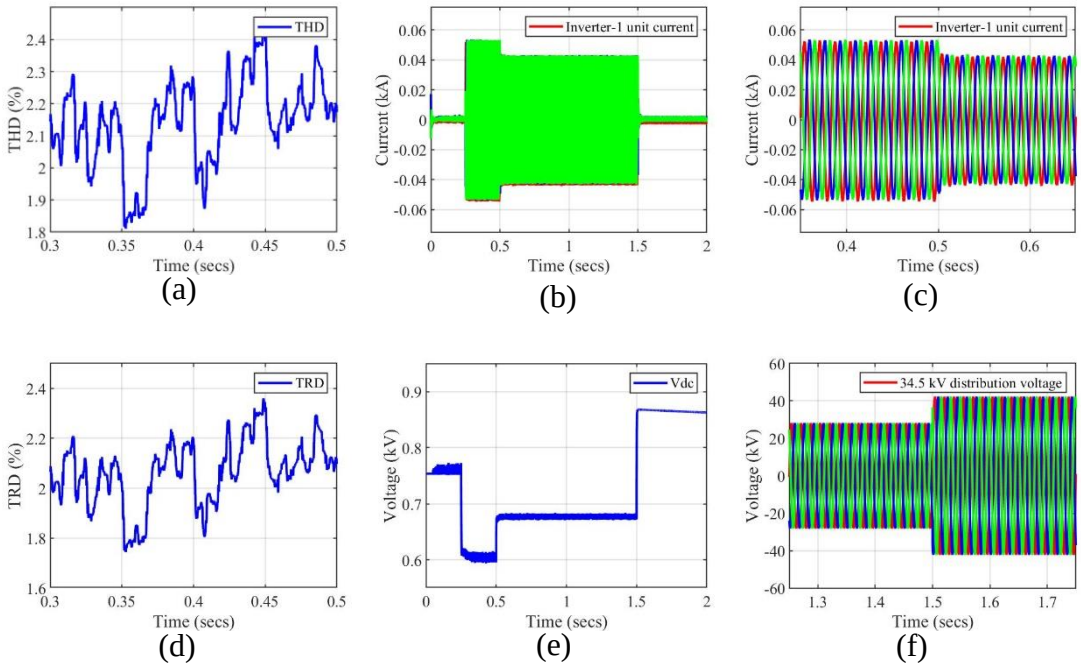

Fig. A17.3-5: Simulation results for inverter-1.

PV System-2: The upgrades in PV system-1 are introduced into PV system-2, but the implementations are very different owing to a different inverter configuration. Additionally, the filter configuration has been upgraded in the systems in PV system-2 to reflect the development in the field.

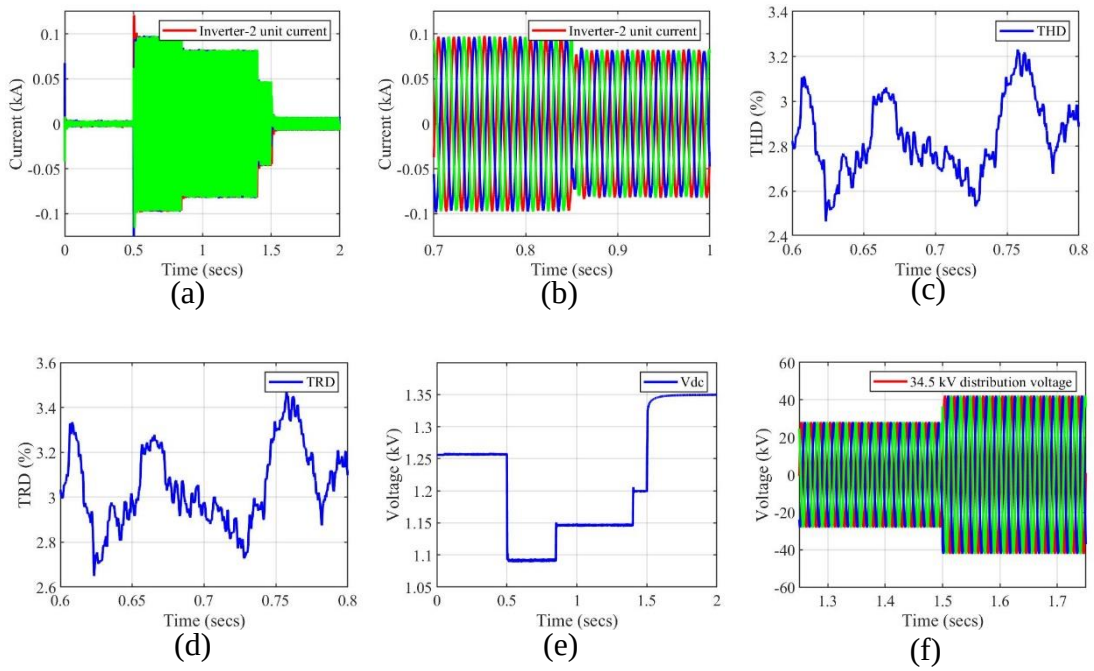

Fig. A17.3-6: Simulation results for inverter-2.

The simulation results for the upgraded inverter-2 module at different operating conditions are shown in Fig. A8.1-6. The inverter ac-side currents during different dynamic operating conditions, the THD and TRD of the inverter ac-side currents, dc-link voltage, and distribution bus voltages are shown in the figure. Fig. A8.1-6(a) shows the inverter ac-side currents for different dynamic events. The different dynamic events include change in PV power operating conditions, which may be noted from the changes observed in the currents until t = 1.5 s. At t = 1.5 s, an overvoltage condition is introduced in the ac distribution voltage. The zoomed-in inverter ac-side currents during a specific change in operating condition are shown in Fig. A8.1-6(b). The THD and TRD of the inverter ac-side currents are shown in Fig. A8.1-6(c)–(d). From the figures, it is observed that the THD and TRD are within the limits prescribed by the inverter manufacturers. The dc link voltage is accurately tracking its reference as observed in Fig. A8.1-6(e), whereas from Fig. A8.1-6(f), the change in the ac distribution voltage given at t = 1.5 s owing to an overvoltage event can be observed. This overvoltage leads to the protection features within the inverter being triggered as expected. This then leads to the zero currents observed in Fig. A8.1-6(a) after t = 1.5 s.

ST-8.2. Advanced model in PSCAD/PSSE

Data Generation: The data required in the advanced model include the three-phase ac-side voltages at the inverter terminals, the PV power generated, reactive power at the terminals, and the three-phase ac-side currents at the inverter terminals. In this report, this dataset is generated from the simulation in PSCAD of the dynamic model that includes a single inverter connecting through a transformer and a distribution line to a controlled voltage source. The voltage and frequency of the controlled voltage source are varied to provide data for grid events where voltage and frequency variations are observable. The voltage variation may happen when there are unbalanced line-line

faults and three-phase faults in the ac grid. The frequency variation may happen with a loss of generation in the ac grid. Additionally, the PV power generation capability is varied for each voltage and frequency variation to generate a comprehensive dataset. Another important parameter in the dataset generation is the sampling frequency required for the dataset. This comprehensive dataset will be used to train the RNN model. The dataset generated from an individual PV inverter in a PV plant forms basic building blocks for the advanced model that includes multiple feeders and multiple PV inverters. The dataset generation process has been fine-tuned after multiple combinations of data, sampling frequency of data captured, and operating conditions at which data are generated have been tried and tested. The dataset finally generated includes three-phase ac-side voltages at inverter terminals, PV power generated, reactive power at the terminals, and three-phase ac-side currents sampled at 50 µs. This dataset is generated at seven different PV power generation set points; at each generation set point, three different distribution grid voltage magnitude and two different distribution voltage frequencies are considered. About 160,000 data points are available. To automate the data generation process, python scripts are developed to start PSCAD simulation and record the data.

Data Processing and Storage: Once the data are generated from the simulation of the PV plant model in PSCAD, the stored file with data from PSCAD is converted to a format that supports further data processing (i.e., conversion from .out to .csv). Thereafter, the data in the file are processed to develop six different data files: an input file and an output file for each phase. Each input file contains three-phase ac-side voltages, PV power generated, and reactive power at the terminals. Each output file contains the individual ac-side phase current. The data in these files are marked for easier access in the training stage. This process is automated through Python scripts.

Training: Once the dataset is generated from PSCAD, it is used to train an RNN model in Python. The number of layers, number of neurons in each layer (and the corresponding weights and biases), type of activation function, number of history layers, and input-output combinations are the parameters available to tune in the RNN model. Multiple training runs are completed on the generated dataset to fine-tune the parameters that result in the best fit of the available data to the RNN model. The optimum RNN model uses four layers—an input layer, 10 neurons in layer-1, 3 neurons in layer-2, and 1 neuron in layer-3. It uses relu, tanh, and tanh activation functions, respectively, in the layers (with no function in the input layer), and it uses one history layer. This RNN model generates each phase's ac-side current with inputs being three-phase ac-side voltages, PV power generated, and reactive power at the terminals. Therefore, three RNN models are needed to generate the three-phase ac-side currents. The same model with different parameterization based on the training process is generated for each phase. The results from phase-a are shown in Fig. A8.2-1, with the blue curve generated from the advanced model and orange curve generated from the high-fidelity single PV inverter

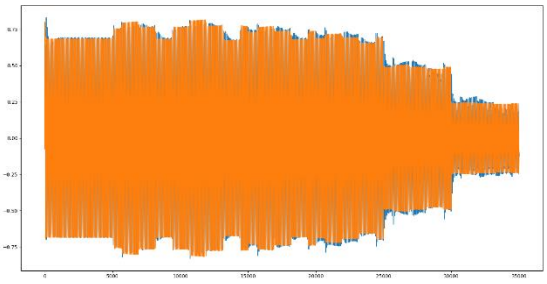

Fig. A8.2-1: Phase-a current from a four-layer RNN model.

module's model. Once training is completed, the RNN model's gains and biases are formatted and stored in files so that they can be accessed by the C code that implements the RNN model. This helps with generalization of the RNN model developed in C code and ease of re-use of the C code for multiple training runs.

C Code Development: The structure of the RNN model in Python is used to develop the C code representation of the RNN model. A sample RNN model is shown in Fig. A8.2-2 (with m = 1 in this case because there is only one history layer). In the C code, one set of RNN layers at a single time step (marked in the figure by the dashed violet line) is implemented. The inputs, value of history hidden or output states from previous time step, and outcome of the history hidden or output states from the current time step are parameters passes from PSCAD to the C code. Additionally, gains and biases at each layer are also passed. The passing of the gains and biases enable ease of re-use of the C code for every change new training completed and/or for different system configurations (PV systems, plants, etc.). The parameters passed to the function from PSCAD to C code are pointers in the C code. This enables the updates in C code to be reflected in the corresponding variables in PSCAD seamlessly. The function defined in C code needs to end with an underscore for it to be callable from PSCAD/Fortran scripts.

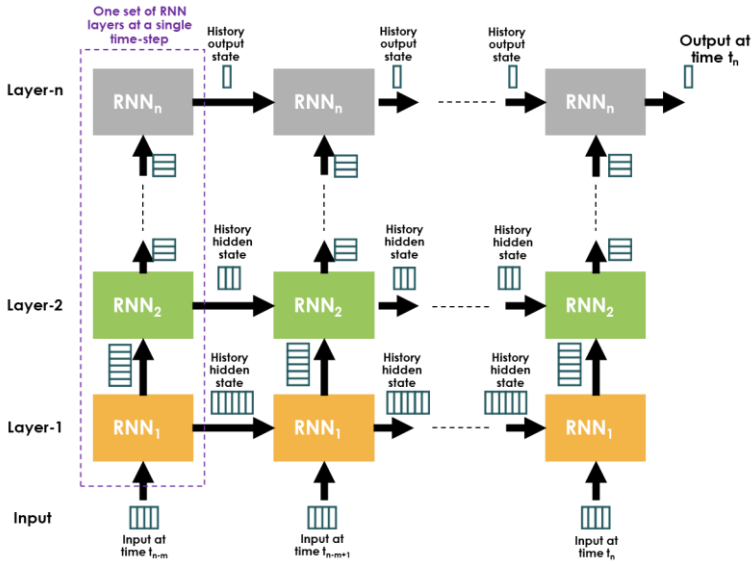

Fig. A17.3-2: General RNN model structure (implemented in C code)

PSCAD-C Advanced Model: To integrate a C code in PSCAD, the source C code needs to be incorporated in the project settings. The C code is called from within a Fortran script in the PSCAD file. In the PSCAD/Fortran script used to generate ac-side current for one phase in the advanced model, a call to a C script initializes the biases and gains in each layer of the RNN model. The C script for initialization accesses the file in which the biases and gains are stored during the training process and sends the information back to the PSCAD/Fortran script. Thereafter, the three-phase ac-side voltage, PV power generated, and reactive power at the terminals are prepared by removing the mean from the data and normalizing with respect to a predefined standard deviation that is consistent with the training process. Then, the C code is called from within the Fortran script to process the first history layer. The output from the history layer is again prepared (i.e., the mean is removed and the result is normalized with respect to the standard deviation) and the C code is again called to process the current time step layer. Once the output from the current time step layer is obtained in the Fortran script, it is post-processed by multiplying with a predefined standard deviation and summing with the mean to generate the final output. Three such PSCAD/Fortran scripts generate the three-phase ac-side current in the advanced model. Finally, a circuit is setup for

integration of the advanced model with the power grid. The three-phase ac-side voltages from the power grid are fed as inputs to the C code (through the PSCAD/Fortran script) along with the active and reactive power conditions. The output from the C codes (through the PSCAD/Fortran scripts) are the three-phase ac-side currents.

T-9. Evaluation and redesign of dynamic models

ST-9.1. Evaluation of high-fidelity model

Generic PV Plant: The simulation results from simulation of the high-fidelity PV plant model are compared with the results from the baseline PV plant model. The time taken to run 0.25 s of the baseline PV plant model is 58 hours. The extremely long time taken to simulate the baseline PV plant model limits the simulation time to only 0.25 s. The single A and multiple A (MA) matrix models, on the other hand, complete the simulation of 0.25 s in 2.58 hours and 0.18 hours, respectively. The speed-up observed is 22.4 times and 326.4 times, respectively. The simulation time step for all cases was 1 µs. The simulation results from the baseline model and the high-fidelity models are presented in Fig. A9.1-1 and Fig. A9.1-2; the information includes inductor currents, dc link voltages, inverter filter voltages, inverter filter currents, distribution transformer voltages, and distribution transformer current. The results indicate a close match, with greater than 95% accuracy.

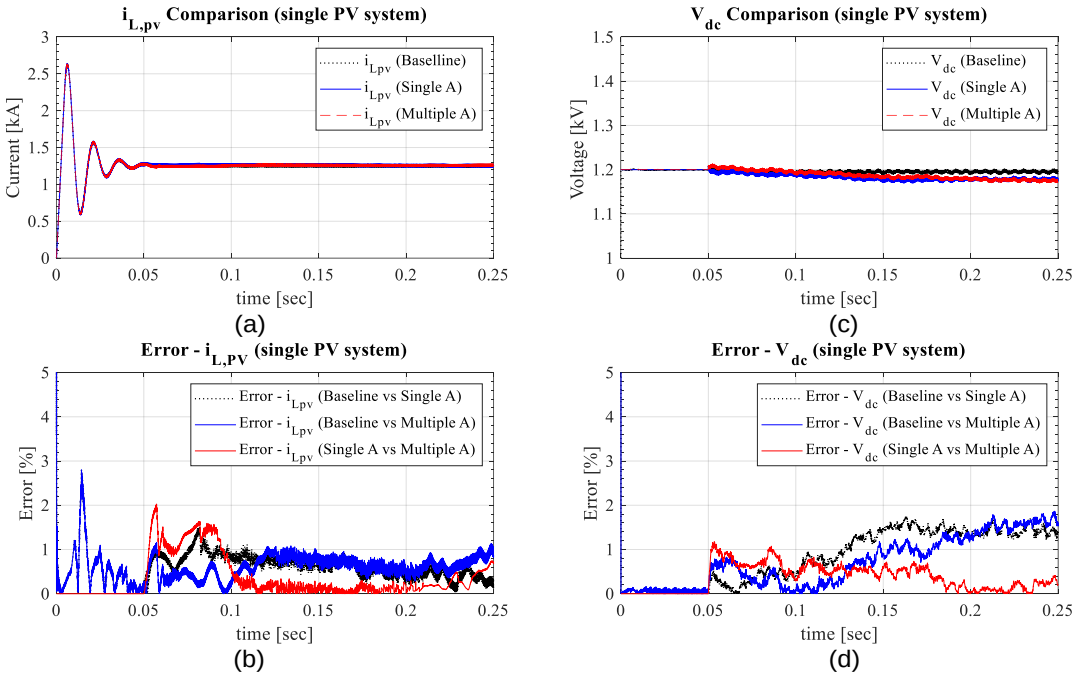

Fig. A17.3-1: Comparison of the simulation of MV distribution grid with a large number of PV inverter modules based on the proposed simulation algorithms: (a) dc-dc boost converter inductor current ($i_{L,\mathrm{pv}}$) in one PV module, (b) errors of the inductor current ($i_{L,\mathrm{pv}}$), (c) dc link voltage (v_{dc}), and (d) error of the dc link voltage (v_{dc}).

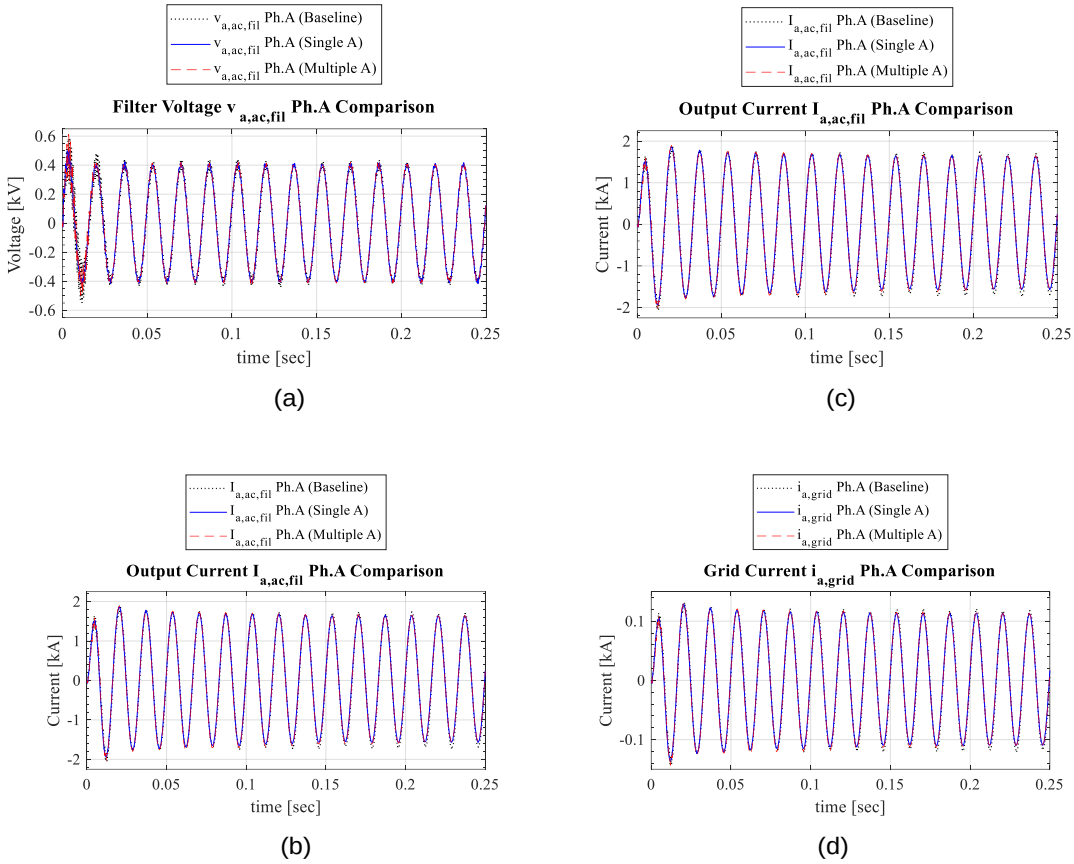

Fig. A17.3-2: Comparison of the simulation of MV distribution grid with a large number of PV inverter modules based on the proposed simulation algorithms: (a) filter capacitor voltage ($v_{a,\mathrm{ac,fil}}$) phase A in one PV inverter module, (b) dc-ac inverter output current ($i_{a,\mathrm{ac,fil}}$) phase A in one PV inverter module, (c) grid voltage ($v_{a,\mathrm{grid}}$) phase A at the primary side of distribution transformer, and (d) grid current ($i_{a,\mathrm{grid}}$) phase A at the primary side of distribution transformer.

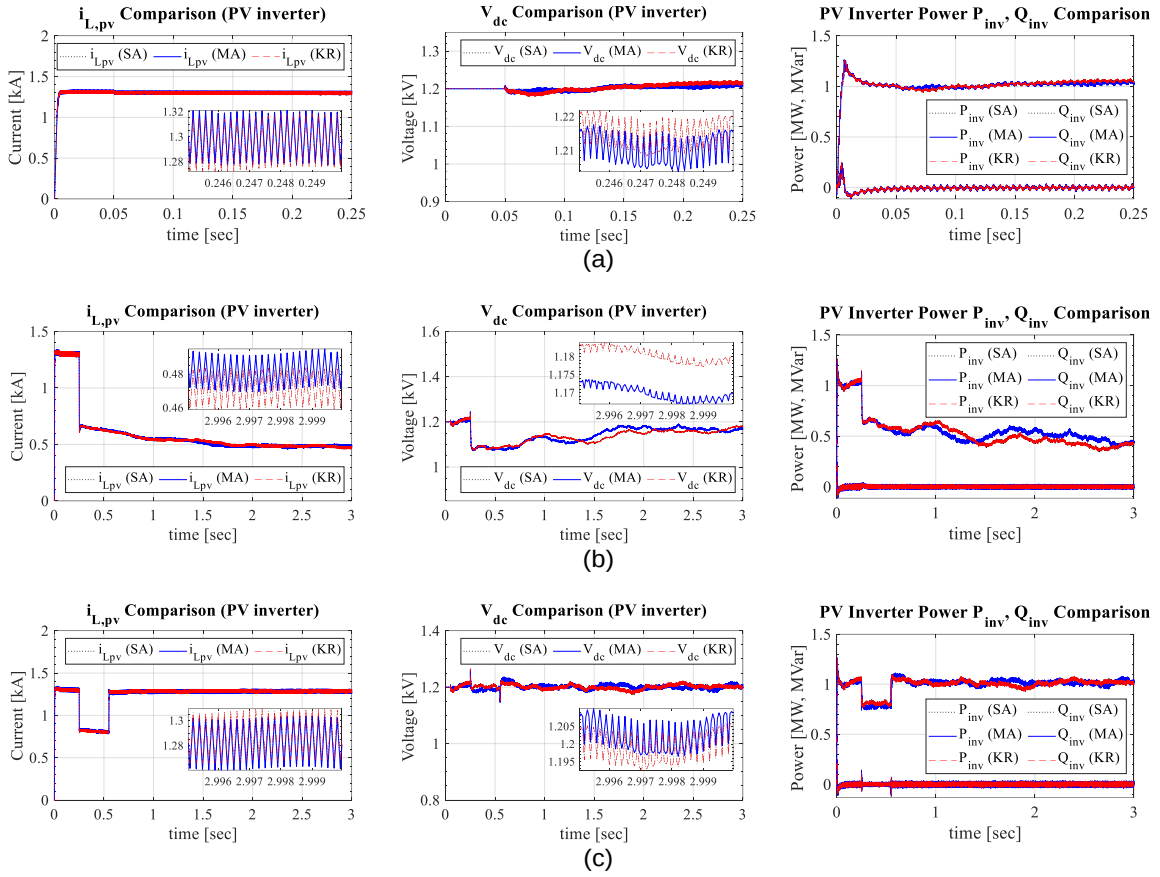

Fig. A17.3-3: Comparison of converter inductor current ($i_{L,\mathrm{pv}}$), dc link voltage (v_{dc}), and inverter output power (P_{inv} and Q_{inv}) in the simulated system based on the numerical simulation algorithms: (a) Case 1, steady-state; (b) Case 2, power step change; and (c) Case 3, grid fault condition.

Three different cases are considered to compare between the simulation results from baseline and high-fidelity PV plant models:

- Case 1: Initialization and steady-state operation
- Case 2: A step change in power reference provided to the PV inverters from 1.0 pu to 0.5 pu at 0.25 s
- Case 3: A grid fault condition, given by a grid voltage step change from 1.0 pu to 0.8 pu at 0.25 s

The fault is cleared in three cycles upon the fault occurrence. Some of the states from the simulation results are illustrated in Fig. A9.1- and Fig. A9.1-. The inductor current of the dc-dc boost converter ($\mathrm{i_{L,pv}}$), dc link voltage ($\mathrm{V_{dc}}$), and output active and reactive powers ($\mathrm{P_{inv}}$ and $\mathrm{Q_{inv}}$) in the PV inverter module are shown in Fig. A9.1- for the three cases. As can be seen from the results in Fig. A9.1-4, the similarities of the states are observed between the models in the different cases. It should be noted that the results of the single A model are identical with the ones of the Schur complement model for all cases, which can be seen by the overlapping trajectories of the states from the simulation of the two models. In the MA model, the results present similar trajectories

with small differences that can be seen in the dc link voltage (V_{dc}) and inverter output power (P_{inv}) in Fig. A9.1-(b)–(c). The differences are produced by the single time step delay and small capacitors introduced in the multiple subsystems in the MA algorithm.

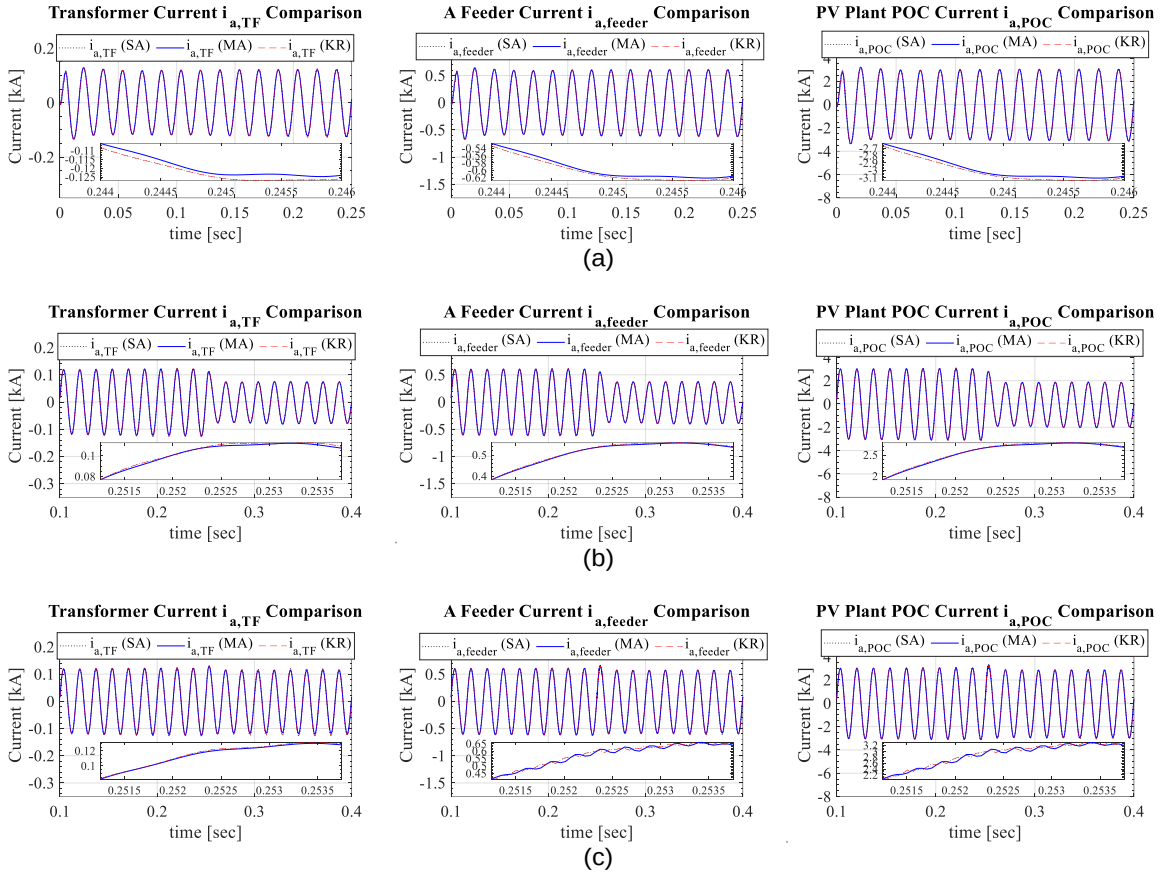

Fig. A17.3-4: Comparison of secondary side current ($i_{a,TF}$), feeder current ($i_{a,feeder}$), and plant current ($i_{a,POC}$) in the simulated system based on the numerical simulation algorithms: (a) Case 1, steady-state; (b) Case 2, power step change; and (c) Case 3, grid fault condition.

The secondary side transformer current ($i_{a,TF}$), the feeder current ($i_{a,feeder}$), and the PV plant POI current ($i_{a,POC}$) from the simulation of the different PV plant models in the three cases are shown in Fig. A9.1-. As observed from Fig. A9.1-, the Fig. A9.1- results show that the states from the three simulated models follow similar trajectories in all the cases. It should be noted that the states from the simulation of the single A model and KR model are identical in all the three cases. However, small differences are observed between the states from the simulation of MA model and KR model. The observed differences in states from both Fig. A9.1- and Fig. A9.1- arise from the single time step delay and the additional small capacitor introduced in the MA model.

ST-9.2. Evaluation of advanced model

As the initial step, the dynamic model of the PV system-2 in PSCAD is started using Python, and data are captured. The PV system-2 dynamic model includes the inverter connected to the transformer. The generated data include 160,000 data points used to train the RNN models. These data points include three-phase ac-side voltages, PV

power generated, reactive power at the terminals, and three-phase ac-side currents sampled at 50 µs. After the data generation, the data are further processed into six different .csv data files (from .out files); each .csv file includes an input file and an output file for each phase. Each input file contains three-phase ac-side voltages, PV power generated, and reactive power at the terminals. Each output file contains the individual ac-side phase current. The RNN model uses four layers—10 neurons in layer-1, 3 neurons in layer-2, and 1 neuron in layer-3 along with relu, tanh, and tanh activation functions, respectively. The same model with different parameterization based on the training process is generated for each phase. The results from phase-a are shown in Fig. A17.3-53(a)–(c), with the blue curve generated from the advanced model and orange curve generated from the high-fidelity single PV inverter module's model. Once the training is completed, the RNN model's gains and biases are formatted and stored in files.

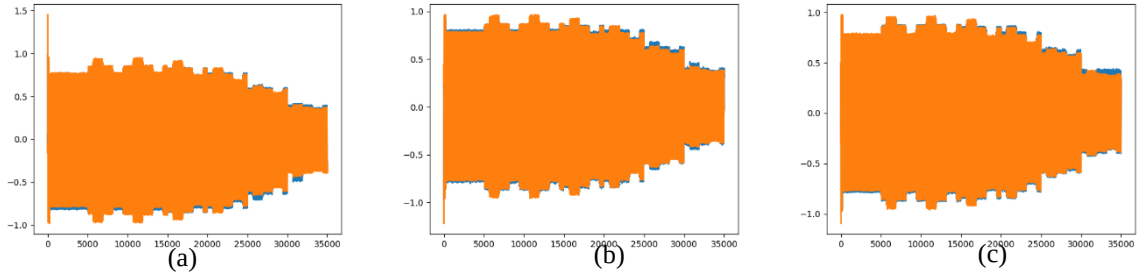

Fig. A17.3-53: Currents from the four-layer RNN model: (a) phase-a; (b) phase-b; and (c) phase-c.

After the gains and biases are formatted and stored in the files, the corresponding C code is generated that can interact with the trained RNN AI model parameters along with Fortran scripts in PSCAD that can interact with the C code.

T-10. Present scenario development

ST-10.1. Incorporate suite of dynamic PV system models

Quasi-Dynamic Model Integration in PSCAD

Aggregating PV plant quasi-dynamic model: The aggregation of multiple PV systems in a quasi-dynamic model has been investigated via Kron's elimination. The objective is to replace many PV systems with an equivalent PV system by capturing the network that interconnects the PV systems into the equivalent. The method is flexible because it can either reduce the equivalent circuit to a single three-phase bus or retain equivalents of parts of the system, such as filters. The application of this method on the Santa Fe facility to develop an aggregated quasi-dynamic model for the PV plant with two PV systems has shown remarkable similarity in simulation results compared with the corresponding baseline model in PSCAD. The corresponding simulation results are shown in Fig. A17.3-54.

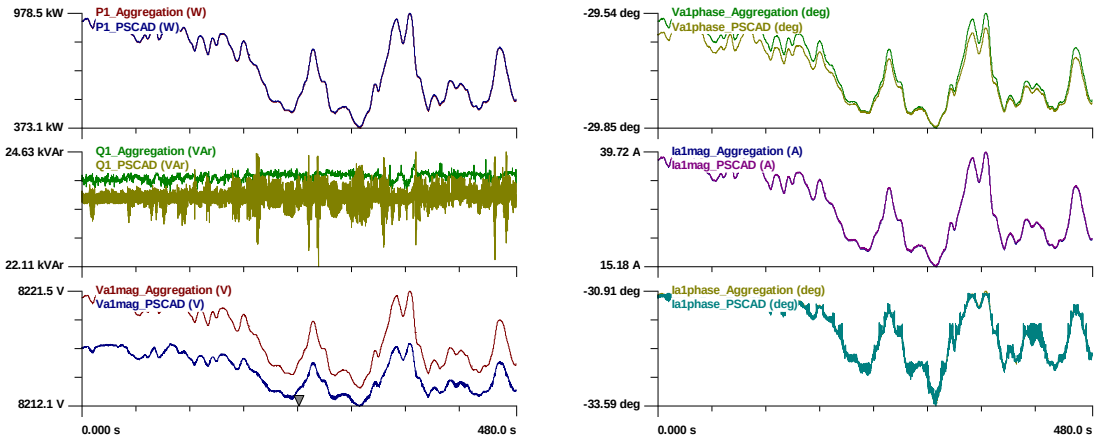

(a) (b)

Fig. A17.3-54: Comparison of an aggregated quasi-dynamic model to a detailed model for Santa Fe facility: (a) active power, reactive power, and ac-side voltage magnitude; and (b) ac-side voltage magnitude, ac-side current magnitude, and ac-side current phase angle.

High-Fidelity PV Plant Model Integration with EMT Model of Power Grid in PSCAD

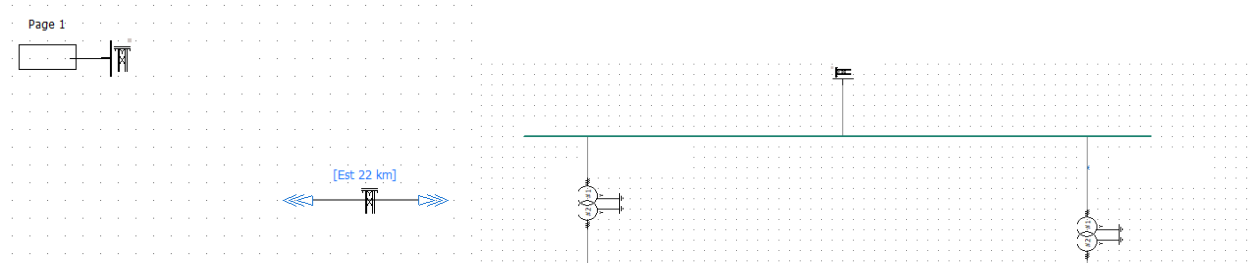

(a) (b)

Fig. A17.3-2: Integrating the power grid present scenario EMT model (a) with a high-fidelity model of the specific PV plant-1 (b) using a transmission line with remote ends.

Upgrades in EMT Model of Power Grid near the Affected PV Plants

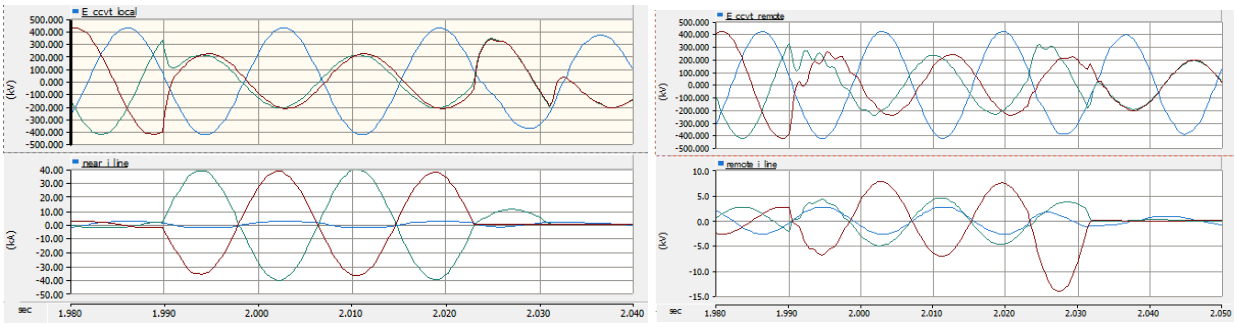

Fig. A17.3-3: Local end and remote end voltage and current plots from the EMT simulation of the present scenario grid model for the Angeles Forest fault event (based on the upgraded EMT model).

Upgrades to the Specific PV Plant-1's High-Fidelity Model:

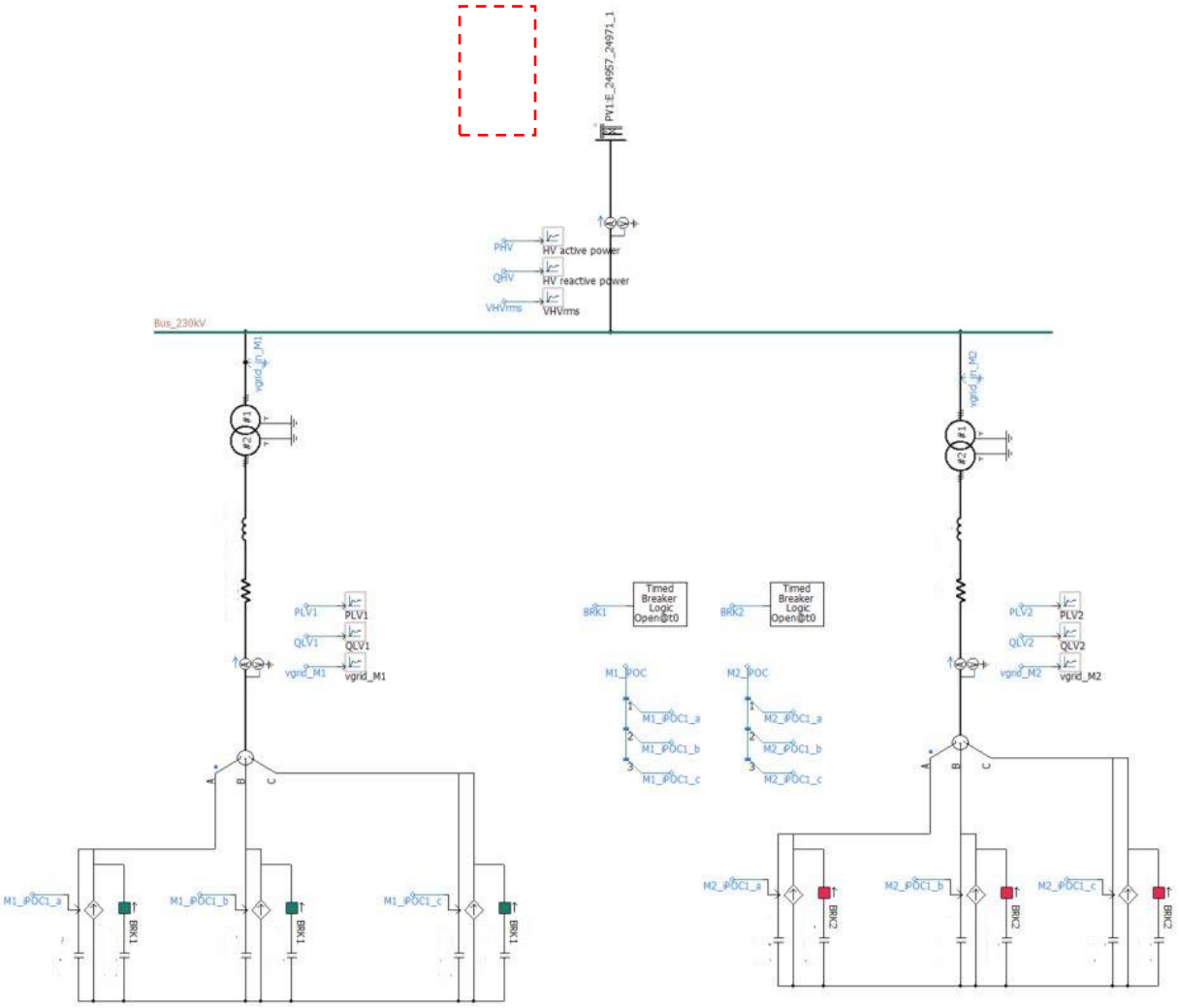

Fig. A17.3-4: Simulation model for the specific PV plant-1.

Equivalencing of the EMT Model for Present Grid Scenario:

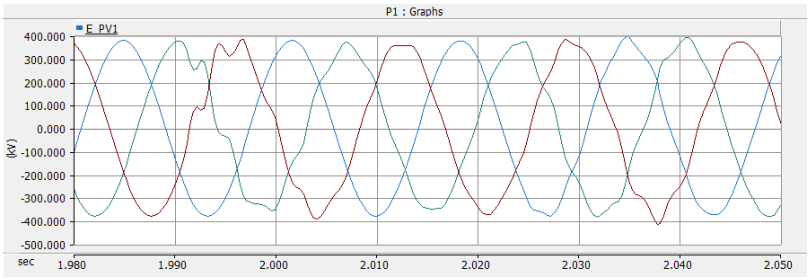

(a)

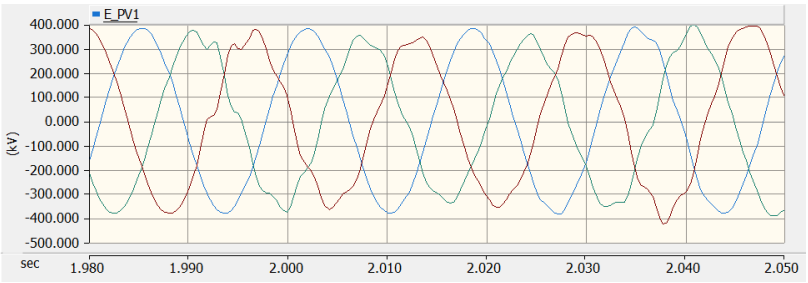

(b)

Fig. A17.3-5: Voltage plots near PV plant -1 from the EMT simulation of the present scenario grid model for Angeles Forest fault event: (a) original model, and (b) after equivalencing the EMT model to hide sensitive WECC information.

C code development for High-Fidelity Model of PV plant in RSCAD

The voltages and currents in the high-fidelity MA model of the specific PV plant-1 in RSCAD are shown in Fig. A17.3-. These plots indicate the stability of the proposed simulation algorithms and high-fidelity models in RSCAD, and the results are as expected (when compared with the corresponding results in PSCAD).

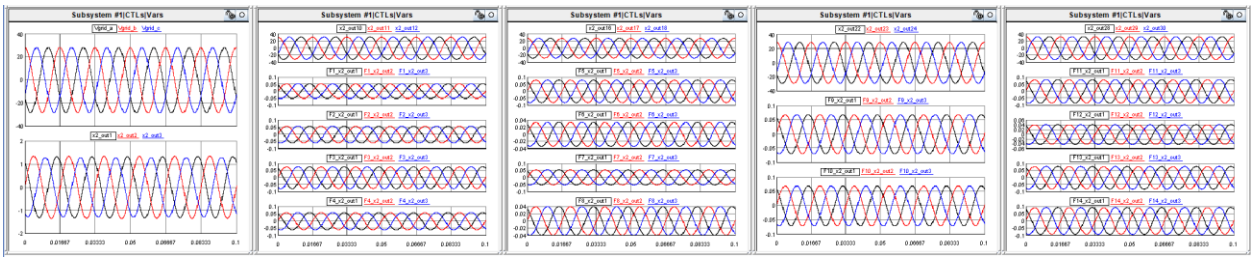

Fig. A17.3-55: Voltages and currents from test simulation results of the MA high-fidelity model of the specific PV plant-1 in RSCAD.

T-11. Future scenario model development

ST-11.1. Upgrade present model with future model in PSCAD

Identification of the Plants that will Potentially Retire:

Different sources used to identify the retired plants are summarized in Table A17.3-.

Table A17.3-1: Information on conventional power plants that are likely to retire in the next 10 years

S. No.	Link	Source	Plant	Unit	Pgen in WECC	Pmax in WECC	Utility
1	link1	EIA site [36]	2	2	520	1061	LADWP
2	link2	IID site [37]	1	1	23	75	IID
3	link3	Utility dive news [38]	2	5	611	645	LADWP, PG&E
4	link4	S&P news [39]	2	2	68	109.5	PG&E
5	link5	KBPS news [40]	1	6	629	629	SDG&E
6	link6	Sierra club news [41]	2	3	228	260	PG&E
7	link7	Planetizen news [42]	1	2	51	87	LADWP
8	link8	SMUD report [43]	2	2	52	63.1	PG&E
9	link9	Report on plant retirement by UCSUSA [44]	11	26	2,915	3,206	PG&E, SCE, SDG&E
10	link10	Report by PSE health energy [45]	13	32	2,434	2,568	PG&E, SCE, SDG&E
Total			**37**	**81**	**7,531**	**8,703.6**	

Pgen = Generated power; Pmax = Maximum power.

Upgraded Future Grid Scenario 1: The summary of power generation in the modified scenario is summarized in Table A11.1-2.

Table A17.3-2: Power generation in California in the upgraded WECC power grid TS model

Plant Type	% of total power
Solar, wind and BESS in the original case	28
Large hydro, geothermal and biomass	17
Plants which may potentially retire in next 10 – 15 years	10
Old plants that may potentially retire in next 10 – 15 years	5
Proposed bio-fuel plants [14], [15]	1
Others (include the conventional and unidentified plants)	39

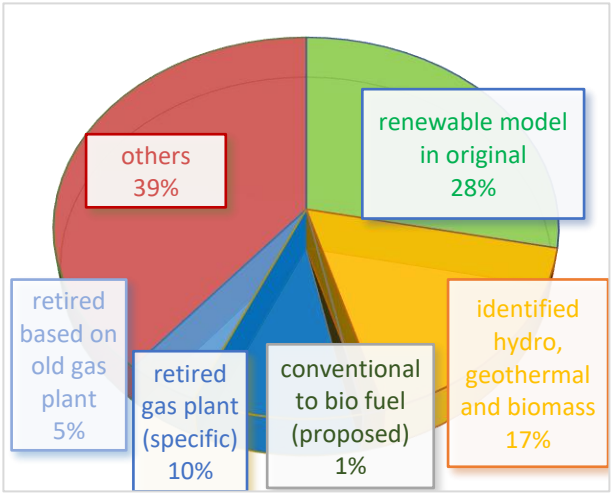

These identified plants are similar to the plant retirement information provided in the California ISO (CAIS) study report [46], summarized in Table A11.1-3. According to this CAISO transmission planning, conventional plants with a total power generation of ~15 GW will be retired.

Table A17.3-3: Power capacity in different regions

Local capacity area	Capacity (MW)	WECC utility (from map)
Greater Bay Area	4,427	PG&E
Sierra	153	PG&E, LADWP
Stockton	361	PG&E
Fresno	669	PG&E
Kern	407	SCE, PG&E
LA Basin	3,632	LADWP
Big Creek-Ventura	695	SCE
San Diego-IV	131	SDG&E
CAISO System	3,933	SCE, SDG&E
Total	**14,408**	

Scenario 2: In this scenario, all the conventional plants in California are replaced with renewable plant models. For this scenario, all the replaced model parameters are the same in all the replaced plants.

Dynamic Model Replacement in the Existing TS Model of the Grid: A Python-based tool is built using the PSSPY library to replace the dynamic model of the identified conventional power plants with the renewable plant model. The model parameters are used from the existing renewable plant with similar power ratings. The following dynamic models are used in the renewable plants:

1. Plant generator model—REGCA1
2. Plant power control model—REPCA1
3. Electrical control model (inverter control)—REECB1

The steps used for this process are described in the flowchart in Fig. A17.3-56.

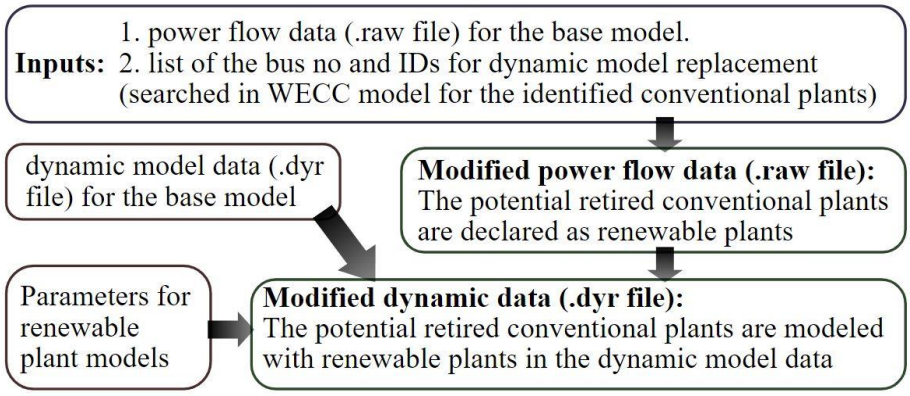

Fig. A17.3-56: Process taken to update the existing TS dynamic model of power grid (26HS2) to increase renewable penetration in the dynamic model.

Plant Dynamic Model: The parameters in the replaced renewable plant models are set based on the existing active renewable plants in the 26HS2 model. The voltage and frequency controls in the PPC models are shown in Fig. A17.3-57. The electrical control is shown in Fig. A17.3-58. This model has provisions to enable voltage and frequency control.

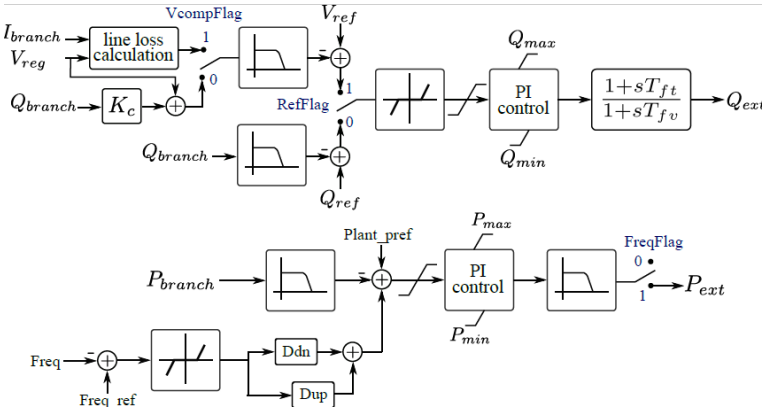

Fig. A17.3-57: Renewable power plant model (REPCA).

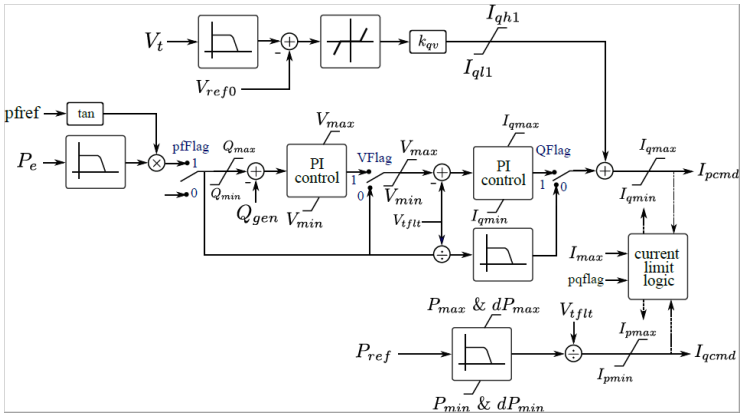

Fig. A17.3-58: Renewable energy electrical control model (REECB).

Enabling the frequency control causes the active power reference to be drooped with the frequency deviation from the nominal value. Also, this PPC model regulates either the reactive power output or the terminal voltage, depending on whether the voltage control is disabled or enabled. The electrical control model (representing the inverter controller) for the replaced renewable plants is shown in Fig. A17.3-58. Here, the droop-based voltage control at inverter through reactive current injection gain k_{qv} is present (in addition to control of reactive power or voltage at inverter terminals). All the flags are set to zero for this work, enabling constant reactive power regulation through the reactive current control. Additionally, the parameter k_{qv} is used to provide fast voltage control at inverter terminals.

ST-11.3. Test and redesign in real-time simulations in a real-time simulator (like RTDS)

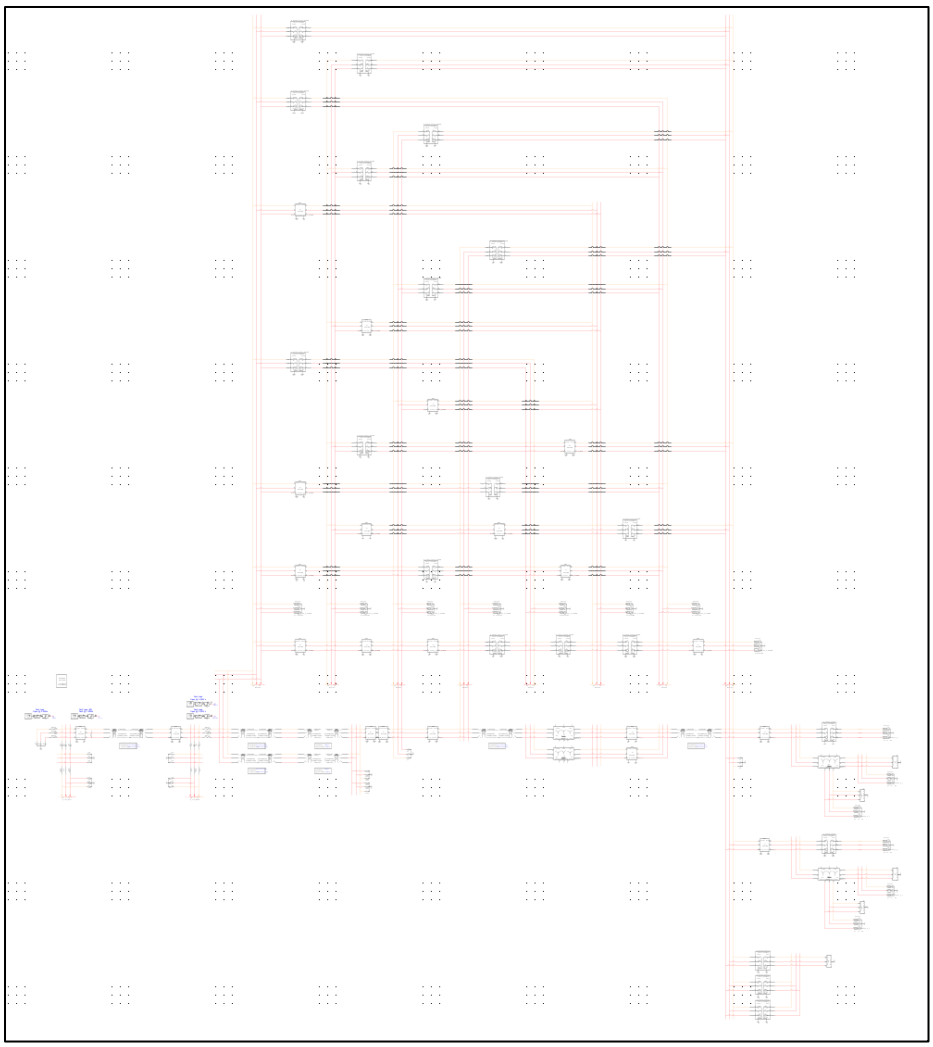

Fig. A17.3-59: Future scenario grid model in RSCAD (RTDS) for real-time simulation.

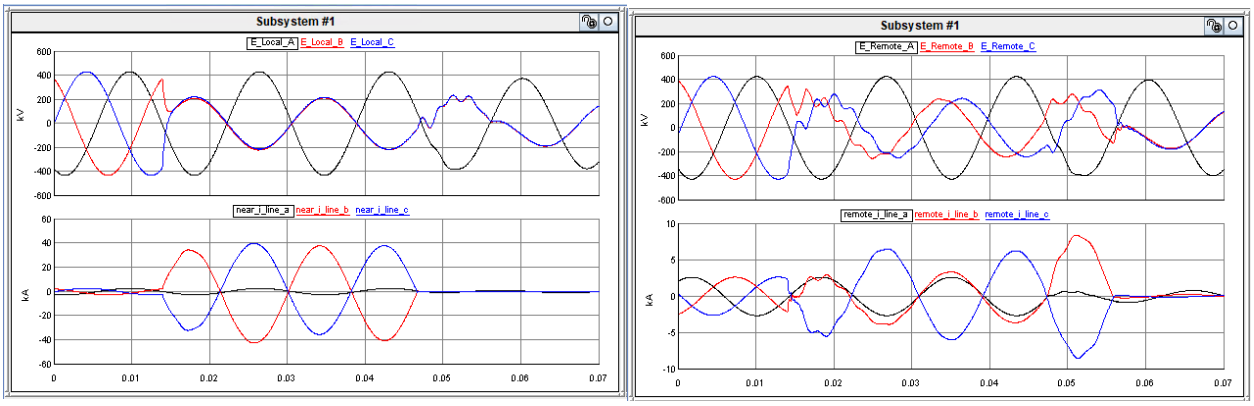

Fig. A17.3-60: Simulation results of the developed model of the future scenario of power grid in RSCAD (RTDS) for line-to-line fault: left, voltages and current measured at the local end of the fault; and right, voltages and currents measured at remote end of the fault.

T-13. Advanced control functionalities

ST-13.1. Incorporate designed control methods

Model in MPC

To apply the model-based predictive control (MPC) for improving the voltage response during faults for any generic PV plant, the model development process for any generic PV plant is first identified. A model aggregation methodology is developed through recursively implementing a Norton-Thevenin equivalencing approach. The aggregation method considers the output voltage of each PV inverter and the impedance of LCL filter, step-up transformer, and feeder line parameters to generate a single series-connected impedance with a voltage source.

In this report, a 125 PV inverter-based generic PV plant is considered, as shown in Fig. A17.3-61. Note that the plant consists of five feeders with five PV systems in each branch. Each PV system consists of five two-level converters, each in series with an LCL filter. These two-level converters are connected to a single step-up transformer.

A single step in the aggregation method is shown in Fig. A13.1-2 In this step, there is recursive aggregation of two PV systems (marked by the dashed line in the left most figure)—first through equivalent voltage source and an impedance in series representing each PV system, then performing Norton equivalencing and applying Kirchhoff's current law/impedance reduction, and finally performing Thevenin equivalencing to represent the two PV systems with a single voltage and series connected impedance. The same step is applied again and again until all the PV systems in a feeder are equivalenced by a single voltage source with a series-connected impedance. Once all the feeders are reduced to a voltage source with a series-connected impedance, Norton followed by Thevenin equivalencing is performed to generate a single voltage source with a series-connected impedance for the whole PV plant.

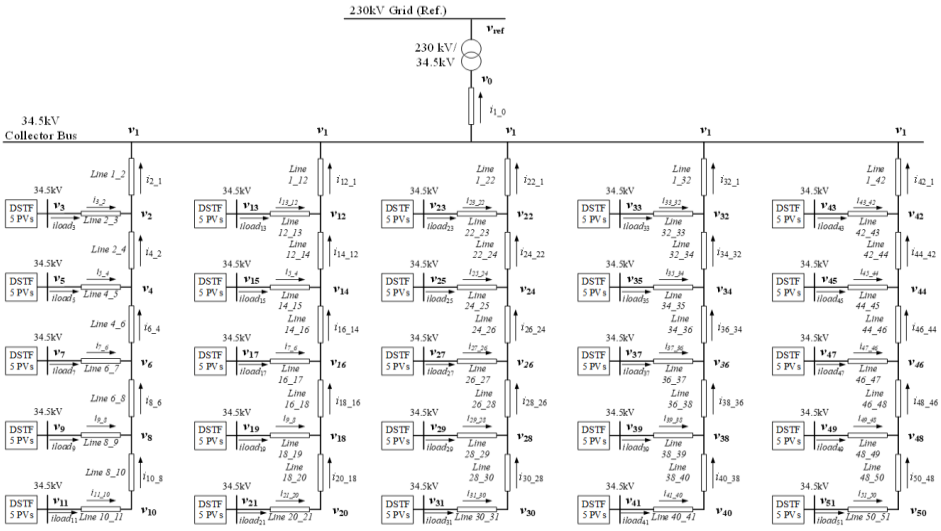

Fig. A17.3-61: Schematic of the baseline model.

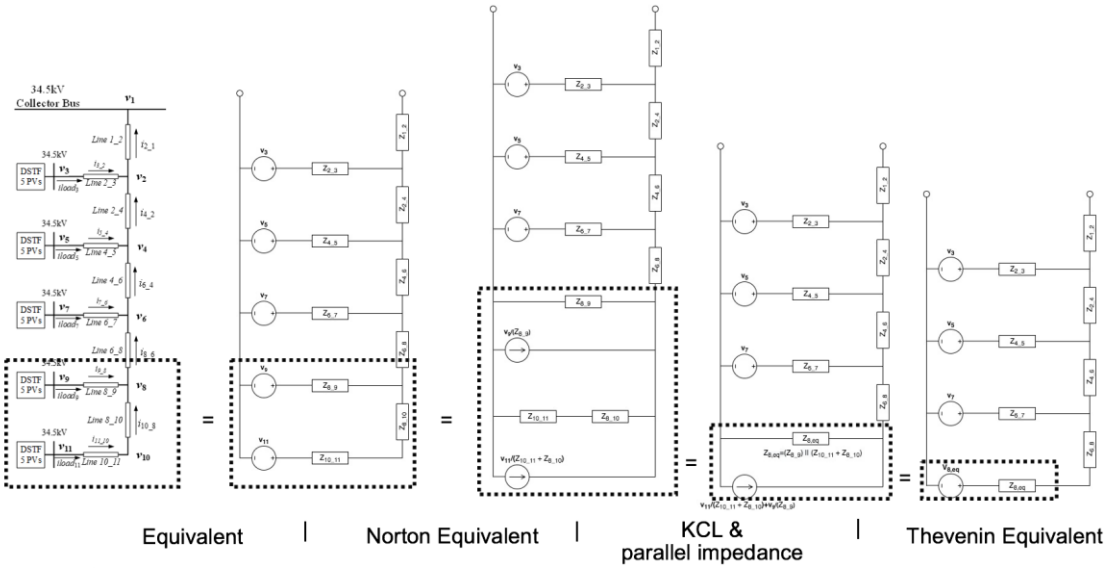

Fig. A17.3-62: Demonstration of a single step in the aggregation methodology.

The motivation behind aggregating the model is to represent the 125 PV inverter-based PV plant by a single aggregated voltage source connected to an equivalent aggregated impedance. In addition to the diagram shown in Fig. A13.1-2, the following pseudocode details the recursively defined algorithm for aggregating a single feeder.

Algorithm 1: Recursive Branch Equivalencing Algorithm

```
Procedure Equivalence(N Source Feeder)
    if N = 1 then
        return V_N, Z_N
    else
        //Norton-Thevenin equivalencing of N^th and (N-1)^th voltage sources
        V_{N-1} ← V_N/Z_N + V_{N-1}/Z_{N-1}
        V_N ← 0
        Z_{N-1} ← Z_N || Z_{N-1} + Z_{N-1,N-2}
        Z_N ← ∞
        Equivalence(N-1 Source Feeder)
```

The simulation results in Fig. A13.1-3 demonstrate the aggregation of (a) a single PV system, (b) a single feeder, and (c) the entire PV plant. These models are compared with the simulation results from the baseline model, and the results are closely matched.

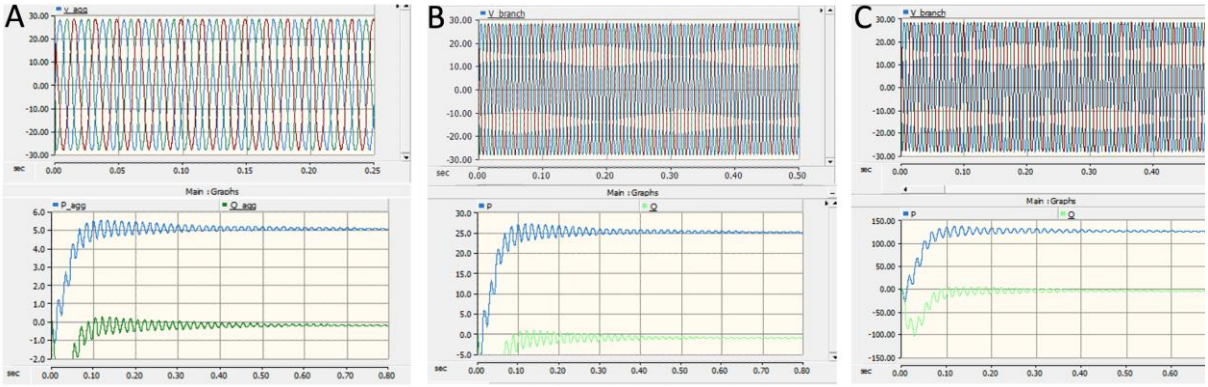

Fig. A17.3-63: Voltage and reactive power measurements for aggregation of (a) a single PV system, (b) a single feeder, and (c) the entire PV plant.

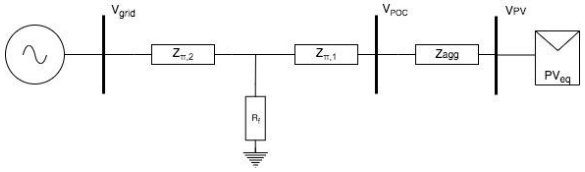

Fig. A17.3-64: Schematic of a grid connected PV system (three-phase-to-ground).

Based on the aggregated model, the 125 PV inverter-based PV plant connected to the ac grid is modeled as shown in Fig. A13.1-4. In this case, a three-phase-to-ground fault is assumed on the transmission line connected to the PV plant. Assuming a three-phase-to-ground fault in between two 7 km pi sections, the following equation with the assumption that the voltage at fault location ≈ 0 can be obtained:

$$Q_{ref} = \frac{v_{ref}^2}{\gamma^2 |Z_{eq}| csc\ (\theta_Z)}$$

$\mathrm{Q_{ref}}$ is the calculated reactive power value needed to regulate the voltage at the POC during the mentioned fault. $\mathrm{Z_{\pi,1}}$ is the impedance of the first pi section, $\mathrm{Z_{agg}}$, is the equivalent impedance of the PV plant obtained from aggregation method, $\mathrm{Z_{eq}} = \mathrm{Z_{\pi,1}} + \mathrm{Z_{agg}}$, and $\gamma = 1 - \frac{\mathrm{Z_{agg}}}{\mathrm{Z_{eq}}}$. Using the aggregated line parameters obtained and substituting $\mathrm{Z_{eq}}$ in the equation above, the MPC implementation is tested on the generic PV plant model.

To further generalize the MPC formulation, it has been updated to include the fault resistance value and avoid the zero-voltage assumption at the location of the fault.

Based on the single line diagram shown in Fig. A17.3- for the connection of the generic PV plant to the power grid, the updated closed-form solution from the MPC by solving an optimization problem (that minimizes the voltage difference at the plant's point of interconnection with respect to a defined reference voltage) is:

$$Q = -\frac{1}{4|Z_{eq}|}|V_r|^2 \sin^2\left(\theta_z + \theta_{v_1} - \theta_{v_r}\right) csc(\theta_z)$$
$$+ \frac{1}{4\left|Z_{eq}\right| \csc(\theta_z)}\left(|V_r| \sin\left(\theta_z + \theta_{v_1} - \theta_{v_r}\right) \csc(\theta_z)\right.$$
$$\left. + V_r e^{-j2\theta_{v_1}} \left(\frac{Z_{plant}}{Z_{plant} + Z_{rest} + Z_r}\right) - 2v_{ref} \frac{e^{-j\theta_{v_1}}\left(Z_{plant} + Z_{rest} + Z_r\right)}{(Z_{rest} + Z_r)}\right)^2$$

where,

$$Z_{eq} = \left[R_{plant} + R_{TX_2} + R_{\pi_1} + R_r\right] + j\left[X_{plant} + X_{TX_2} + X_\pi + X_r\right]$$

$$V_1 = V_{poc}\left(\frac{Z_{plant} + Z_{rest} + Z_r}{Z_{rest} + Z_r}\right) - V_r\left(\frac{Z_{plant}}{Z_{rest} + Z_r}\right)$$

$$Z_r = Z_{\pi_2} || R_f = \frac{Z_{\pi_2} \cdot R_f}{Z_{\pi_2} + R_f}$$

$$V_r = V_{grid} \cdot \frac{R_f}{Z_{\pi_2} + R_f}$$

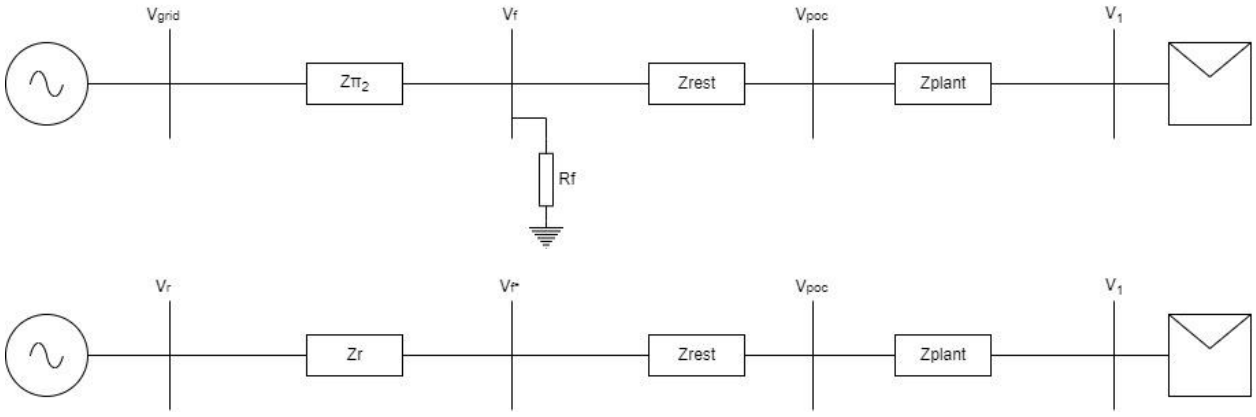

Fig. A17.3-5: Top: One-line diagram of a generic PV plant connected to the power grid (with a three-phase-to-ground fault on the line connecting to the PV plant). Bottom: Equivalent one-line diagram that removes the fault resistance based on equivalencing.

ST-13.2. Evaluate performance in suite of dynamic models and redesign

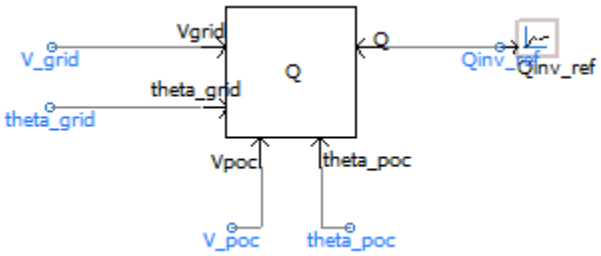

Fig. A17.3-65: Reactive power reference generator module in PPC using MPC formulation.

```
!IMPEDANCES
!Plant impedance
      Leq1 = 0.0176
      X_Leq1 = 2.0 * pii * 60.0 * Leq1 ! / Zbase
      Req1 = 0.0231 ! / Zbase
      Zplant = CMPLX( Req1 , X_Leq1) * alpha**2
!pi section line impedance
      pi_len1 = 18500.0
      pi_len2 = 1500.0
      Xpi = 0.593346E-6
      Rpi = 0.336786E-7
      Zpi1 = CMPLX( Rpi * pi_len1 , Xpi * pi_len1 ) * (230**2/125)
      Zpi2 = CMPLX( Rpi * pi_len2 , Xpi * pi_len2 ) * (230**2/125)
!Fault resistance
      Rf = 0
      Rf_pu = Rf ! / ( 230**2 / (125) )
!Zr
      ! temp1= Zpi2 + CMPLX( REAL(Zpi2 + Rf_pu) , IMAG(Zpi2) )
      Zr = ( Rf_pu * Zpi2 ) / ( Rf_pu + Zpi2)
!Zrest
      Xtx = 0.06 * (230**2/125)
      Zrest = Zpi1 + CMPLX ( 0 , Xtx )
!Zeq
      Zeq = Zplant + Zrest + Zr
!Voltages and temporary values
      Vpoc = $Vpocc
      V_gridd = CMPLX( $Vgrid * COS($theta_poc - $t_g) , $Vgrid * SIN($theta_poc - $t_g) )
      Vr = 230000 * V_gridd * ( ( Rf_pu ) / ( Zpi2 + Rf_pu ) )
      denom = ABS( Zeq ) * ( Zrest + Zr )
      V1 = Vpoc * ( (Zplant + Zrest + Zr) / (Zrest + Zr) ) - Vr * ( Zplant / ( Zrest + Zr ) )

!Angles
      t_v1 = ATAN (IMAG(V1) / REAL (V1)) + pii

      ! t_v1 = ARG(V1)
      t_z = ATAN (IMAG(Zeq) / REAL (Zeq)) ! + pii

      t_vr = ATAN (IMAG(Vr) / REAL (Vr)) ! + pii


!Closed form Q
      Q_complex = ((Vpoc*(Zplant + Zrest + Zr) - Vr*(Zplant)) * (V1 - Vr) )/ denom ! for the line 74 to be true this has to be actual value not pu value.

!Objective function Q
      a = CMPLX (COS(-2*t_v1),SIN(-2*t_v1))
      b = CMPLX (COS(-t_v1),SIN(-t_v1))
      sqr_term= ABS(Vr)*SIN(t_z+t_v1-t_vr)*(1/SIN(t_z)) + Vr*a*(Zplant/(Zplant+Zrest+Zr)) - 2*Vpoc*b*((Zplant+Zrest+Zr)/(Zrest+Zr))
      Q_obj= (1/(4*ABS(Zeq)*(1/SIN(t_z))))*((ABS(Vr)*SIN(t_z+t_v1-t_vr)*(1/SIN(t_z)))**2 + sqr_term**2)
      $Q= ABS(Q_complex)/(125E6)
```

Fig. A17.3-66: MPC-based reactive power reference generator implementation in the PSCAD.

T-14. Demonstration of future scenario

ST-14.1. Evaluate performance of advanced control functions

HIL Test Setup to Evaluate Inverter Control

The MPC-based reactive power voltage controller formulated in the previous task of the report will be further evaluated through control hardware-in-the-loop methodology. The overview of the control hardware-in-the-loop setup is shown in Fig. A17.3-40, where the signal flows are shown between the inverter controller in DSP and the inverter hardware implemented in the real-time simulation (real-time inverter model).

The DSP controller takes the inverter output voltage and current in addition to the active and reactive power reference (from the simulated PPC of the power plant) to generate the PWM signals that are used to control the real-time inverter model in Opal-RT. The control of voltages and currents in the *dq* domain will be carried out in the DSP controller in addition to generating the PWM output. Note that the reactive power reference (from the simulated PPC) is obtained from the MPC formulation mentioned earlier in the report. The DSP control code is being developed for a F28335 DSP via the Texas Instruments–based development environment Code Composer Studio.

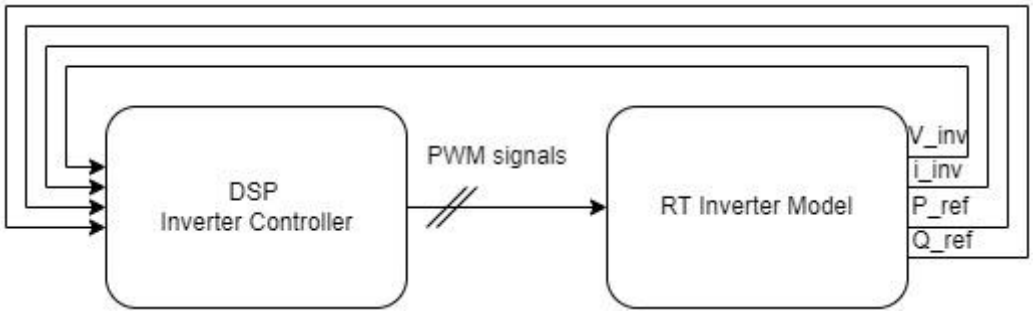

Fig. A17.3-1: DSP inverter controller interaction with real time inverter model.

T-15. Advanced control functionalities

ST-15.1 Evaluate performance in future grid scenarios and redesign

Quasi-Dynamic EMT Model of PV Plant: Real and imaginary current references are converted to three-phase current references as shown in Fig. A17.3-67.

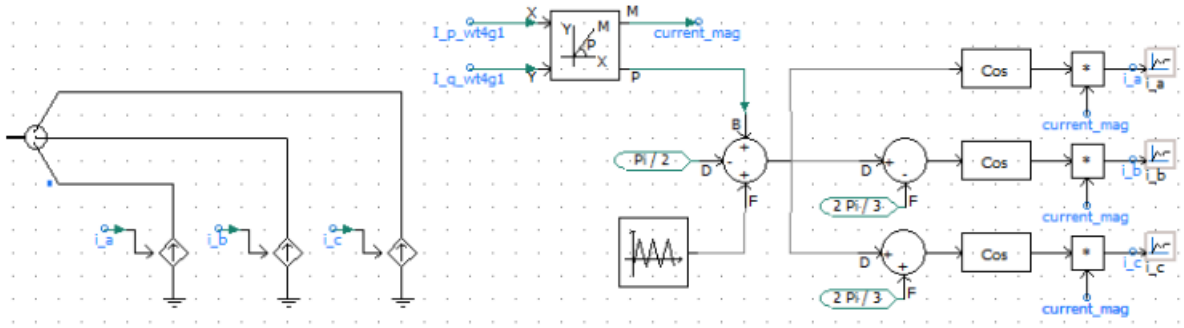

Fig. A17.3-67: PSCAD model for the PV plant representation.

Responses from various models discussed in Table 15.1-1 are shown in Fig. A17.3-68 after a three-phase fault simulation.

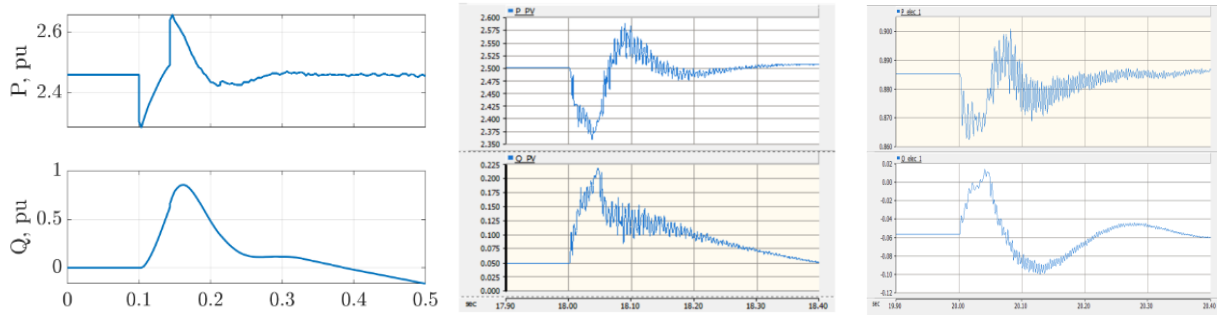

Fig. A17.3-68: (a) Output power plots at the PV plant terminal: (1) PSSE simulation, (b) PSCAD simulation (WT model without PLL for PV plant), and (c) PSCAD simulation (RE model without PLL).

Observation: The following observations are made:

- The active power output trend at the inverter terminal is similar between TS simulation and EMT simulation with WT.
- The reactive power magnitudes are different between all these models.
- In the RE model, reactive power oscillates before reaching steady state.

Now, the Angeles Forest fault is simulated for all the PV plant models. The plots are shown in Fig. A17.3-69.

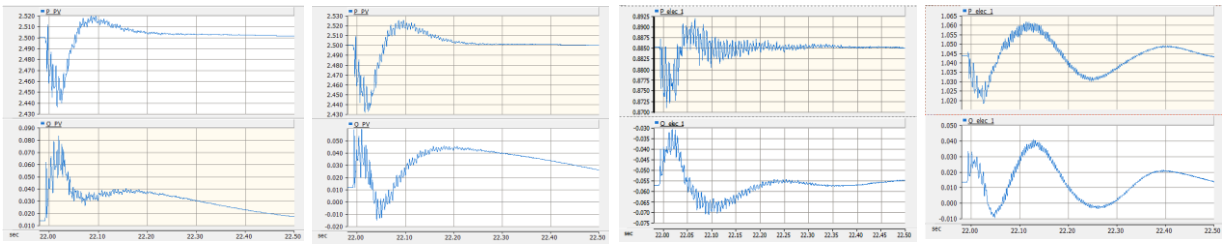

Fig. A17.3-69: Output power plots near the affected PV plant: (a) WT model without PLL, (b) WT model with PLL, (c) RE model without PLL, and (d) RE model with PLL.

Observation: The following observations are made:

- Power output changes after adding PLL in the model.
- Power output oscillates before reaching the steady state for the RE model with PLL.

The simulation results for inverter-1 and inverter-2 filter size increase for two times are shown in
Fig. A17.3-(a)–(c). From the figure, it is observed that with the two times increase in filter size for inverter-1 and inverter-2, there is a reduction in partial loss of output power observed in comparison to the original plant. The PV plant tests for filter size increases of five times and 10 times did not result in stable operation of the PV plant. The simulation results for the interchange of inverters are shown in
Fig. A17.3-(a)–(c). From

Fig. A17.3-(a), it is observed that where all the inverter-2s are replaced with inverter-1s, there is no partial loss of power observed during the event in contrast to the original PV plant scenario. However, as shown in
Fig. A17.3-(b)–(c), in the other two cases where all inverter-1s are replaced with inverter-2 and where inverter-1s and inverter-2s are interchanged, the PV plant could not provide any output power (i.e., the power output is zero).

The simulation results for change in line length for original, two times, and three times are shown in
Fig. A17.3-(a)–(c). From the figure, it is observed that during the line length increased to two times, the total power reduction is the same as the power reduction observed in the original case. In the case of line length increased to three times, the total power loss is observed to be 85 MW, which is different from the original scenario. The inverter profile in each case is also shown in
Fig. A17.3-(d)–(f). From
Fig. A17.3-(d)–(e), it is observed that the inverter profiles during the event are the same for the original case and two times line length increase. In the case of a three times increase, the inverter profile is different from the original case.

In addition to the above case studies, another case study performed changed the inverter-2 switching frequency to 2.5 kHz and 10 kHz and changed the controller gain parameters. Where the switching frequency is reduced to 2.5 kHz and the controller gains are decreased (inner current controller, PLL, and outer current controller) in inverter-2, the simulation results were not satisfactory in steady-state. In the case where the switching frequency was original 5 kHz and the controller gains are reduced, the PV plant simulation is stable and like that of the original PV plant case. Also, in the case of 10 kHz with inner current control gains and reduced PLL gains (original controller gains multiplied by 0.75 and 0.75^2), the PV plant simulation is stable and the partial power reduction is similar to that of the case of the original PV plant simulation. The simulation results for these cases are shown in
Fig. A17.3-.

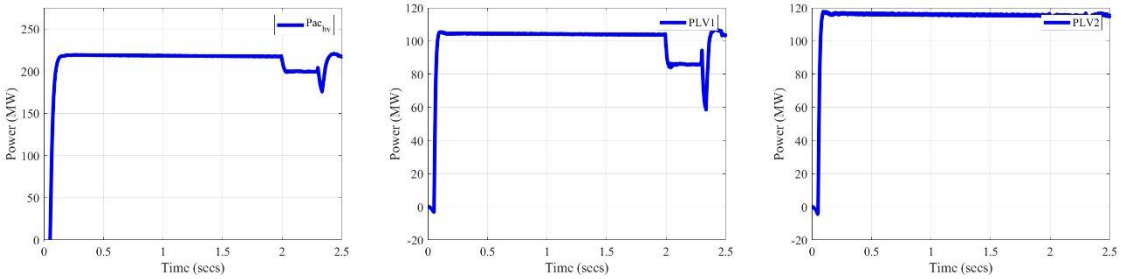

(a) (b) (c)

Fig. A17.3-4: PV plant results for the filter size increase of two times of: (a) HV-side ac power, (b) LV-side ac power of a module, and (c) LV-side ac power of another module.

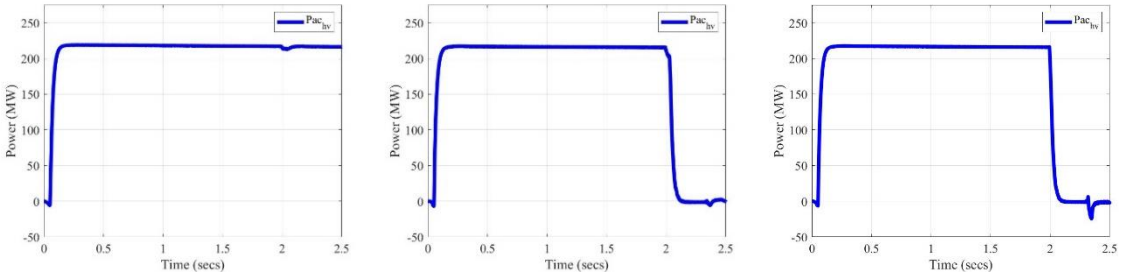

Fig. A17.3-5: Interchange of inverters: (a) plant with all inverter-1s; (b) plant with all inverter-2s, and (c) plant with inverter-1s and inverter-2s interchanged.

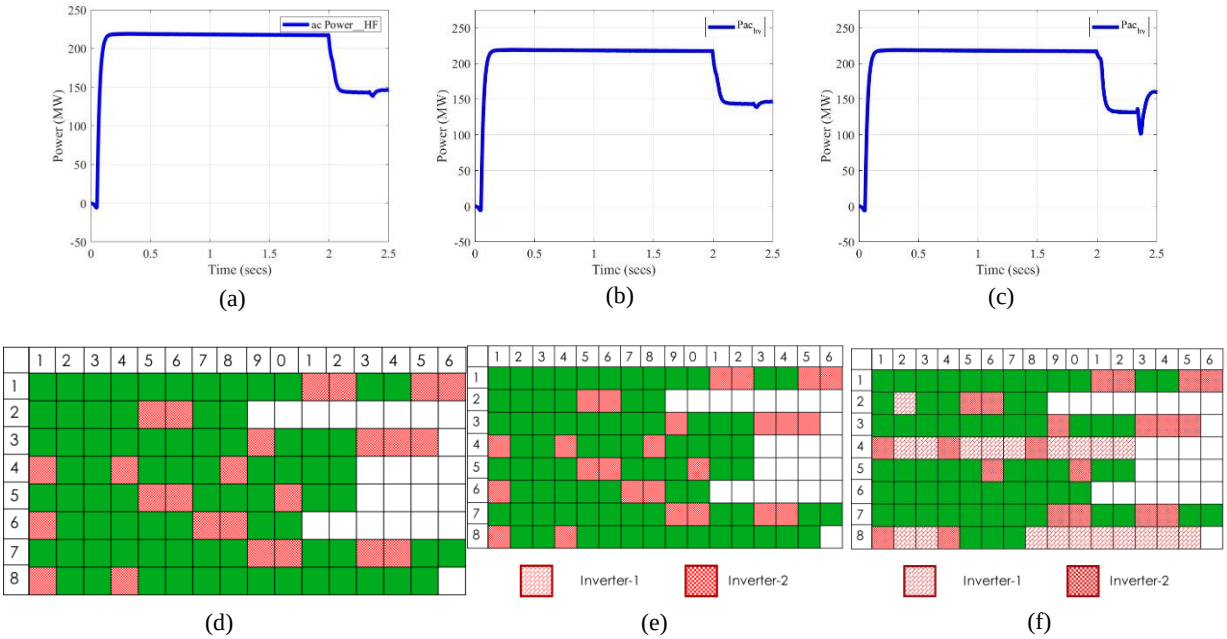

Fig. A17.3-6: Increase in line length for inverters (a) with original lengths, (b) with a two times increase, (c) with a three times increase, (d) inverter profile in the original case, (e) inverter profile in case with a two times increase, and (f) inverter profile in case with a three times increase.

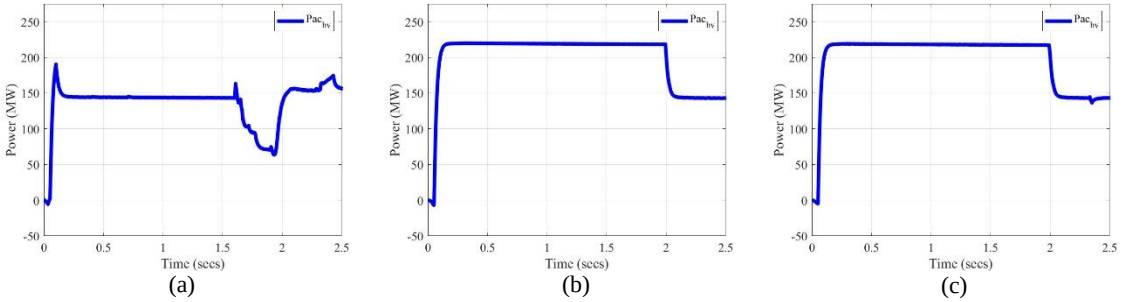

Fig. A17.3-7: PV plant with different switching frequencies for inverter-2: (a) 2.5 kHz (original controller gains multiplied by 0.5 and 0.5^2); (b) 5 kHz (original controller gains multiplied by 0.5 and 0.5^2); and (c) 10 kHz (original controller gains multiplied by 0.75 and 0.75^2).

Fig. A15.1- and Fig. A15.1- demonstrate the MPC performance compared with 100 ms and 1 ms PI controllers and the case with no support for different fault resistance values. The simulation waveforms are obtained for a three-phase-to-ground fault at 0.6 s applied to the high-fidelity generic PV plant model. The responses indicate the faster settling time and improved response observed with MPC compared with PI controllers.

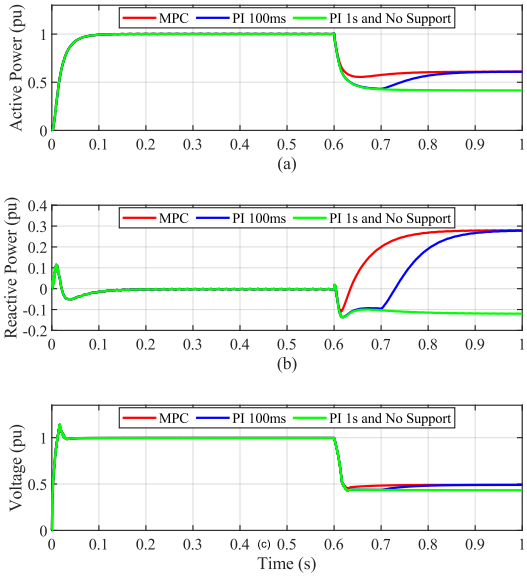

Fig. A17.3-8: Simulation results for Rf = 0.2 Ω with support using MPC, with support using PI, and without support: (a) POI active power, (b) POI reactive power, and (c) POI voltage.

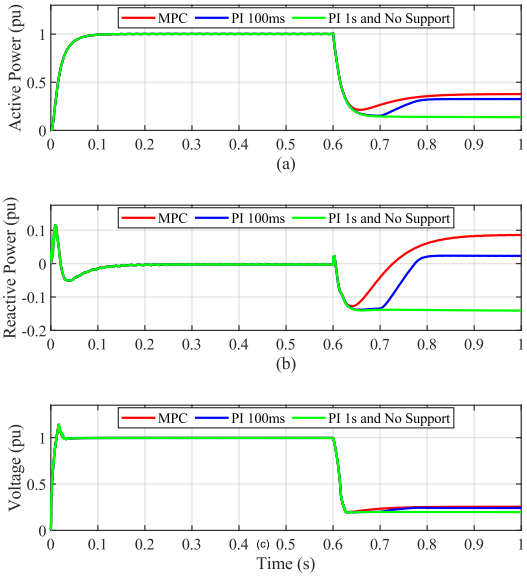

Fig. A17.3-9: Simulation results for Rf = 0.1 Ω with support using MPC, with support using PI, and without support: (a) POI active power, (b) POI reactive power, and (c) POI voltage.

Future Grid TS Model Development with 100% Renewable in California

Sensitivity Analysis of PI Controller Gains in REPCA Model: The parameters for the PI controller in plant power control to generate the reactive power reference (Q_{ex}) are crucial for this grid scenario. After generation loss, the responses are shown in Fig. A17.3-70 for different values of PI control parameters in REPCA. It is observed that a set of K_p and K_i values can lead to undesirable oscillations in the frequency after the Palo Verde generation loss simulation.

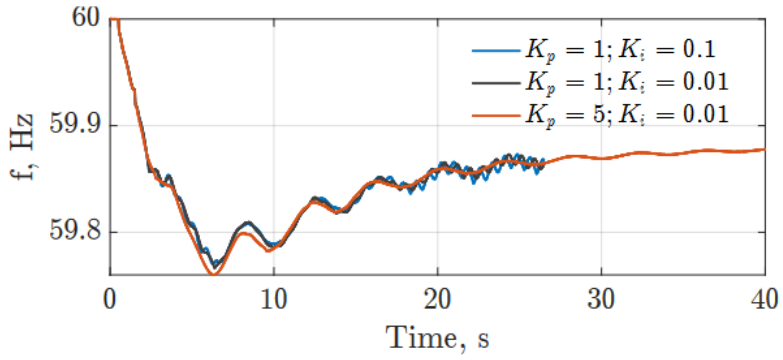

Fig. A17.3-70: Response of the generation loss event in the developed WECC scenario with 100% renewable in California for different PI controller values in REPCA.

Sensitivity Analysis of Deadband Parameter in PPC

The deadband in REPCA1 is set to ±0.01 for the voltage error, as shown in Fig. A17.3-71. It is observed that the response after a generation loss event is sensitive to this deadband. When the deadband is set to ±0.02, undesirable oscillations continue around the post-disturbance steady state frequency as shown in Fig. A17.3-71.

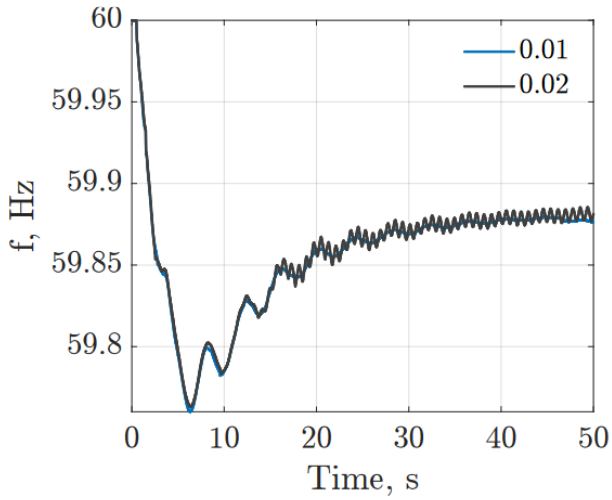

Fig. A17.3-71: Response of the generation loss event in the developed WECC scenario with 100% renewable in California for different deadband values in REPCA.

EMT Model Development with the Future Grid

Objective: In this work, a future power grid with 100% renewable penetration in California is considered for developing the EMT model. The objective is to evaluate the fault that happened in the Angeles Forest 2018 event in this scenario.

Developed models: The TS model of the WECC grid (2026 Heavy Summer scenario) after the modification with 100% renewable in California is considered here. E-Tran software is used to convert the TS model to an EMT model for the fault event simulation. In this modified grid scenario, all the plants in California are modeled with IBRs. Apart from PV plant -1 and PV plant-2, two additional large renewable plants (plant-8 and plant-9) near this location are being considered for a study of their response during the fault. For the EMT model development using E-Tran, the buses

from the fault location to PV plant-1 and all the plants are represented in the EMT model. The rest of the WECC grid is modeled with equivalent constant voltage sources and network at the boundary buses. The PV plants are also represented as constant voltage sources in this E-Tran converted model. Additional EMT models are also developed, as follows:

1. P9: plant-9
2. P19: PV plant-1 and plant-9
3. P129: PV plant-1, PV plant-2, and plant-9
4. P1289: PV plant-1, PV plant-2, plant-8, and plant-9

Near the fault location of the EMT model, necessary changes are made to replicate the fault event more accurately to match the voltage and current responses with the NERC report. This includes the addition of underground cables, shunt devices, breakers voltage, and current measurement devices. These developed models then are compared by their simulation responses.

Simulation responses: The responses after the fault simulation are shown in Fig. A17.3-72 for the EMT model of case P1289. The responses are similar to the present grid model scenario. However, the grid models are different for the present and future grid models, so the responses are not identical.

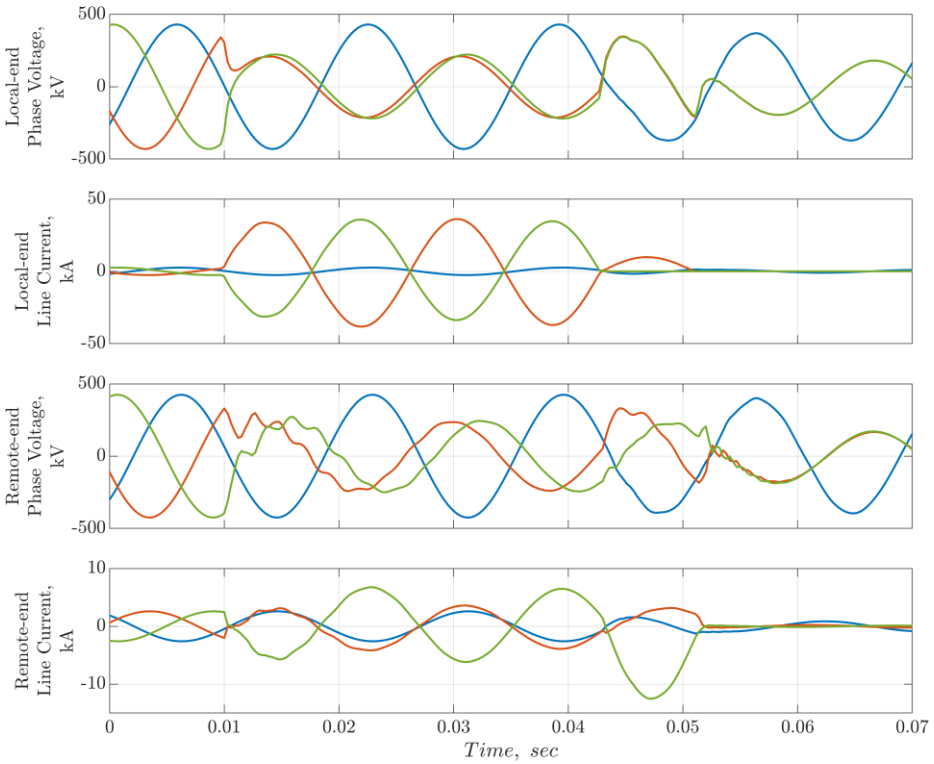

Fig. A17.3-72: Voltage and current plots near the fault location for the EMT model case P1289.

Responses from the cases are then compared with P1289 near the fault location. The differences between the two cases are plotted in Fig. A17.3-73 after normalizing with the peak value.

It is observed that the P129 case is sufficient for this simulation to replicate the response near the fault location. However, this case does not have plant-8 in the EMT model. Therefore, P1289 is considered the best case for the Angeles Forest fault representation in the EMT model of a future grid scenario. When more buses are added to the EMT model, it is found that the responses are the same as the P1289 case, as shown in Fig. A17.3-74. The voltage responses at the renewable plants are plotted in Fig. A17.3-75. Transient under-voltages are observed near all the plants for green and red phases.

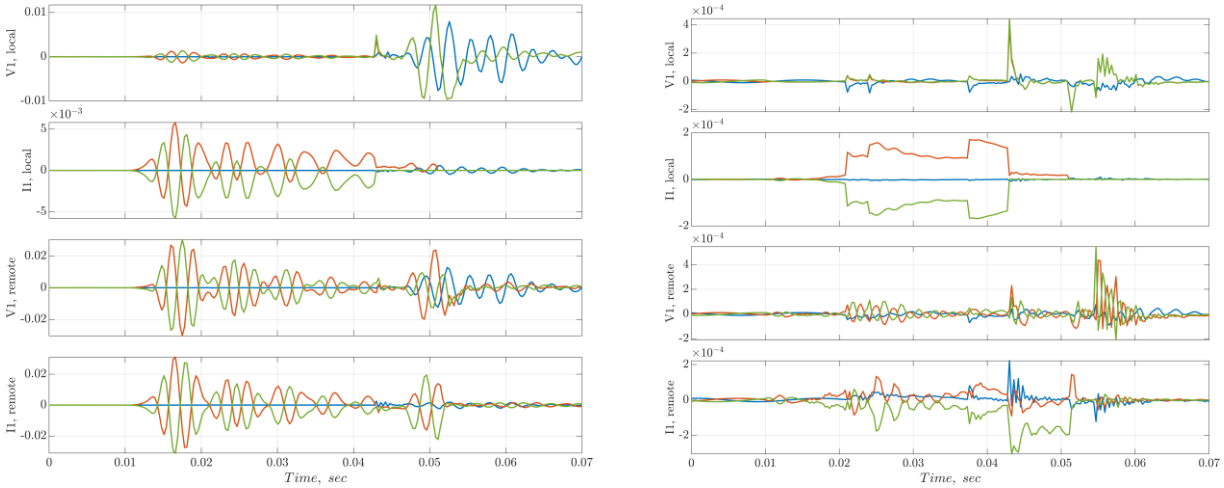

Fig. A17.3-73: Differences between the voltage and current plots near the fault location for the EMT model cases: (left) between P9 and P1289 and (right) between P129 and P1289.

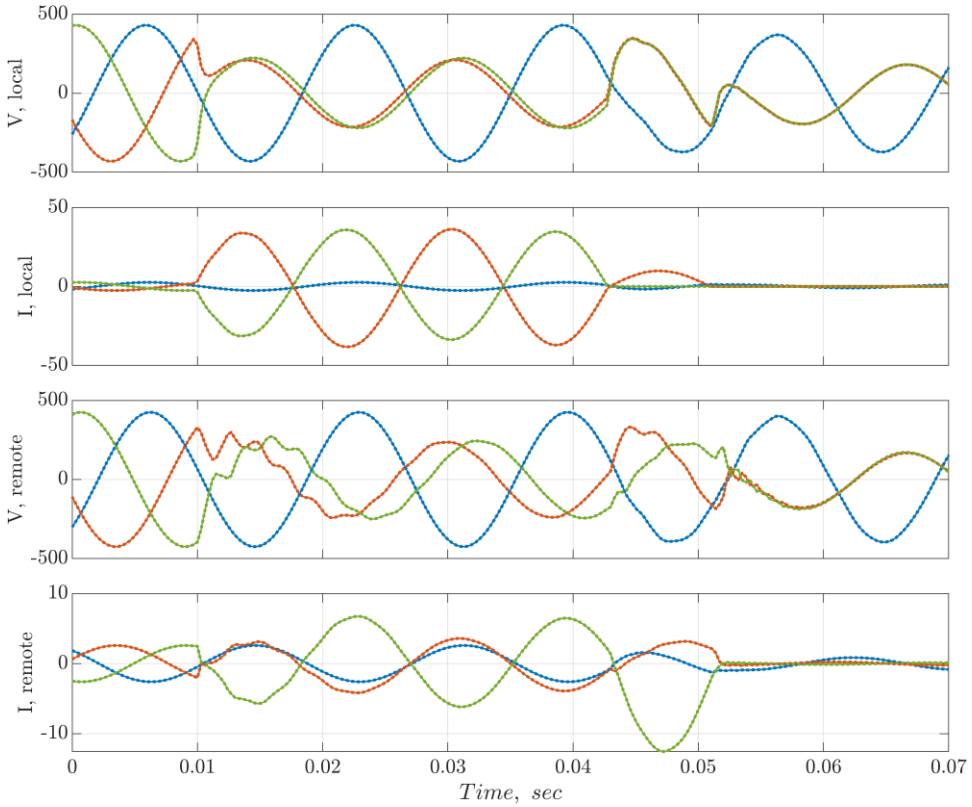

Fig. A17.3-74: Comparison of the voltage and current plots near the fault location for the EMT model cases: solid line, P1289; and dashed line, larger model with more buses added to P1289.

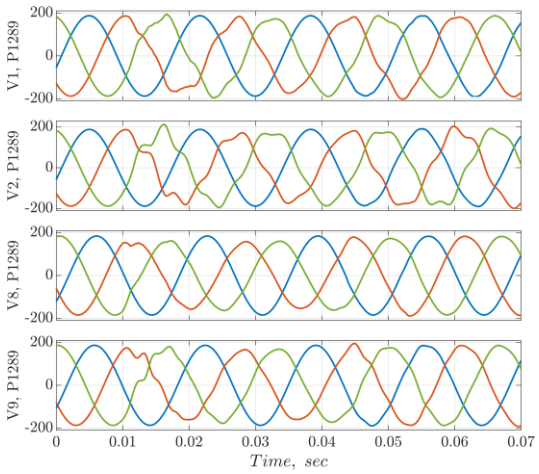

Fig. A17.3-75: Voltage plots near the PV plants in the future grid EMT model case P1289.

Next, the EMT-TS cosimulation model is developed for this event. It is observed that the responses are very different between the EMT-only and EMT-TS cosimulation, as shown in Fig. A17.3-. Because of the presence of multiple renewable sources near this event, the EMT-TS cosimulation seems to represent the event in a future grid more accurately.

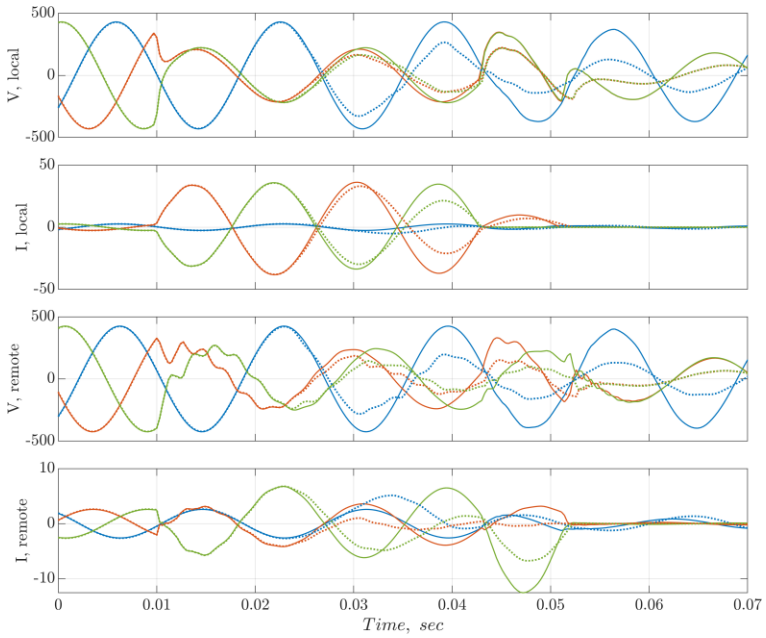

Fig. A17.3-16: Responses near the fault for EMT (solid) and EMT-TS cosimulation (dashed).

Future grid scenario with high-fidelity PV plant model:

In this future grid scenario, the specific PV plant-1 and two generic PV plants are integrated. The line-to-line fault similar to the Angeles Forest event is incepted at t = 1.9932 s. The simulation results for the three PV plants are shown in Fig. A17.3-. In this scenario, the specific PV plant-1 and generic PV plant-2 (IBR-2) are operating stably at 225 MW and 125 MW, respectively. The generic PV plant-1 (IBR-1), however, is operating at 0 MW. All the plants are stable in the pre-fault condition. During the fault,

partial power loss is observed in the specific PV plant and IBR-2, as shown in Fig. A17.3-(b)–(c). This scenario mimics the case P1289, with the specific PV plant-1 and plant-8 modeled with high-fidelity models.

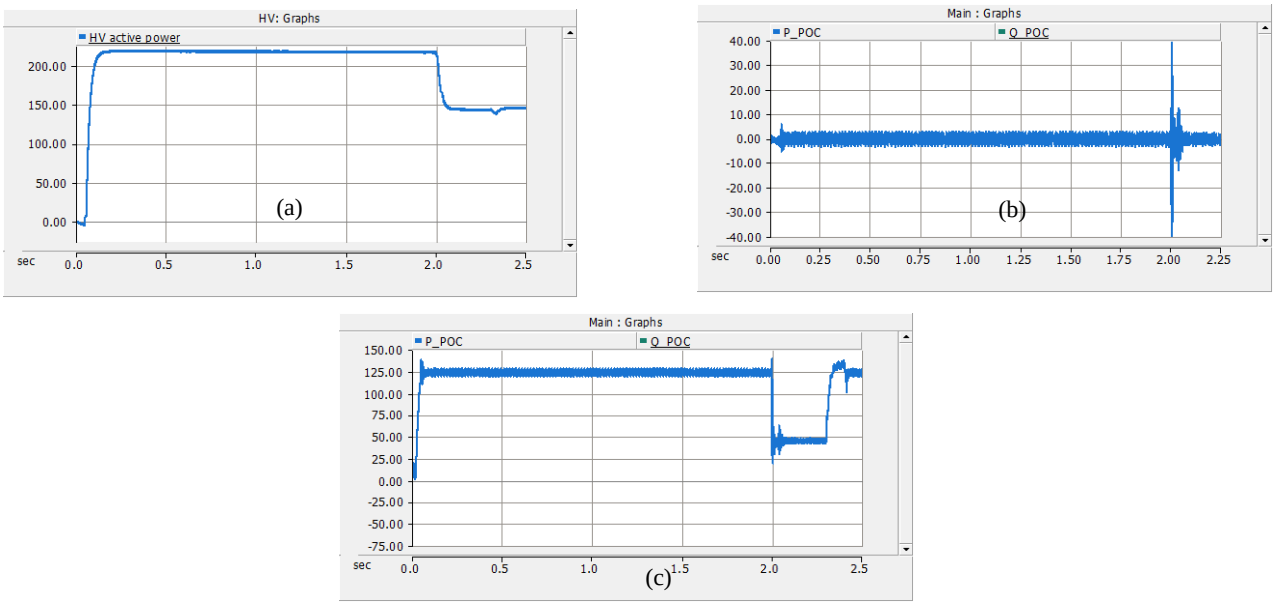

Fig. A17.3-17: Simulation results for the three PV plants: (a) specific PV plant-1, (b) IBR-1, and (c) IBR-2.

Sensitivity Analysis on High-Fidelity EMT Model of PV Plants in Future Grid Scenario: A sensitivity analysis on high-fidelity EMT models of different PV plants connected to the future grid scenario is presented. In this analysis, the specific PV plant-1, generic PV plant-1 (IBR-1), and generic PV plant-2 (IBR-2) are connected to the future grid scenario, and their dynamic response is captured during the power grid event. The generic PV plants are operated at 125 MW, and the specific PV plant-1 is operated at ~220 MW. The power grid event is a line-to-line fault incepted at t = 1.9932 s, similar to that of the Angeles Forest event. The following scenarios are simulated to understand how the multiple PV plants in the vicinity have an effect on their response during a power grid event:

- Specific PV plant-1 connected to the future grid scenario
- Specific PV plant-1, IBR-1 (operated at 125 MW), and IBR-2 (operated at 125 MW) connected to the future grid scenario
- Specific PV plant-1, IBR-1 (operated at 0 MW), and IBR-2 (operated at 125 MW) connected to the future grid scenario
- IBR-1 (operated at 125 MW) and IBR-2 (operated at 125 MW) connected to the future grid scenario
- IBR-1 (operated at 0 MW) and IBR-2 (operated at 125 MW) connected to the future grid scenario

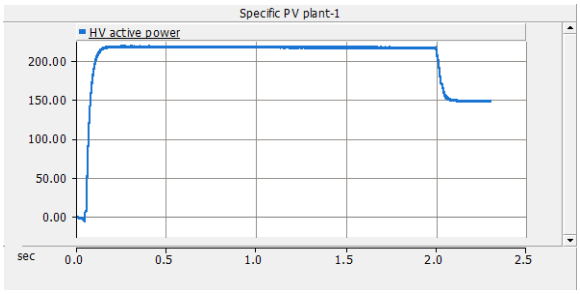

Fig. A15.1-18: The specific PV plant-1 with the future grid scenario.

Simulation results: The simulation results for each scenario are shown in Fig. A15.1-18–Fig. A15.1-22. In Fig. A15.1-18, the response of the PV plant-1 connected to the future grid scenario is displayed. From the figure, during the power grid event, it is observed that the power reduction is slightly lower than that of the power reduction of the original PV plant case. The response of the three PV plants when connected to the future grid scenario is shown in Fig. A15.1-19(a)–(c). From the figures, during the power grid event, it is observed that the specific PV plant-1's power reduction is much higher in comparison to that of the original case. Furthermore, the output power from both IBRs is completely reduced, indicating 100% power loss during the power grid event. Before the event, each of the IBRs operated at the maximum capacity of 125 MW. The response of the three PV plants when connected to the future grid scenario where IBR-1 is operated at 0 MW is shown in Fig. A15.1-20(a)–(c). From the figures, it is observed that the specific PV plant-1 has power loss of ~75 MW during the event. The observed power loss in this case is like that of the original PV plant case. In addition, partial power loss of ~60 MW is observed in IBR-2. Before the power grid event, the specific PV plant-1 is operated at ~220 MW, IBR-1 is operated at 0 MW, and IBR-2 is operated at 125 MW. The response of two IBRs (both operated at 125 MW) connected to the future grid scenario without the specific PV plant-1 are shown in Fig. A15.1-21(a)–(b). From these figures, it is observed that, during the power grid event, there is 100% power loss in both IBRs. The response of two IBRs (where IBR-1 is operated at 0 MW, and IBR-2 is operated at 125 MW) connected to the future grid scenario without the specific PV plant-1 is shown in Fig. A15.1-22(a)–(b). From the figures, it is observed, during the fault, there is 100% power loss in IBR-2.

From Fig. A15.1-18–Fig. A15.1-22, the following important observation can be deduced. The response of the PV plants is heavily dependent on the IBRs present in the region of the PV plants. Therefore, to accurately capture the dynamic behavior of the PV plants, employing high-fidelity EMT models of all the PV plants in the region is essential because interactions among the PV plants are affecting their response during the power grid events.

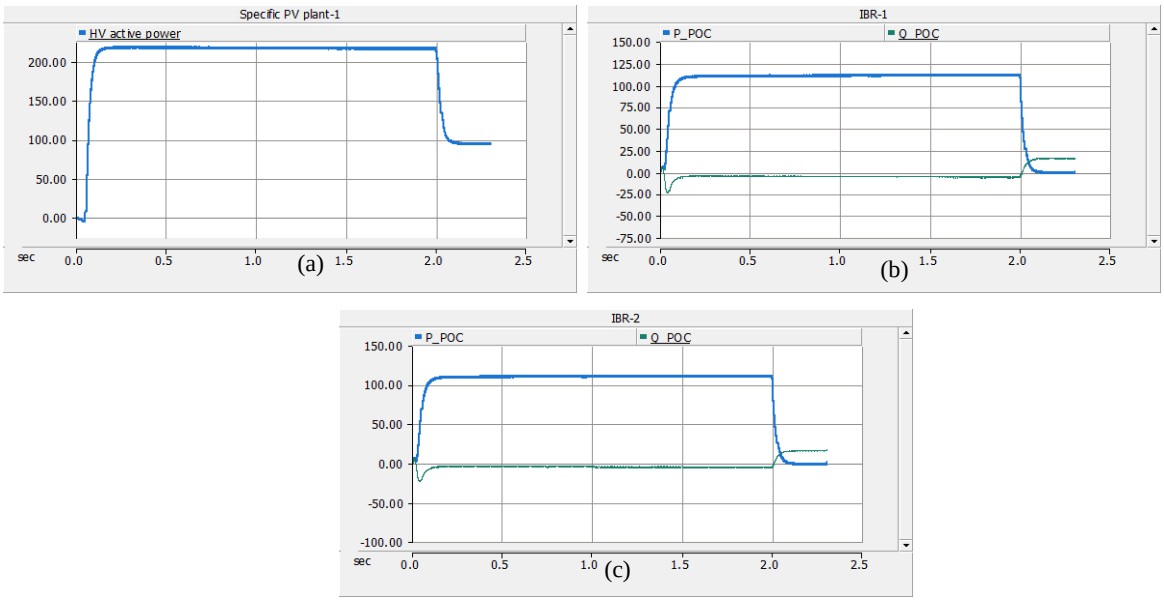

Fig. A15.1-19: Three PV plant responses during the power grid when connected to the future grid (IBR-1 and IBR-2 operated at 125 MW): (a) specific PV plant-1, (b) IBR-1, and (c) IBR-2.

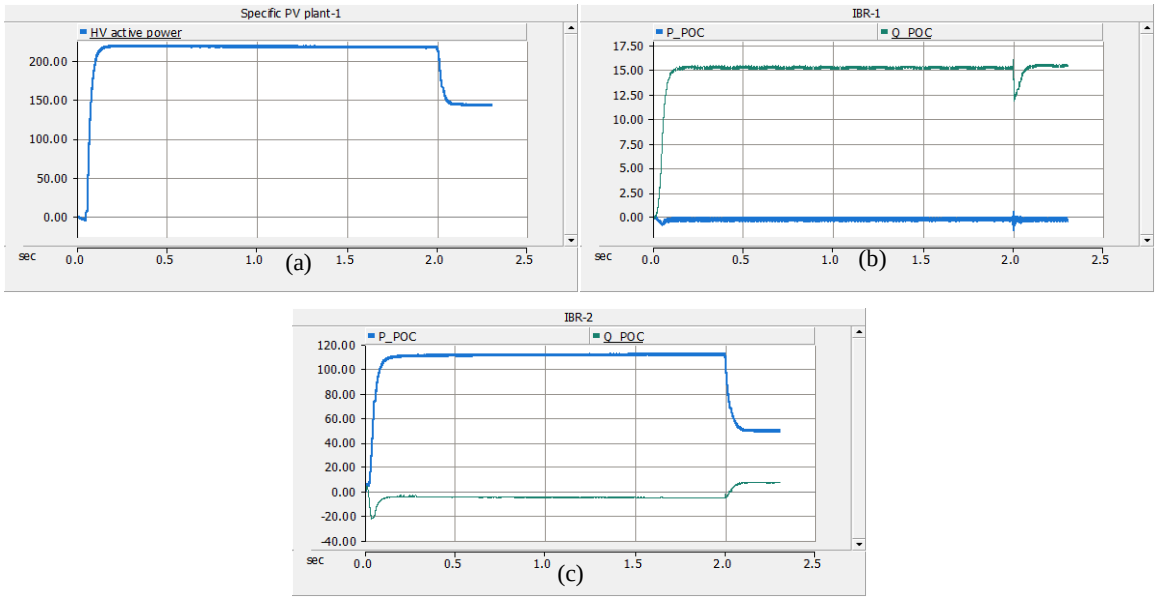

Fig. A15.1-20: Three PV plant responses during the power grid when connected to the future grid (IBR-1 operated at 0 MW and IBR-2 operated at 125 MW): (a) specific PV plant-1, (b) IBR-1, and (c) IBR-2.

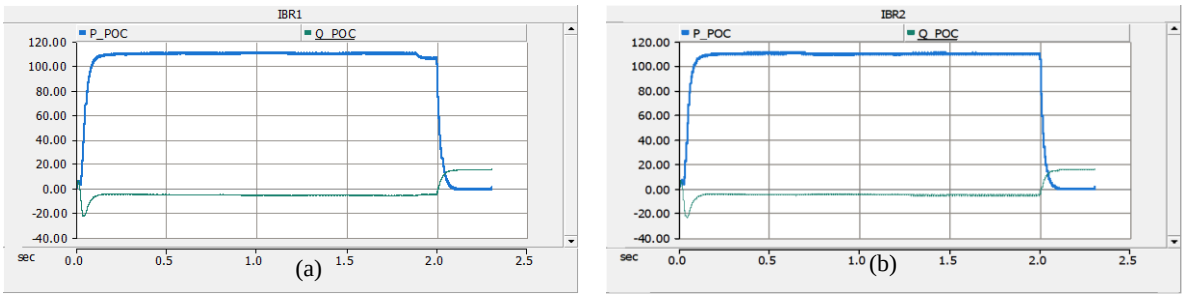

Fig. A15.1-21: Two PV plant responses during the power grid when connected to the future grid, both operated at 125 MW: (a) IBR-1 and (b) IBR-2.

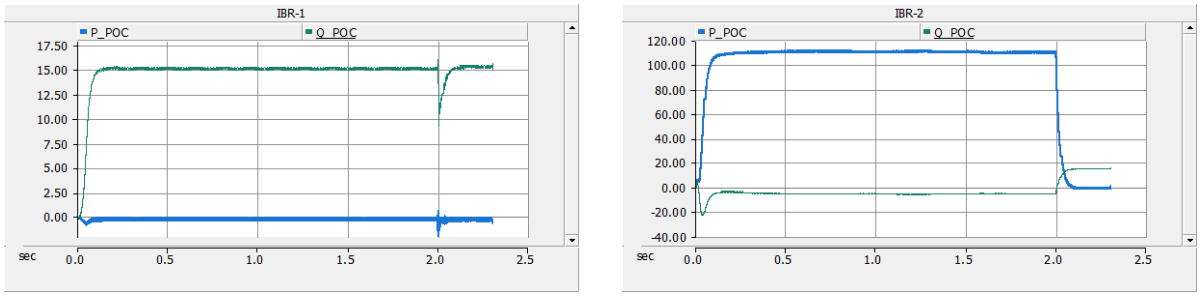

Fig. A15.1-22: Two PV plant responses during the power grid when connected to the future grid: (a) IBR-1 operated at 0 MW and (b) IBR-2 operated at 125 MW.

T-16. Investigation of future scenario

ST-16.1. Incorporate advanced control functionalities into future grid scenarios in real-time simulation

Advanced Model of PV Plant

These updates have improved the stability of the advanced model of the PV plant. The PV plant simulation results are shown in Fig. A17.3- and Fig. A17.3-. From the figures, it may be noted that the voltages are stable, and the active power reference results in the power generated from the PV plant on the order of 220 MW (as noted in the high-fidelity model of the PV plant).

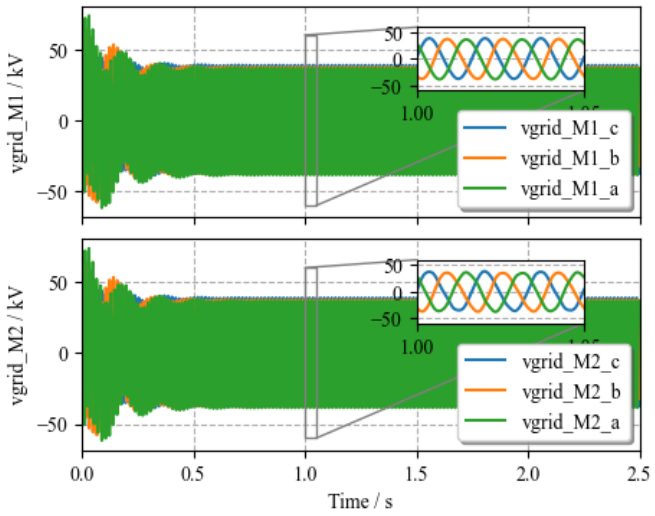

Fig. A17.3-1: Grid side voltage for PV plant modules 1 and 2.

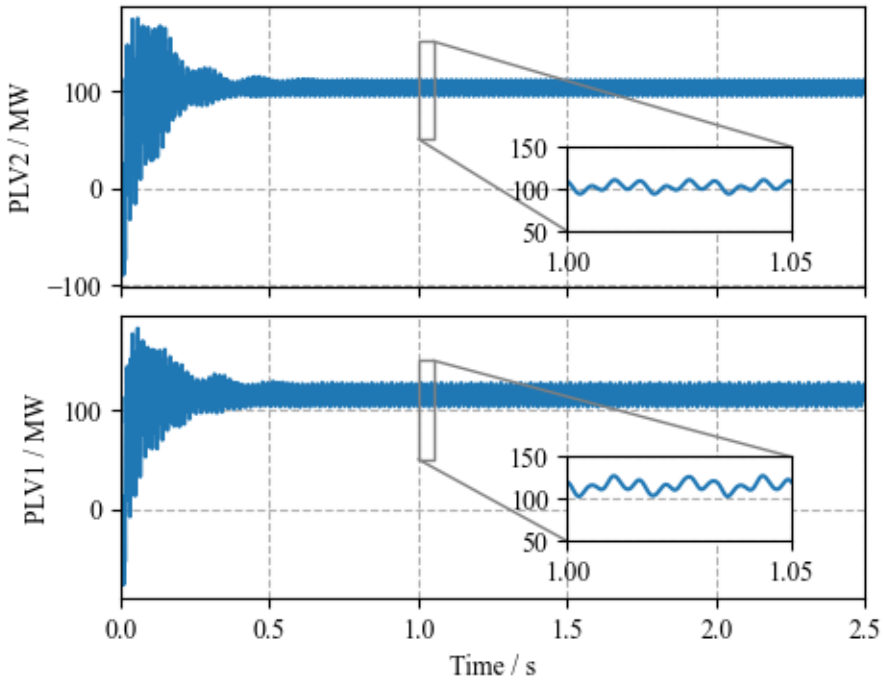

Fig. A17.3-2: Active power for PV plant modules 1 and 2.

Development of Quasi-Dynamic Model of Specific PV Plant-1 in RSCAD

The quasi-dynamic model was manually converted into RSCAD for real-time simulation from the corresponding PSCAD model. As developed in PSCAD, the quasi-dynamic model in RSCAD was developed using library components. The model and controller parameters were extracted from the developed model in PSCAD and used in the RSCAD model, which is illustrated in Fig. A17.3-.

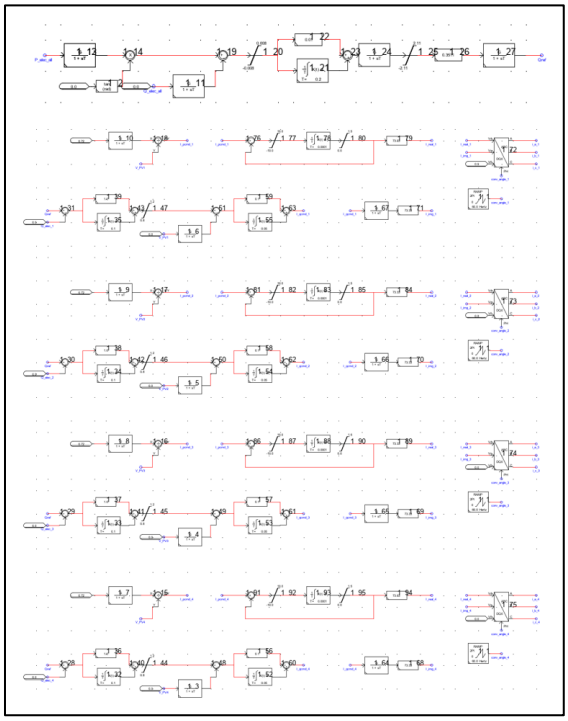

Fig. A17.3-3: Quasi-dynamic model of the specific PV plant-1 in RSCAD for real-time simulation.

Integration of Quasi-Dynamic Model of Specific PV Plant-1 with the Future Grid Scenario in RSCAD

After developing the quasi-dynamic model of specific PV plant-1, the quasi-dynamic model is integrated with the future scenario grid model. The quasi-dynamic model is integrated by controllable current sources in the future scenario grid model. The model takes voltages from the grid model and generates currents injected back to the grid. Because the quasi-dynamic model was connected to low voltage within the specific PV plant, additional transformers were inserted to integrate the quasi-dynamic model. The entire quasi-dynamic model of the specific PV plant-1 with the future scenario grid model in RSCAD is presented in Fig. A17.3-.

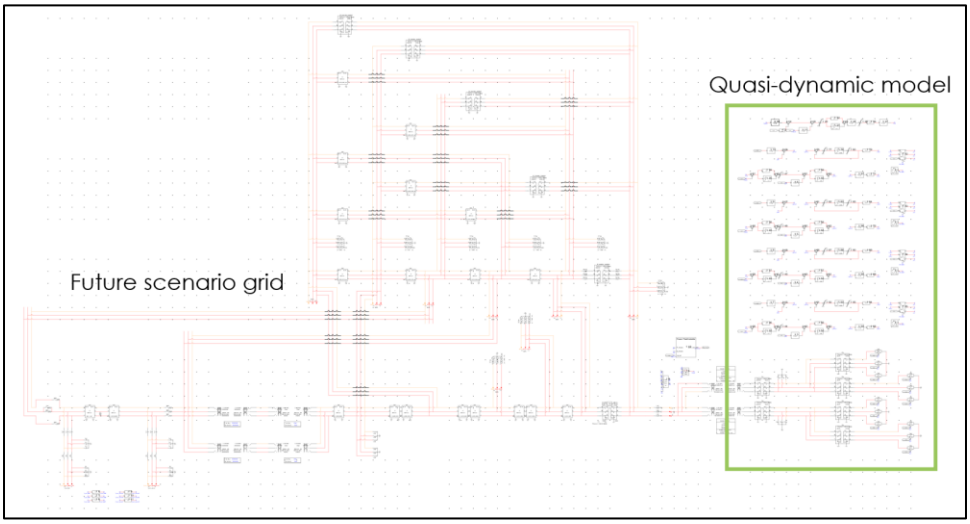

Fig. A17.3-4: Quasi-dynamic model of the specific PV plant-1 integrated with the future scenario grid model in RSCAD for real-time simulation.

Development of High-Fidelity Model of Specific PV Plant-1 with the Present Grid Scenario Implemented in a Single Rack in RTDS

In addition to a high-fidelity model of specific PV plant-1 developed and implemented in eight racks in RSCAD for real-time simulation, a high-fidelity model of specific PV plant-1 was implemented in a single rack. This development assists in identifying the effect of rack communication and time step delay between racks in RTDS. This analysis will be helpful in optimizing the hardware-based EMT simulation implementation. With eight-rack implementation, two racks with 10 PB cards are used for feeders, and six racks with 30 PB cards are used for PV systems including PV inverter modules and distribution transformers within specific PV plant-1. Because there is a single time step delay between racks (or between components like feeders and PV systems in different racks) caused by rack communication, the eight-rack implementation introduces multiple time step delays within the PV plant model, resulting in numerical instability. To address the numerical instability in real-time simulation of specific PV plant-1 in RTDS, a pseudo real-time implementation technique was applied by extending the solution time step, while keeping the simulation time step. Thus, the simulation time step and the solution time step are 0.25 µs and 100 µs, respectively, with eight-rack implementation. To implement the PV plant in a single rack in RTDS, all the component of specific PV plant are allocated in a single rack with six PB cards. However, the solution time step is extended to 1,000 µs while keeping the simulation time step at 0.25 µs. The RSCAD

simulation results are presented in

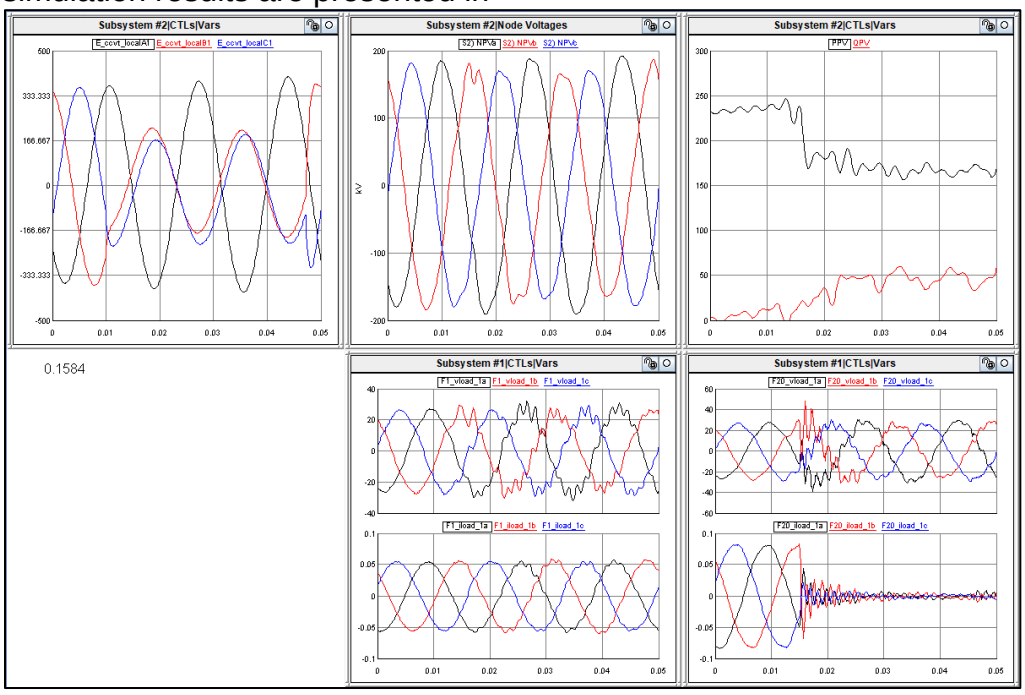

Fig. A17.3- for a single-rack case. As seen from the figure, the partial reduction in the active power from the PV plant was observed during the fault event in the present scenario grid.

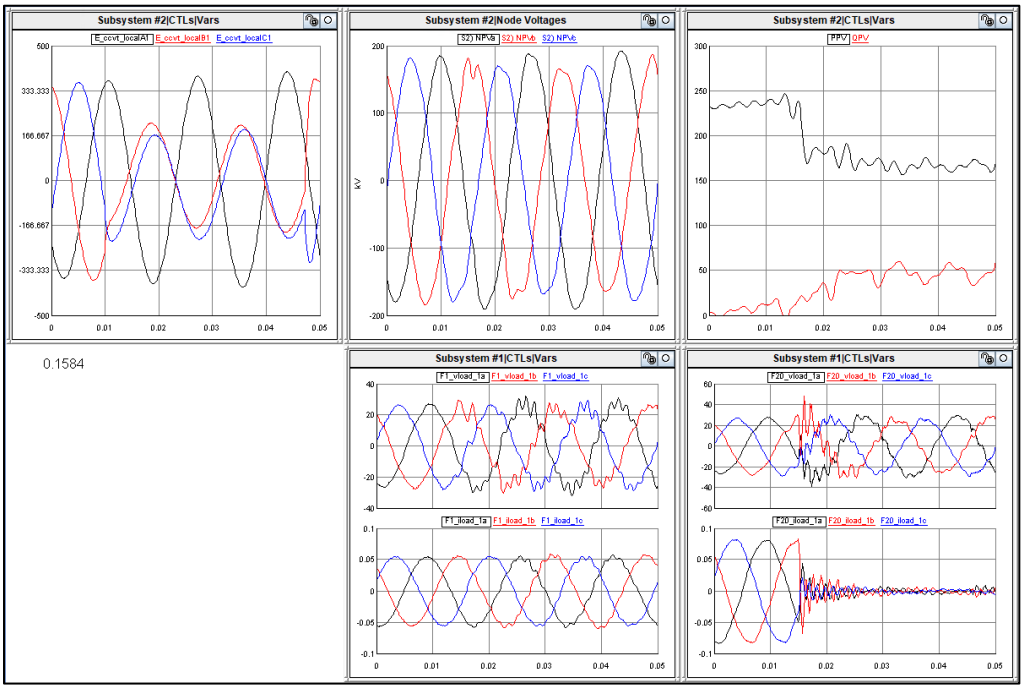

Fig. A17.3-5: Results of the high-fidelity model of specific PV plant-1 integrated with the present scenario grid model in a single rack with six PB cards in RTDS (from top left to bottom right: voltages at grid near the fault, voltages at terminal of the PV plant, active and reactive power of the PV plant, voltages at the first feeder and inverter currents at the first feeder, voltages at the 20th feeder, and inverter currents at the 20th feeder).

Compared with the PV plant model by eight-rack implementation shown in

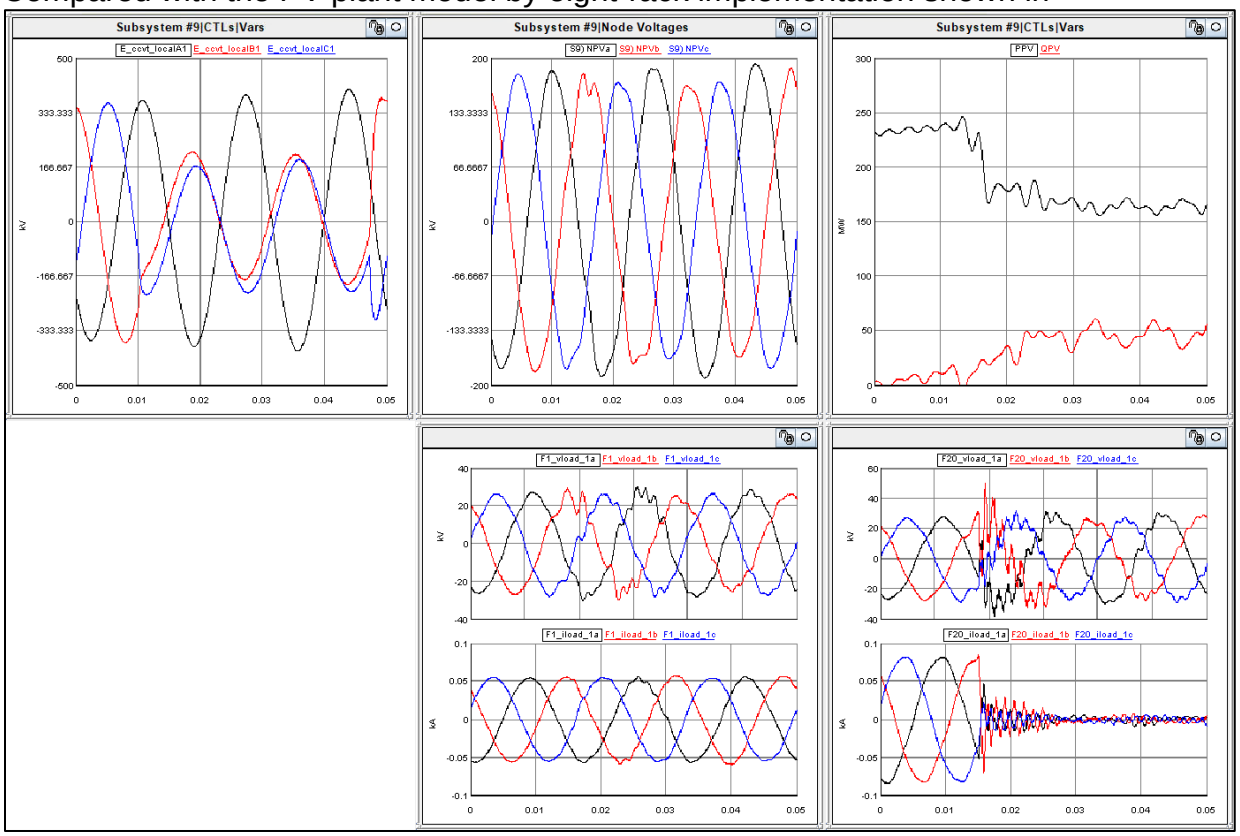

Fig. A17.3-, the active and reactive power monitored at the terminal of the PV plant are almost identical between the models. However, feeder voltages and inverter currents show different responses, especially with the first feeder and PV systems connected with the first feeder. With eight-rack implementation, the inverter in the first feeder ride through the fault event. On the other hand, the inverter with a single-rack implementation is tripped by the fault event. Because all other settings are identical, this is the expected effect of rack communications and multiple time step delays within the PV plant model.

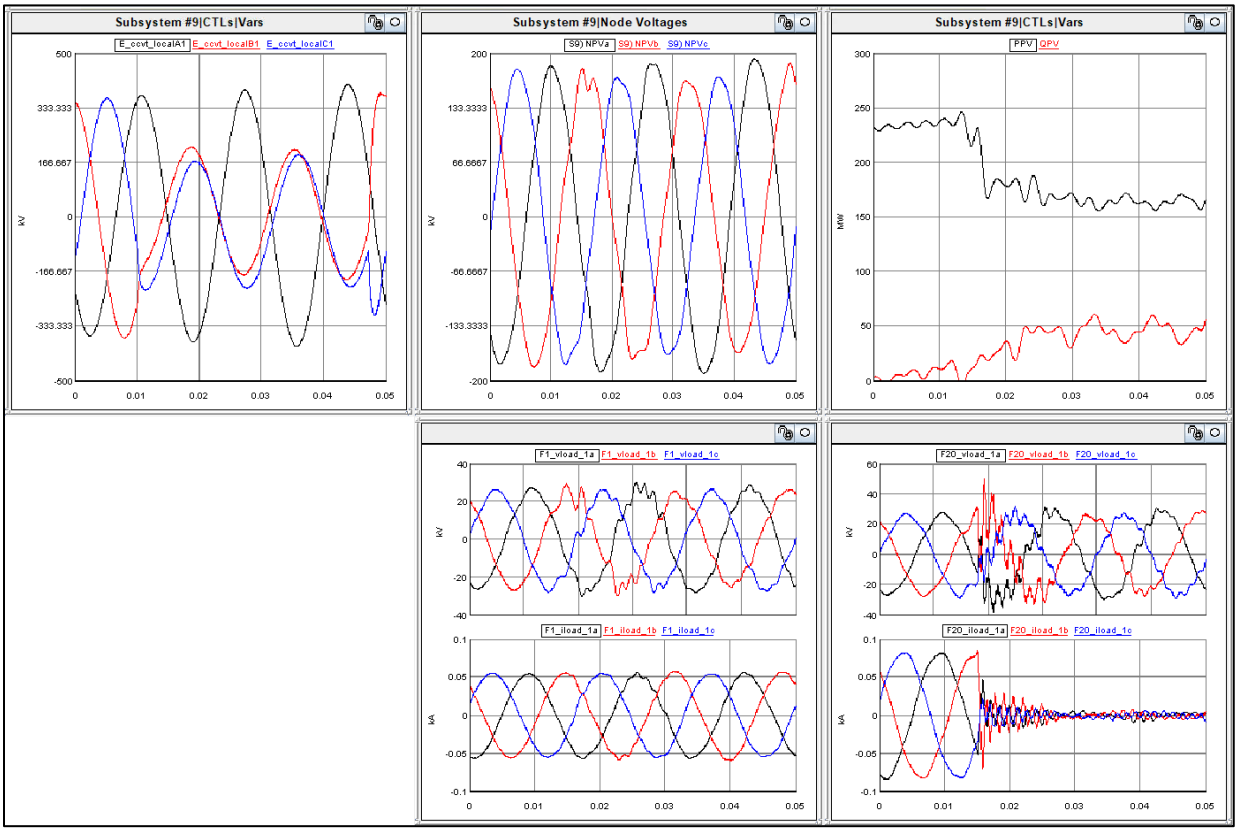

Fig. A17.3-6: Results of the high-fidelity model of specific PV plant-1 integrated with the present scenario grid model in eight racks with 40 PB cards in RTDS (from top left to bottom right: voltages at grid near the fault, voltages at terminal of the PV plant, active and reactive power of the PV plant, voltages at the first feeder and inverter currents at the first feeder, voltages at the 20th feeder, and inverter currents at the 20th feeder)

Development of High-Fidelity Model of Specific PV Plant-1 with the Present Grid Scenario Implemented in 13 Racks in RTDS

A high-fidelity model of specific PV plant-1 was implemented in 13 racks to reduce the solution time step of a pseudo real-time implementation technique. This analysis will be helpful in optimizing the hardware-based EMT simulation implementation. With 13-rack implementation, two racks with 10 PB cards are used for feeders, and 11 racks with 55 PB cards are used for PV systems including PV inverter modules and aggregation transformers within specific PV plant-1. The RSCAD simulation results are presented in Fig. A16.1-7 for the 13-rack case.

With eight-rack implementation, the simulation time step and the solution time step are 0.25 µs and 100 µs, respectively. With 13-rack implementation, the solution time step is reduced to 51 µs with the simulation time step of 0.5 µs.

Compared with the PV plant model by eight-rack implementation shown in

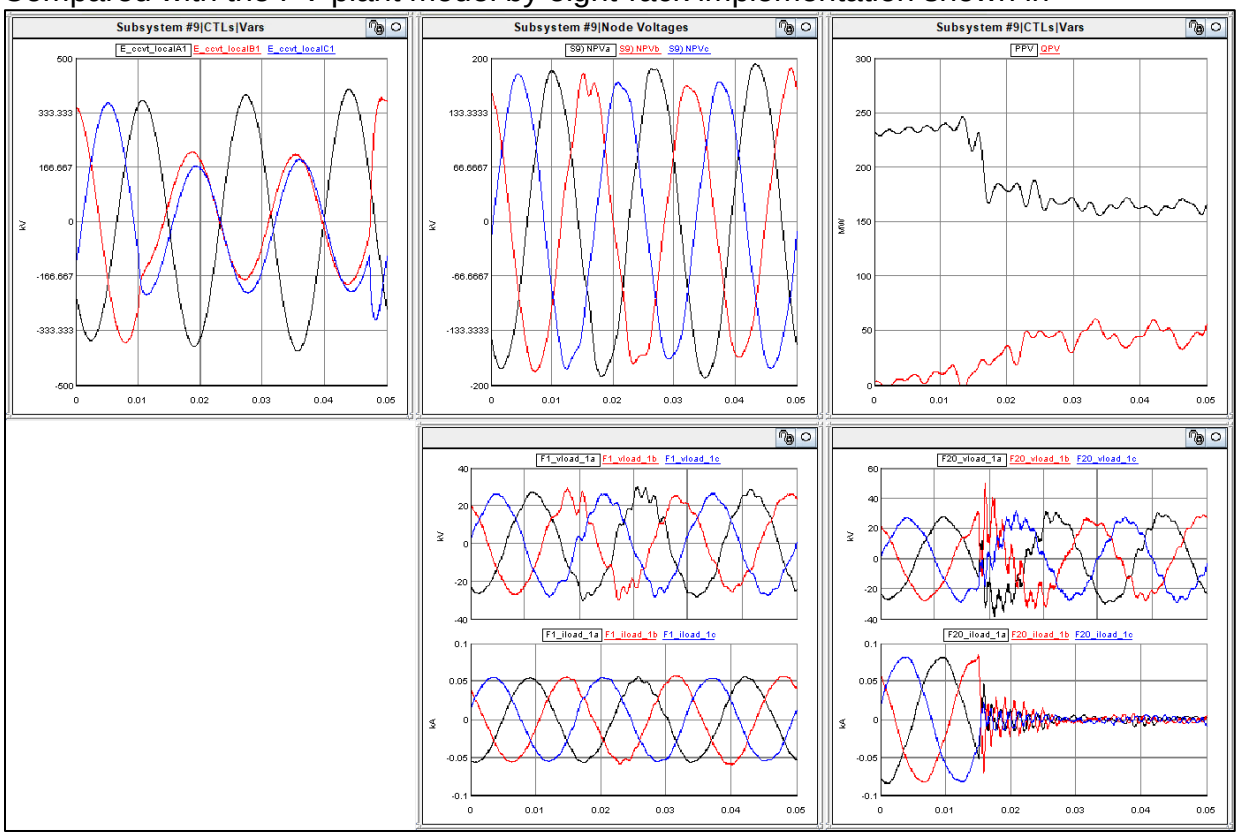

Fig. A17.3-, the active and reactive power monitored at the terminal of the PV plant present similar partial reduction between the models. However, feeder voltages and inverter currents show different responses, especially with the first feeder and PV systems connected with the first feeder. Because all other settings are identical, this is the effect of rack communications and multiple time step delays within the PV plant model.

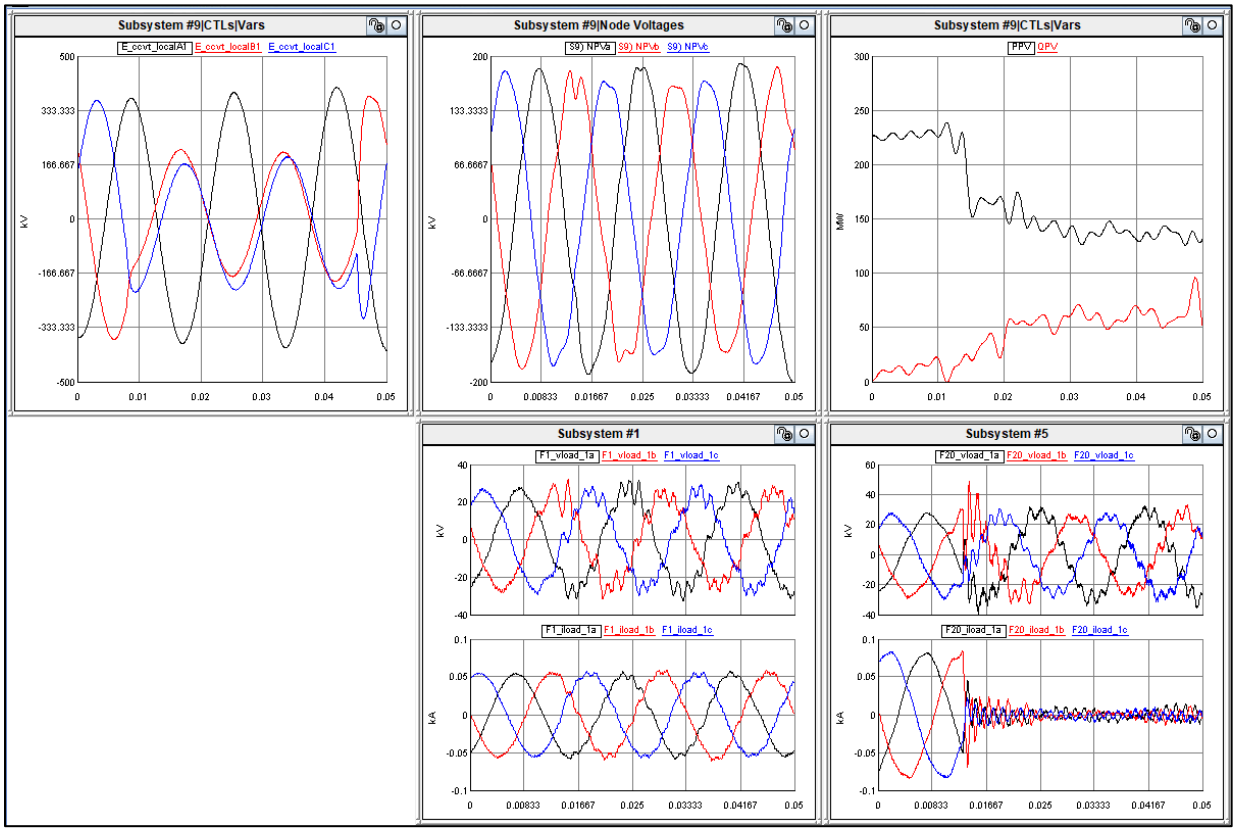

Fig. A17.3-7: Results of the high-fidelity model of specific PV plant-1 integrated with the present scenario grid model in 13 racks with 65 PB cards in RTDS (from top left to bottom right: voltages at grid near the fault, voltages at terminal of the PV plant, active and reactive power of the PV plant, voltages at the first feeder and inverter currents at the first feeder, voltages at the 20th feeder, and inverter currents at the 20th feeder).

T-17. Demonstration of generic present grid scenario

ST-17.2. Integrate generic PV plant in IEEE case study

Develop advanced model for generic PV plant

Comparison of different neural networks for advanced model of generic PV plant: In the advanced model of the generic PV plant, four different neural networks were employed to enhance its performance and accuracy. This report presents a comparison of these neural networks based on trainable parameters, testing loss, and their ability to match the original waveform. The results are summarized in Table A17.3-8.

Table A17.3-8 Comparison of different neural networks for an advanced model of a generic PV plant

Model	Trainable parameters	Testing loss	Match with original waveform
RNN	295	0.0090	medium
GRU	1271	0.0110	low
BiRNN	281	2.3422e-05	high
BiLSTM	1091	9.6691e-06	high

Recurrent Neural Network: Used in the advanced model of the specific PV plant, RNN is a type of neural network widely used in sequential data analysis, including time series data such as the output of a PV plant. Unlike traditional feedforward neural networks,

RNN has a recurrent connection that allows it to retain information from previous time steps, making it suitable for modeling sequential data. The RNN model employed has 295 trainable parameters, and testing loss achieved is 0.0090, indicating a medium level of accuracy. No overfitting is observed from the learning curve. The model summary is shown in Fig. A17.3- and the test results are shown in

Fig. A17.3-.

Gated Recurrent Unit (GRU): GRU is a variant of the RNN architecture designed to mitigate the vanishing gradient problem and improve training efficiency. It introduces gating mechanisms that selectively update and reset information in the hidden state, enabling better information flow and preventing the loss of valuable information over time. The GRU network in the advanced model of the generic PV plant also uses a dropout layer, which is introduced to increase the generalizability of the model by randomly dropping out a fraction of the neuron outputs during training. This regularization technique helps prevent overfitting and encourages the network to learn more robust, generalizable representations. However, the results show that the GRU network has the worst performance although it has the highest training parameters. The model summary is shown in

Fig. A17.3-, and the test results are in Fig. A17.3-.

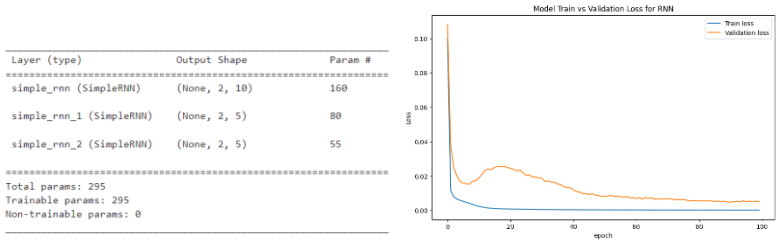

(a) (b)

Fig. A17.3-1: (a) RNN model summary and (b) learning curve.

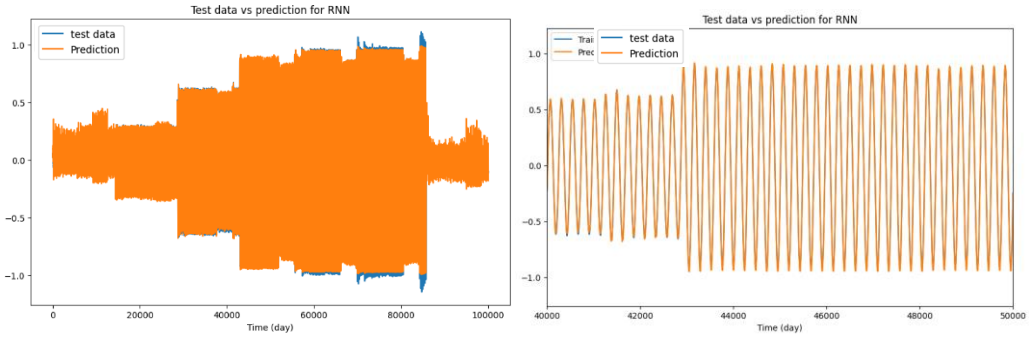

(a) (b)

Fig. A17.3-2: (a) Test data vs. prediction results from RNN model and (b) zoomed-in result between 4 and 5 s.

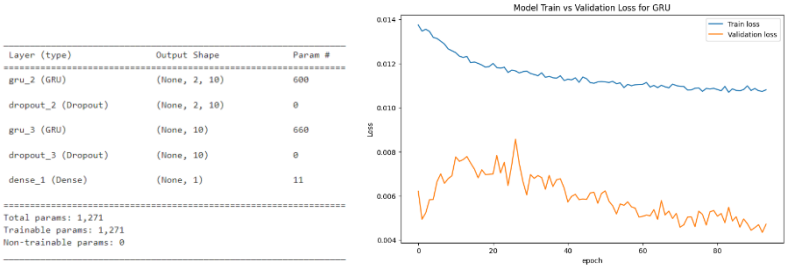

(a) (b)

Fig. A17.3-3: (a) GRU model summary and (b) learning curve.

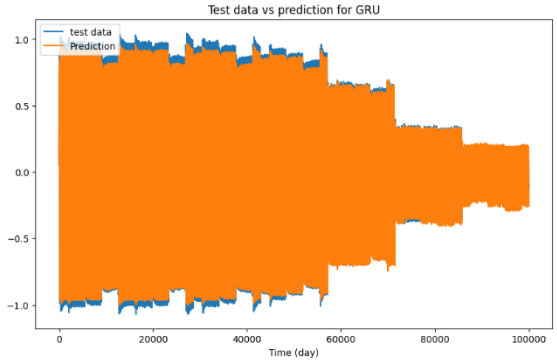

Fig. A17.3-4: Test data vs. prediction results from GRU model.

Bidirectional RNN: Bidirectional RNN is an extension of the RNN architecture that addresses the limitation of capturing only past information. It consists of two RNNs: one processing the input sequence in the forward direction and another processing it in the reverse direction. By leveraging both past and future information, bidirectional RNN achieves better results even with a lower number of trainable parameters. This enables it to effectively leverage the available information and enhance prediction accuracy without sacrificing computational efficiency. The model summary is shown in Fig. A17.2-5, and the test results are shown in Fig. A17.2-6.

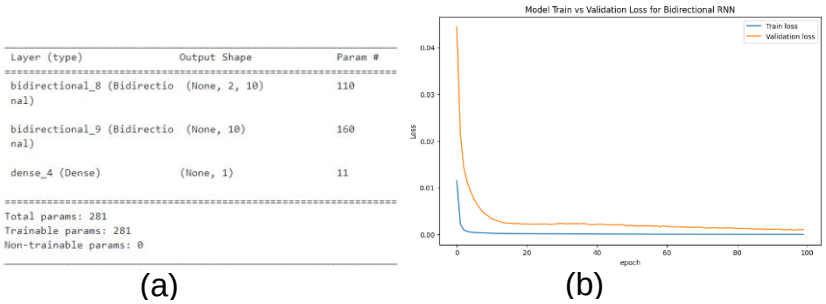

(a) (b)

Fig. A17.3-5: (a) Bidirectional RNN model summary and (b) learning curve.

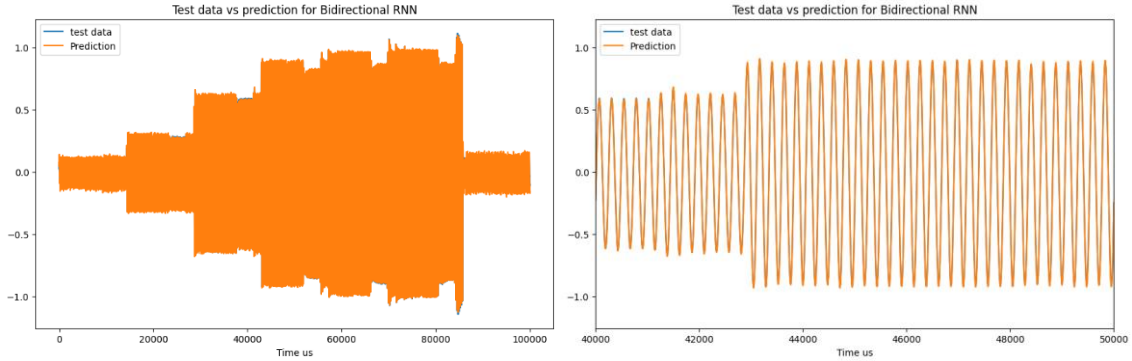

(a) (b)

Fig. A17.3-6: (a) Test data vs. prediction results from bidirectional RNN model and (b) zoomed-in result between 4 and 5 s.

Incorporate advanced control functionalities into generic PV plant: Similar to the specific PV plant, the training process for the advanced PV model of the generic PV plant has faced challenges in fully capturing the transient behavior of the high-fidelity PV model. As a result, when integrating the advanced PV model into the distribution grid, the system becomes unstable. To address this issue, a solution involving the addition of a damper using capacitors has been implemented.

Additional capacitance is incorporated at the lateral bus of each PV cell location. A thorough investigation is conducted by sweeping the added capacitance at each location to identify the minimum additional capacitance required to minimize the total reactive power for the PV plant. By leveraging this minimum additional capacitance, the advanced generic PV model can achieve stability and reliable performance.

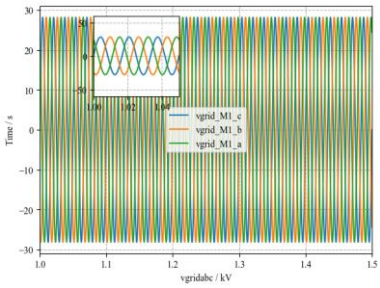

Fig. A17.3-76: Grid side voltage for a generic PV plant.

As illustrated in Fig. A17.2-7, the grid-side voltage of the PV plant exhibits improved stability with the integration of the additional capacitance. Additionally, Fig. A17.2-8 demonstrates that the active power tracks its reference values, with some harmonics. The presence of non-zero reactive power in Fig. A17.2-8 is a consequence of the additional capacitance.

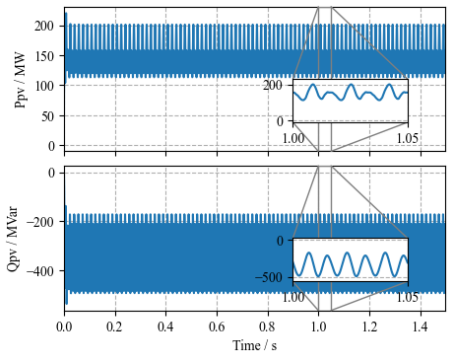

Fig. A17.3-77: Active and reactive power for all PV modules.

ST-17.3. Demonstration of generic PV plant in generic grid model

EMT and TS Simulations in IEEE Nine-Bus System with 75% Renewable Penetration:

Generation loss simulation comparison: The generation loss events are compared between EMT and TS simulations of the IEEE nine-bus scenario with 75% renewable generation. Here, one unit of Gen 3 with 15 MW power generation is tripped. The frequency response at bus 8 is shown in Fig. A17.3-1.

It is observed that the steady state values of the frequencies after the gen loss are almost the same. However, the frequency nadir is deeper in the PSCAD simulation.

Effect of voltage dependent current limit (VDL) logic in inverter control: Next, the effect of VDL is added in the inverter control of the replaced plants in the TS models. The responses after a three-phase self-clearing fault simulation at bus 4 are shown in Fig. A17.3-2 for the 75% renewable scenario. It is observed that, when voltage drops below 0.25 pu, the active and reactive power generation ceases for Gen 1 and 2 (which are renewable plants) in the presence of VDL logic.

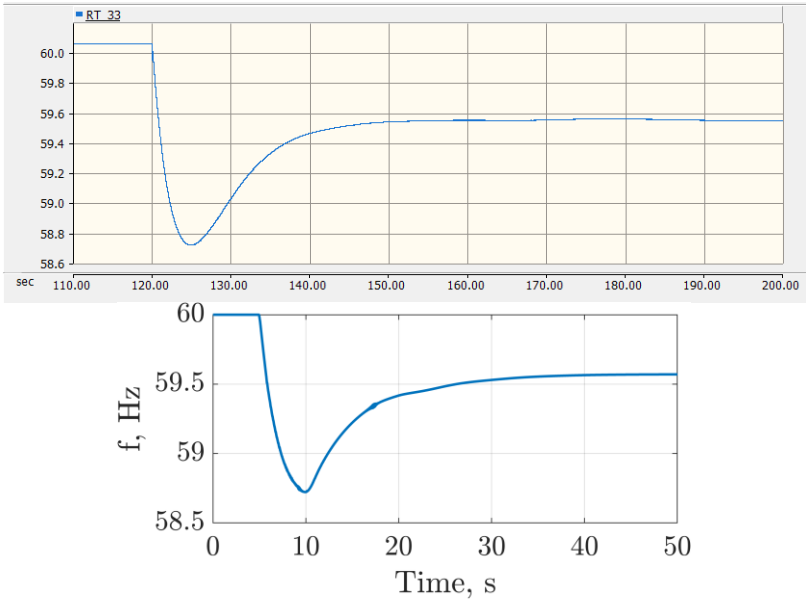

Fig. A17.33-1: Frequency plot after the generation loss event from: (top) PSCAD simulation and (bottom) PSSE simulation.

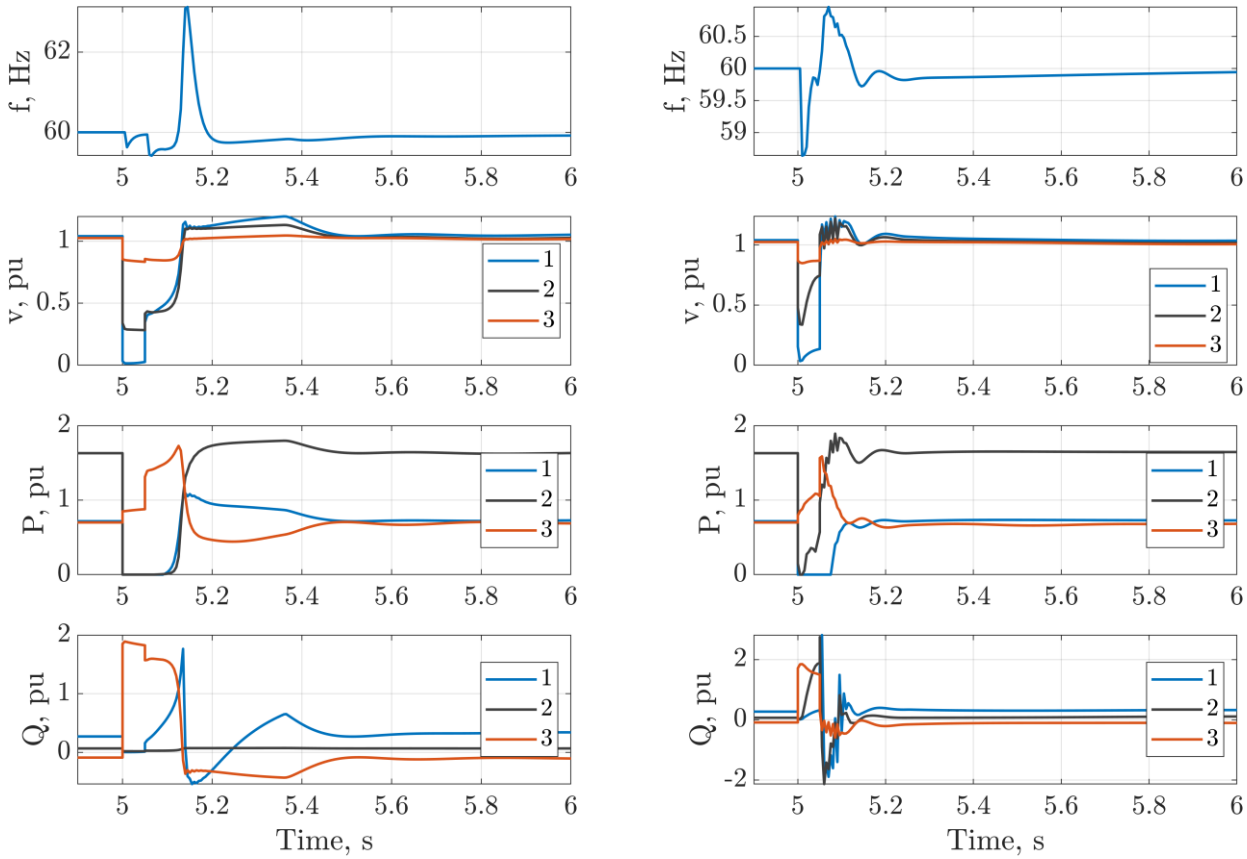

Fig. A17.3-2: Response from TS model after three-phase self-clearing fault event at bus 4: (left) with VDL logic and (right) without VDL logic.

References:

[1] North American Electric Reliability Corporation. *1200 MW Fault Induced Solar Photovoltaic Resource Interruption Disturbance Report.*

[2] North American Electric Reliability Corporation. *900 MW Fault Induced Solar Photovoltaic Resource Interruption Disturbance Report.*

[3] North American Electric Reliability Corporation. *April and May 2018 Fault Induced Solar Photovoltaic Resource Interruption Disturbances Report.*

[4] Enernex LLC, *Utility Scale Solar Forecasting, Analysis and Modeling Report,* February 2017.

[5] AECOM, *EMT and RMS Model Requirements: Findings on Concerns Raised by the AEMC*, June 2017.

[6] North American Electric Reliability Corporation, *April and May 2018 Fault Induced Solar Photovoltaic Re-Source Interruption Disturbances Report*, Jan. 2019.

[7] North American Electric Reliability Corporation. *San Fernando Disturbance*, Joint NERC and WECC Staff Report, November 2020.

[8] Electranix Corporation, E-Tran, version 5.2, 2021. [Online]. Available: https://www.electranix.com/.

[9] PSCAD/EMTDC v. 4.2.1, Manitoba HVDC Research Centre, Winnipeg, MB, Canada.

[10] Western Electricity Coordinating Council, en-us. [Online]. Available: https://www.wecc.org.

[11] E-TRAN, ELECTRANIX Corporation, Winnipeg, Canada, http://www.electranix.com/ETRAN/.

[12] Suman Debnath, Madhu Sudhan Chinthavali, Jingfan Sun, Phani Ratna Vanamali Marthi, Supriya Chinthavali, Sangkeun Lee, Marcelo Elizondo, Yuri V. Makarov, Qiuhua Huang, Yuan Liu, Ahmed A. Tbaileh, Mallikarjuna Vallem, Harold Kirkham, Nader Samaan, Qian Zhang, Joshua Novacheck, and Jessica Lau. *Models and methods for assessing the value of HVDC and MVDC technologies in modern power grids*, GMLC Technical Report, United States, 2019.

[13] North American Electric Reliability Corporation, “Reliability Guideline: Improvements to Interconnection Requirements for BPS-Connected Inverter-Based Resources,” Sep. 2019.

[14] North American Electric Reliability Corporation, Western Electricity Coordinating Council, *900 MW Fault Induced Solar Photovoltaic Resource Interruption Disturbance Report*, Atlanta, GA, Feb. 2018.

[15] North American Electric Reliability Corporation, Western Electricity Coordinating Council. *April and May 2018 Fault Induced Solar Photovoltaic Resource Interruption Disturbances Report*, Atlanta, GA, Jan. 2019.

[16] North American Electric Reliability Corporation, Western Electricity Coordinating Council, “San Fernando Disturbance,” Atlanta, GA, Nov. 2020.

[17] IEEE Standard for Interconnection and Interoperability of Distributed Energy Resources with Associated Electric Power Systems Interfaces, IEEE Standard 1547-2018 (Revision of IEEE Std 1547-2003), pp.1–138, 6 April 2018.

[18] Standard for Interconnection and Interoperability of Inverter-Based Resources Interconnecting with Associated Transmission Electric Power System, IEEE Standard P2800, 2020.

[19] North American Electric Reliability Corporation, Standard PRC-024-2 “Generator Frequency and Voltage Protective Relay Settings,” Atlanta, GA, Jan. 2018.

[20] C. Loutan, P. Klauer, S. Chowdhury, S. Hall, M. Morjaria, V Chadliev, N Milam, C. Milan, V. Gevorgian, *Demonstration of Essential Reliability Services by a 300-MW Solar Photovoltaic Power Plant*, National Renewable Energy Laboratory, CO, USA, Tech. Rep. NREL/TP-5D00-67799, 2017.

[21] North American Electric Reliability Corporation, *1,200 MW Fault Induced Solar Photovoltaic Resource Interruption Disturbance Report*, Atlanta, GA, June 2017.

[22] Reigh Walling, Abraham Ellis, Sigifredo Gonzalez, *Implementation of Voltage and Frequency Ride-Through Requirements in Distributed Energy Resources Interconnection Standards*, Sandia Technical Report, SAND 2014-3122, April 2014.

[23] R. K. Varma and H. Maleki, “PV Solar System Control as STATCOM (PV-STATCOM) for Power Oscillation Damping,” in *IEEE Transactions on Sustainable Energy*, vol. 10, no. 4, pp. 1793–1803, Oct. 2019, doi: 10.1109/TSTE.2018.2871074.

[24] Midcontinent Independent System Operator, “Reliability Integration Impact Assessment,” July 2019.

[25] John Schmall, Electric Reliability Council of Texas, “IBR Damping Support Revision Request Update,” August 2020.

[26] The Massive InteGRATion of power Electronic devices (MIGRATE), https://www.h2020-migrate.eu/_Resources/Persistent/b955edde3162c8c5bf6696a9a936ad06e3b485db/19109_MIGRATE-Broschuere_DIN-A4_Doppelseiten_V8_online.pdf.

[27] ENTSO-E Technical Group on High Penetration of Power Electronic Interfaced Power Systems, "High Penetration of Power Electronic Interfaced Power Sources and the Potential Contribution of Grid Forming Converters," Brussels, Belgium, Jan. 2020.

[28] *2021 SB 100 Joint Agency Report, Achieving 100% Clean Electricity in California*. https://www.energy.ca.gov/publications/2021/2021-sb-100-joint-agency-report-achieving-100-percent-clean-electricity

[29] PSS/E, *Program Operation Manual*, SIEMENS Power Technologies, Inc., New York, USA.

[30] R. Rosso, S. Engelken and M. Liserre, "Robust Stability Investigation of the Interactions Among Grid-Forming and Grid-Following Converters," in *IEEE Journal of Emerging and Selected Topics in Power Electronics*, vol. 8, no. 2, pp. 991–1003, June 2020, doi: 10.1109/JESTPE.2019.2951091.

[31] P. Kundur, N. Balu, and M. Lauby, *Power System Stability and Control*, from EPRI *Power System Engineering Series*. McGraw-Hill Education, 1994.

[32] California Energy Commission, GIS Open Data. Available: https://cecgis-caenergy.opendata.arcgis.com/.

[33] North American Electric Reliability Corporation, "San Fernando Disturbance," Nov. 2020.

[34] D. Bucco et al. "Protection challenges for North America's first combined cable/overhead double-circuit 500 kV transmission line with mutual coupling," *2017 70th Annual Conference for Protective Relay Engineers (CPRE)*, 2017, pp. 1–15,

[35] Pierno, L. P. Di Noia, L. Rubino, "Ancillary services provided by PV power plants," *Leonardo Electronic Journal of Practices and Technologies*, Issue 28, 15. 57–76, January–June 2016.

[36] https://www.eia.gov/electricity/monthly/epm_table_grapher.php?t=table_6_06.

[37] https://www.iid.com/home/showpublisheddocument/9280/636927586520070000.

[38] https://www.utilitydive.com/news/la-scraps-plan-to-rebuild-3-gas-plants-moves-towards-100-renewable-energy/548218/.

[39] https://www.spglobal.com/marketintelligence/en/news-insights/trending/f6k0ng9h0mexdz6lgba_9g2.

[40] https://www.kpbs.org/news/2021/apr/05/after-nearly-50-years-carlsbads-iconic-landmark-co/.

[41] https://www.sierraclub.org/press-releases/2021/04/smud-commits-retire-all-gas-plants-reach-100-clean-energy-2030.

[42] https://www.planetizen.com/news/2019/08/105583-repowered-southern-california-natural-gas-power-plant-will-have-lots-green.

[43] https://www.smud.org/-/media/Documents/Corporate/Environmental-Leadership/ZeroCarbon/2030-Zero-Carbon-Plan-Technical-Report.ashx.

[44] https://www.ucsusa.org/sites/default/files/attach/2018/08/Turn-Down-Technical-Appendix.pdf.

[45] https://www.psehealthyenergy.org/wp-content/uploads/2020/05/California.pdf

[46] California ISO, “Reliability Assessments and Study Updates,” 2021–2022 Transmission Planning Process Stakeholder Meeting September 27–28, 2021, http://www.caiso.com/InitiativeDocuments/Day1Presentation-2021-2022TransmissionPlanningProcess-Sep27-28-2021.pdf.